Università degli Studi di Firenze
Dottorato di ricerca in Fisica e Astronomia
Dipartimento di Fisica e Astronomia

Metal abundances of star forming regions and young open clusters: towards a new paradigm with the Gaia-ESO Survey

Candidate
Lorenzo Spina

Supervisors
Dr. Francesco Palla

Dr. Sofia Randich

PhD Coordinator
Prof. Roberto Livi

---

ciclo XXVI, 2010-2013

Università degli Studi di Firenze, Dipartimento di Fisica e Astronomia.

Contents

Chapter 1

Introduction

> The principal value of abundance determinations from stellar spectra is the clues they give to the nuclear history of stellar matter and, more generally, of the matter in the whole Galaxy.
>
> R. Cayrel, 1966

1.1 Why elemental abundances?

The study of the formation and evolution of galaxies and their constituent stellar populations is still one of the major challenges in contemporary astrophysics. Observations of galaxies at great distances and large look-back times are fundamental for this effort, as is the detailed examination of the various stellar components of the Milky Way.

Beyond the natural curiosity to know what stars are made of, a vast amount of underlying information is locked up in the specific stellar distribution of chemical elements. In fact, through the elemental composition, we can obtain evidence concerning the type of nuclear reactions occurring inside the stars and the internal mixing mechanisms, as well as information on the stellar interiors. In addition, light elements (such as lithium and beryllium), whose depletion in the stellar atmospheres is a function of age, can be used as a stellar clock providing insights on the evolutionary stage of stars. Last but not the least, abundances of given chemical elements in stars are excellent tracers of the formation and evolution of our Galaxy and are also commonly used as signatures of their evolutionary stage, as well as the environment where those stars were born (bulge, halo, thin and thick disk). This approach is commonly dubbed ”Chemical tagging”, as vividly synthesized in the following citation:

> *We now conjecture that the heavy element metallicity*[1] *dispersion may provide a way forward for tagging groups of stars to common site of formation. With sufficiently detailed spectral line information, it is feasible that the chemical tagging will allow temporal sequencing of a large fraction of stars in manner analogous to building a family tree through DNA sequencing.* (Freeman & Bland-Hawthorn 2002)

It is well known that different elements are produced in different environments, under different physical conditions and by stars with different masses and evolutionary timescales. The α-elements (such as silicon, calcium, oxygen and titanium) are mostly produced during the explosions of massive stars (M>8$M_{\odot}$) in type II supernovae (SNII), with a small contribution from type Ia supernovae (SNIa).On the other hand, iron-peak elements (such as iron, manganese, cobalt, chromium and nickel) are produced mainly by SNIa. Most remarkably, the timescales over which the two phenomena occur are very different: SNII have short timescale ($\sim$10 Myr) compared to the $\sim$1.5 Gyr of the SNIa that for this reason show a delayed contribution to the chemical evolution of the Milky Way. Thus, each component of our Galaxy presents a characteristic abundance pattern of elements, iron-peak and α-elements with respect to iron. A recent evidence of the capabilities of detailed chemical analysis is giving clues on the nature of the Galaxy is provided in a recent study by Recio-Blanco (2014). These authors have separated different components of the Milky Way in a diagram with the α-elements over iron abundances [α/Fe] as a function of the metallicity for a sample of stars targeted by the Gaia-ESO Survey. Their result, displayed in Fig 1.1, shows that the thick disk and halo stars are richer of α-elements than

---

[1] In the astronomical community, all elements other than hydrogen and helium (the main components of stars) are considered as ”metals”. The star metallicity (M) is the proportion of its matter made up of metals. Often, the iron content is used as a proxy for the overall metallicity.

those of the thin disk and that halo stars are significantly more metal-poor. These properties of the Galaxy components reflect different star formation and evolution of their stellar populations. The different behavior of the thin and thick disk in terms of [α/Fe] abundances has been observed by many other authors, such as Fuhrmann (2004); Reddy et al. (2006); Bensby et al. (2007); Adibekyan et al. (2013), among others.

Spectroscopy is one of the most important tools that an astronomer has for studying the universe. The importance of spectroscopy is that the light is "broken" in its components making it possible to identify several spectral features, such as absorption and emission lines. Thus, in conjunction with atomic physics and models of stellar evolutions, stellar spectroscopy allows us to determine a variety of physical conditions in distant stars: their age, temperature, luminosity, extinction from interstellar dust, accretion activities, projected rotational velocity, membership, space motion and the presence of hidden companions such as tight binaries and even exoplanets. Last but not least, spectroscopy allows us to determine the chemical composition of stellar atmospheres.

1.2 Why elemental abundances in young clusters and star forming regions?

Stellar clusters are groups of stars that are formed within the same nebula. As a result, members of a cluster share approximately the same age, kinematics and elemental content. Young Open Clusters (YOCs) and Star Forming Regions (SFRs) represent associations with ages $\lesssim$100 Myr. They are characterized by the presence of pre–main-sequence (PMS) stars, whose gravitational contraction is still in progress, and, only in SFRs (age$\lesssim$5 Myr), embedded protostars and molecular clumps, whose dense cores are the site in which the gas-to-star process takes place. The evolution of these young stellar systems partially depends on how quickly the gas is dissipated. The presence of one or more high-mass star may boost this process causing an expansion of the group of stars, after the sudden removal of the parental cloud through ionizing radiation and powerful winds. These systems, known as "OB associations", are extended as ordinary clusters (1-10 pc) or large several hundred of parsec. Famous associations like Orion, Scorpius-Centaurus and Vela are characterized by the presence of several massive members.

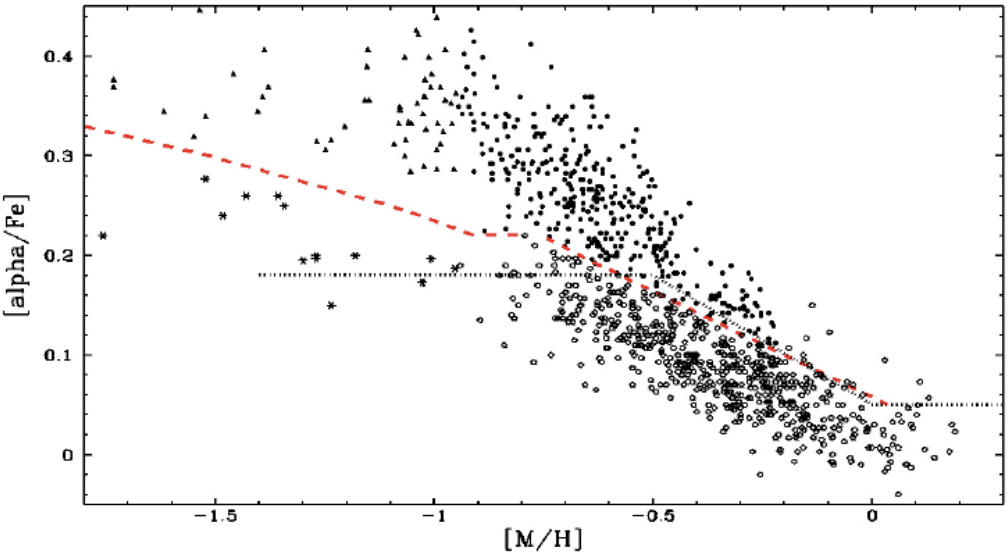

Figure 1.1: α-elements over iron abundances as a function of metallicity for a sample of field stars (Gaia-ESO Survey data). Filled dots are thick disk stars, open circles are thin disk objects. Metal-poor stars ([M/H]<-1.0) from the galactic halo are marked with filled triangles and asterisks, depending on their [α/Fe]. A red dashed line is plotted in order to identify the separation between the thick and thin disk sequences. For comparison, the dotted line represent the separation found by Adibekyan et al. (2013). From Recio-Blanco (2014).

Other systems, born in dark cloud complexes that never contained massive stars, are called "T associations" and their extension reflects the initial dimension of the cloud. Nearby examples include Chamaeleon I and Rho Ophiuchi.

Many photometric and spectroscopic surveys of young stars, both with circumstellar accretion disks (the so-called classical T-Tauri stars) and without disks (weak-lined T-Tauri stars), have been performed in order to characterize these regions. Members of these young associations can be identified through several observational methods. A widely used method to reveal PMS stars is through the Hertzsprung-Russell diagram, since these objects have not yet reached the main sequence. Also near- and far-infrared photometry is widely used, since it allows us to detect the infrared excess of circumstellar disks or from the residual envelope of the protostellar cores. All T Tauri stars have an elevated X-ray flux and atmospheric emission of several lines (such as Hα at 6563$\mathring{A}$, He I at 5876$\mathring{A}$, Hβ at 4861, etc...). Also, the detection of the strong lithium absorption line at $6708\mathring{A}$ is a main youth indicator: every star at birth has a Li reservoir equal to the interstellar Li abundance (log N(Li) + 12 = 3.3) that is then depleted as the star ages.

In principle, this large variety of diagnostics, that are independent and complementary to each other, makes the identification of stars associated to young stellar systems more straightforward than that of older cluster members. The consequence is that YOC/SFRs have been widely studied and, so far, their features and characteristics, such as age, distance, Initial Mass Function (IMF)[2], fraction of stars with disks, are well constrained for many of them. On the other hand, the chemical content of these young associations is difficult to determine, mainly because of the presence of circumstellar gas, accretion activity, or fast stellar rotation that affect the spectral lines and continuum.

Nevertheless, determining the metal content of YOC/SFRs members provides a tool to address different issues, such as the determination of cluster fundamental parameters, the timescale of disk dissipation, the metal-rich nature of planet-host stars, the chemical tagging and the possibility of chemical pollution due to environmental effects.

1.2.1 Determination of cluster fundamental parameters

One of the most powerful tool in stellar astronomy is the color-magnitude diagram (CMD). This plot, together with the theoretical models of stellar evolution, is widely used to derive many important parameters that characterize each YOC/SFR, including distance, age, IMF, stellar formation history, etc.. In this well-known procedure, beside the accuracy of the photometric observations, a significant source of uncertainty is represented by the model assumptions, especially on the stellar metallicity (Forestini 1994).

Metallicity has an effect on the internal structure of stars and on their surface proprieties through opacity: a large variety of atoms in the stellar atmospheres absorb photons of determined energies giving birth to the many absorption features, peculiar of each element. Lowering the metallicity decreases the opacity, the property of stellar material to obstruct and absorb photons. *Viceversa*, more metals absorb more energy from the interior of

---

[2] The IMF is an empirical function that describes the distribution of initial masses for a population of stars.

the star. Thus, the visible properties of stars and their position in CMDs are affected in three ways:

- Lower-metallicity stars are slightly more luminous (at fixed mass).
- Lower-metallicity stars have smaller radii and higher temperatures and earlier spectral types at a given mass.
- Lower-metallicity stars have less line-blanketing, making them bluer than higher-metallicity stars of the same spectral type.

Sherry et al. (2008), discussing the case of σ Ori in the Orion OB association, quantified the effect of metallicity variation on the visual properties of the stars and on the derivation of the distance through the fitting of the cluster sequence in a CMD. They examined the change in absolute magnitude M_V of the ZAMS from the models of Lejeune & Schaerer (2001) at $(\mathrm{B}-\mathrm{V})_0=-0.21$ mag as the metallicity varies from z = 0.040 ([Fe/H][3] = +0.3 dex) to z = 0.004 ([Fe/H]=−0.7 dex). Figure 1.2 shows that the relative change is given by $\Delta\mathrm{V}\sim-0.75\times[\mathrm{Fe/H}]$. The dashed line marks the average value of [Fe/H]=−0.16±0.11 dex derived by Cunha et al. (1998) for the Orion OB association and the two dotted lines are the $\pm1\sigma$ values indicating that the large uncertainty in [Fe/H] result in a correction to the ZAMS in the range of +0.04 and +0.2 dex. Sherry et al. (2008) concluded that, assuming the sub-solar composition, the distance of σ Ori would be 420 pc instead 444 pc obtained with a solar value. The effect is small, but the same authors underline that stars with greater B−V colors are more sensitive to metallicity, proving that different assumptions on the metal content can affect our interpretation of observational data.

1.2.2 Disk dissipation and planet formation

Stellar metallicity has an impact on the evolution of circumstellar disks and on their lifetimes. Ercolano & Clarke (2010) used their models, based on thermal and photoionization calculations, to determine a power-law dependence of the disk lifetime on metallicity due to photoevaporation $t_{phot}\propto Z^{0.5}$. Their result is specific to a photoevaporation mechanism driven mainly by X-ray radiation as it relies on the significant reduction of the gas opacity

---

[3] The metallicity is usually indicated as [Fe/H]=log(n(Fe)/n(H))-log(N(F$e_\odot$)/n($H_\odot$))

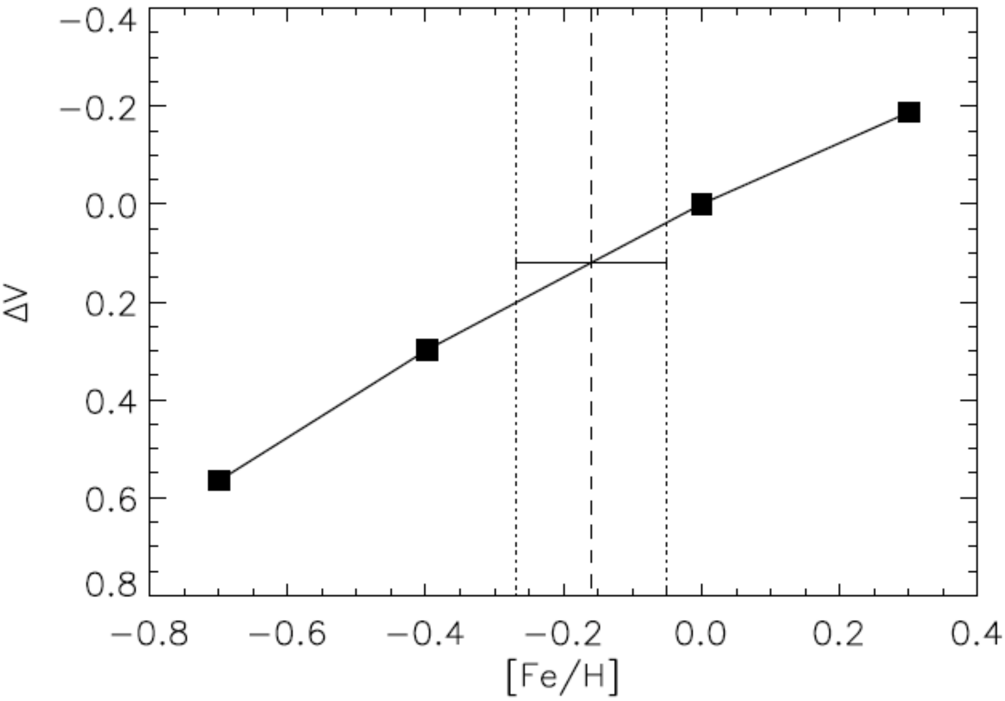

Figure 1.2: The relative change in M_V of the 2 Myr isochrone as a function of the iron abundance (Sherry et al. 2008).

with metallicity. On the other hand, they have also shown that a dispersal mechanism based on planet formation yields disk lifetimes characterized by a strong negative power of metallicity $t_{planet} \propto Z^{-2.5}$-$Z^{-5}$. Observational studies of the Cloud 2 in the extreme outer Galaxy conducted by Yasui et al. (2010) find shorter disk lifetimes (<1 Myr) for this metal-poor environment ([O/H]∼−0.7 dex), compared to the solar metallicity environments (∼5-6 Myr). Viceversa, Spezzi et al. (2012), based on HST mass accretion rate measurements, suggest that disks in the metal poor clusters in the Large Magellanic Clouds may be long-lived with respect to the Milky Way.

A census of disk fractions in regions of lower metallicities than the solar neighbourhood will be crucial to determine which is the dominant mechanism responsible for the rapid demise of protoplanetary discs. If this scenario is confirmed, the metallicity would have also a direct impact on the ability of a circumstellar disk to form planets.

1.2.3 Metallicity and planet-host stars

There are essentially two main and competitive planet formation models: the core-accretion model (e.g. Pollack et al. 1996; Ida & Lin 2004; Mordasini et al. 2009) and the disk instability model (e.g. Boss 1997, 2002). In the conventional core-accretion scenario, the formation of planetesimals starts from the condensation of heavy elements (metals). In this context, the study of the metallicity is very important. Previous studies that aimed to clarify whether the planet-hosting stars are different from stars without planets in their content of individual heavy elements (other than iron) yielded contradictory results. Since the discovery of the first exoplanet around a solar-type star, 51 Peg b (Mayor & Queloz 1995), more than 1000 exoplanets have been discovered to date. Although the strong correlation observed between the planet-hosting stars metallicity and the frequency of Jupiter-like planets (Santos et al. 2001, 2004; Valenti & Fischer 2005) lends support to the scenario of planetary growth through accretion of solid, metal-rich material; this evidence appears to almost vanish when dealing with the less massive planets, such as Neptune and super-Earth-like planets (Udry et al. 2006; Sousa et al. 2008, 2011; Mayor et al. 2011; Adibekyan et al. 2012; Buchhave et al. 2012). Several studies have shown that iron-poor planet-hosting stars tend to be enhanced in refractory elements[4], such as Mg, Al, Sc, Ti, Si, V, and Co (e.g. Haywood 2008, 2009; Kang et al. 2011; Adibekyan et al. 2012). This property gives us interesting hints about the planet formation process. In fact, even if the iron content is used as a proxy of the overall metallicity of planet hosts, iron is not the only abundant refractory element in the solar system. There are other fairly abundant elements (e.g., Mg and Si) with condensation temperatures comparable to iron (Lodders 2003) that are very important contributors to the composition of dust in planet forming regions and represent the principal components of rocky-type planets (e.g. Gonzalez 2009). The discovery of YOC/SFRs with high content of iron or other refractory elements would allow us to study their stellar population during the phase of planet formation.

It is important to note that the presence of planets may also have an effect on the host-star metallicity. A fair number of recently discovered extrasolar planet candidates have surprisingly small orbits (even smaller than

---

[4] The term refractory elements denotes metals with a very high melting point ($\gtrsim$1300 K). The opposite of refractory is volatile.

the orbit of Mercury), which indicate that considerable orbital migration takes place in protoplanetary systems. A natural consequence of orbital migration is the accretion, destruction, and through mixing into the convective envelope of the central star, a metallicity enhancement. However, the effect of planet accretion on stellar metallicity is strongly dependent upon the stellar mass. Stars with masses comparable to that of the Sun have large convective envelopes for nearly the entire time interval over which planets are expected to be accreted. These stars will show essentially no metal enhancements, because the accreted material would be more diluted in the extended outer convection zone. Higher mass stars with M_{*}>1.5 $M_{\odot}$, have much smaller convective envelopes during their PMS phase and can suffer relatively larger metal enhancements (e.g., Laughlin & Adams 1997; Théado & Vauclair 2012).

1.2.4 Environmental effects and chemical tagging

Knowledge of the chemical content of YOC/SFRs allows us to investigate the common origin of different sub-groups in a given association and sheds light on the possible presence of enrichment effects caused by the explosion of a nearby SN (Cunha et al. 1998; Preibisch & Zinnecker 2007; D'Orazi et al. 2009; Biazzo et al. 2011a and references therein). It is expected that members of an association that formed from the same parent nebula should display the same elemental abundances. However, many OB associations consist of distinct sub-groups with different ages. In this so-called *sequential star formation* scenario, supernovae shocks are thought to trigger new star formation events and, since these explosions are nucleosynthesis sites, they can chemically enrich parts of the surrounding interstellar gas with some specific elements (α-elements or iron-peak elements; Cunha & Lambert 1992, 1994). A cartoon of the triggered star formation scenario for the Sco-Cen OB association is shown in Fig. 1.3. Finding direct evidence of such selective enrichment in YOC/SFRs would clearly give insights into a process that has occurred innumerable times in the past, not just in our own Galaxy.

The possible presence of chemical enrichment due to triggered star formation has so far been investigated in one SFR, i.e. the Orion OB1 association. This region iscomposed of four sub-groups of different ages: the oldest is OB1a with an age of ~10-15 Myr and the youngest is OB1d, with $\tau \lesssim 3$ Myr. In a plausible scenario, the star formation history begun about 10 Myr ago

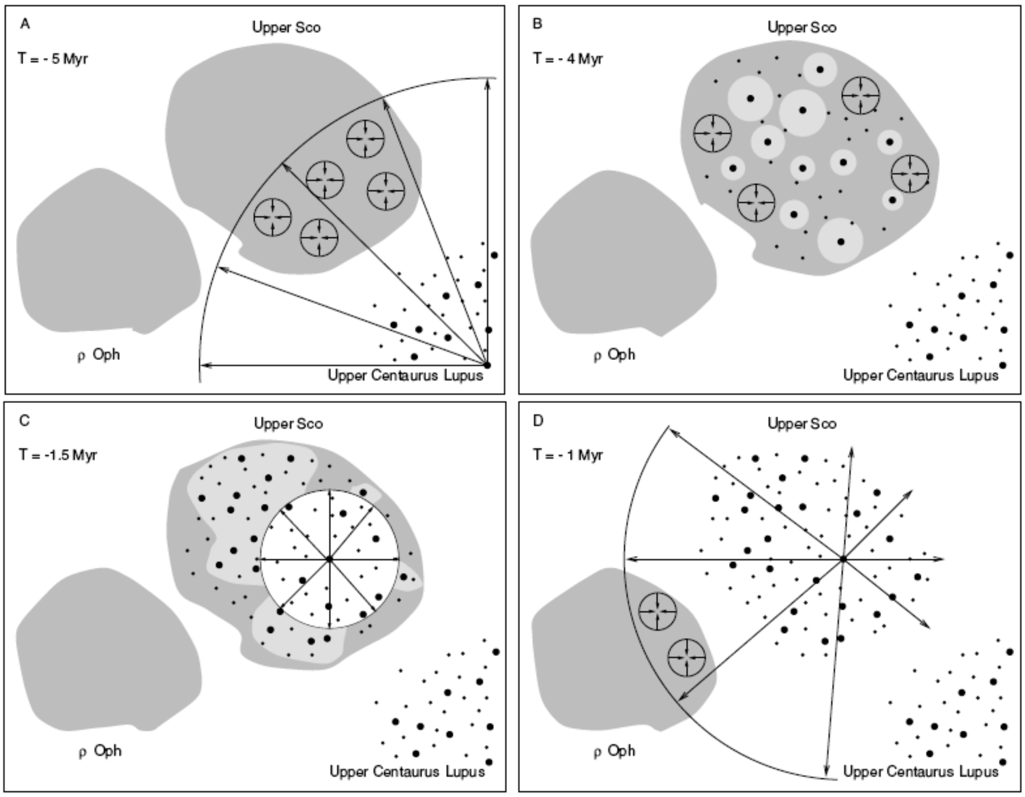

Figure 1.3: Cartoon of triggered star formation in the Sco-Cen association (from Preibisch & Zinnecker 2007). Panels show the sequential star formation process, from its beginning (panel A; up-left) to triggering of star formation activity that is still ongoing in Rho Oph (panel D; low-right).

at one extremity of the association, namely OB1a and then propagated to the other regions as the result of compression by supernovae shock waves. If this scenario is indeed correct, the nucleosynthetic products might have enriched the gas from which the younger generation of stars have subsequently formed. Then, one would expect to detect different abundances across the cluster subgroups with the youngest ones showing a distinctive chemical enrichment. Studies of this region have produced controversial results. In particular, the most recent work of Biazzo et al. (2011a) has found that all the various subgroups show the same solar iron and α-elements abundance, with the notable exception of the youngest association (OB1d, the Orion Nebula Cluster) which has the lowest iron content [Fe/H]$=-0.13\pm0.03$, contrary to expectations.

1.2.5 Tracers of the current chemical composition of the Solar neighborhood

The study of the chemical composition of the Milky Way, as well as its structure and kinematic, is of fundamental importance for the understanding of its formation and evolution. The abundance determinations of open clusters, with a wide range of properties (age, Galactocentric distance, Galactic azimuth, orbital eccentricity, etc...) allow us to trace the chemical pattern of the Galactic thin disk and its evolution in space and time (e.g., Friel 1995). In this regard, YOC/SFRs are of particular interest since they are still close to their birthplaces and contain homogeneous stellar populations that have not had time to disperse through the Galactic disc. Thus, they are key objects in order to trace the current chemical composition of the Solar neighborhood.

1.2.6 State of the art and open questions

In spite of all these exciting aspects, even if in the last decade elemental abundances have been obtained for numerous open clusters with ages >100 Myr Magrini et al. (2009), only few studies have addressed the issue of the metal content of PMS clusters and star forming regions (see, e.g., Padgett 1996; James et al. 2006; Santos et al. 2008; D'Orazi et al. 2009; D'Orazi & Randich 2009; Biazzo et al. 2011a,b). So far, the evidence is for a metallicity close to, or slightly lower than the solar value (DOrazi et al. 2009; Biazzo et al. 2011a), suggesting that either the Sun was formed in an inner region of the Galactic disk, or that the nearby interstellar medium experienced a recent infall of metal-poor gas. On the other hand, D'Orazi & Randich (2009) demonstrated that the abundance pattern of YOC in the solar neighborhood is identical to the solar distribution, concluding that the Sun was most likely born at the present location.

Biazzo et al. (2011a) presented a brief, but comprehensive review of the metallicity determinations in YOC/SFRs. In Fig. 1.4, taken from their paper, they compare the distribution of [Fe/H] of the SFRs within 500 pc of the Sun with that of i) open clusters younger than ∼150 Myr within the same distance from the Sun, and ii) young nearby loose associations. Biazzo et al. note that the three distributions are characterized by a small dispersion; even though, the cluster distribution is shifted towards somewhat higher metallicities than SFRs and young associations. Thus, they conclude that, not only the SFRs are more metal-poor than the Sun, but they are on average more metal-poor than YOCs, which should be representative of the metallicity in the solar neighborhood. However, the [Fe/H] values of the SFRs are based on a small number of members. Moreover, the offset between the two distributions is small and significant discrepancies in the metallicity determination exist for some regions: for example, Santos et al. (2008) find [Fe/H]=−0.08±0.12 for Rho Ophiucus, compared to the value [Fe/H]= 0.08±0.07 derived by Padgett (1996). This indicates that additional homogeneous studies must be carried out before the conclusion that SFRs are more metal-poor than the Sun and open clusters can be definitely drawn.

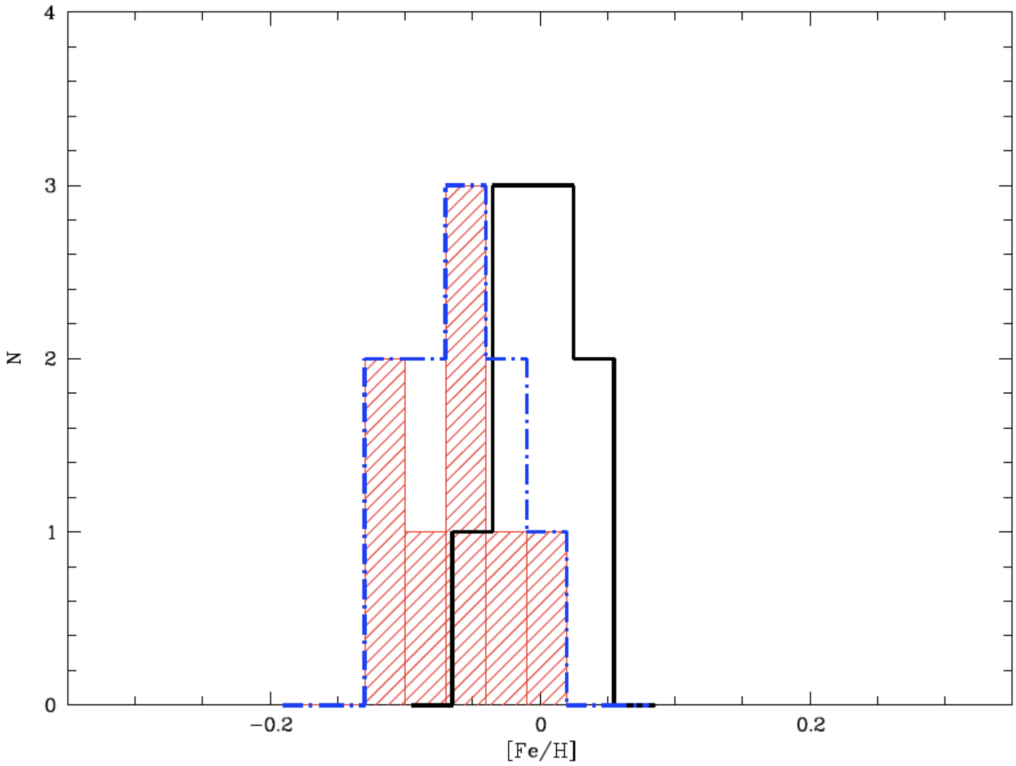

Figure 1.4: [Fe/H] distribution for: SFRs within 500 pc from the Sun (dashed histogram), young nearby loose associations (dot-dashed line), and open clusters younger than 150 Myr and within 500 pc from the Sun (solid line). From Biazzo et al. (2011a).

To summarize:

- Determinations of cluster fundamental parameters, such as age and distance, are often based on the assumption of solar metallicity. How this assumption is realistic for YOC/SFRs and how it affects their final parameters?
- It has been strongly debated if metallicity has an effect on the dispersal of circumstellar disks. Do disks in metal-poor SFRs have significantly shorter lifetimes?
- Several studies have proposed correlations between the chemical abundances of some peculiar elements in stars and their probability to host planets. Are SFRs rich of these elements? Is it possible to infer by their abundance determinations if these young environment are forming planets?
- Can events of planet accretion affect the stellar metallicity?
- In a sequential star formation scenario triggered by SNe, the nucleosynthetic products might enrich the gas from which the younger generation of stars have subsequently formed. Is it possible to observe clear chemical segregation in different sub-groups of the same association due this pollution of metals?
- YOCs and SFRs are critical objects to study the current chemical composition of the Solar neighborhood. How is their chemical content in relation to that of Sun and of the oldest stars in vicinity?
- Are SFRs more metal-poor than YOC? If so, which is the reason?

So far, the absence of a statistically significant sample of YOC/SFRs with a metallicity determination prevented us from addressing these fundamental issues. The study carried out during the period of my PhD provides a first endeavor for a more comprehensive and homogeneous understanding of the chemical content of the youngest generation of stars in the Solar neighborhood.

Thesis organization This thesis is organized as follows: in Chapter 2 I illustrate the scientific rationale of the Gaia-ESO Survey, its observing strategy, management and structure. Chapter 3 describes the methods, tools and technical details of the abundance analysis determination. As validation of my own analysis procedure, in Chapter 4 I present the determination of atmospheric parameters and chemical abundances on 1700 spectra. This work will be ready for publication in the first terms of 2014. In Chapter 5 I describe my role and my contribution to the Gaia-ESO Survey during the period of my PhD. Chapters 6 and 7 include the papers on metallicity determinations in Gamma Velorum and Chamaeleon I respectively. The first paper has been already submitted to Astronomy & Astrophysics, while the second is under the internal Gaia-ESO refereeing. Finally, the concluding remarks and the future perspectives are presented in Chapter 8.

Chapter 2

The Gaia-ESO Survey

> The history of the living world can be reduced to the elaboration of ever more perfect eyes at the heart of a cosmos where it is always possible to discern more.
>
> ---
>
> Pierre Teilhard de Chardin, 1955

The crucial requisites to addressing all the topics mentioned in the previous chapter and, more in general, understanding the history of the formation and evolution of the Galaxy and its components, consist in three aspects: i) mapping the chemical element distribution, which gives insights on timescales of chemical evolution, as well as chemical mixing and accretion length scales (in terms of space and time), star formation histories, nucleosynthesis and internal processes in stars; ii) spatial distributions, which delineate structures and gradients in the Milky Way; iii) kinematics, which relates the dynamical histories of the clusters with the current Galactic chemical distribution.

The Gaia-ESO Survey[1] (Gilmore et al. 2012; Randich & Gilmore 2012) is a Large Public Spectroscopic Survey that benefits of 300 nights on the VLT targeting with FLAMES more than 10^5 stars with well-defined samples covering the bulge, the thick and thin disk and the halo component of the

---

[1] Co-PI are G. Gilmore (University of Cambridge, UK) and S. Randich (INAF - Osservatorio Astrofisico di Arcetri, I)

Milky Way, as well as a very significant sample of 100 open clusters of all ages and masses. The FLAMES spectra will yield: precise radial velocities and good astrometric positions down to V$\sim$19 mag; main stellar parameters; [Fe/H] for several species with GIRAFFE and precise multi-element abundances [X/Fe] with UVES. Thus, the GES is the first survey yielding homogeneous datasets for large samples of both field and cluster stars.

This exceptional amount of data has a considerable stand-alone value because will allow addressing, *inter alia*, the following top-level scientific goals: open cluster formation, evolution, and disruption; calibration of the complex physics that affect stellar evolution; quantitative studies of halo substructure, dark matter and rare stars; nature of bulge; origin of thick disk; formation, evolution, structure of the thin disk; kinematic distribution of the Solar neighborhood.

However the GES will show its extraordinary effort when its data will be combined with the Gaia astrometry. The Gaia mission has been launched on December 19^{th} 2013 and will provide parallaxes and proper motions for 10^9 stars of the Milky Way with an unprecedented precision. It will measure distances for individual stars in open clusters with a precision better than 1% for clusters closer than $\sim$1kpc and better than 10% for almost the open clusters that will be targeted by the GES. Higher accuracies are expected for proper motions, yielding a precision in individual tangential velocities (V_t) of the order of 0.2-0.3 km/s for low-mass stars in clusters up to $\sim$1.5 kpc, and up to larger distances for bright O/B stars. This would allow resolving both peculiar velocities and internal dispersions, which are typically of the order of 0.8-3 km/s (Meibom et al. 2002; Furesz et al. 2008). Gaia will also provide good photometric information, helping to characterize cluster members. Crucially, Gaia, like all spacecrafts, has limited spectroscopic capability[2] and cannot compete with the existent large ground-based telescopes. For these reasons, the GES and Gaia projects will provide complementary information that, combined together, will offer the complete kinematical and chemical view of the Milky Way. In fact, this large amount of information of high quality will allow us, not only, as previously mentioned, to understand how cluster form, evolve, dissolve, and populate the Milky Way, but also to calibrate the complex physics that affects stellar evolution and to measure the Galactic metallicity gradient at different ages with unprecedented accuracy.

---

[2] The spectroscopic instrument on board of Gaia, the Radial Velocity Spectrometer, is a near-infrared (847-874 nm), medium-resolution (R$\sim$11500), integral-field spectrograph.

2.1 Top level science goals for the cluster component

Open cluster are dynamically bound groups of stars that formed together from the same giant molecular cloud, thus their members also have a similar age and chemical composition. Many mechanisms can trigger the cloud collapse and the formation of the cluster. Similarity a variety of internal or external agents can cause the cluster disruption, populating the Milky Way of unbounded stars. Furthermore, stellar populations in open clusters cover stars of all masses and evolutionary stages: each cluster is a snapshot of stellar evolution. For these reasons, the study of open clusters is fundamental for the comprehension of the formation and evolution of stars and the Milky Way, with a strong impact on our understanding of key open issues, such as star formation processes, the cluster dynamical evolution, their eventual disruption and how they populate the Galaxy. In addition, clusters of different ages and born in different locations of the Milky Way, also reveal information on the abundance distribution in the thin disk and its evolution with time. The answer to all these question need the homogeneous data of many open cluster at a wide range of Galactocentric radii and ages.

2.2 Instrument and observing strategy

FLAMES is a multi-fiber instrument with a field of view of 25’ in diameter feeding two different spectrographs covering the whole visual spectral range: GIRAFFE and UVES. GIRAFFE allows the observation of up to 130 targets at the same time or integral field spectroscopy with intermediate resolution (R$\sim$25000 or R$\sim$10000). On the other hand, UVES provides the highest resolution (R=47000) for only up to 7 stars at the same time. Thus, considering the instrumentation in the Southern hemisphere, FLAMES on VLT is the most suitable one to perform an efficient high-resolution survey of the Milky Way.

The Gaia-ESO Survey observing strategy has been designed to deliver the top-level Survey goals. As mentioned before, the Survey includes the Galactic bulge, thick and thin discs and the halo. There is special focus on open clusters at all ages, and on solar neighborhood field stars, as these trace both stellar and Galactic evolution, complement Gaia astrometry, and will benefit most from the most precise Gaia data. The open clusters have mostly been selected from the Dias et al. (2002); Kharchenko et al. (2005) catalogues, and the WEBDA database[3]. Only clusters with excellent available photometry and astrometry, and adequate membership information, have been selected. Cluster selection is optimized to fine-sample age-[Fe/H]-Galactocentric distance-mass parameter space. Open clusters in all phases of evolution (except highly embedded), with ages from 1 Myr to 10 Gyr will be included, sampling different environments and star formation conditions. This provides sufficient statistics to explore the dynamical evolution of clusters. The cluster sample covers the Galactocentric distance range from about 6 up to ∼20 kpc. The same sample will quantify the distribution of metallicity as a function of Galactocentric radius and time. This is a key input to models of the formation and evolution of the disc: it constrains the star forming efficiency as a function of Galactocentric radius, the initial mass function at the time of formation of the disc, the nature of infall from the halo, the role of possible mergers (Magrini et al. 2009); it assesses the radial streaming of gas, the influences of the bulge and of our Galaxys spiral pattern. The total sample includes ∼100 clusters. The YOCs and SFRs sample consists in about 30 associations including: i) targets closer than ∼1500 pc, the distance up to which Gaia will provide transverse velocity with precision better than internal velocity dispersion, matched with equally precise Survey radial velocities (RVs); ii) clusters at larger distances, where O-, B-, A- spectral type stars will be targeted. In the former, the Survey targets the whole population, down to the M-dwarf regime, while in the latter it observes RGB and clump giants, and early main sequence stars.

For all clusters, GIRAFFE will observe faint cluster members (down to I=19), while UVES brighter objects (down to V=16.5), to be used for accurate abundance determination or for which better precision in RV is required. Seven GIRAFFE set-ups will be employed: for late-type stars HR15N/21 are used (spectral ranges 6470-6790 and 8484-9001 $\mathring{A}$ respectively), while for early-type stars (A-O) HR03/05A/06/09B/14A are employed. They access a large enough number of lines to derive RVs, as well as to retrieve key information on the star characteristics (e.g., temperature, gravity, iron and Li abundances, accretion rates, chromospheric activity, rotation). UVES CD3 is most suitable both for early-type (520-nm setting) and late-type (580-nm setting) stars.

---

[3] www.univie.ac.at/webda

2.3 Management and structure of the GES

The Gaia-ESO Survey is lead by Gerry Gilmore and Sofia Randich. The consortium includes some 400 participants in over 90 institutes in Europe, USA, Brazil and Australia. All Survey activities are distributed among 20 Working Groups (WGs), WG0 to WG19, each of which has a WG coordinator. The WG coordinators report to the Co-PIs through a Steering Group, that is composed by 12 members (plus the two Co-PIs) and acts as the project management board to assist the Co-PIs in supporting the whole consortium activities. The tasks of the WGs are to implement the data flow, from target selection, to telescope configuration and observations, from pipeline data processing, detailed spectrum analysis quality/sanity checking and homogenization, to science quality control, documentation and delivery of external data products to both ESO and a dedicated public archive. An overview of the Gaia-ESO Survey data flow process is presented in Fig 2.1.

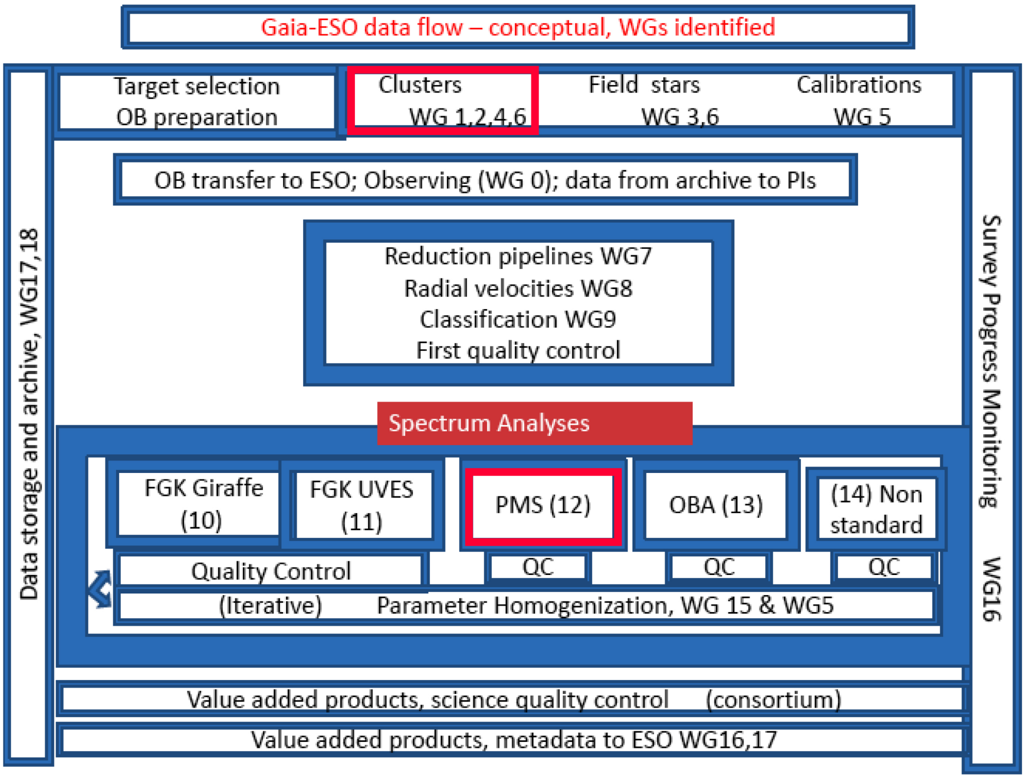

Figure 2.1: Overview of the Gaia-ESO Survey data flow system. The WGs in which I am involved are marked with rex boxes.

2.3.1 Target identification, fiber positioning and OB preparation (WG0,1,2,3,4,5,6)

The overall target selection and strategy is done by the CoPIs. The selection and preparation of the observations of individual targets and fields is conducted by different WGs.

The WGs from 0 to 6 are thought to work in close collaboration between themselves with the main objective of defining the sample of stellar objects that will be targeted by the Survey. WG1 is supposed to perform cluster membership analysis of GES target clusters to the GES astronomical community. WG2 provides auxiliary data (available photometry, proper motions, information on binarity, etc...) for cluster target selection and for the preparation of observations. All this information produced by WG1 and 2 is passed onto WG4 that select the targets of the clusters sample. Likewise WG3 is devoted to the target selection of the field star sample.

Concerning the cluster observations, UVES targets have to be secure members, since FLAMES ensure only 7 UVES ”shots” per exposition and their spectra are the only ones that provide detailed information about the chemical composition. Because of their importance, the few UVES fibers are always assigned to the most secure member stars. This means, depending on the cluster type, that we consider auxiliary literature information on radial velocities and proper motions (for the older clusters) and additionally on X-rays properties, Li abundance, emission, photospheric activity, rotation (for the younger clusters and the SFRs). Also information on stellar rotation and binarity should be taken into account to ensure that chemical analysis can effectively be performed.

On the other hand, about 130 stars can be simultaneously observed with GIRAFFE, thus not such strict selection is requested for this kind of targets. In fact, since one of the fundamental aspects of the Gaia-ESO project is its legacy character, the selection of targets must produce a catalogue representative of a complete and unbiased sample, which is also potentially useful and easily accessible to the astronomical community interested in the same or similar scientific objectives. While the Gaia-ESO aims at reaching a complete coverage of the clusters, practical considerations on the time required force the Survey to limit itself to a representative sample. There are three main constraints that should be considered for tailoring the primary list of target stars:

- *Homogeneity:* the procedure has to be as homogeneous as possible even if the data are not and the clusters under study have very different observational characteristics, such as different magnitude ranges, different degrees of field star contamination, different photometric systems, existence of radial velocity data or good-quality proper motions, etc.
- *Simplicity:* the tools utilized should be easily accessible for anyone, in such a way that the verification and control of the final product can be reproduced by anyone who wishes to do so.
- *Unbiased samples:* only those stars considered with certainty as non-members should be excluded from the final list (i.e., the evident outliers from the stellar distribution of the cluster). Although this criterion entails the possible inclusion of (a significant fraction of) field stars, the final list will be more in line with the general objectives of the project and its character as a legacy program than if a more restrictive purge would be performed.

All this means that the Survey selects the candidate cluster members on the basis of photometry alone, since this is the only way to produced representative and unbiased samples.

WG5 critically selects targets to be observed for internal and external calibrators. The fiber allocation and the configuration of the OBs is entrusted to WG6. Finally, the observing team is coordinated by the WG0. Note that each WG complies with specific guidelines that have been approved by the Steering Group and that regulate all the activities.

2.3.2 Pipeline processing of raw data (WG7,8)

Raw data reduction is performed at CASU[4]/Cambridge (GIRAFFE spectra) and Arcetri (UVES spectra) by WG7. The instrument-specific reduction pipelines are the current ESO systems. Reduction of spectra also involves quality checks performed on all the products of the pipeline and the measure of radial velocities (RVs) and projected rotational velocities (v sin i) for most of the observed sources. In addition, WG7 checks the binarity of the UVES targets through the cross correlation functions (CCFs) of their spectra.

---

[4] Cambridge Astronomical Survey Unit

A dedicated GIRAFFE pipeline has been developed for the special purpose to derive RVs and v sin$i$ with a higher accuracy than the values obtained from the ordinary ESO pipeline. With this new procedure, WG8 achieves RVs with a precision about of 200 m/s.

2.3.3 Object classification (WG9)

The objective of this WG is i) to provide a top-level object classification (e.g., stars vs. quasar or galaxy contaminants) for field targets observed with GIRAFFE; ii) to deliver a preliminary estimate of stellar astrophysical parameters (e.g., effective temperature, surface gravity). This is performed through dedicated algorithms that cross-correlate with templates. The object classification algorithms additionally provide objective quality control information for every spectrum.

2.3.4 Spectrum analysis (WG10,11,12,13,14,15)

The spectrum analysis is performed by five WGs. WG10 and WG11 perform the analysis of GIRAFFE and UVES spectra, respectively, of normal FGK stars. WG12 focuses on cool PMS stars, both GIRAFFE and UVES. WG13 analyzes hot stars. WG14 is devoted to unusual objects, such as white dwarfs, close binaries, symbiotic stars, etc. The task of the five WGs is to process extracted spectra to refine astrophysical parameters, to deliver elemental abundances to a level appropriate for the relevant stellar type and available SNR, to derive stellar properties (e.g. activity, accretion, rotation, etc...) and to provide detailed analysis-level quality-control. Within each WG several nodes participate in the analyses. Specifically, more than one group is expected to analyze and produce results for (nearly) all relevant Survey targets. It is a strength of this Gaia-ESO Survey consortium that it includes a majority of spectrum analysis groups in Europe, which have available expertise in several complementary standard, as well as special-purpose, spectrum analysis methodologies. This ensures that a full analysis, including any assumption-dependent and method-dependent systematic effects is indeed implemented. On the other hand, it is not a trivial task to compare and merge in a unique final set of parameters all the results provided by different teams that use different tools and, in some cases, are specialized in the analysis of a specific type of stars (i.e., giants or dwarfs, metal-poor or metal-rich, etc...). This duty requires a great effort in quality checking of the results, as well as synergy and cooperation between the members of the teams. In fact, the major part of this homogenization process is done inside each WG dedicated to the spectrum analysis, where the outputs of different analysis tools are compared and combined. Bringing together a final best parameter set requires, in addition to the internal analyses, careful analysis of calibration targets and targets observed in more than one setting and instrument. The task of WG15 is to provide a communications channel between all spectrum analysis WGs, ensuring verification all along the teams that the physical parameters and analysis tools employed by the different WGs and nodes produce consistent results.

The main input to the spectrum analysis WGs consists of reduced spectra. These have been put on a wavelength scale, have been velocity shifted to a barycentric reference frame, and have been normalized. Quality information is also provided, including variance spectra, SNR ratio, non-usable pixels, etc. Additional inputs are the radial and rotational velocities derived by WGs 7 and 8, photometric data, and first guess atmospheric parameters derived by WG9. For field stars, cluster distances and reddening values will also be available as input to the spectrum analysis. Line lists, atomic and molecular data (gf-values, broadening constants, etc.), adequate for the different categories of targets and spectral intervals, are compiled by the WGs prior to the beginning of the analysis and distributed among the analysis nodes. These actions are taken to seek homogeneity in the derived quantities. Similarly, one single set of 3D model of atmospheres (MARCS models from Uppsala) will be used for the analysis of both UVES and GIRAFFE spectra.

2.3.5 Operational database and Survey archive (WG17,18)

The Gaia-ESO project will utilize both an operational database and an archive to hold all relevant information.

WG17 is devoted to the operational database that holds all data which remains incomplete, or subject to change. All WGs submit to the database all relevant data for an internal fruition: information associated with target selection, up to and including OB preparation, to the operational database (WG1-WG6); raw data from ESO and pipeline products (WG7-WG9); results from the spectrum analysis (WG10-WG15).

After pipeline and analysis processing, including atmospheric parameter and abundance determination etc., the spectroscopic Survey data are made available to the consortium for quality control, science verification and preliminary analysis via an archive system specifically developed for the GES community. This system, provided by WG18, will act not only as the "internal" archive system for the consortium, but also as a publicly accessible portal that will provide enhanced database. Data are released periodically: the first internal data release has been in August 2013 and regarded all the fields observed until December 2012. The first public data released has been scheduled for early 2014.

2.3.6 Survey progress monitoring and outreach and communication (WG16,19)

Survey progress monitoring is a major task, sufficiently critical to efficient Survey progress that the relevant WG (WG16) is led by the Co-PIs directly. Its activity is a complex mix of management, monitoring, communications, and book-keeping.

Outreach to the wider community will be organized by WG19. This will ensure the fullest science community awareness and exploitation of the Gaia-ESO Survey.

Chapter 3

Spectral Analysis

> If we were to go to the sun, and to bring some portions of it and analyze them in our laboratories, we could not examine them more accurately than we can by this new mode of spectrum analysis.
>
> Warren de la Rue, 1861

Very dense, hot material in the inner regions of a star produces a bright continuum spectrum with light of all wavelengths. As the photons move outwards into space, some are absorbed by atoms in the cooler outer layers of the stellar atmosphere. Since, each species of atom or ion has a set of discrete energy levels, these can absorb photons whose energy exactly matches the difference between their current energy value and that of the higher level. For this reason, each type of atom can completely determine energy transitions producing specific absorption features (or absorption lines) in the stellar spectra. Since these features embodies the flux of absorbed photons at the correspondent energy, in first approximation, their depth is proportional to the abundance of the element responsible of the transition. However, the strength of the absorption lines also contains information on physical quantities of the stellar atmosphere, such as the temperature, surface gravity, and microturbulence: the so-called atmospheric parameters.

This Chapter deals with the methodologies of the spectral analysis that are used to derive the atmospheric parameters and elemental abundances.

I will first describe the general approach; then, I will highlight the method and the tools specific for my analysis. In stellar spectroscopy there are two main approaches, namely the "equivalent widths analysis" and the direct comparison with templates.

3.1 General procedures

3.1.1 Equivalent width analysis

This method rests on the measurement of the strength of absorption lines of a specific element. I refer to this measurable quantity as the equivalent width (hereafter, EW), that corresponds to the total absorption due to a determined atomic transition. It is defined in the following way:

$$EW = \int_{line} \frac{F_c - F_\lambda}{F_c} d\lambda \tag{3.1}$$

where F_c is the flux level of the continuum normalized at 1 and F_λ is the stellar flux at the specific λ. Thus, as illustrated in Fig. 3.1, the EW is the width of a rectangle of depth of 100% in a normalized spectrum that covers the same area as the real line.

This technique relies substantially on the relation between the EW value of a line and the abundance of the correspondent element responsible of the transition. The line strength can be expected to increase with an increase in the chemical abundance of the absorber, nevertheless this is true only for weak lines. For these latter the relation between EWs and abundances, known as *curve of growth* (CoG), is linear: EW$\propto N_{abs}$, where N_{abs} is the number of absorbers. Increasing the abundance the lines saturate and the correlation between the two quantities becomes flatter (i.e. the saturation regime). Furthermore, the CoG is a function of several atomic parameters related to the transition, such as the central wavelength of the line (λ), the excitation potential (χ), the collisional damping constant or the oscillator strengths (*gf*). It is also function of the physics of the stellar atmosphere where the photons are absorbed. Models have been developed in order to describe the physics of this environment through some quantities, such as temperature, density, surface gravity, opacity, etc... (see Gray 1992 for a wide treatment of the subject).

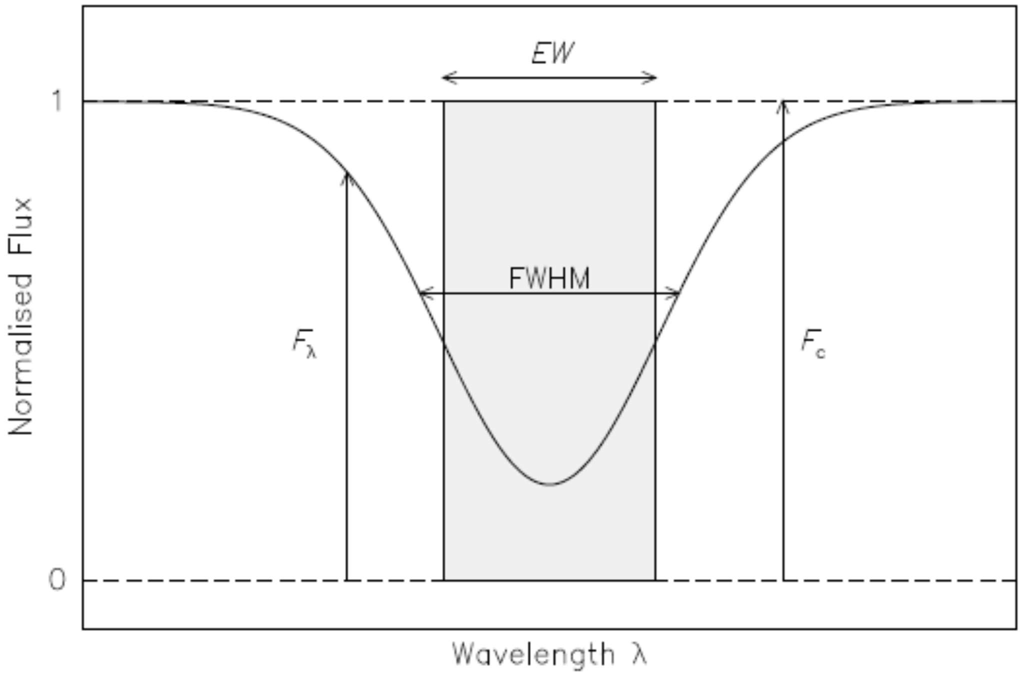

Figure 3.1: The EW is the width of a rectangle of depth of 100% in a normalized spectrum that covers the same area as the real line. Adapted from Figure 9.18 of Carroll & Ostlie (1996).

Thus, the EWs approach for the determination of atmospheric parameters and elemental abundances requires i) some input ingredients; ii) a procedure that iteratively determines the best set of atmospheric parameters; iii) the derivation of the elemental abundances, given the final atmospheric parameters.

Input ingredients:

- a master list of line transitions for the elements of interest;
- EW measurements of the features listed in the linelist. This can be performed by hand[1] or by adopting some automated routines. The latter is reproducible and less time consuming, but, in the case of noisy spectra and/or blended features, it requires special checks and accuracy;

---

[1] The IRAF task "splot", widely used for the visualization of the spectra, also allows us an interactive gaussian fitting of the absorption features.

- a set of atmospheric models;
- a set of atmospheric parameters or first guesses (i.e. temperature, surface gravity and microturbolence) used to determine the initial model adopted for the iterative procedure. Since the temperature drops by more than a factor of two from the bottom to the top of the photosphere, instead of choosing a temperature at some depth, it is customary to use the T_{eff}, defined in terms of the total power per unit area radiated by the star,

  $$\int_0^\infty F_\nu d\nu = \sigma T_{eff}^4. \tag{3.2}$$

  The T_{eff} values can be derived from spectral types (if known) or from photometry and using in both cases the calibrations tables that relate these quantities, e.g. Bessell et al. (1991); Kenyon & Hartmann (1995); Alonso et al. (1996, 1999, 2000). The values of the surface gravity g can be derived from photometry. Since

  $$g = \frac{GM}{R^2} \tag{3.3}$$

  where M is the stellar mass, G the gravitational constant, and R the stellar radius, one can use the Stefan-Boltzmann law for the stellar luminosity (L)

  $$L = 4\pi R^2 \sigma T_{eff}^4 \tag{3.4}$$

  to obtain:

  $$\log\left(\frac{g}{g_\odot}\right) = 4\log\left(\frac{T_{eff}}{T_{eff,\odot}}\right) + 0.4(M_{bol} - M_{bol,\odot}) + \log\left(\frac{M}{M_\odot}\right). \tag{3.5}$$

  The use of this formula requires the knowledge of the distance of the star, hence its absolute magnitude. Finally, the microturbolence (ξ) is an *ad hoc* parameter that has been introduced to take into account the effect of the saturation of the lines. Microturbolence mimics the effects of small motions ($\lesssim$5 km/s) that broaden the spectral lines and contribute to the line width. Generally, initial values of ξ can be retrieved from approximations as a function of T_{eff} and log g (Nissen 1981; Carretta et al. 2004).

Iterative procedure

Given the input ingredients, it is possible to derive the abundances for each measured EW of a specific element. Generally, one obtains the elemental abundance from the lines of neutral and (multi)ionized element, A_{eI} and A_{eII} respectively. Assuming the condition of local thermodynamic equilibrium[2], it is found that i) the abundances of the neutral and ionized species do not depend on their χ; ii) each measured EW has to yield the same elemental abundance; iii) the abundance from the neutral and ionized species must be the same, A_{eI}=A_{eII}.

Imposing the lack of correlation between A_{eI} and χ for a specific element, i.e. assuming conditions of excitation equilibrium, it is possible to determine the best T_{eff}. In fact, as a first approximation, the strength of the lines depends on the elemental abundance (the number of absorbers, N_{abs}) and on a function of T_{eff}, the so-called partition function, that describes the fraction of N_{abs} that actually play the role of absorbers with electrons in the lower level of a given transition:

$$EW \propto N_{abs} \times \exp(-\chi/kT_{eff}). \tag{3.6}$$

Thus, if T_{eff} is overestimated the EW of lines with higher χ are matched by lower abundances (negative slope). On the other hand, if T_{eff} is underestimated, the EW of lines with higher χ are matched by higher abundances (positive slope). So, in order to achieve the correct T_{eff}, all the lines of a specific element require the same abundance regardless of the χ.

Furthermore, the parameter ξ is introduced to increase the strength of the lines near or on the flat-part of the CoG, so as to bring the calculated strengths of saturated lines into consistency with the weak ones. Therefore, only the abundances derived from saturated, strong lines are affected by the choice of ξ, while those from sufficiently weak lines on the linear part of the CoG are essentially ξ-independent. Hence, as usually done, this parameter

---

[2] The local thermodynamic equilibrium assumes that all thermodynamic properties in a small volume have the thermodynamic equilibrium values at the local temperature and pressure. This means that: i) the electron and ion velocity distributions are Maxwellian; ii) the photon source function is given by the Planck function at the local temperature; iii) the excitation equilibrium is given by the Boltzmann equation; iv) the ionization equilibrium is given by the Saha equation. Real atmospheres are not in local thermodynamic equilibrium since their effective infrared, ultraviolet, and visible brightness temperatures are different.

can be determined by requiring that the abundances of each line do not show any dependence on their EWs.

Finally, since the ionization rate (through the Saha Equation) is highly related to the gas pressure (thus, to the surface gravity), the log g value strongly affects the features produced by the ionized element, but it has a weak influence on those of the neutral state. For this reason the final value of log g can be obtained assuming the ionization equilibrium: A_{eI}=A_{eII}.

Starting from the parameters of the first guess, the procedure yields the best atmospheric parameters after a number of iterations needed for the removal of the trends and of the difference between A_{eI} and A_{eII}.

Outputs

The main output of the procedure is the determination of atmospheric parameters: T_{eff}, log g and ξ. Given the atmospheric model corresponding to these parameters, the EWs of each element will produce a set of abundances. The final elemental abundance is taken to be the mean of the computed abundances.

3.1.2 Direct comparison with templates

The second method to derive the main stellar parameters and abundances consists in the comparison of the observed spectrum with a grid of synthetic templates. Given the linelist, atomic parameters and atmospheric models, dedicated codes are run to compute the complete spectral interval in which all the observed lines are included, i.e. the so-called spectral synthesis. Also a sample of observed spectra of stars with well known atmospheric parameters and abundances can be used as a grid of observational templates. The numerical codes for this type of analysis perform of the convolution of their grid of templates with the instrumental and rotational profiles and subsequently compare the resulting spectrum with the observed one. This direct comparison can be performed, for example, by a χ^2 fitting procedure.

The two methods, the comparison with templates and the classical analysis with EWs, differ particularly in their use of the knowledge of the physics governing the stellar atmospheres. While the classical method makes an intensive use of physics available in high-resolution stellar spectra, the comparison with templates looses part of the information trying to optimize the atmospheric parameters by seeking the best match between the observed spectrum and a grid of templates. The latter method is particularly indicated in cases where stellar rotation is significantly elevated (v sin$i\gtrsim$18−20 km/s). In these conditions many spectral features become blended and the EW measurements of individual features are no longer feasible. The comparison with templates is more reliable also in the case of cold ($T_{eff}\lesssim$4000 K) or hot ($T_{eff}\gtrsim$6500 K) stars. In fact, the spectra of cold stars have few or weak lines of the ionized element for which the EW are barely measurable. Viceversa, in hot star atmospheres most of the iron is ionized and the spectrum contains a small number of absorption lines usable to minimize the trends between iron abundances and χ or EWs.

3.2 My own procedure

My approach follows the "EW analysis" of the iron lines. The choice of iron is motivated by the fact that the stellar spectra in the optical range are very rich of absorption features. Moreover, the atomic parameters related to the iron transitions are well known from laboratory experiments or can be easily retrieved from the inverse solar analysis.

3.2.1 The case of large samples

Current large spectroscopic surveys, like the Gaia-ESO survey (see Chapter 2), make use of new multifiber spectrographs that greatly increase the amount of data acquisition. These high quality performances require the implementation of advanced data reduction pipelines capable to automatically process and analyze the spectra in accordance with specified requirements, such as:

- the analysis needs to be performed in a reasonable amount of time;
- the method of analysis should be homogeneous for all the different types of stars and the data products should be free of systematic errors.

Therefore, a well defined procedure is necessary to process all the spectra uniformly using the same atmospheric models and physical parameters for the atomic transitions. Part of my work has focused on the development of a method to analyze homogeneously the spectra of a very large sample of sources and in a reasonable time using available tools like IDL, DOOp and FAMA (see below) in order to derive the main stellar parameters and the elemental abundances through the "iron EW method". In particular, I developed a procedure that performs a quality check of the EW measurements and contributed to the development of the FAMA (Fast Automatic MOOG Analysis) code that allows an automatic determination of stellar parameters and abundances through the "EW method".[3]

In the following, I will describe (i) the linelist and the stellar atmospheric models adopted for my analysis; (ii) the procedure used to measure the EWs and to select those that satisfy specific criteria of quality; (iii) the FAMA code. Note that the approach, the tools and the codes described below have been employed for the spectral analysis performed for all the projects carried out during my PhD, including the Gaia-ESO Survey.

3.2.2 Tools: linelist and models of stellar atmospheres

The master-list of atomic lines suitable for the spectral analysis has been the third version of the Gaia-ESO Survey linelist and, from its release in August 2013, the fourth version (Heiter et al., in prep). These lists contain about 1350 lines (of whom ∼550 of FeI and ∼40 of FeII) in the spectral ranges covered by the settings of the Gaia-ESO Survey (4750-6850$\AA$ and 8455-8900$\AA$, respectively). For each line the list gives the wavelength, the atomic number of the element, the ionization stage, the value of log gf, the energy of the transition levels, the damping constant and the reference where all the information has been retrieved. Along with the data on the atomic transitions, there are two quality-flags on the log gf and on the blending properties. For my analysis I rejected all the lines having a flag indicating a low quality of the log gf parameter.

As to the atmospheric models, I have adopted the complete grid of MARCS (Gustafsson et al. 2008) which includes both spherical and plane-parallel models. Spherical models are adopted for stars with log g<3.5, i.e. giant evolved stars. The MARCS library contains about 52,000 stellar atmo-

---

[3] This code, described in Section 3.2.4, has led to the following publication:
L. Magrini, S. Randich, E. Friel, **L. Spina**, H. Jacobson, T. Cantat-Gaudin, P. Donati, R. Baglioni, E. Maiorca, A. Bragaglia, R. Sordo & A. Vallenari, FAMA: An automatic code for stellar parameter and abundance determination, 2013, A&A, 1307, 2367

spheric models of F-, G- and K- spectral types derived under the assumption of local thermodynamic equilibrium.

3.2.3 EWs measurements

In order to fit and measure the EWs of all the transitions in the linelist, I processed each spectrum using the DOOp code (Donati 2014). This is a programme that uses bash, IRAF, and DAOSPEC scripts in an iterative way to compute the best DAOSPEC parameters. The programme has also been implemented to process automatically each spectrum with DAOSPEC (Stetson & Pancino 2008), a code that (i) finds all the absorption lines in stellar spectra, (ii) fixes the continuum, and (iii) measures the FWHM that best fits all the features. This code works with iterative gaussian fitting and subtraction procedures, thus it is particularly useful when dealing with spectra that are heavily crowded with absorption lines. The output of DAOSPEC are two files containing the normalized and residual spectra, plus another file that lists the wavelength of all the fitted features along with their EWs and a quality parameter (Q_{line}) derived from the comparison between the residuals observed in the spectrum in the immediate vicinity of the line, and the typical residuals of the whole spectrum. The header of this file also contains the estimated RV of the star, the FWHM used to fit all the features, the number of spectral lines, and another quality parameter (Q_{spec}) defined as the root-mean-square value of the pixel-by-pixel flux residuals remaining in the spectrum after subtraction of all the fitted lines.

Furthermore, I developed a quality control procedure that, from the normalized and residual spectra produced by DAOSPEC, derives for each line a quality parameter determined only on the wings of the lines (Q_{wings}). This Q_{wings} is defined as the sum of the residuals between 1 and 2 FWHMs from the central wavelength on both sides of the line. If the continuum has been overestimated in the proximity of the line, the result is Q_{wings}<0, viceversa we obtain Q_{wings}>0. This parameter allows the identification of the features that have not been properly de-blended from adjacent lines. The resulting Q_{wings}-distribution of all the features in each spectrum peaks in proximity of the zero-value (see Fig. 3.3).

As mentioned in the previous chapters, PMS stars are usually fast rotators. Furthermore, very often the sample contains a significant number of cold stars rich of absorption lines. All these properties require special care.

For this reason the same procedure that derives the Q_{wings} parameter also operates a selection of the EW values for the analysis in accordance with the following quality criteria:

- The centre wavelength of the rest line (corrected for the derived RV) has to be within $0.05\AA$ of the wavelength of the transition tabulated in the linelist.

- The EW values accepted for the analysis are only those in the interval from 15 to 120 m$\AA$. In fact, the lines have to be strong enough to be measurable (lower limit), but not too deep in order to avoid saturated lines or important differences from a gaussian fit (upper limit). This is a standard criterion for all types of stars.

- The Q_{line} has to be less than a threshold value determined on the basis of the Q_{line}-distribution of all the identified features (see Fig. 3.2).

- The accepted lines are those having Q_{wings} within $\pm 2\sigma$ from the mean of the Q_{wings}-distribution (see Fig. 3.3).

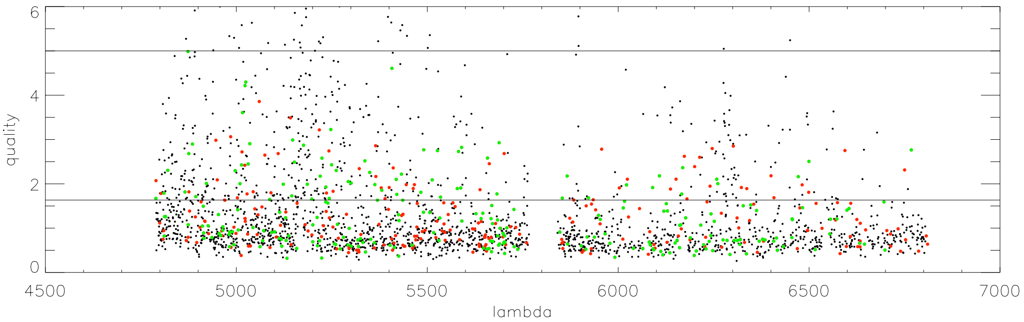

Figure 3.2: Q_{line} as a function of wavelength ($\AA$) for all the detected features in the Gaia-ESO Survey spectrum of the star 2MASS J11060511-7511454, targeted in the Chamaeleon I fields. Red dots correspond to the iron lines contained in the linelist, while green dots correspond to the transitions of all the elements other than iron. Black dots are all the lines that do not match any transition of the linelist.

As a further check, the normalized and the residual spectra allow me to generate for each spectrum a plot that shows the observed spectrum along with the DAOSPEC fit (see Fig. 3.4).

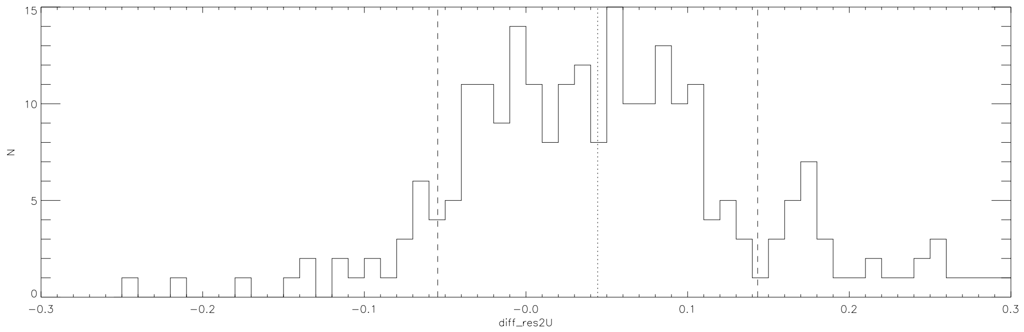

Figure 3.3: Q_{wings}-distribution of all the detected features in the Gaia-ESO Survey spectrum of the star 2MASS J11060511-7511454, targeted in the Chamaeleon I fields. The dotted lines correspond to the mean value, while the dashed lines to ±1σ.

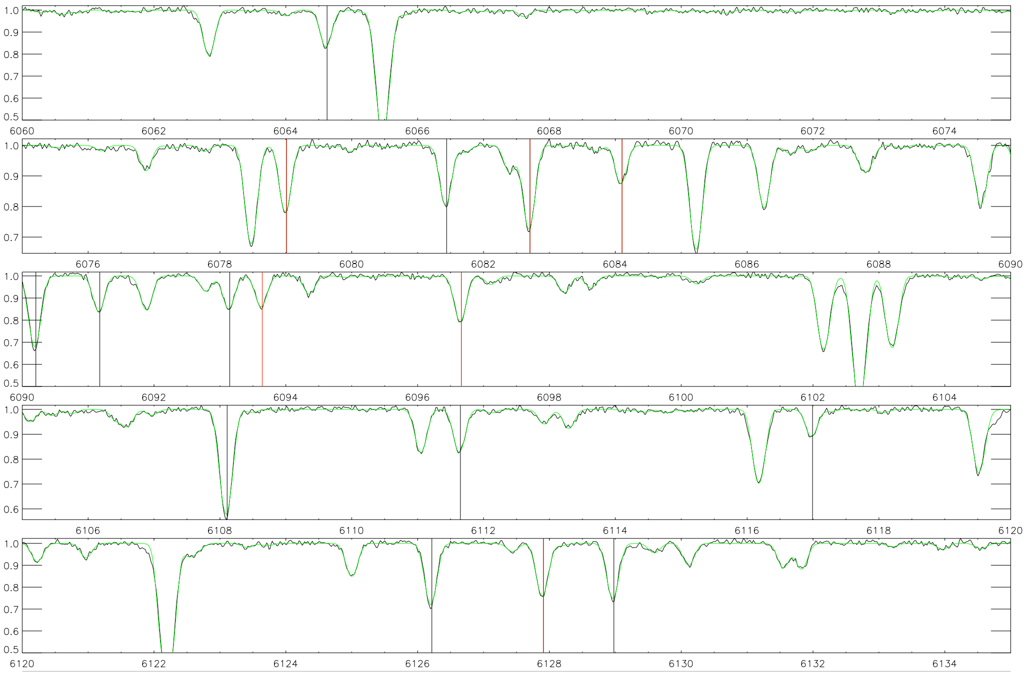

Figure 3.4: Portion of the observed spectrum (black line) of the star 2MASS J11060511-7511454, targeted in the Chamaeleon I fields. The green line represent the DAOSPEC fit. Vertical red and black lines represent the selected iron lines and those of other elements used in the abundance analysis, respectively.

The list of EWs accepted for the analysis are then used in the FAMA code for the determination of main stellar parameters and elemental abundances.

3.2.4 FAMA

FAMA is based on an iterative use of MOOG (Sneden 1973; Sneden et al. 2012), a code capable to determine the chemical abundances, the slopes of their relations with χ and EWs along with the difference between log n(FeI) and log n(FeII). Its philosophy consists in the search for the three equilibria (excitation, ionization, and the trend between log n(FeI) and EW) with a series of recursive steps starting from a set of *first guess* atmospheric parameters, and arriving to a final set of atmospheric parameters which fulfills the three equilibrium conditions. The order followed in the search for the three equilibria is also important since T_{eff} is the controlling parameter for the ultimate solution. Thus, it is necessary first to regulate it, then to move to the second most important parameter, the surface gravity, which adjusts the ionization equilibrium, and finally to fix the microturbulence.

Figure 3.5 shows the workflow of the FAMA code. The ingredients with which FAMA is fed are: i) EW files: two files, one containing EWs of iron in the two ionization stages and the second one containing EWs belonging to the complete list of elements, and ii) parameter file: a file with the *first guess* atmospheric parameters which includes the T_{eff}, log g , ξ and the abundance of iron with respect to the solar value, [Fe/H]. This file is given to an interpolator code of model atmosphere, in my specific case MARCS models (Gustafsson et al. 2008), and an atmospheric model with the input parameters is produced. This latter and the files containing the iron EWs are given to the MOOG for the determination of the abundances and trends. A σ-clipping[4] is performed on FeI and FeII lines based on an initial run of Moog, that is run again with the cleaned list of EW.

The iteration strategy is the following: first the T_{eff} is adjusted by an amount that depends on how far the initial T_{eff} is from the excitation equilibrium. Subsequently, the surface gravity is modified by an initial amount that depends on the difference between log n(Fe I) and log n(Fe II). Finally, ξ is varied on the basis of the slope of reduced EW versus log n(Fe I). This is repeated in three cycles (see the first and last cycle in Fig. 3.5). In each cycle, the minimization requirements on the slopes and neutral/ionized iron

---

[4] All the abundances differing of more one σ from the mean value have been discarded.

abundances are varied and becomes stricter with each cycle. In particular, the minimization requirements for the first cycle are three times larger than those of the last cycle, and those of the second cycle are two times larger. The value of the smallest minimization requirement is calculated using the information on the quality of the EW measurements. Since the EW measurements are affected by errors, it is not reasonable to minimize the slopes to infinitely low values, yielding zero slopes. This would have no physical justification and would lead us to find local minima in the three-dimensional space of T_{eff}, log g and ξ. Thus, the minimum reachable slopes (MRS in Fig. 3.5) in FAMA are strictly linked to the quality of the spectra, as expressed by the dispersion of log n(Fe I) (σ_{FeI}) around the average value <log n(Fe I)>.

To ensure the final solution, independent from the initial parameters, FAMA is designed to repeat the complete convergence path up to six times, starting each time from the previous set of stellar parameters which ensured the convergence. At each step, the requirements of minimization of the three slopes become stricter and they are parametrized by the so-called QP quality parameter. This parameter QP assumes six values, 10, 8, 6, 4, 2, and 1. The last step (indicated in Fig. 3.5 with red lines and arrows) corresponds to QP=1. At the end of this step, the final stellar parameters are obtained. Then the interpolator derives the atmospheric model related to these final values and the EWs of all elements are given to Moog, a σ-clipping is then performed and the final abundances are derived. The last step of the procedure is for the evaluation of the errors. This is accomplished keeping the slope of the excitation equilibrium, the slope of the trend between log n(Fe I) and reduced EWs, and the difference between Fe I and Fe II abundances to the values given by the dispersion of the abundances. To do this, FAMA derives for each star the stellar parameters which correspond to the following:

- for T_{eff}: imposes a slope equal to the ratio between the dispersion around the mean value of iron abundance and the range of χ $\pm\sigma_{FeI}/\mathrm{r}(\chi)$, where r($\chi$) is the range in χ;
- for ξ: imposes a slope corresponding to $\pm\sigma_{FeI}/\mathrm{r}(\mathrm{EW})$, where r(EW) is the range in EW;
- for gravity: imposes a difference between log n(Fe I) and log n(Fe II) equal to $\pm\sqrt{\sigma^2_{FeI} + \sigma^2_{FeII}}$.

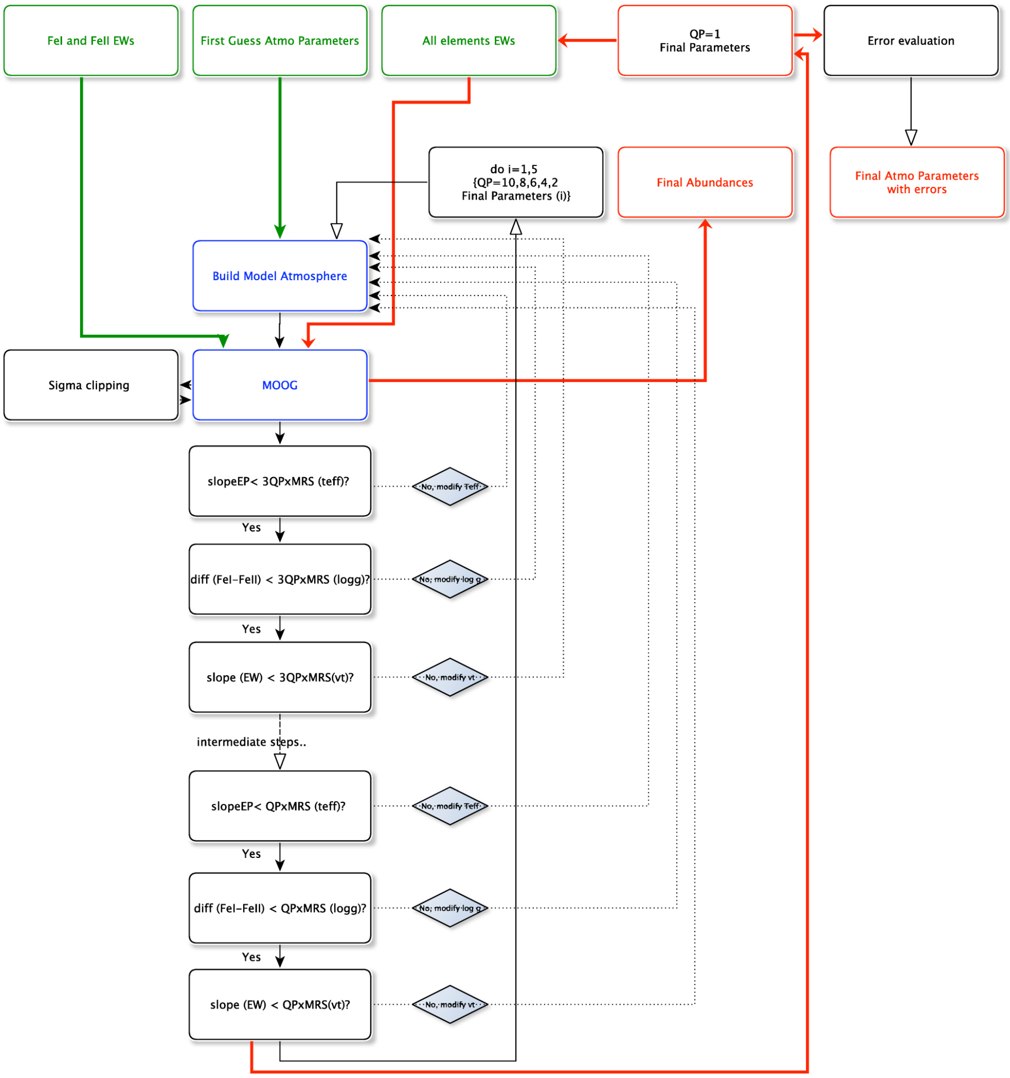

Figure 3.5: Workflow of the FAMA code: the input files in green, the main codes in blue, the iterative steps in black, and finally, the final outputs in red. From Magrini et al. (2013).

This allows us to find the maximum and minimum values for T_{eff}, log g and ξ, which are acceptable within errors due to the dispersion of the abundances. The final errors are assumed to be the half-difference between the maximum and minimum values of each parameter. Concerning the error in the final individual element abundances, there are two types of errors which are considered by FAMA: i) the uncertainties due to the random errors in the EW measurements and to accuracy of the atomic parameters; and ii) the errors on the abundances generated by the uncertainties in the determination of the atmospheric parameters. In general, the latter type of error gives a null or irrelevant contribution to the final budget, thus in my analysis it has been neglected.

At the end of the run of FAMA a control plot is produced with the aim of helping to visually check the quality of the results. In Fig. 3.6 I show an example of the control plot with four panels. In the first three panels the filled (red) circles are the abundances from the FeI EWs accepted after the σ-clipping, while the empty circles are those rejected. In the first two panels, the χ and ξ equilibria are shown: the blue long dashed line is the zero-slope line and the dashed magenta line is the slope of the final convergence point. In the case of good convergence these two lines are coincident. In the third panel, the dependence on iron abundances on the wavelength is shown giving us a further test on the quality of the data and of the EW measurements. In spectra of good quality, we do not expect any dependence of EWs on the wavelength. Finally, the ionization equilibrium is given in the fourth panel by green circles, where the FeII abundances are used for gravity determination, and with empty circles showing rejected lines (not present in this case). The cyan horizontal line in the last panel is the average FeII abundance, while the magenta line is the average Fe I.

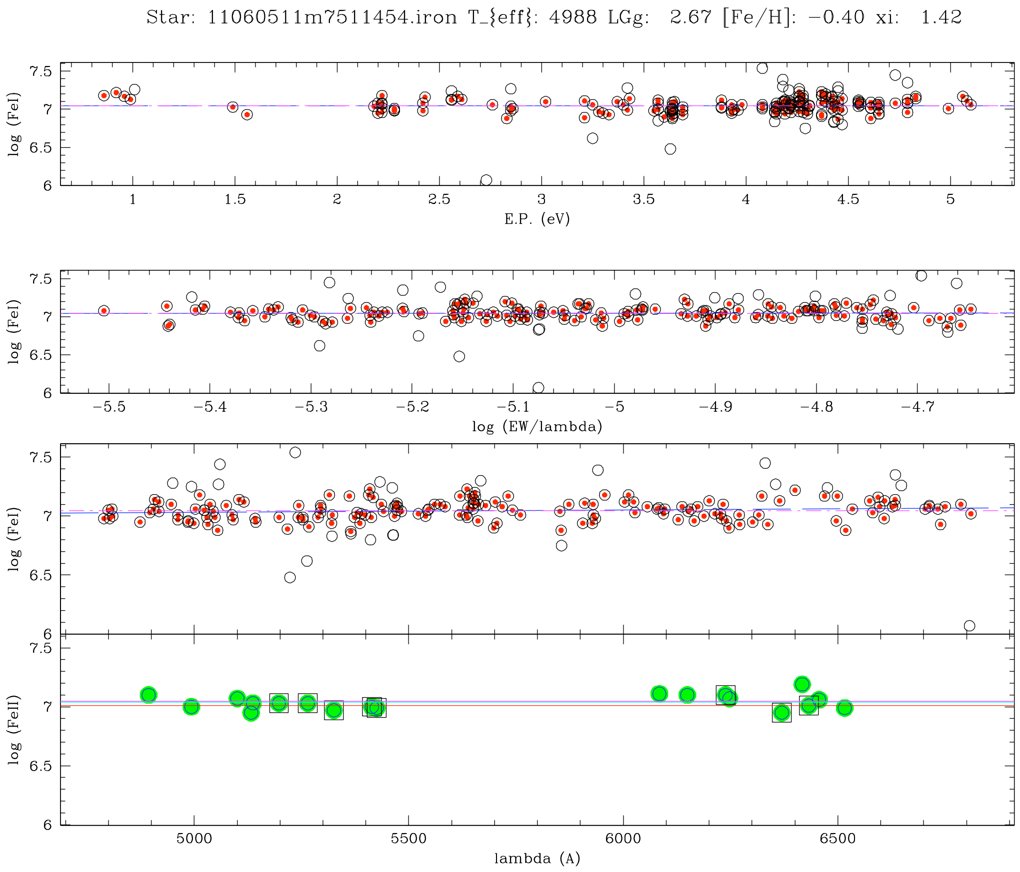

Figure 3.6: The control plot is an output of FAMA. This is related to the analysis of the star 2MASS J11060511-7511454, targeted in the Chamaeleon I fields. The parameters on the top of the panel give the converged stellar parameters and iron abundance. The meaning of the colored lines is explained in the text.

Chapter 4

Analysis of 1700 spectra from the ELODIE Archive

> A reasonable person is one who submits reason to experience.
>
> Jean Guitton

As mentioned in Section 3.1, the importance of the stellar abundance analysis is that it provides insights on general issues related both to the formation and evolution of the Milky Way and to the internal structure of stars. The analysis of high quality spectra is the only primary method to estimate the chemical composition of stellar photospheres, from which other indirect methods of metallicity determinations can be calibrated. The two main approaches of spectroscopic analysis have been described in Chapter 3: the "EWs analysis" and the "spectral classification". However, also within these two approaches, each individual study has its own characteristics: preferred stellar atmospheric models, atomic line data, EWs measurement methods, grid of templates, etc... The consequence is a lack of homogeneity in the results from one study to another, which makes the comparison of the result very complex.

In this Chapter I will discuss the analysis that I performed using 1700 stellar spectra stored in the ELODIE public archive[1] that include a wide variety of stars. This analysis has been performed through the procedure described in Section 3.2. The main aim is to provide a large catalog of

---

[1] http://atlas.obs-hp.fr/elodie/

atmospheric parameters and abundances derived in a homogeneous, automatic and reproducible way for a large sample of spectra available to the public. This task is both necessary and timely because the literature lacks of such homogeneous large catalogs of spectroscopic parameters and also because only recently large spectroscopic surveys, making use of new multifiber telescopes, like the Gaia-ESO Survey, encouraged the development of new pipelines capable to analyze a continuous stream of observed spectra and automatically process the data products. Such a self-consistent collection of data can be used for an accurate calibration of methods devoted to stellar parameter and metallicity determinations and can be also adopted as a grid of observational templates for spectral classification. This analysis does also provide the opportunity to prove the validity of my tools and method of analysis on a large sample of spectra obtained in the optical range (4000 - 6800 $\mathring{A}$) and with a resolution similar to that of the Gaia-ESO UVES targets.

In the following, I will describe the contents stored in the ELODIE archive, the criteria adopted to select the sample of spectra to analyze, the procedure of spectral analysis, and the results.

4.1 The ELODIE spectrograph and the archive

ELODIE is a cross-dispersed echelle spectrograph of the Observatoire de Haute-Provence. This instrument has been in operation since the end of 1993 on the 1.93m telescope and, after more than 12 years of observations, has been decommissioned in mid-August 2006. The ELODIE spectrograph, in one single exposure, records a spectrum from 3906$\mathring{A}$ to 6811$\mathring{A}$ with a resolution of 42,000. For more details on the instrument and on the spectral reduction pipeline, see Baranne et al. (1996). All spectra achieved with ELODIE can be accessed through a dedicated archive. The ELODIE archive (Moultaka et al. 2004) contains 35,535 public spectra with SNR[2]>5 of about 7952 distinct objects. The histogram in Fig. 4.1 shows the SNR distribution of the whole sample of archive spectra. Note that the distribution is peaked at SNR$\sim$40 and its median value is SNR=68.

For about 23,000 spectra the archive stores also the RV results calculated at the telescope. Along with the RV, the CCF and other related information

---

[2] The reported SNR is the mean signal to noise ratio per pixel in the spectral order number 47, i.e. near 555 nm, computed at the telescope by the data reduction software

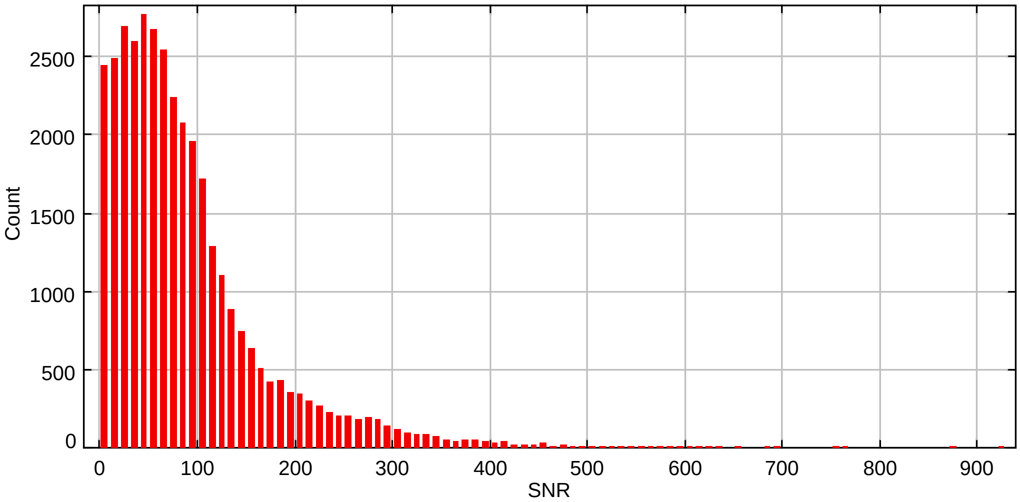

Figure 4.1: The histogram shows the SNR distribution of the 35,535 ELODIE spectra stored in the archive.

is stored in the archive: the σ value of the gaussian fit of the CCF, the depth of its profile and the number of single gaussians needed to fit the profile. This latter information is particularly useful since it permits to identify spectra with a double gaussian CCF corresponding to spectroscopic binaries. Finally, note that telluric lines (and any remaining CCD defects) have been masked in all the spectra.

4.2 Stellar libraries and selection of the sample

Since my method of analysis is appropriate only for stars of K-, F- and G-spectral type, I selected a subsample of objects suitable for this approach. For this selection a first T_{eff} estimation has been necessary. The two largest catalogs containing a significant number of atmospheric parameter values of stars observed by ELODIE are the "ELODIE stellar library" (Prugniel et al. 2007) and the "PASTEL catalogue" (Soubiran et al. 2010). The former is a catalogue of 1388 stars whose spectra are stored in the ELODIE archive. This compilation is mainly based on values reported in a list of 55 bibliographical references providing T_{eff} and/or log g and/or [Fe/H] (when available). Otherwise, the missing parameters have been derived from an internal comparison using the spectra with known parameters as a grid of templates. The PASTEL catalogue includes 31,724 determinations of either T_{eff} or the three atmospheric parameters together for 17391 different stars corresponding to ~900 references. Nearly 6500 stars have a determination of the three parameters. While in the ELODIE library each star has only one entry with the corresponding parameters, in PASTEL every star can have more than one entry. In these cases, I averaged the multiple determinations from different authors in a final value performing a 2σ-clipping. For the final catalog I assumed the parameters from the ELODIE library, if available. Otherwise I considered the values obtained from PASTEL. Hereafter, I will refer to these parameters obtained from the literature as $T_{eff-lit}$, log g_{lit} and $[Fe/H]_{lit}$.

I used this large amount of data for my selection procedure that is summarized in Tab. 4.1. Among the 7952 sources of the ELODIE archive, I identified 3055 stars with at least one ELODIE spectrum with SNR>30 and with a $T_{eff-lit}$ determination. Among the first selection I selected the 1959 stars with $T_{eff-lit}$ ranging from 4500 and 6500 K. The large majority of these have the CCF available in the archive, along with the related data. I used this information to reject 92 spectroscopic binaries showing a double-peaked CCF, reducing the sample to 1867 stars. I did not perform any selection based on the amplitude of the CCF profile that is related to the stellar rotation, since the DAOSPEC code provides accurate estimates of the spectral line FWHM which allowed me to reject rapidly rotating stars in a subsequent step.

Thus, 1867 stars suitable for abundance analysis have been identified through this procedure. For each of these stars I singled out and downloaded from the ELODIE archive the spectrum with higher SNR. Figure 4.2 shows the SNR distribution of these spectra.

4.3 Analysis

The first step of my procedure has been to reduce the spectral interval of all the spectra from 4000-6800$\mathring{A}$ to 4800-6800$\mathring{A}$, in order to remove the bluest part. In fact, at short wavelengths ($\lambda \lesssim 4500\mathring{A}$), the spectra of the considered type of stars are crowded with absorption lines and molecular bands that make the identification of the stellar continuum a very difficult task. Due to the large number of spectra, it is impossible to check by eye every single fit.

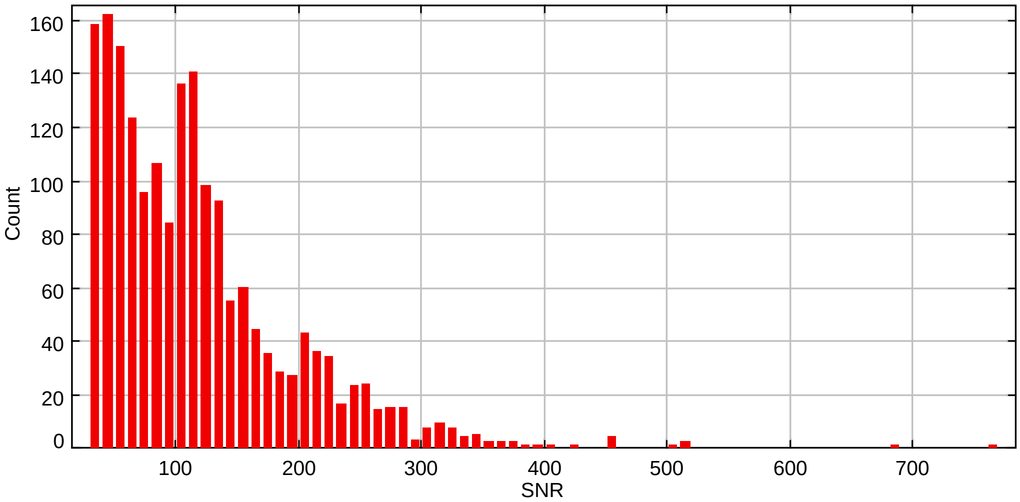

Figure 4.2: The histogram shows the SNR distribution of the ELODIE spectra selected for the analysis.

Table 4.1: Summary of the selection and analysis procedures

stars with ELODIE spectra	7952
stars with T_{eff} determination and SNR spectrum $>$ 30	3055
stars with T_{eff} ranging from 4500 and 6500 K	1959
after removal of spectroscopic binaries	1867
after removal of fast rotators and defective spectra	1827
after removal of low quality fit	1699

Thus, to avoid that a wrong continuum determination could affect the entire analysis, I cut off *a priori* the bluest 800$\mathring{A}$ of each spectrum using ”scopy”, an IRAF procedure designed for this task.

A first iteration of DOOp has been necessary to fit all the features of the 1867 spectra and to measure the FWHM. This allowed me to identify 36 fast rotators (FWHM>20 km/s) that have been rejected from further analysis. Moreover, the DOOp procedure did not converge for 5 spectra, that have been discarded. The remaining 1827 spectra have been processed to a second DOOp iteration that provided the EW measurements of all the absorption features, along with the quality parameters Q_{line} for each feature and Q_{spec} for each spectrum. Figure 4.3 shows the distribution of the Q_{spec} parameter for all the 1827 spectra. Most of the outputs have a Q_{spec}<1, as expected for good quality fits. However, DAOSPEC also produced fits with very high Q_{spec}, because the sample of analyzed spectra contained a number of unidentified spectroscopic binaries or sources with strong emission lines that highly affected the analysis. The rejection of all the 128 DAOSPEC outputs with Q_{spec}>2 allowed me to remove most of the stars for which my analysis fails. For the remaining 1699 stars I selected the EWs of the lines from the same linelist used by the Gaia-ESO Survey and adopting the quality criteria described in Section 3.2. The resulting lists of EWs have been processed with FAMA adopting $T_{eff-lit.}$, log $g_{lit.}$ and [Fe/H]$_{lit.}$ as first guesses and the same atmospheric models used by the Gaia-ESO Survey. The FAMA code provided the atmospheric parameters and abundances of all these 1699 stars.

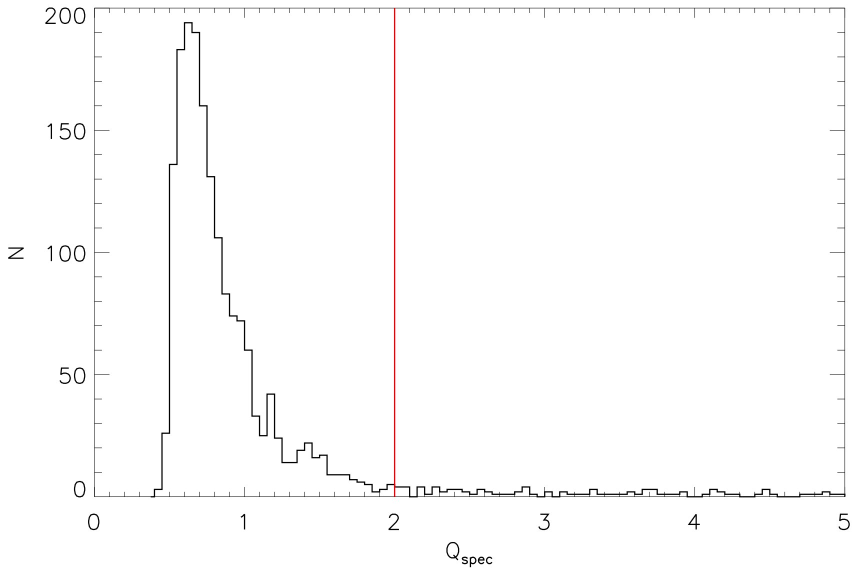

Figure 4.3: Distribution of the Q_{spec} parameter produced by DAOSPEC for all the 1827 spectra. Only the spectra with a high quality fit (Q_{spec}<2, red line) have been accepted for the further analysis.

4.4 Results

4.4.1 Atmospheric parameters

The final set of parameters have T_{eff} values in the range 4200-6600 K, log g values between 0.5-4.9 dex and metallicity from -2.4 to $+0.5$ dex. T_{eff} has a typical error of ±150 K, log g of ±0.2 dex and iron abundances of ±0.12 dex. Comparison between the new parameters determinations with those from the literature ($T_{eff-lit}$, log g_{lit} and $[\mathrm{Fe/H}]_{lit}$) are shown in Figs. 4.4, 4.5 and 4.6. Figure 4.4 shows that there is a very good agreement between the two sets of parameters with the remarkably absence of any significant systematic shift. On the other hand, there are a number of stars whose new parameters greatly differ from the literature values and are hence scattered. However, it is necessary to observe that these literature parameters have been derived through different methods and tools, thus there is an internal inconsistency in the whole set that, as a result, increases significantly the scatter. From these plots it is also possible to observe the lack of significant trends between the parameters, indicating that the EWs measurements and convergence of the FAMA code to the final parameters are insensitive to the type of star to be analyzed (hot or cold, giant or dwarf, metal-rich or metal-poor). The only remarkably exceptions consist in the very metal-poor sources (i.e. [Fe/H]<-1.0 dex) for which my analysis underestimates all the three parameters (see Fig. 4.6). This effect could be due to lack of absorption features that characterizes this kind of stars.

4.4.2 Abundances

Once the atmospheric parameters have been derived the elemental abundances are also determined from the EWs of their absorption features. Specifically, in addition to iron, I obtained abundances for 28 other elements, but not all of these have been detected in every star. Most of the elements have the abundances of the neutral species, but for 7 elements the abundances of both the neutral and ionized states have been obtained, while for 8 elements only the abundance of the ionized state has been derived. Figure 4.7 shows the abundance ratios [X/Fe] for those elements with a significant number of detections as a function of the iron abundance. The abundances are scaled to the solar values from Grevesse et al. (2007). The elements in the first row are α-elements (Si, Ca and Ti), the second row is for iron-peak elements (V, Cr and Ni) and the last row shows other elements not belonging to the previous classes (Mg, Al and Co). In the plot, <Ti> and <Cr> refer to the mean abundance of the neutral and ionized elements, i.e. [A(CrI)+A(CrII)]/2. Each element has its peculiar distribution, i.e. the α-elements show a trend with [Fe/H], but this is not present for the iron-peak elements. The mean values of the three α-elements abundance ratios are shown in Fig. 4.8 versus [Fe/H]. The classical decreasing evolution of [α/Fe] with metallicity is clearly visible. In addition, as in Fig 1.1, it is possible to distinguish the two sequences separated by a low-density region: the thick disk in the high-α regime and the thin disk in the low-α regime. The two populations overlap in [Fe/H] from about -0.8 to 0 dex, but the thick disk sequence seems to be extended to -1.0. A flat sequence of stars occupy the diagram at lower [Fe/H] values: this sample likely is the halo population also visible in Fig. 1.1.

4.5 Conclusions

The aim of the analysis presented in this Chapter was to show the potential of a procedure capable of an automated, fast and homogeneous spectral analysis. However, my findings also offer a glimpse into the nature of the Galactic stellar components (thin/thick disk and halo) and their chemical separation. Beyond the scientific content provided by Fig 4.8, the most important point is that procedures with these properties offer significant benefits for ambitious projects that make use of large databases. Furthermore, my results also indicate that the method, tools and codes described in Section 3.2 produce a reliable determination of atmospheric parameters and abundances not affected by systematics depending on the type of star.

These results will be made available to the community very soon. Codes for the spectral classification that make use of observational templates will benefit of this self-consistent and homogeneous data-set. A first example of this consists in ROTFIT, a code for the spectral classification through a grid of observational templates and that already included in its grid about 300 stellar parameters from my catalog along with the corresponding ELODIE spectra. Also, I plan to expand my catalog analyzing a large fraction of the spectra present in the ELODIE archive that have not been included in this first iteration.

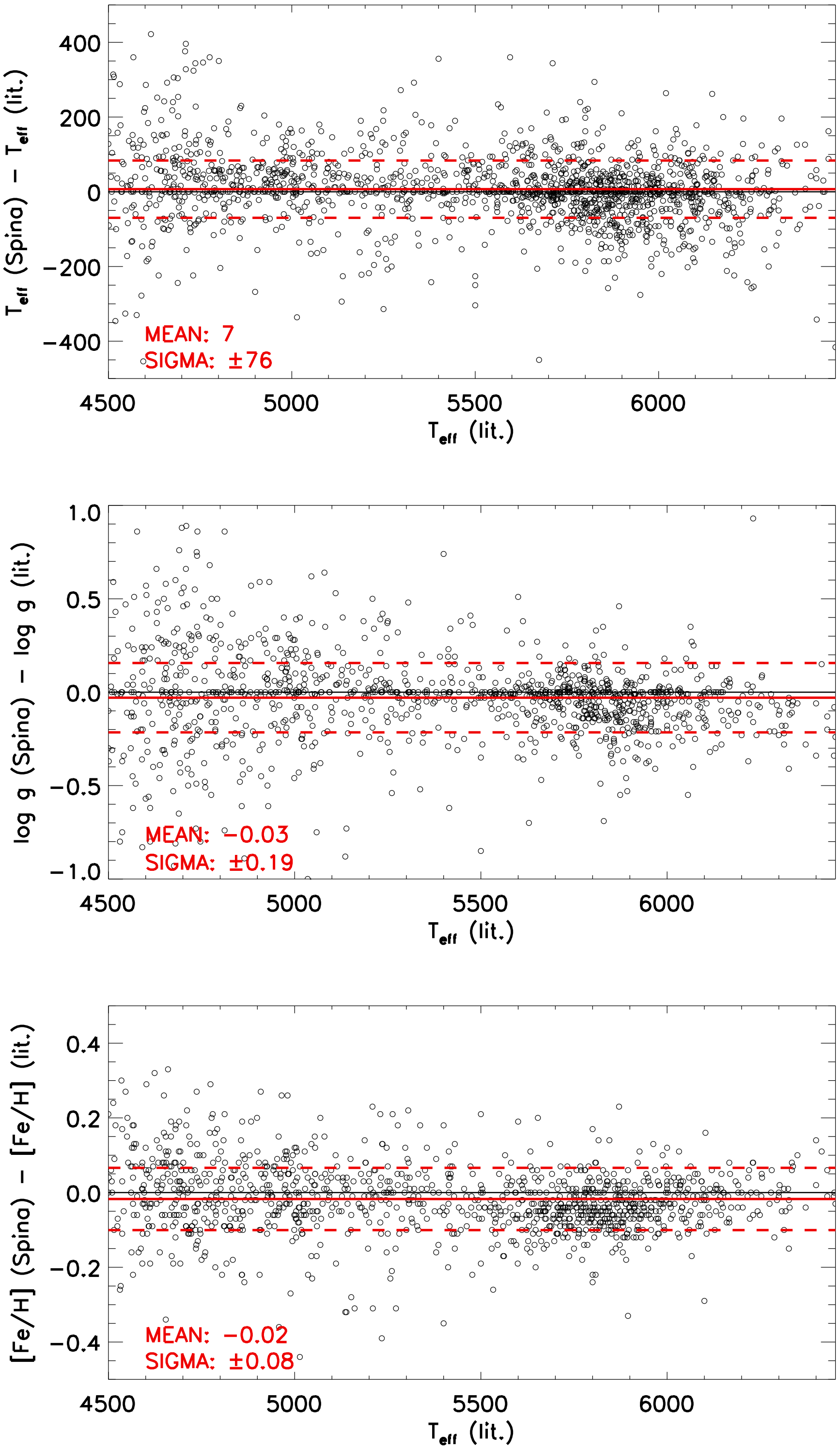

Figure 4.4: Difference between the new parameters and those from the literature as a function of $T_{eff-lit.}$. The red solid and dashed lines represent the mean and $\pm 1\sigma$ values of the differences.

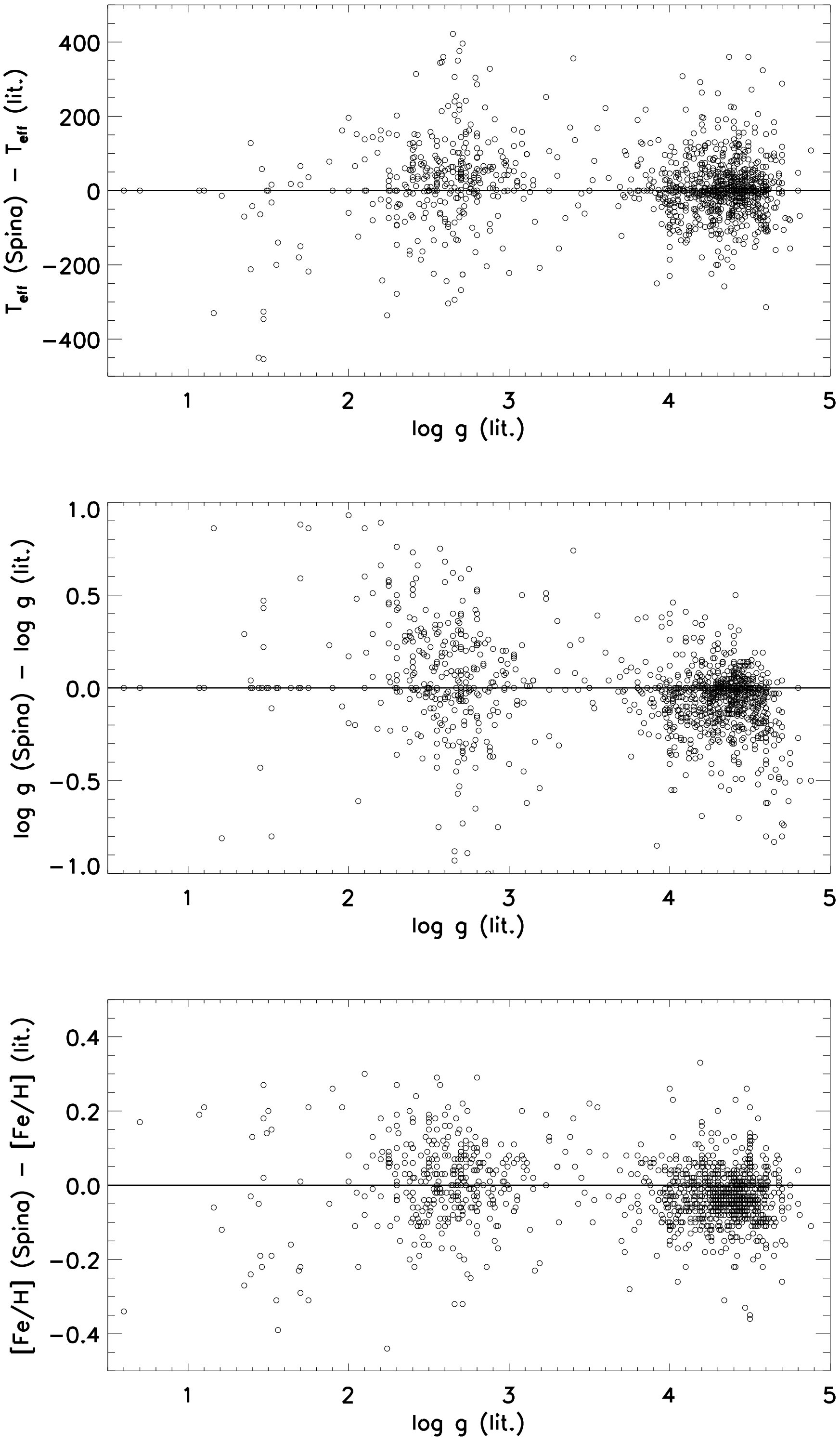

Figure 4.5: Difference between the new parameters and those from the literature as a function of log $g_{lit.}$.

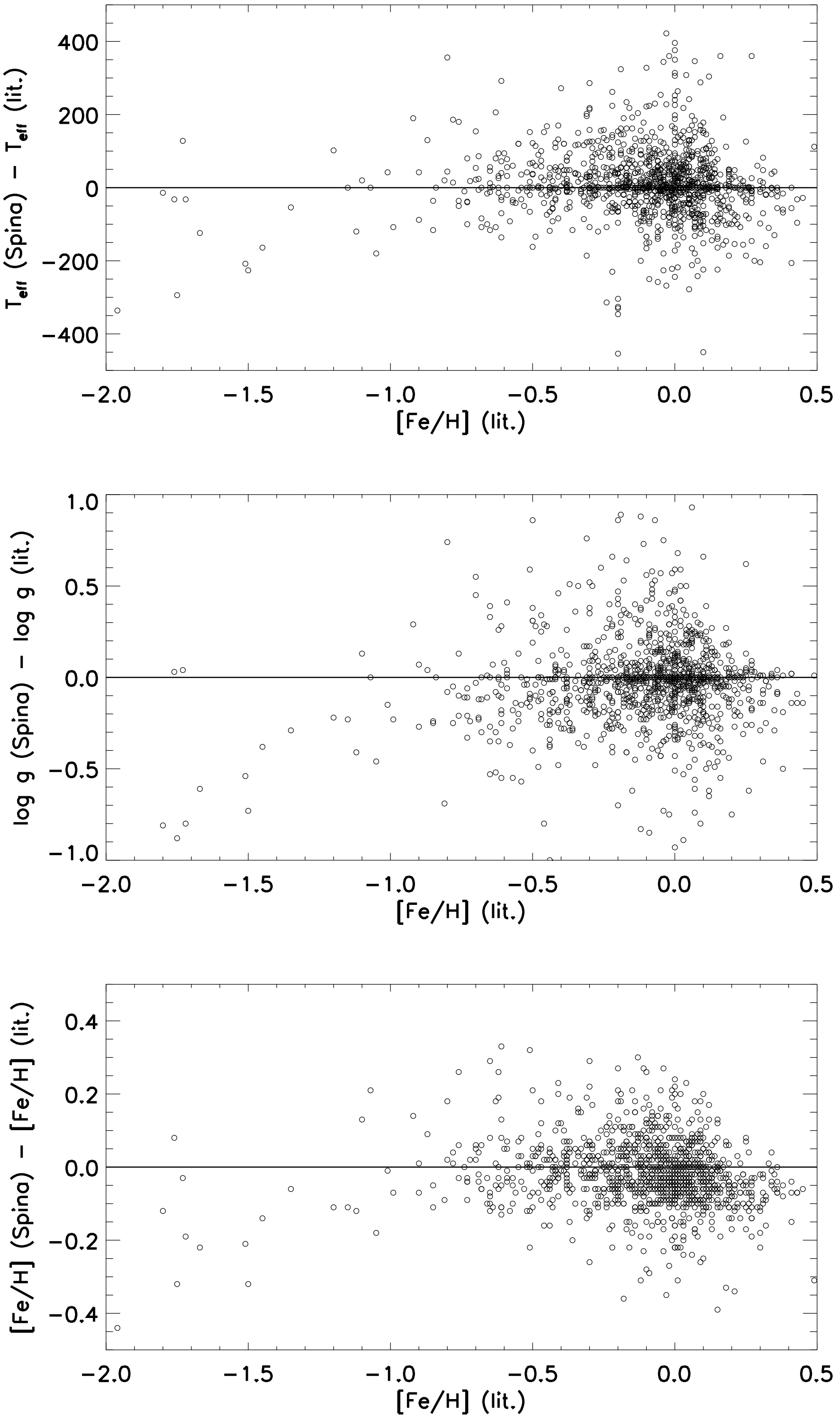

Figure 4.6: Difference between the new parameters and those from the literature as a function of $[\mathrm{Fe/H}]_{lit.}$.

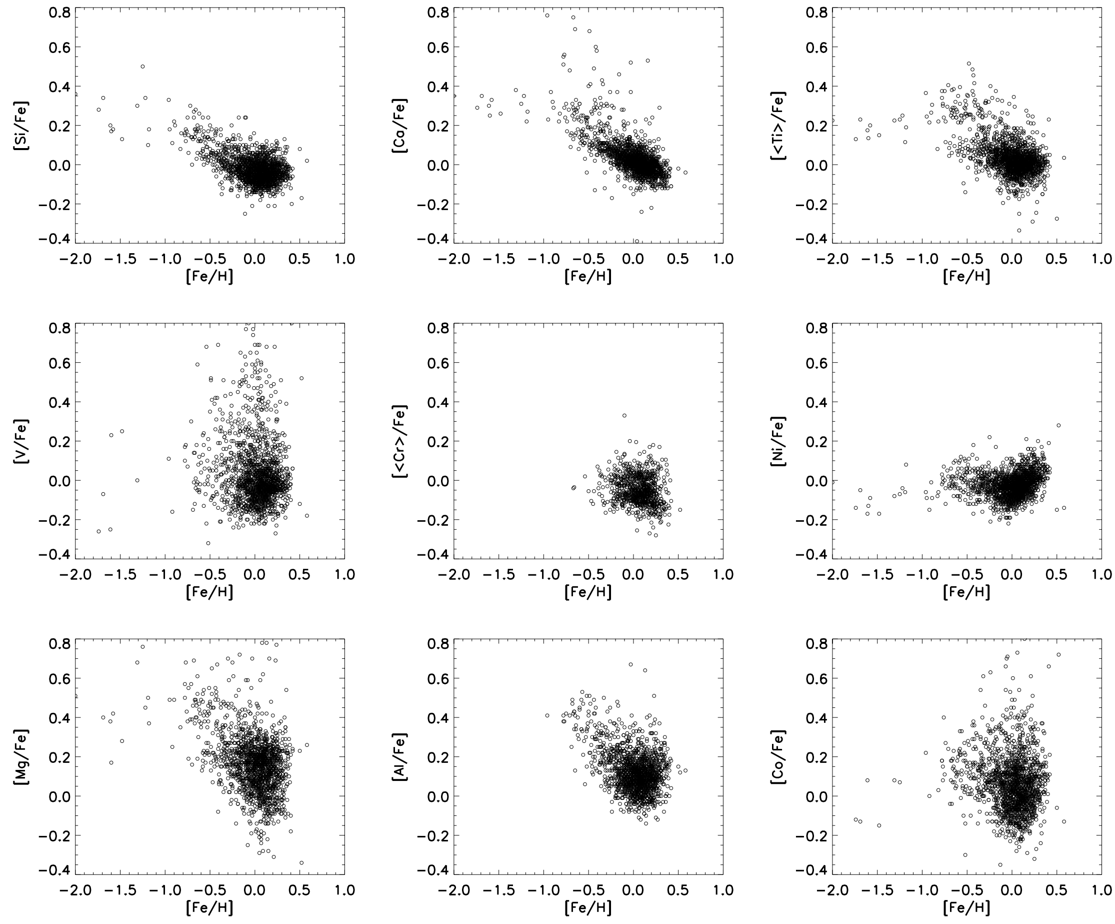

Figure 4.7: Abundance ratios [X/Fe] as a function of [Fe/H] for α-elements (top), iron-peak (middle), and other elements (bottom).

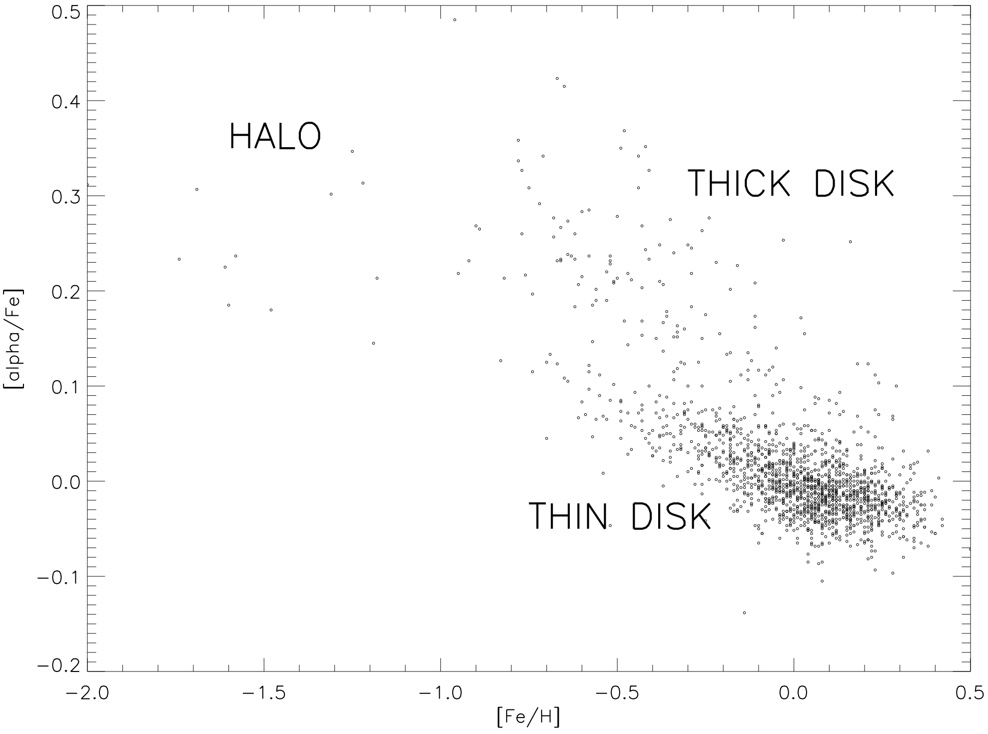

Figure 4.8: Abundance ratios of the α-elements [α/Fe] as a function of [Fe/H]. As in Fig. 1.1, three stellar components of the Milky Way (thin/thick disk and halo) are separated in the diagram.

Chapter 5

My role within the Gaia-ESO Survey

> A few observations and much reasoning lead to error; many observations and a little reasoning to truth.
>
> Alexis Carell

Since the very beginning of the Survey activities (Spring 2011), I participated in the tasks of the WGs 1, 2, 4, 6 and 12. In this framework, my contribution to the Gaia-ESO Survey has been fundamental for the observations, the data analysis of the observed YOC/SFRs and homogenization of the final products. It consisted in the recover of information from literature, such as photometry, proper motions, disk population and binarity, necessary for the membership analysis and the target selection candidates of Chamaeleon I, the configuration of the telescope for the observations of Chamaeleon I and Rho Ophiuchi and in the analysis of the full sample of the UVES spectra as well as the quality check of the obtained results from the following observed SFRs:

- **Chamaeleon I**: age=2 Myr; distance=160 pc;
- **Rho Ophiuchi**: age=1 Myr; distance=120 pc;
- **NGC2264**: age=3 Myr; distance=760 pc;

the observed YOCs:

- **Gamma Velorum**: age=5-10 Myr; distance=350 pc;
- **NGC2547**: age=35 Myr; distance=360 pc;

and the more evolved open cluster:

- **NGC6705**: age∼250 Myr; distance∼1900 pc.

The data of the first two observed YOC/SFRs (Gamma Velorum and Chamaeleon I) have been internally released by the Gaia-ESO consortium in August 2013 for science exploitation. A second release of data of the other clusters (Rho Ophiuchi, NGC2264, NGC2547 and NGC6705) is expected for early 2014.

5.1 Identification of the candidate targets of Chamaeleon I (task of WG1 and WG2)

A fundamental task for the cluster observations is the definition of a sample of target candidates within the field of the association of interest. The identification of that sample relies on the photometry catalogs and on the information about the membership, spectral types, proper motions, binarity and disk population reported in the literature and collected by myself for the Gaia-ESO community as a task of the WG2.

The current census of the cluster contains 237 confirmed members of which 33 are classified as brown dwarfs (spectral type >M6; Luhman 2007; Luhman & Muench 2008). However, as mentioned in Section 2.3.1, the aim of the target selection is to consider not only the known members, but to include in the sample other sources of the association field (including its suburbs) that could be members, in order to test the completeness of the census and to study the possible presence of contaminants. Thus, for the selection of candidate targets I adopted a general and inclusive criterion based on homogeneous photometric data. Nevertheless, like for many SFRs, there is no optical data for the entire region of Chamaeleon I. The largest data sets are the USNO-R magnitudes (Monet et al. 2008) and the JHK 2MASS catalog (Cutri et al. 2003). Thus, the list of target candidates has been chosen considering only the sources with 2MASS detections, having R_{USNO}<17 mag (all the sources without R_{USNO} photometry have been rejected) and lying in the following box-field that is centered on regions of highest extinction, but that is wide enough to cover also the cluster boundary: 10 45$\leq$R.A.$\leq$11 30; -79 00$\leq$DEC.≤-75 00. Assuming these selection criteria, I obtained a sample of $\sim$64,000 sources. Among these stars, I selected as candidate targets all those stars lying in a K/H-K diagram above the 10 Myr from the models of Siess et al. (2000) and having K<12 mag (see Fig. 5.1). Finally, I obtained a sample of 1792 stars that includes 141 known members. From the latter, I selected 16 high priority sources suitable for UVES observations adopting the following criteria:

- accept stars with G or K spectral types;
- accept stars with R_{USNO}<14 mag;
- reject stars with full width at 10% of the Hα maximum $\geq$400 km/s or EW(Hα)$\geq$40$\AA$;
- reject stars with v sin$i$>30km/s;
- reject stars with a companion closer than 1".

However, other 33 bright stars not satisfying at least one the the previous five criteria have been observed with UVES.

Figure 5.2 shows the map of the final candidate targets. A spatial concentration of the known members is evident; however, many members have been selected also at large distances from the main cloud. Most of the members not included in the sample are embedded objects and, in fact, lye in the regions of higher extinction.

Following this selection I have performed the fiber allocation and the telescope configuration.

5.2 Target selection and observing blocks configurations for the Chamaeleon I and Rho Ophiuchi fields (task of WGs4 and 6)

The fiber configuration has been set up with the appropriate selection of sources to be observed, the position of the sky fibers and the appriopriate exposure time. Each of these procedures is not independent, thus the target selection has been performed at the same time of the telescope configuration.

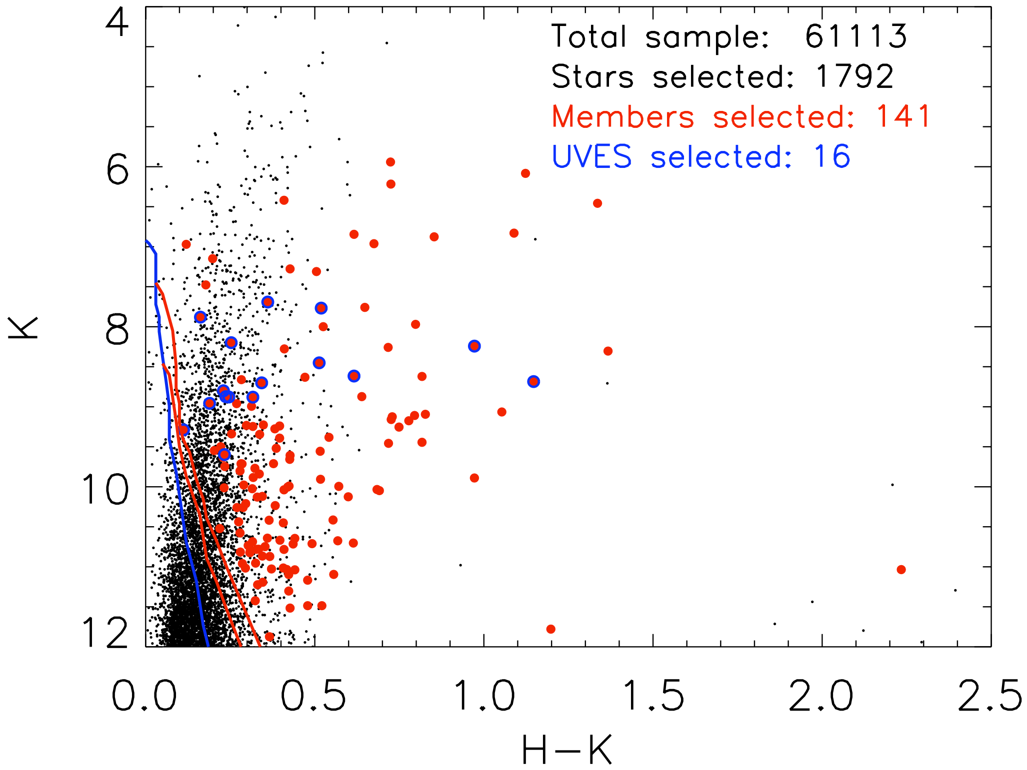

Figure 5.1: K/H-K diagram of the sources in the field box considered for the candidate target selection of Chamaeleon I. Red lines correspond to the 20, 10 Myr isochrones assuming the evolutionary models from Siess et al. (2000) and blue one to the ZAMS. The 141 known members are shown with red dots, while the 16 members suitable for UVES observations are marked with blue circles.

The telescope configuration consists in the identification of the guide stars for the adaptive optics and the fiducial stars which provide the needed coordinate references and the position of the observing blocks (OBs) in order to spatially cover each system as much as possible and the fiber allocation on the targets and the sky.

- **Guide and fiducial stars.** The identification of these stars in SFRs is often a difficult duty. In fact, the guide and fiducial stars need to be point-like and bright sources. However, since both Chamaeleon I and Rho Ophiuchi are very close to the Sun (160 and 140 pc, respectively) most of the sources in their fields are background objects, thus are obscured by the clouds. In addition, because of the elevated proper motion of these associations (especially for Chamaeleon I for which

Lopez-Marti et al. 2013 estimated $\mu_\alpha\cos\delta$=$-$24.3:$-$14.7 mas/yr), it is best to use known members as fiducial stars to better allocate the fibers to their members. However, for almost all cases this option could not be implemented owing to the small number of bright unextended members and to their low spatial density in the region.

- **Location of the fields.** I determined the location of each field on the basis of the distribution of the candidate targets and of the guide and fiducial stars. My aim has been to obtain a good coverage not only of the center of the clusters, but also of their ”suburbs” that are generally poorly studied, but that are of great interest in order to analyze the completeness of the members and their radial velocity dispersion. Because of the high density of the members in the center of these associations and their wide range of magnitudes, some of these OBs have been split in two different exposures with two different exposure times.

- **Fiber allocation.** During the fiber allocation procedure, the highest priority has been given to the known members (candidate GIRAFFE and UVES targets). Then, the remaining fibers have been allocated to the outstanding candidate targets paying attention to keep the range of R magnitudes always within 4 mag, as imposed by the WG6 main guidelines. For this reason, in some cases, to avoid the risk of contamination of the GIRAFFE allocated sample with much brighter objects, I allocated UVES fibers to other bright sources even if these were not previously selected as candidate UVES targets. Once the best configuration has been achieved, I determined the exposition time following the main guidelines. The last step of the procedure consisted in allocating as many as possible unassigned fibers to the remaining candidate targets, fainter than the range of 4 mag.

- **Sky fiber allocation.** Since the central regions of Chamaeleon I and Rho Ophiuchi are characterized by different gradients of nebulosity, the allocation of the sky-fibers is a critical step of the OBs generation. The goal is to cover the entire field using as many as possible of the remaining unallocated fibers. I used the Skycat tool to visualize the Digitized Sky (I + II) ESO images of each field in order to identify the position of each Sky-fiber paying attention to avoid background sources and to cover each gradient of nebulosity. Special care has been taken for the UVES sky-fibers that have been placed as close as possible to the UVES targets.

The Chamaeleon I cluster and the adjacent regions have been covered with 23 fields. Some of these fields are partially or totally overlapping in order to avoid saturation of the brighter sources and to obtain the largest number of spectra (see Fig 7.1). The configuration that I obtained amounts 25 OBs: 17 OBs with a short exposure (20 min) and 8 OBs with a long exposure (50 min). The total exposure time for Chamaeleon I is 12 hours and 20 min. In Fig. 5.4 I show the *finding chart* of one of the central OBs of the cluster. The northern part of this field is partially extincted by the residual nebulosity of the SFR. In that region, where the density of stars is lower, the allocation of sky fibers takes an important role. In the Chamaeleon I I allocated the FLAMES fibers to a total of 716 stars: 671 stars targeted by GIRAFFE, 45 by UVES plus 3 stars that have been observed by both the spectrographs. Among these there are 97 previously known members allocated to GIRAFFE and 18 to UVES. Observations of the Chamaeleon I have been successfully concluded on April 2012.

I accomplished the same task for the Rho Ophiuchi cluster, after that WG1 provided to me the list of candidate targets. In that region I identified 8 fields. About 200 stars have been targeted by GIRAFFE and 23 with UVES. The observations of Rho Ophiuchi have been achieved on August 2012.

5.3 Spectral analysis: WG12

This has been my main activity in the framework of the Gaia-ESO Survey.

As mentioned in Section 2.3.4, the tasks of WG12 is to analyze all the UVES and GIRAFFE spectra observed in the YOC/SFR fields, in order to derive their atmospheric parameters (T_{eff}, log g, [Fe/H] and microturbolence), elemental abundances and lithium EWs. Ii is a duty of this WG to derive parameters specific for PMS stars, such as chromospheric activity, veiling and accretion rates. This has been my main activity in the framework of the Gaia-ESO Survey.

Four nodes of the GES consortium are charged with the analysis of these spectra adopting different methods: Arcetri[1], CAUP[2] and UCM[3] adopted the “iron-EWs method” (described in detail in Section 3.1.1, while OACt[4] makes use of ROTFIT. For each star and each parameter, the median of the results obtained by the different nodes has been adopted as the final parameter recommended by the Survey, while the largest between the combined sigma and the dispersion has been assumed as the final error.

My activity within the WG12 consists in the coordination of the Arcetri node and in the analysis of all the UVES spectra of its duty. I analyzed about 300 spectra observed by the Survey. The outputs of this analysis that I provide to the Gaia-ESO Survey community are the main stellar parameters (T_{eff}, log g, [Fe/H] and microturbolence), elemental abundances, lithium EWs and the width of the Hα emission line at 10% of its height.

I also contribute to the checks and comparisons of the results provided by all the WG12 nodes necessary for the homogenization of the different analysis approaches. In particular, my studies showed an inconsistency on the microturbolence values derived by CAUP and UCM with the those obtained by other nodes of the consortium, revealed a lack of templates corresponding to metal-rich giant stars in ROTFIT grid and highlighted the critical need of adopting the same linelist. Furthermore, before the Survey started its observations, part of my work has been devoted to the implementation of automatic tools that would be able to analyze a large number of spectra in a homogeneous way and in a reasonable amount of time (see Chapter 3).

5.4 Scientific exploitation

The main project of my PhD regards the study of the elemental abundances of YOC/SFRs: I used iron and other element abundances of confirmed members observed by the Gaia-ESO Survey to determine the metal content of these environments. In particular, I studied the Gamma Velorum YOC that, due to its age, location (within a large region rich in clusters of different ages), and apparently low disk fraction, represents a very interesting case. The second case is Chamaeleon I: a SFR divided in two sub-clusters with different star forming histories (Luhman 2007). The results of these analysis are re-

---

[1] INAF - Osservatorio Astrofisico di Arcetri

[2] Centro de Astrofsica da Universidade do Porto

[3] Universidad Complutense de Madrid

[4] INAF - Osservatorio Astrofisico di Catania

ported in Chapters 6 and 7. Being Gamma Velorum and Chamaeleon I the first PMS clusters observed by the Survey, analysis of elemental abundance results and uncertainties also allowed me to perform science verification and validation studies on Gaia-ESO data.

Besides these two main projects, I participated to other studies that I found of interest. Here I list the abstracts of these projects:

- **Membership and dynamics of the Chamaeleon I star forming region.** Chamaeleon I is a very young (∼2 Myr) and close (∼160 pc) cluster composed of about 240 stellar members associated with a molecular cloud that is still forming stars. Due to its favorable properties is one of the most interesting regions for studying the dynamical evolution of young clusters of small size, during the first phases of the star formation process when a significant amount of interstellar gas is still present. The observations of this have been completed during the run of August 2012. We plan to use the radial velocities and the information on membership provided by the Gaia-ESO Survey for investigating the star formation history and the dynamical status of the cluster, and for better understanding the role played by the interstellar gas in the earliest phases of the cluster evolution.

  Publication: "Membership and Dynamics of the Young Cluster Chamaeleon I with the Gaia-Eso Survey"; G. Sacco, **L. Spina**, F. Palla, E. Franciosini; Protostars and Planets VI, Heidelberg, July 15-20, 2013. Poster#1K084

- **Abundance ratios in old and intermediate-age open clusters: a comparison with field stars.** The thin disk of our Galaxy is believed to be formed by dissipation of star clusters, and thus, in principle, we expect that the abundance ratios of field stars and present-day open clusters should be similar. Several studies are however showing that the abundances of some elements behave in a different way in clusters and in the field (e.g., Friel et al. 2010; Carrera & Pancino 2011; Reddy et al. 2011), and, in addition, the abundance ratios might be different in clusters with different age and/or located at different Galactocentric distances. A possible explanation might be that the youngest clusters are still intact, while the oldest ones may be totally disrupted, and consequently the field stars do not fully sample the age distribution of open clusters with the youngest stellar generations are under-represented by field star. The Gaia-ESO Survey is giving us, for the first time, the unique opportunity to analyze a large sample of cluster and field stars in a completely homogeneous way. The first three old and intermediate age open clusters observed within the Gaia-ESO Survey, namely Trumpler 20, NGC4815, and NGC6705, allow us to give a first look not only to the metallicity but also to their abundance ratios.

Publication: "The Gaia-ESO Survey: Abundance ratios in the inner-disk open clusters Trumpler 20, NGC4815, NGC6705"; L. Magrini, S. Randich, D. Romano, E. Friel, A. Bragaglia, R. Smiljanic, H. Jacobson, A. Vallenari, M. Tosi, **L. Spina**, P. Donati, E. Maiorca, T. Cantat-Gaudin, R. Sordo, G. Tautvaisiene and GES builders; submitted to A&A.

- **Membership, dynamics and star formation history of the young cluster NGC 2547.** NGC 2547 is a young cluster located in the Vela SFR, with a rich stellar population, a well determined age (∼35 Myr) and evidence of mass segregation. We plan to use accurate velocities and Li abundances from the Gaia-ESO Survey to perform an accurate selection of members, to determine the dynamical properties of the cluster and to study its star formation history in the broad context of the Vela SFR.

- **The abundance of refractory elements to discriminate the population of stars with planets.** Recent works (Gilli et al. 2006, Kang et al. 2011) have confirmed difference in chemical abundances between stars with or without exoplanets. In particular, they have found that the [Mn/Fe] ratios of planet host stars are higher than those of comparison stars over the entire metallicity range. They also found that in metal-poor stars ($[Fe/H]<-0.4$) the abundance differences between the two group of stars are larger for Mg, Al, Sc, Ti, V, and Co. We propose to investigate the existence of these correlations, and to analyze if there are differences in cluster and field stellar populations.

- **Characterization of the contaminant population in young clusters.** Besides confirmed cluster members, the samples of young cluster stars observed with UVES may contain a fraction of non-members, or contaminants. We aim to characterize the properties of these contaminant stars in young clusters, investigating their main stellar parameters including metallicity, Li abundances and radial velocities.

- **The evolution of lithium depletion in open clusters.** The study of Li abundances in open clusters is very important to understand the evolution of Li depletion with age, metallicity and stellar mass and to constrain non-standard models of stellar evolution. Currently available data have shown a complex pattern of Li depletion on the main-sequence that is not yet understood. We will use the Li abundances derived from the Gaia-ESO Survey to investigate this issue in intermediate-age and old open clusters.

- **The evolution of lithium depletion in open clusters** The study of Li abundances in open clusters is very important to understand the evolution of Li depletion with age, metallicity and stellar mass and to constrain non-standard models of stellar evolution. Currently available data have shown a complex pattern of Li depletion on the main-sequence that is not yet understood. We will use the Li abundances derived from the Gaia-ESO Survey to investigate this issue in intermediate-age and old open clusters, starting with Trumpler 20.

- **Accretion, chromospheric activity, and rotation in Chamaeleon I.** The study of accretion properties and magnetic activity of members of star-forming regions and very young clusters (<10 Myr) is important for our understanding of stellar and planetary formation. In this context, we plan to use the optical spectroscopy of the Gaia-ESO Survey with the aim to catch information on the astrophysical properties of the central star and on the accretion/disk characteristics. Thanks to several spectroscopic diagnostics (Hα, Hβ, HeI, etc.), we will be able to analyze accretion signatures. Connection between accretion and stellar physical parameters will be also investigated.

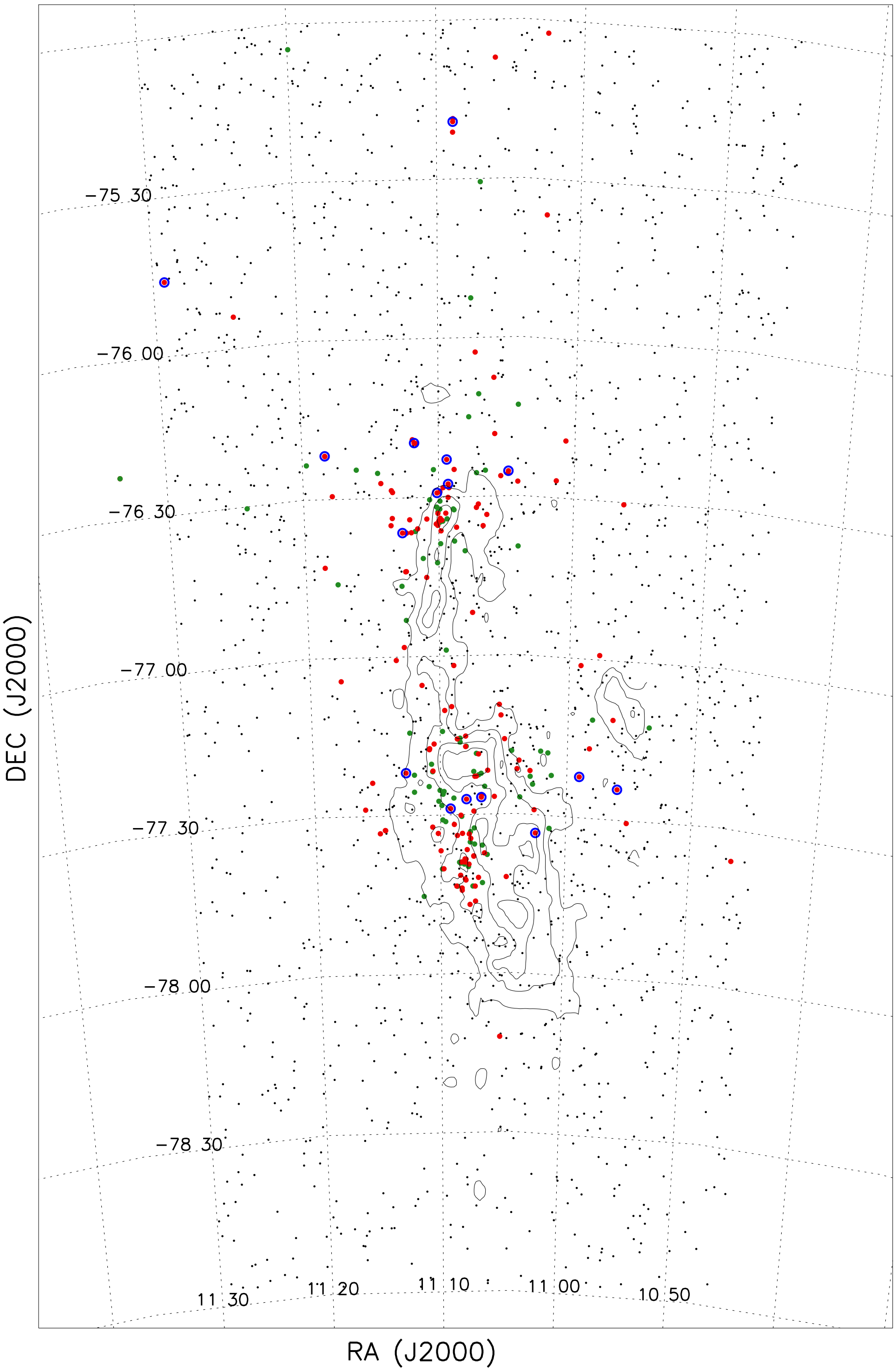

Figure 5.2: Map of the sources selected ad candidate targets. Red dots and blue circles are the same of Fig. 5.1. The known members not included in this sample are shown with green dots. The contours correspond to the extinction levels A_V=2, 4, 6 and 8 mag from Cambresy (1998).

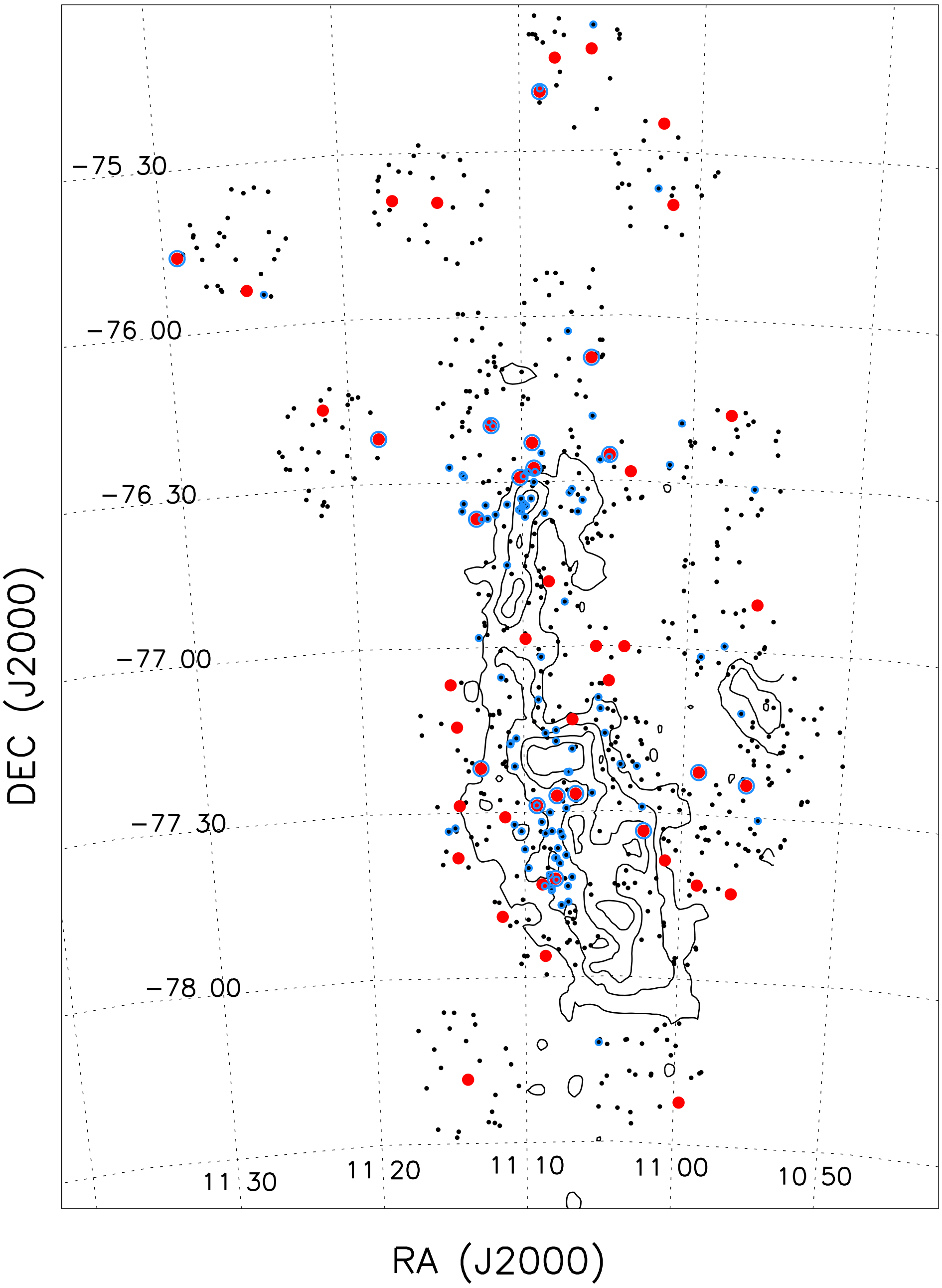

Figure 5.3: Map of the sources observed with GIRAFFE (black dots) and UVES (red dots) in Chamaeleon I. Previously known members are marked with blue circles. The contours correspond to the extinction levels A_V=2, 4, 6 and 8 mag from Cambresy (1998).

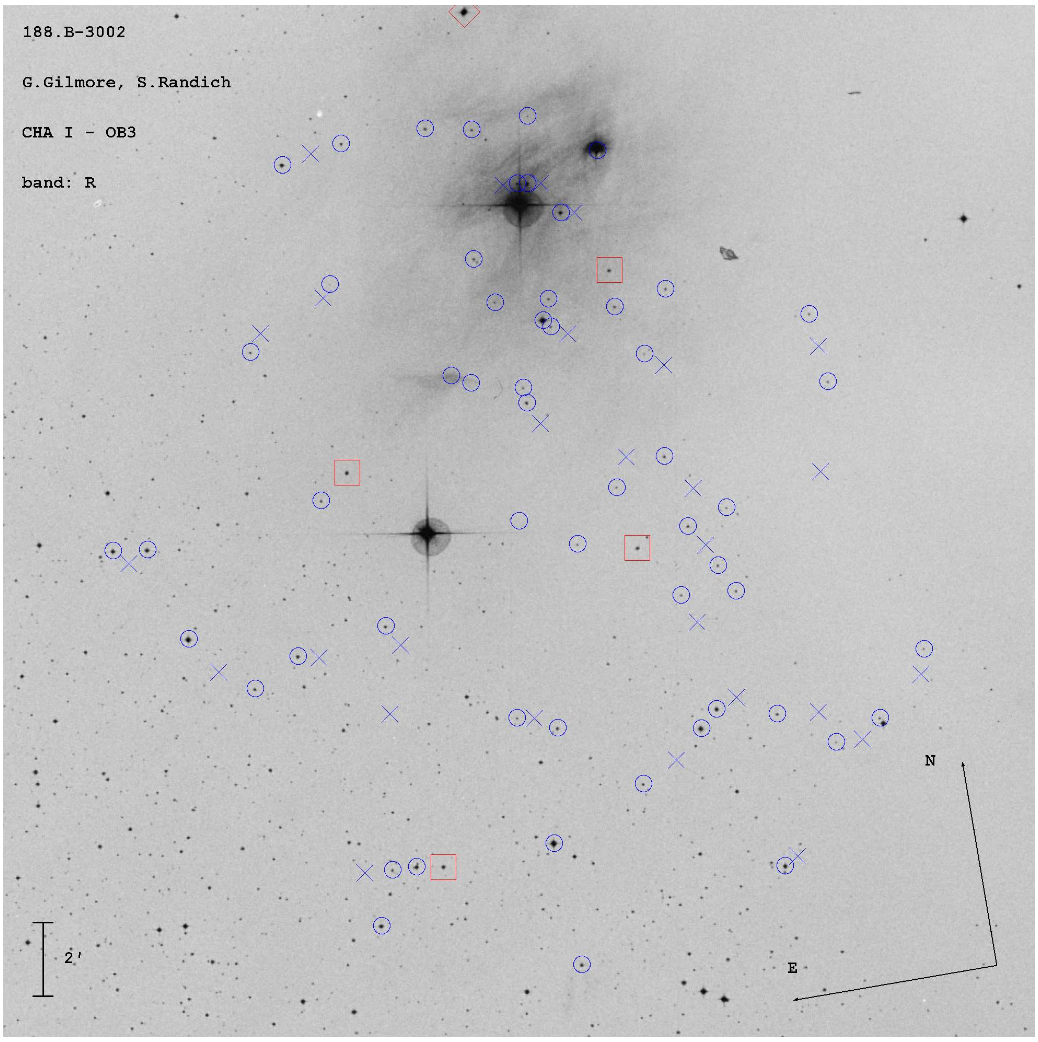

Figure 5.4: Finding chart of one of the Chamaeleon I field centered at 11 00 22 −77 45 38. The R band image is from the Digitized Sky (I + II) ESO. Blue circles indicate the fiber positions of both the spectrographs, blue crosses the location of the sky-fibers, while red squares and the red rumble mark the fiducial and the guide stars respectively.

Chapter 6

Gaia-ESO Survey: the first abundance determination of the pre–main-sequence cluster Gamma Velorum

L. Spina
S. Randich - INAF–Osservatorio Astrofisico di Arcetri
F. Palla - INAF–Osservatorio Astrofisico di Arcetri
L. Magrini - INAF–Osservatorio Astrofisico di Arcetri
E. Franciosini - INAF–Osservatorio Astrofisico di Arcetri
G.G. Sacco - INAF–Osservatorio Astrofisico di Arcetri
E. Alfaro - Instituto de Astrofísica de Andalucía
K. Biazzo - INAF–Osservatorio Astrofisico di Catania
J.I. González Hernández - Instituto de Astrofisica de Canarias
D. Montes - Departamento de Astrofsica, UCM
H. Tabernero - Departamento de Astrofsica, UCM
and Gaia-ESO Survey builders

In this Chapter I present my results on the determination of metallicity for a sample of stars in the Gamma Velorum cluster adopting the recommended products of the Gaia-ESO Survey. Gamma Velorum is a nearby cluster for which Gaia will give very precise proper motions and distances. It also lies in the Vela complex that experienced in the past several supernovae explosions and contains other young clusters of age similar to that of Gamma Velorum and that have been already targeted by the Gaia-ESO Survey. Thus, Gamma Velorum is a very suitable young cluster for a spectroscopic survey not only because, regardless of its youth, most of its members have already dissipated their disks, but also because the determination of its metallicity will allow us to compare the chemical patterns of the clusters belonging to the complex.

Gamma Velorum has been the first cluster observed by the Gaia-ESO Survey and a significant number of targets have been observed with both the spectrographs UVES and GIRAFFE. Thus, the analysis presented in this paper will also provide the opportunity for a science verification of the first data produced by the Survey.

This work has been submitted for publication to Astronomy & Astrophysics.

6.1 Abstract

Context. Knowledge of the abundance distribution of star forming regions and young clusters is critical to investigate a variety of issues, from triggered star formation and chemical enrichment by nearby supernova explosions to the ability to form planetary systems. In spite of this, detailed abundance studies are currently available for relatively few regions.
Aims. In this context, we present the analysis of the metallicity of the Gamma Velorum cluster, based on the products distributed in the first internal release of the Gaia-ESO Survey.
Methods. The Gamma Velorum candidate members have been observed with FLAMES, using both UVES and GIRAFFE, depending on the target brightness and spectral-type. In order to derive a solid metallicity determination for the cluster, membership of the observed stars must be first assessed. To this aim, we use several the membership criteria including radial velocities, surface gravity estimates, and the detection of the photospheric lithium line.
Results. Out of the 80 targets observed with UVES, we identify 14 very likely members (8 low-mass stars, 5 early-type stars, and one double-lined binary system) showing a lithium content consistent with the young age of the Gamma Velorum association. We find that the metallicity of the cluster is slightly sub-solar, with a mean [Fe/H]=-0.057 ± 0.018. A high probability member, star J08095427−4721419, shows a metallicity greater than the clus-

ter average. We speculate about its origin as the result of recent accretion episodes of rocky bodies of $\sim$60 $M_\oplus$ hydrogen-depleted material from the circumstellar disc.

6.2 Introduction

Open clusters are excellent tracers of the chemical pattern of the Galactic thin disc and its evolution (e.g., Friel 1995). The youngest clusters, the so-called pre-main-sequence (PMS) clusters with ages $\lesssim$ 50 Myr, are of particular interest since they are still close to their birthplaces and contain a homogeneous stellar population that has not had time to disperse through the Galactic disc. Thus, they are key objects in order to trace the current chemical composition of the Solar neighborhood and its evolution in space and time.

Furthermore, and more specifically, determination of the chemical content of young clusters and star forming regions (SFRs) is critical for a variety of reasons which we summarize below. First, as originally discussed in the series of papers by Cunha and collaborators, it allows investigating the common origin of different sub-groups in a given association and it sheds light on the possible presence of enrichment effects caused by the explosion of a nearby supernova (Cunha et al. 1998; Biazzo et al. 2011a, and references therein). Indeed, in the triggered star formation scenario, massive stars belonging to a first generation of stars and ending their lifetime with supernova explosions, are thought to trigger new star formation events; since supernovae are nucleosynthesis sites, these explosions, may also chemically enrich parts of the surrounding interstellar gas, and hence the newly formed second generation of stars, with some specific elements (i.e., α-elements or iron-peak elements; Cunha & Lambert 1992, 1994). Finding direct evidence of such selective enrichment in young clusters and SFRs would clearly give insights into a process that has occurred innumerable times in the past, not just in our own galaxy.

In addition, as in the case of old populations, the metal content of PMS clusters is a critical parameter for the determination of their distance, age, and individual stellar masses of their members. Metallicity has an effect on the internal stellar structure and on the surface properties through opacity and even relatively minor changes could imply differences in the derived cluster ages, distances, and masses (Sherry et al. 2008). These parameters in turn are critical for the determination of the Initial Mass Function (IMF) and the star formation history within each region, as well as for investigating of different properties such as disc lifetimes and the rotational evolution of young stars.

Recent theoretical studies have suggested that metallicity has an important impact on the evolution of circumstellar discs and their ability to form planets. For example, Ercolano & Clarke (2010) have shown that discs should dissipate quickly in a metal-poor environment. Observational studies on the disc lifetime at low-metallicity are controversial. On the one hand, support for the theoretical predictions has been provided by Yasui et al. (2010) who found that the disc fraction (f_d) in low-metallicity clusters (with [O/H]~-0.7) declines rapidly and approaches $f_d \sim 10\%$ in $\lesssim 1$ Myr, significantly earlier than solar-metallicity clusters for which the timescale is ∼5-7 Myr (Sicilia-Aguilar et al. 2006; Mordasini et al. 2012). On the other hand, based on Hubble Space Telescope mass accretion rate measurements, Spezzi et al. (2012) suggest that discs in metal-poor clusters of the Large Magellanic Cloud may be long-lived with respect to the Milky Way.

Finally, it is worth mentioning the correlation between elemental abundances and the presence of giant planets around solar-type stars (Gonzalez 1998; Santos et al. 2004; Johnson et al. 2010). In particular, Gilli et al. (2006), Neves et al. (2009) and Kang et al. (2011) have shown that the chemical differences between stars with or without exoplanets are not limited to the iron content, but also to the abundance of some refractory elements (e.g. Mg, Al, Sc, Ti, V and Co). Thus, a nearby, metal-rich PMS cluster hosting a number of T-Tauri stars with a circumstellar disc would represent a prime target for the study of planet formation scenarios and their timescales.

In spite of all these exciting aspects, relatively few studies have addressed the issue of the metal content of PMS clusters and SFRs (see, e.g., James et al. 2006; Santos et al. 2008; Biazzo et al. 2011a,b), focusing on the most well studied regions like Orion and Taurus-Auriga. A metallicity close to or slightly lower than the solar value (D'Orazi et al. 2009; Biazzo et al. 2011a) has been measured for all the studied regions; interestingly, and at variance with older clusters, none of them appears to be metal-rich. Since, as mentioned, only few regions and only very few stars per region gave high resolution abundance measurements, additional studies are clearly warranted.

The Gaia-ESO Survey (Gilmore et al. 2012; Randich 2014) is a Large Public Spectroscopic Survey observing all the components of the Galaxy (bulge, thin and thick discs, and halo). The project makes use of the FLAMES spectrograph mounted at the VLT to obtain spectra of about 10^5 stars, including candidate members of 90-100 open clusters. This large sample of observations will allow the accurate study of the kinematical and chemical abundance distributions in the Milky Way and also within the open clusters selected to fully sample the age-metallicity-mass/density-Galactocentric distance parameter space. In this framework, the Gaia-ESO Survey represents a unique opportunity not only to extend the sample of young clusters and star forming regions with metallicity and abundance determinations, but also to perform a homogeneous study based on a large stellar sample within each region.

In this paper we present the products released internally to the Gaia-ESO Survey consortium on the first observed PMS cluster: Gamma Velorum. The cluster properties, the target selection and spectral analysis are detailed in Sect. 7.3. The comparison between the main stellar parameters derived with the two different spectrographs in FLAMES is given in Sect. 6.4. The identification of the cluster members on the basis of radial velocities, surface gravity and the detection of lithium in the stellar atmosphere are presented in Sect. 7.4. The results of the elemental abundance determination is discussed in Sect. 7.6. The conclusions are outlined in Sect. 6.7.

6.3 Observations and data processing

The analysis presented in this paper is based on the results of the analysis of the spectra obtained during the first six months of observations (January - June 2012) and released internally in the GESviDR1Final catalog (August 2013). In the following, we describe the properties of Gamma Velorum, the target selection, the observations and the spectroscopic analysis.

6.3.1 The Gamma Velorum open cluster

Gamma Velorum is a nearby (∼350 pc) open cluster for which Jeffries et al (2009) originally claimed an age of ∼5-10 Myr, but that could instead be older than 10 Myr (but younger than 20 Myr - see discussion in Jeffries et al. 2014). Its low-mass members are distributed around a double-lined spectroscopic binary system (hereafter γ^2 Vel, as in Jeffries et al. 2009), composed of a Wolf-Rayet (hereafter WR) WC8 star (the closest Wolf-Rayet star to the Sun; Smith 1968) and a O8 massive star (Schaerer et al. 1997). Pozzo et al. (2000) were the first who recognized the presence of low-mass stars around the more massive objects. Due to the low extinction (A_V=0.131 and E_{B-V}=0.038), the sparse disc population and youth of the Gamma Velorum association, the sequence of the cluster is clearly visible in the optical color-magnitude diagrams presented by Jeffries et al. 2009).

On a larger scale Gamma Velorum lies in the so-called Vela complex (see Pettersson 2008; Sushch et al. 2011), a very composite region characterized, *inter alia*, by the presence of a number of PMS clusters (e.g, Gamma Velorum, Tr 10 and NGC 2547), three OB associations (Humphreys 1978; Brandt & Maran 1971; Slawson & Reed 1988) and two supernova remnants (the Gum Nebula and the Vela SNR). The latter have been created by two or more supernovae explosions that occurred 1-6 Myr and 11400 yr ago, respectively (Pettersson 2008). The shocks from the latter SN have not yet reached the Gamma Velorum cluster (Sushch et al. 2011), but it is clear that the environment has been subject to a fast dynamical evolution. Recently, the analysis of the Gaia-ESO Survey GIRAFFE kinematic data has led Jeffries (2014) to conclude that the members of the Gamma Velorum cluster are grouped in two distinct kinematic populations. Jeffries et al. through a maximum-likelihood fit of the RV distribution have found that the first kinematic component, centered at RV_1=16.70 km/s, is narrower and consistent with virial equilibrium (σ_1=0.28 km/s), while the second is much broader (σ_2=1.85 km/s) and centered at higher velocities, i.e. RV_2=18.58 km/s.

Interestingly, γ^2 Vel appears to be younger than the low-mass stars. Indeed, the relation and interactions of γ^2 Vel with the low-mass cluster members is still debated, mainly because of the age of the central WR star. In fact, even if the most recent γ^2 Vel distance determinations 368^{+38}_{-13} pc (Millour et al. 2007), 336^{+8}_{-7} pc (North et al. 2007) and 334^{+32}_{-40} pc (van Leeuwen 2007) support its association with the cluster, the age estimates of 3.5 ± 0.4 Myr (North et al. 2007) and 5.5 ± 1 Myr (Eldridge 2009) indicate that it is younger than the majority of the low-mass members of the cluster.

In spite of the remarkable properties of the cluster and of the Vela complex that makes Gamma Velorum a suitable target for a spectroscopic survey, its iron abundance is still unknown. Gaia-ESO Survey observations hence allow us to perform the first abundance study of this cluster.

6.3.2 Target selection and Observations

The Gaia-ESO Survey observations are performed with the multi-object optical spectrograph FLAMES at the VLT (Pasquini et al. 2002). This instrument feeds two spectrographs, GIRAFFE (132 fibers) and UVES (8 fibers).

The target selection criteria were based on homogeneous photometric data, covering a large area of the cluster field. In particular, the list of targets was chosen considering only the sources within a region of 0.9 square degrees centered on γ^2 Vel and studied by Jeffries et al. (2009). The selection (detailed in Prisinzano 2014) was done mostly following the guidelines for cluster observations (see Bragaglia 2014).

The final sample was chosen so as to include all candidate members in a region of the diagram around the cluster sequence, defined by previously known members. All stars falling within ±1 mag of the cluster sequence have been considered as high priority targets. A few lower priority stars have also been targeted to use spare fibers. The CMD of the selected sources is shown in Fig.6.1. The cluster sequence identified by Jeffries et al. (2009) is clearly visible as the upper concentration of red dots with (V$-$I) $\sim$1.8$-$3.2. The spectroscopic survey is limited to V$\lesssim$13.5 mag and V$\lesssim$19 mag for UVES and Giraffe, respectively.

A total of 18 Observing Blocks (OBs), forming a mosaic around γ^2 Vel, were completed during runs A (nights from 2011-12-31 to 2012-01-02) and B (night 2012-02-12) of P88, using for UVES the CD#3 cross disperser (λ =4770-6820 $\AA$; R=47000) and for GIRAFFE the HR15N grating (λ =6440-6820 $\AA$; R$\sim$17000). Each field was observed for either 20 min (9 OBs) or 50 min (9 OBs), respectively. Exposure times for the UVES targets hence vary from 20 min for stars brighter than V$\sim$ 12 to 50 min for stars with 12<V<13.5 mag. A few stars lying in overlapping fields have longer exposure times. Spectra for a total of 1242 and 80 individual stars were acquired with GIRAFFE and UVES, respectively. 39 stars were observed with both spectrographs. S/N ratios for the UVES spectra are in the range 20-300, with a median value of 116. .

6.3.3 Available data

The Gaia-ESO Survey is structured in 20 working groups (WGs) dedicated to different tasks. Pipeline data reduction is performed by WG7 (see Sacco et al. 2014; Lewis et al. 2014), while radial velocities (RV), projected rotational

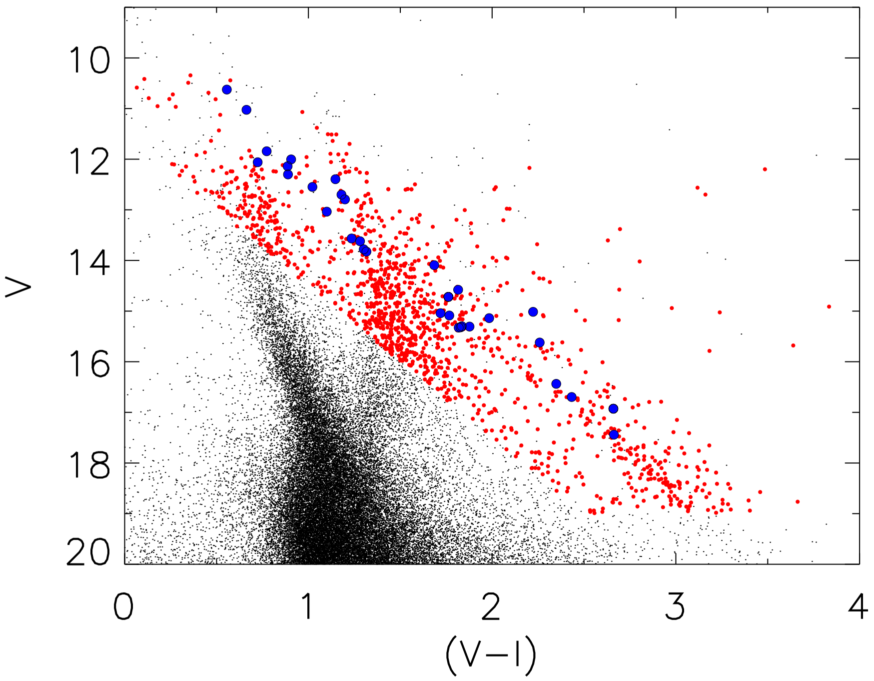

Figure 6.1: Color-magnitude diagram of the 1283 stars observed in Gamma Velorum (in red), along with all the stars (in black) located in the field of view centered on γ^2 Vel with photometry reported in Jeffries et al. (2009). The known members from this paper are shown in blue.

velocity (vsin i), and cross-correlation functions (CCFs) are derived by WG8. As for spectrum analysis, WG11 (including the contribution of up to 14 nodes) is dedicated to the analysis of the UVES spectra of F-G-K stars, whilst WG12 focuses on young stars, analyzing both UVES and GIRAFFE spectra. UVES spectra not affected by veiling are analyzed by both WG11 and WG12. In both working groups the final recommended parameters, which are released to the consortium, are the combination of the results of the contributing nodes. Both WG11 and WG12 benefit of the contribution of nodes that use different methods (e.g.,equivalent widths, synthesis, etc... see Smiljanic 2014; Lanzafame 2014). Note however, the consortium uniformly makes use of MARCS models of stellar atmospheres (Gustafsson et al. 2008) that assume the solar abundances from Grevesse et al. (2007). Also, common atomic data from Heiter (2014) has been used for GES analysis.

Release product for Gamma Velorum include radial and rotational velocities, CCFs and the products of the spectrum analysis have been made available. The latter include the main atmospheric parameters ($T_{\rm eff}$, log g and [Fe/H]) and other parameters (including veiling, measurements of the Li line at 6708 $\mathring{A}$, Hα, etc.) along with their uncertainties (Gilmore 2014; Randich 2014; Smiljanic 2014; Lanzafame 2014). Individual elemental abundances are also provided for UVES spectra whenever they can be measured. More specifically, WG11 and WG12 have produced recommended values for a common sample of 47 of the 80 UVES spectra. An additional sample of 20 UVES spectra have been analyzed by WG12 only, while the remaining 13 stars could not be analyzed due to their low signal-to-noise-ratio. Finally, GIRAFFE spectra have been analyzed by WG12 only. In this paper we adopt the parameters and abundances obtained by WG11 for the 40 stars analyzed by both WGs, since they are the combination of the results of a much larger number of nodes (14 vs. 4) and are hence characterized by a more solid estimate of the uncertainties. For the 20 UVES spectra analyzed by WG12 only and for the GIRAFFE analysis we consider instead the results of WG12. The agreement between WG12 and WG11 products for the stars in common is indeed good (see Lanzafame et al. 2014).

To summarize, we have:

- RV estimates of 73 of the UVES targets and of all the GIRAFFE targets; hereafter we disregard the RV values of 50 sources (5 UVES + 45 GIRAFFE) with poor quality spectra, or because they are early-type stars or fast rotating sources (vsin i>100 km/s). Thus, the final sample of stars with available and reliable RV estimates consists of 68 and 1197 stars observed with UVES and GIRAFFE, respectively.

- A measurement or an upper-limit of the equivalent width of the Li line for all these spectra with the exception of four warm stars in the UVES sample that do not show any Li feature in their spectra. For these four stars we assume a 3σ detection upper-limit using the Cayrel formula (Cayrel 1988).

- Finally, 68 stars observed with UVES and 1078 observed with GIRAFFE have an estimate of the fundamental parameters. Note that these are available for 36 of 39 stars observed with both spectrographs. The mean uncertainties of the parameters are: $<\sigma_{Teff}>$=120 K, $<\sigma_{log\ g}>$=0.17 dex, $<\sigma_{[Fe/H]}>$=0.10 dex.

Note that not every star with atmospheric parameters has also a RV estimate and *viceversa*. The sample stars with RVs and parameters, when available, are listed Tables 5 and 6.

6.4 UVES vs. Giraffe

As mentioned, fundamental parameters and [Fe/H] values have bee released for also for the stars observed with GIRAFFE. However, since the analysis of high-resolution spectra should yield more reliable iron abundance values (see Sect. 5.1), most of our scientific analysis will focus on the results of the UVES observations. On the other hand, we will mostly use the GIRAFFE sample as a control sample to infer the membership of the UVES targets; therefore, in this Section we take advantage of the stars observed with both UVES and GIRAFFE to check for their consistency. In particular, we will make a detailed comparison of the RVs, lithium equivalent widths, and atmospheric stellar parameters ($T_{\rm eff}$, log g and [Fe/H]).

6.4.1 Radial velocities

In Fig. 6.2 we show the difference between the values of the RV as a function of the projected rotational velocity derived from the UVES spectra. In the case of UVES, we adopt as final RV the mean of the two values obtained using the upper and lower spectral regions. As for the error bars, we assume the largest value between the error quoted in the Survey Catalog (±0.6 km/s) and the difference between the RVs measured independently in the two CCDs (Sacco 2014a). We note that $RV_{\rm GIRAFFE}$ is systematically higher than $RV_{\rm UVES}$ by 1.1±0.4 km/s (red dashed line in Fig. 2). The origin of this offset needs further investigation (see Sacco et al., 2013.). The increase in the offset for vsin i >20 km/s is likely due to line broadening and blending of lines.

6.4.2 Li equivalent widths

In Fig. 6.3 we show a comparison of the equivalent width (EW) of the Li 6707.8 line measured in GIRAFFE and UVES spectra, respectively. The figure indicates a very good agreement for most of the stars down to about 30 mÅ; a discrepancy between the values is instead present below that value, where the GIRAFFE measurements are systematically higher than

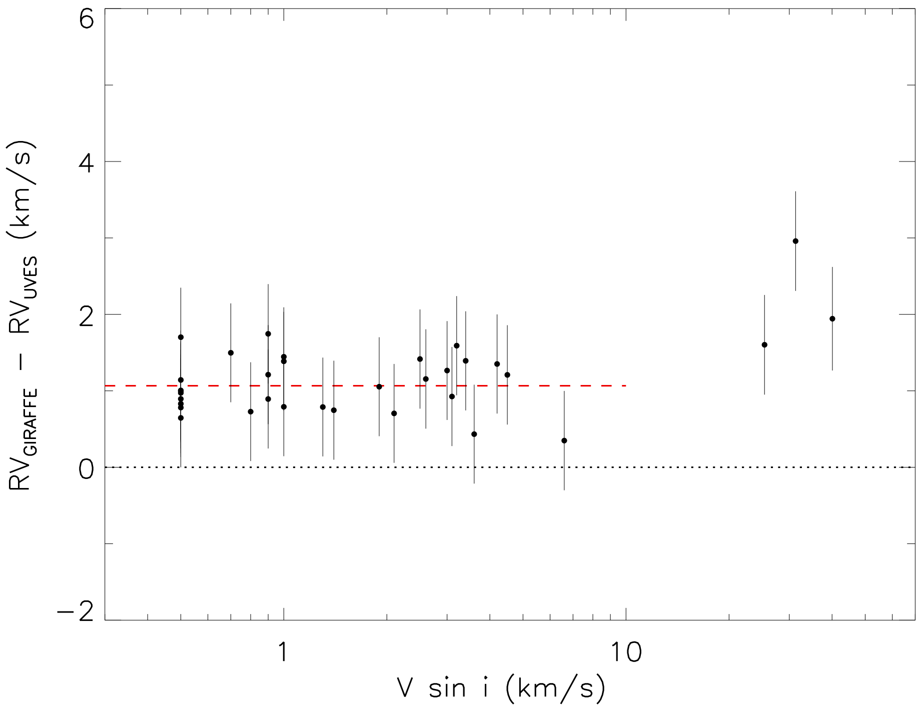

Figure 6.2: Comparison of the RV of the 34 stars with both GIRAFFE and UVES spectra and available RV values. The difference of the RVs is plotted as a function of the stellar rotational velocity ($v\sin\ i$). The red dashed line represents the offset between $RV_{\rm Giraffe}$ and $RV_{\rm UVES}$ for the 31 stars with vsin $i < 10$ km/s.

the UVES ones. While this difference must be further investigated, it will not affect our discussion and conclusions on lithium membership, since the threshold between members and non-members is at higher values of the EWs.

6.4.3 Atmospheric parameters

In Fig. 6.4 we compare the fundamental parameters derived from GIRAFFE and UVES analyses for 36 of the 39 stars. As in the case of EW(Li), we conclude that the two spectrographs yield compatible values within the errors for the majority of the stars. The only discrepancy is for the effective temperature of warm stars ($T_{\rm eff}$ >5500 K) for which the GIRAFFE analysis gives somewhat lower values than UVES, but still marginally consistent Whilst the origin of these differences is under investigation, it does not affect our conclusions on UVES membership. Also note that, due to the lower reso-

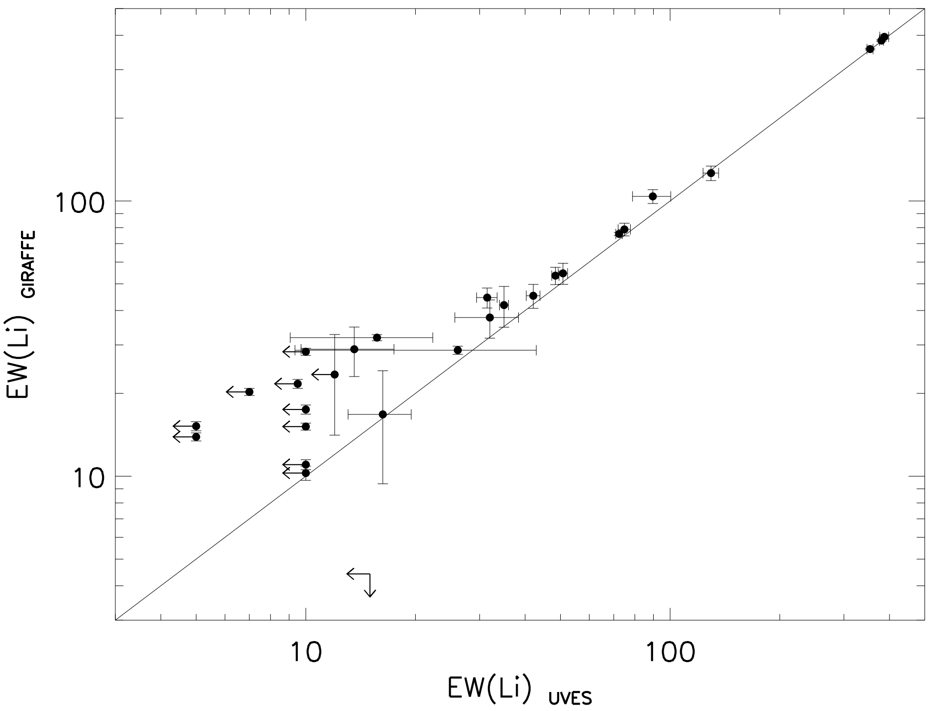

Figure 6.3: Comparison of the 17 EW(Li) measurements obtained from both the Giraffe and UVES spectra.

lution and the shorter spectral range, the uncertainties on the data derived from GIRAFFE are larger. This widens the scatter of the data without a significant implication for our analysis.

To summarize, whereas we will account for the offset between Giraffe and UVES in the following RV membership analysis, no systematic biases are present for lithium and log g values, the additional two criteria that we will use for confirming the membership of UVES candidates.

6.5 Membership analysis

In this Section we will use the spectroscopic information, specifically radial velocities, the strength of the Li line at 6708 *Å*, and the stellar surface gravity, along with the position of the targets in the CMD to perform the membership analysis. In Table 7.1 we summarize each step of the selection procedure that, starting from the 80 stars observed with UVES, leads to a restricted sample of high probability members that will be used for the metallicity analysis, which is the main goal of the present paper.

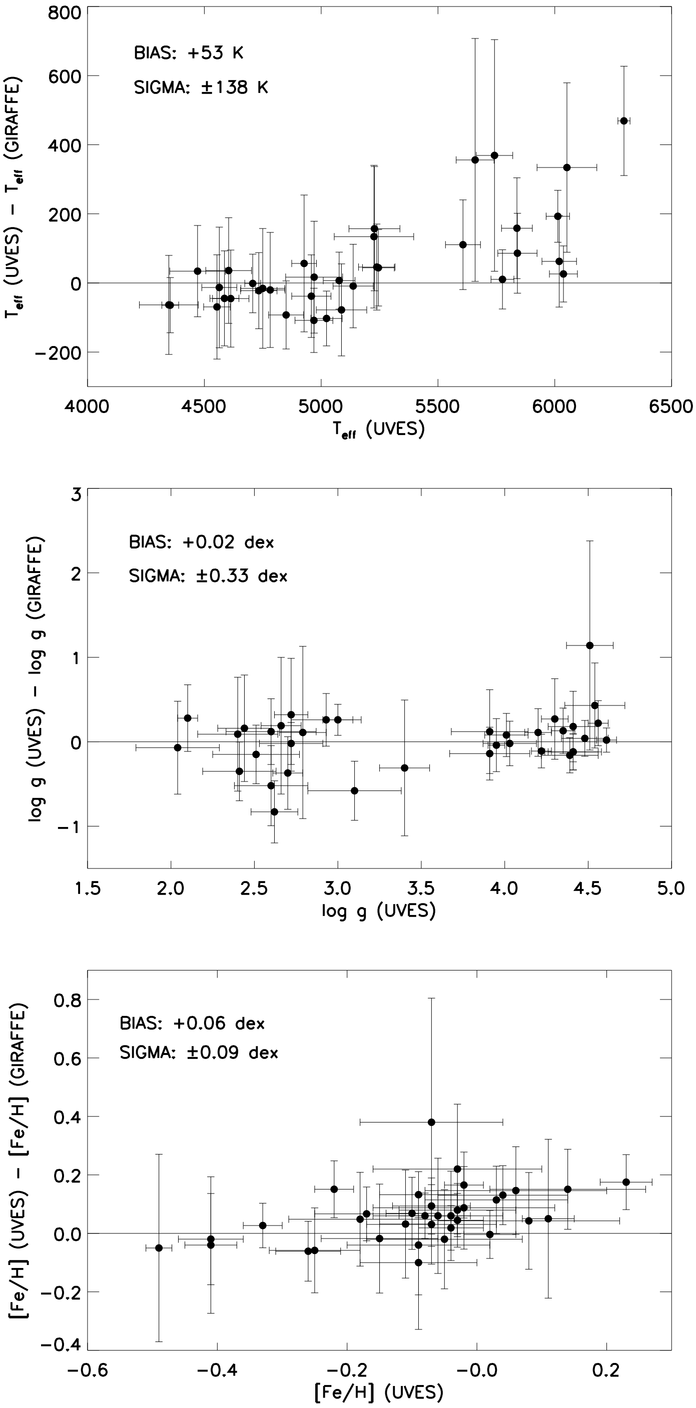

Figure 6.4: Comparison of the stellar parameters of the stars observed with both GIRAFFE and UVES spectra. The upper panel is for the effective temperature; the middle panel is the surface gravity; in the lower panel is the iron abundance. Systematic biases and standard deviations are reported in each panel.

Table 6.1: Summary of the selection procedure of UVES candidate members

Observed	80 candidates	39 in common with GIRAFFE
Binaries	6 SB2	discarded from the sample
RV estimates	62 candidates	7 RV members 55 RV non-members (or SB1)
Fundamental parameters	67 candidates	37 MS/PMS stars 30 giants
EW(Li) excluding giants	80 candidates − 30 (giants) = 44	8 Li members 17 HCM* (7 rejected as RV non-members) 19 Li non-members
CMD	8 (Li members) + 10 (HCM) = 18	7 Li mem. consistent with ZAMS 1 Li mem. below ZAMS 5 HCM consistent with ZAMS 5 HCM below ZAMS (rejected as non-members)
Abundance analysis	8 Li mem with [Fe/H] values 2 Li mem with other elements estimates	

In the text we use “Hot Candidate Members” (HCMs) for the stars with $(B-B)_0<0.3$ for which we cannot use lithium as a membership criterion.

As a first step, we searched for the presence of spectroscopic binaries in the sample of UVES stars. We identify six double-lined binaries (SB2) through their released CCFs: 2MASS J08072516-4712522, J08073722-4705053, J08093589-4718525, J08103996-4714428, J08105382-4719579, and J08115305-4654115. Those systems were hence discarded from the sample analyzed for membership.

6.5.1 Radial velocity distribution

For the radial velocity analysis we have considered all UVES candidates with available RV and that have not been identified as SB2 systems. This adds up to 62 stars. Also, for the estimate of the RV membership, we have added 1.1 km/s to the RVs from UVES spectra in order to account for the systematic offset described in Sect.6.4.1.

Assuming that the UVES targets would be characterized by the same radial velocity distribution as the Giraffe ones, the analysis was performed, adopting the results of Jeffries (2014); specifically, considering the two kinematic components identified by Jeffries et al., their peak velocity and dispersion, we confirmed as RV members all the stars with RVs in the interval between 14.9 and 22.3 km/s, corresponding to $RV_2 \pm 2\sigma_2$ of the broader distribution. Among the 62 UVES candidates, we have identified 7 RV members and 55 RV non-members.

6.5.2 Identification of the giant contaminants

The sequence of Gamma Velorum candidate members is easily identified in optical CMDs at magnitudes V>15 mag (see Jeffries et al. 2009). However the UVES targets are restricted to the brighter part of the CMD where the sequence is heavily contaminated by field stars. In order to identify the population of evolved contaminants, we plot in Fig. 6.5 the spectroscopic surface gravity as a function of $T_{\rm eff}$ for the GIRAFFE and UVES samples. Stars are clearly divided in two groups: main-sequence (MS), PMS and dwarf stars with log g$\sim$4-5 dex and giant branch stars with lower gravity values. In the figure we also show the 5 Myr (solid line), 1 and 10 Myr (dashed lines) isochrones from Siess et al. (2000) models for a metallicity of $Z_{\odot}$=0.01, close to the value of the solar metallicity, Z=0.012, adopted in the MARCS models. Based on this figure, we conservatively consider as giant contaminants all the stars that lie above the 5 Myr isochrone. Using this criterion we find 37 UVES stars among the 67 UVES stars with log g determination that lie below this isochrone: the seven RV members, 22 candidates with RV not consistent with that of the cluster, and eight stars without a RV estimate. The remaining 30 UVES stars, with log g typical of a giant star will be discarded from further analysis. Not surprisingly, all these stars are RV non-members.

6.5.3 Lithium members

As well known, lithium is amongst the most useful membership indicator for young stars. In Fig. 6.6 we show the EWs(Li) as a function of $(B-V)_0$ for the 44 UVES candidates that have not been rejected as SB2 or giant contaminants. Along with the UVES stars, we also plot the 166 GIRAFFE RV members that have not been flagged as giants. The majority of the GIRAFFE targets in the color range $0.5<(B-V)_0<1.4$ have EW(Li)>100 m$\mathring{A}$. Their distribution clearly defines the sequence of Li undepleted members. However, at $(B-V)_0 > 1.4$ we observe a large dispersion in equivalent widths, indicating that a fraction of low-mass stars in the cluster have started depleting lithium and hence suggesting a possible age dispersion (see Jeffries et al. 2014; Franciosini et al. 2014). A gradual decrease of EW(Li) is also observed for hotter stars with $(B-V)_0 < 0.5$, but in this case the drop is caused by the ionization of lithium rather than by its depletion.

In order to assess the membership of the UVES sources on the basis of the lithium content, we also use the information from the members of

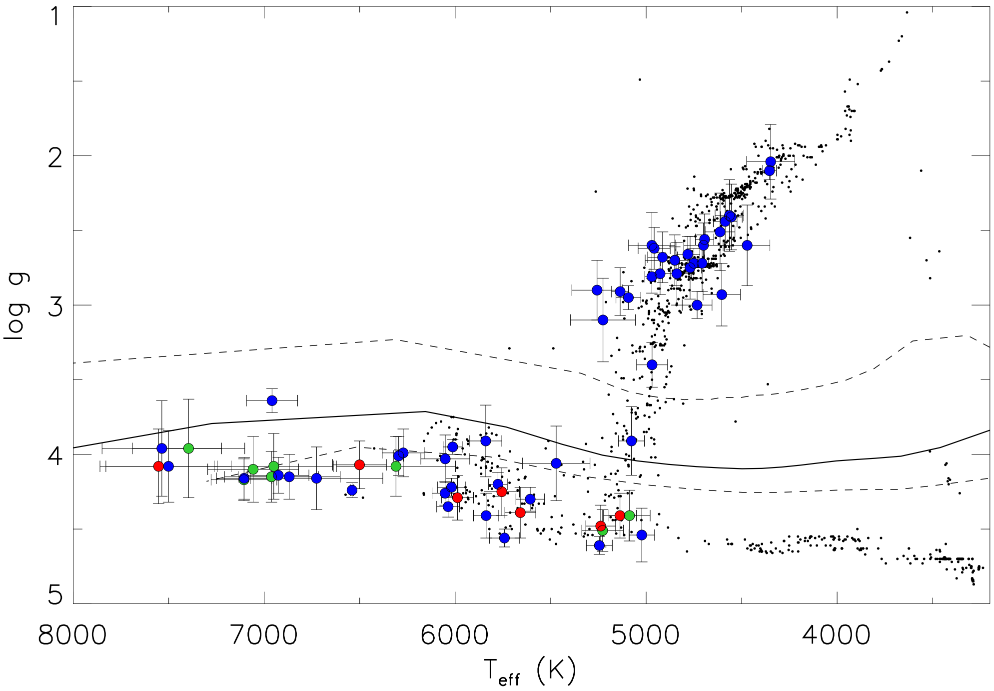

Figure 6.5: Surface gravity versus effective temperature. The diagram allows us to identify the giant field stars in the GIRAFFE (black dots) and UVES (colored circles) samples as the objects that lie above the 5 Myr isochrone (solid line) together with the 1 and 10 Myr (dashed lines) isochrones using Siess et al. (2000) models. The different colors indicate RV members (red), RV non-members (blue), and stars excluded from the RV analysis (green).

the Pleiades cluster (∼120 Myr, van Leeuwen 2009). Their distribution in the EW(Li) vs. (B-V)$_0$ plot is shown in Fig. 6.6. We see that while the coolest Pleiades members have already partially depleted Li, the hotter stars maintain their initial abundances. The position in the diagram of the Pleiades stars along with that of the GIRAFFE stars allows us to identify the locus of the sequence of members as a function of color. This is shown by the solid black line in the figure. Hence, we consider as Li members/candidates all those stars with 0.3 <(B-V)$_0$ < 1.4 lying above the solid line, plus all the sources with (B-V)$_0$ > 1.4, for which lithium depletion may not necessarily imply non-membership (note that all the UVES targets are in any case bluer than this limit). For stars with (B-V)$_0$ < 0.3 we cannot use lithium as a membership criterion, but we will flag them as "hot candidate members" (hereafter, HCM).

To summarize, the analysis of Li allows us to conclude that there are

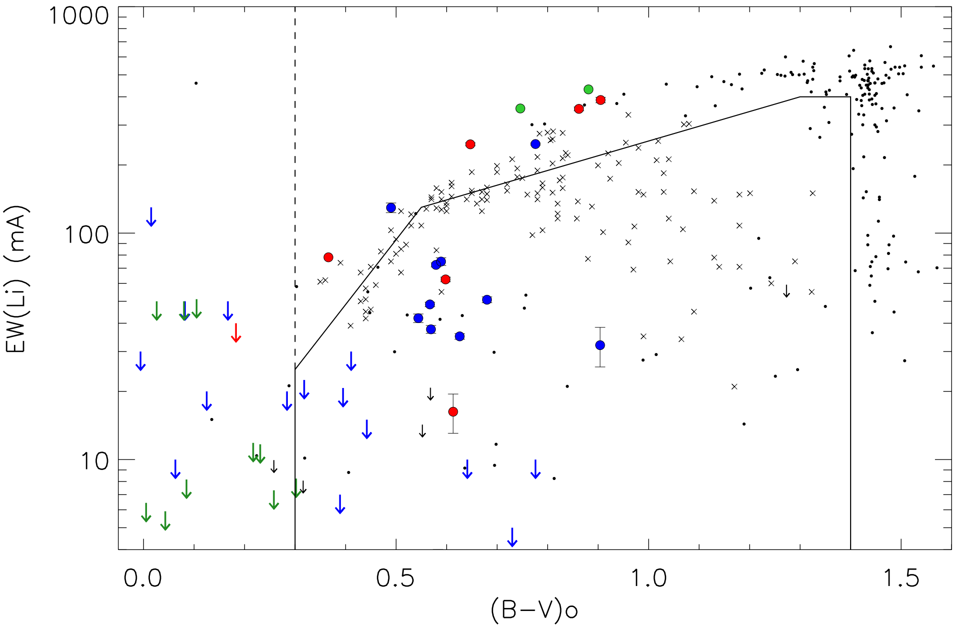

Figure 6.6: Lithium EW as a function of the intrinsic color $(B\text{-}V)_0$. The red and blue symbols (circles and arrows) represent the RV members and RV non members, respectively, from the UVES sample. Green arrows are stars with no RV estimate. The black dots show the GIRAFFE RV members the mean EW(Li) uncertainty of which is ±11 m$\mathring{A}$. The solid line denotes the part of the diagram occupied by the Li members (above) and Li non-members (below). The dashed line separates Li members (right) from hot candidate members (left). As a reference, we have also plotted the data of the ~120 Myr old Pleiades members (crosses; Soderblom et al. 1993; Jones et al. 1996).

eight high probability UVES Li members (four RV members, two RV non-members, and two stars without a RV estimate) that lie well above the sequence of Li undepleted stars. Sixteen RV non-members are also non-members based on lithium, while two RV members have small Li EWs and hence appear to be non members based on lithium. The remaining RV member is a warm star and hence defined as HCMi (see below). As for the hotter stars, there are 10 HCMs on the left side of the dashed line (1 RV member, 9 without RV estimate) that we will consider for further analysis and 7 HCMs which are RV non members that will be rejected. Finally, we count 135 GIRAFFE Li members out of the initial 166 RV members. Interestingly, we also note that one of the six SB2 systems (J08093589-4718525, #46) has both components with EW(Li) larger than 100 m$\mathring{A}$, making it a possible member of the cluster.

6.5.4 Color-magnitude diagram

The CMD is a helpful tool to confirm the reliability of our membership analysis and to provide some additional information about the HCMs for which we were not able to establish a secure membership based on lithium. Figure 6.7 shows the position of the eight UVES and all the GIRAFFE stars considered as Li members, plus the 10 HCMs, using the photometry given by Jeffries et al. (2009) and also released to the Gaia-ESO consortium. For stars not included in this compilation, we have used the photometry from the Tycho-2 catalogue (Høg et al. 2000). Both the distance modulus (DM=7.76) and reddening (E(B−V)=0.038) are taken from Jeffries et al. (2009). As expected, the majority of the stars fall in proximity or above the ZAMS in a sequence close to the 10 Myr isochrone, although a few outliers are present. Among the UVES sample, there are five HCMs (#24, 27, 68, 31, 29) and one Li member (#43) lying significantly below the ZAMS, i.e. more than the ±0.3 mag spread in distance modulus found by Jeffries et al. (2009) (uncertainties on photometry and extinction are negligible for these stars). We will not consider these five HCMs for further analysis since they are likely field dwarfs. On the other hand, we note that the star #43 has a RV value slightly below ($\sim$ 1 km/s) our threshold for membership; however its high EW(Li) and surface gravity ($\log g$=4.03) are consistent with those of other high probability members. Thus, we include it as a likely member in the sample considered for the abundance analysis.

6.5.5 Summary of the membership analysis

In Table 6.5 we list the parameters of the 80 stars observed with UVES. In the last five columns, we give the membership status from the radial velocity, surface gravity, EW(Li), and the position in the CM diagram: “M” stands for member, “N” for field contaminant, and “HCM” for hot candidate member. Table 7.1 summarizes the tally resulting from the analysis of the individual membership indicators. In total, there are eight high probability members, as indicated by their lithium, plus one Li-rich SB2 that can be considered as a likely member. Among the high probability members, four

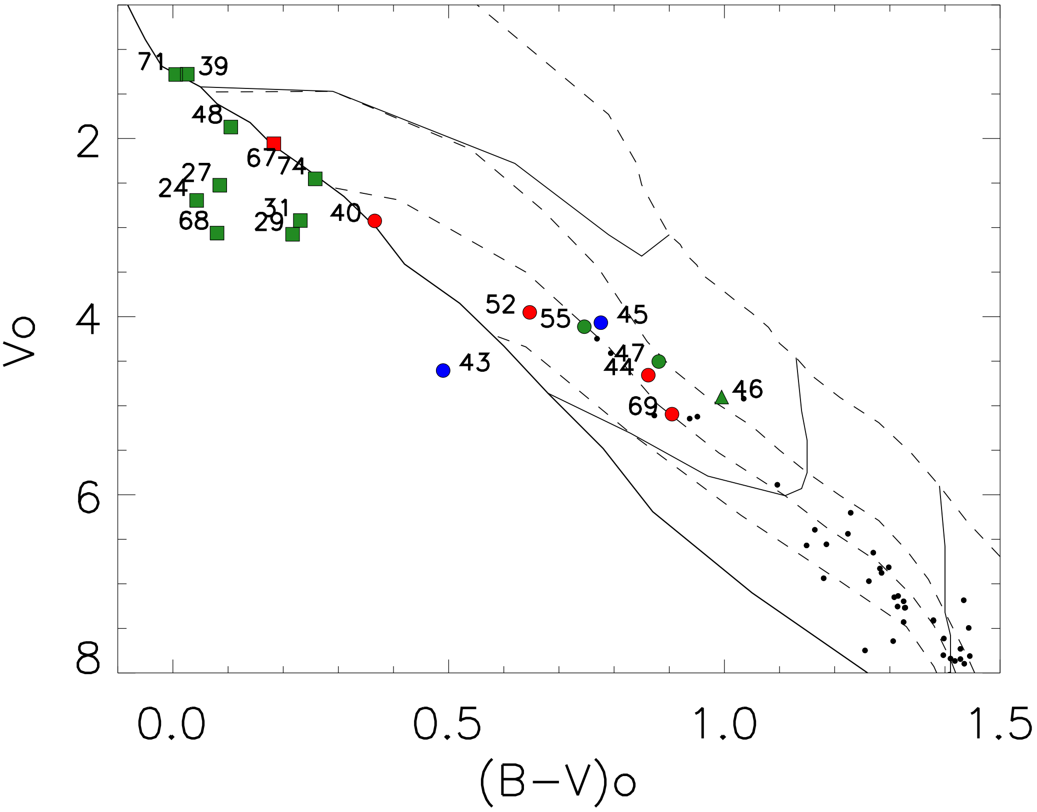

Figure 6.7: V_0 vs $(B\text{-}V)_0$ diagram of the UVES cluster members (circles), HCM (squares) and Li-rich binary system (triangle). Stars are color coded according to the RV membership. Each star is labelled according to the ID number given in Table 7.3. The GIRAFFE members are shown as black dots. The solid and dashed lines are the evolutionary tracks for 0.5, 1 and 2 $M_\odot$ and isochrones for 1, 5, 10, 20 Myr and ZAMS from Siess et al. (2000) for a chemical composition with Z =0.01. The diagram is limited to the color-magnitude range relevant for the UVES targets.

are also RV members. There are also five HCMs that satisfy the criteria for membership based on log g and the CMD. In total we hence have 14 likely members. Nothing can be said on the remaining five SB2 systems. Note that the membership of two out of the seven RV members is not confirmed by the lithium analysis, impliying a contamination of about 30 % in the RV sample.

6.6 Abundance analysis of the members of Gamma Velorum

6.6.1 Iron abundance

Based on the eight UVES high-probability members, we obtain the [Fe/H] distribution of Gamma Velorum shown in Fig. 6.8. The mean iron abundance is $<$[Fe/H]$>= -0.04\pm0.05$, where the error corresponds to 1σ of the distribution. We recall that this [Fe/H] values refer to a solar value of log N(Fe)=7.45 (Grevesse et al. 2007). Seven out of the eight stars have abundances in the narrow range -0.1 to -0.03 dex. The outlier (J08095427−4721419, #52) has [Fe/H]=+0.07 that is $\sim2\sigma$ larger than the mean. Excluding this metal-rich star, we obtain a mean iron abundance of -0.057 ± 0.018. These results indicate that the members of Gamma Velorum have a slightly sub-solar iron abundance with a small dispersion. The mean iron abundance is compatible with that derived in other young open clusters of the solar neighborhood (Biazzo et al. 2011a), while the small dispersion suggests a homogeneous element abundance in Gamma Velorum. Considering the two kinematic groups, we note that among the eight members only one star (J08110285−4724405, #69) is associated to the 1^{st} RV group. Thus, we cannot make a comparative analysis of the abundances in terms of the two RV populations. J08095427−4721419 and the implication of its high iron abundance will be discussed in detail in Sect. 6.6.3.

We now consider the results for the GIRAFFE members since the richer statistics allows a more general study of the iron abundance distribution in Gamma Velorum. In Fig. 6.9 we show the iron abundance of GIRAFFE high-probability members with v$\sin i \leq 50$ km/s. The latter constraint is necessary because, in the spectra of fast rotating stars, the blending of the absorption features makes the iron abundance estimate highly uncertain. We find that $<$[Fe/H]$>_{\rm GIRAFFE} = -0.19 \pm 0.12$, significantly lower than the mean iron abundance based on the analysis of UVES spectra (Fig. 6.8). for the remaining four stars. Therefore, we cannot perform a comparative analysis of the abundances in terms of the two RV populations. Although the metal rich star J08095427−4721419 belongs to the second group, the similarity of [Fe/H] of the remaining seven stars suggests that no difference in metallicity is indeed present between the two groups. A discussion of J08095427−4721419 and a possible explanation for its high iron abundance will be provided in Sect. 6.6.3.

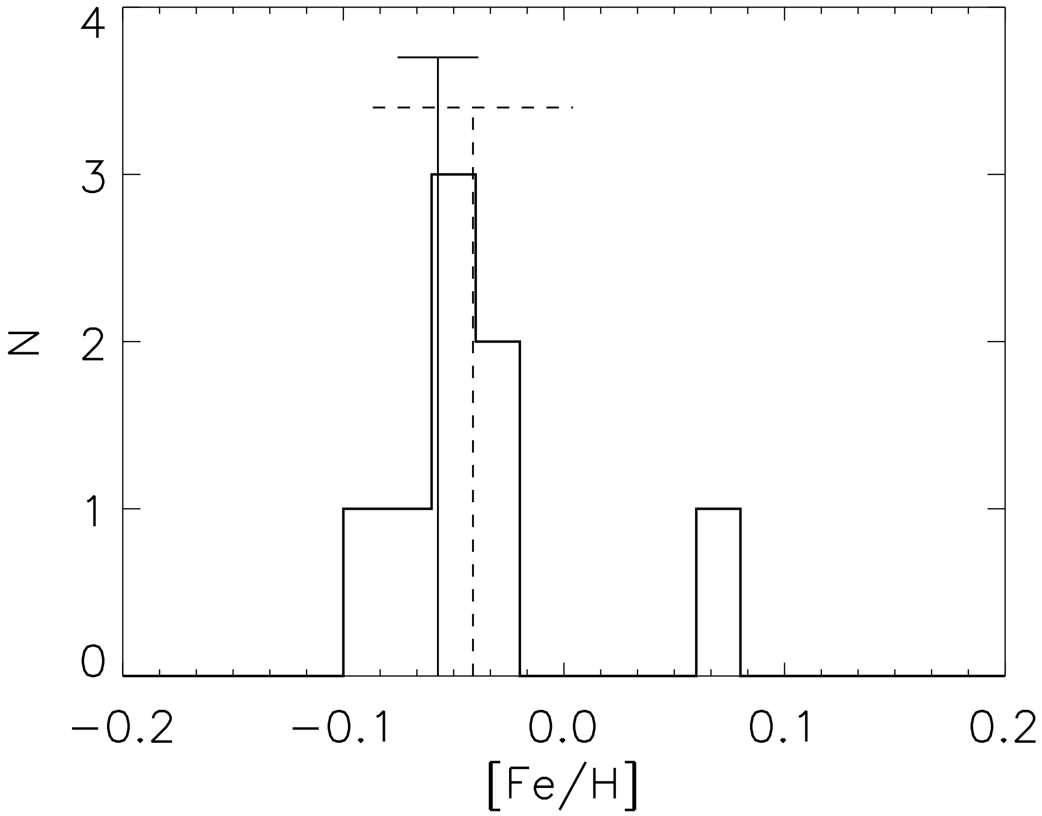

Figure 6.8: Distribution of the iron abundance of the eight UVES high probability cluster members. The mean value is <[Fe/H]>=−0.04±0.05 (dashed line) and <[Fe/H]>=−0.057±0.018 (solid line) discarding the star #52 with [Fe/H]= 0.07.

The much larger number of Giraffe members and the richer statistics allows a more general study of the iron abundance distribution in Gamma Velorum. In Fig. 6.9 we show the iron abundance of GIRAFFE high-probability members with vsin $i \leq 50$ km/s. The latter constraint is necessary because in the spectra of fast rotating stars the blending of the absorption features makes the iron abundance estimate highly uncertain. We find that $<$[Fe/H]$>_{\rm GIRAFFE} = -0.19 \pm 0.12$, somewhat below the mean iron abundance based on the analysis of UVES spectra (Fig. 6.8). The different mean iron abundance and the broader width of the distribution (from −0.34 to +0.13) are partly due to the lower resolution of the GIRAFFE spectra and also to the intrinsic difficulty of the analysis of cool stars. If we restrict the GIRAFFE sample to stars with $T_{\rm eff} > 4000$ K ($\sim$25% of the objects), we derive a mean value of $<$[Fe/H]$>_{\rm GIRAFFE} = -0.03 \pm 0.09$, more similar to that of the UVES sample. Note that a few stars are present in the Giraffe distribution with high metallicity, comparable to that of star J08095427−4721419. Whereas the larger typical uncertainties of the GIRAFFE determinations certainly contribute to broaden the [Fe/H] distribution, we cannot exclude that the GIRAFFE sample also contain a number of as yet unidentified metal-rich outliers.

Finally, considering the GIRAFFE targets with $T_{\rm eff} > 4000$ K, we plot in Fig. 6.10 their iron abundances as a function of the RVs. Although a group of stars with RV values ranging between 18.5 and 20 km/s have lower iron abundances respect to the others, there is a significant scatter between the stars of the two populations without hints of abundance separations. Thus, we conclude that the two groups likely have the same iron abundance.

6.6.2 Other elements

The Gaia-ESO Survey has released for Gamma Velorum the abundance of elements other than iron for stars with $v\sin i$<20 km/s. Unfortunately, this limits the analysis to two confirmed members only: J08095427−4721419 (#52) and J08093304−4737066 (#45). The elemental abundances are listed in Table 6.2.

We see that for the cooler star (#45) the abundances are within ±0.1 dex of the solar values, with the only exception of calcium and nickel. The warmer star (#52) shows abundances significantly larger than solar and very unusual for the solar neighborhood for most of the analyzed elements. Given that this is the metal-rich star these abundances may in principle shed light on the reasons for the high metallicity. However, the errors are much larger than those obtained for #45, with the exception of iron. Hence we do not attempt any conclusions based on the abundance ratios.

6.6.3 The metal rich star J08095427−4721419

J08095427−4721419, one of the eight high probability members of Gamma Velorum, has an iron abundance of [Fe/H] = +0.07 ± 0.07. Its membership is based both on the presence of photospheric Li and on a RV consistent

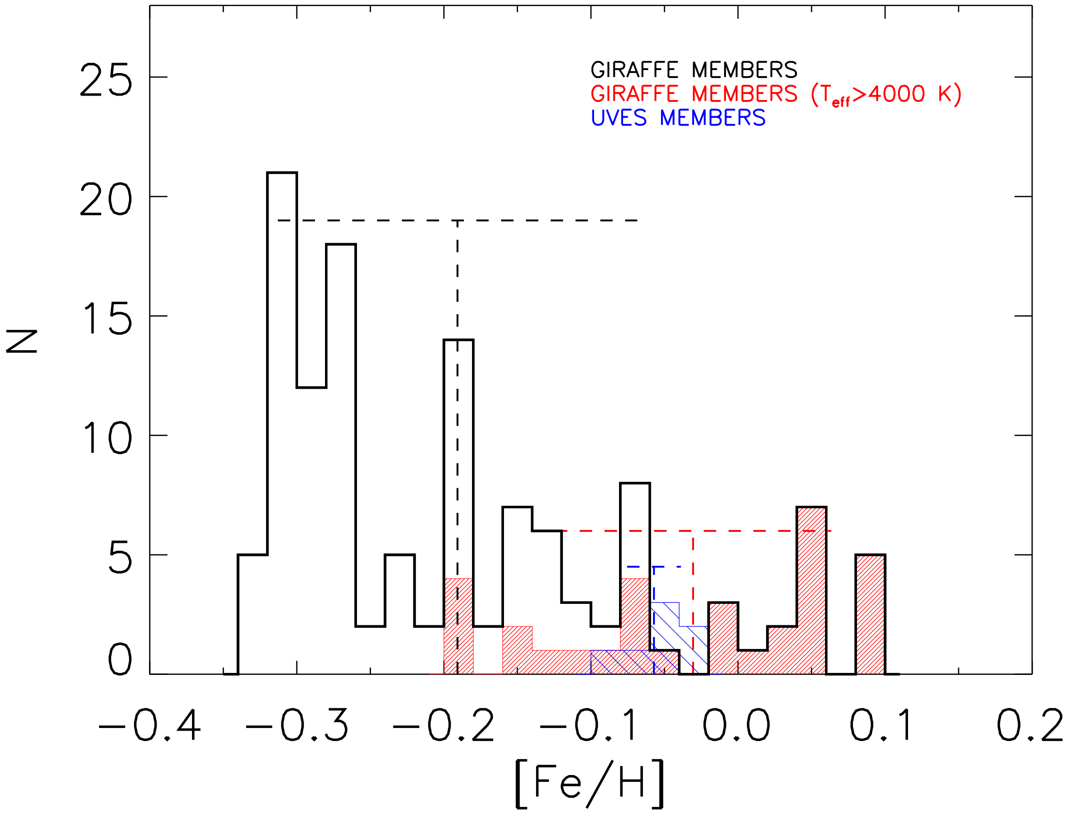

Figure 6.9: Iron abundance of the GIRAFFE members (solid histogram). The other histograms show the iron abundance of the GIRAFFE members with T_{eff}>4000 K (red) and that of the UVES members (blue).

with that of the cluster. Other indirect support comes from the relatively high rotational velocity typical of young stars, a proper motion compatible with the other members of the cluster and an elevated X-ray emission (Jeffries et al. 2009). Furthermore, the star exhibits an IR excess at 24 μm that suggests the presence of a debris disc (Hernández et al. 2008). We also notice that different analysis methods within the Gaia-ESO consortium have derived similar stellar parameters and enhanced metallicity (see Table 6.3). The position in the CMD reinforces the quality of the atmospheric parameters. Thus, we assume that this star is genuinely more metal-rich than the other cluster members.

Based on statistical considerations, one would expect to detect one 2σ outlier in a sample containing more than 20 stars; hence, the probability of

Table 6.2: Elemental abundances

	J08110285−4724405 #45	J08095427−4721419 #52
T_{eff}^{spec} (K)	5471	5756
[Fe/H]	−0.06±0.12	+0.07±0.07
[Si/Fe]	−0.10±0.08	+0.18±0.20
[Mg/Fe]	+0.02±0.14	+0.30±0.40
[<Ti>/Fe]	−0.04±0.07	+0.46±0.29
[Ca/Fe]	+0.18±0.03	+0.08±0.40
[Cr/Fe]	+0.06±0.03	+0.47±0.22
[Ni/Fe]	−0.18±0.05	+0.08±0.52

Table 6.3: Stellar parameters of J08095427−4721419.

	T_{eff} (K)	log g (dex)	[Fe/H] (dex)
WG11 average	5756 ± 93	4.25 ± 0.16	+0.07 ± 0.07
WG12 average	5864 ± 112	4.41 ± 0.08	+0.14 ± 0.09
WG12[a]	5944 ± 57	4.45 ± 0.10	+0.20 ± 0.13
WG12[b]	5785 ± 56	4.37 ± 0.13	+0.08 ± 0.11

a) Iron EWs method.

b) Comparison with templates.

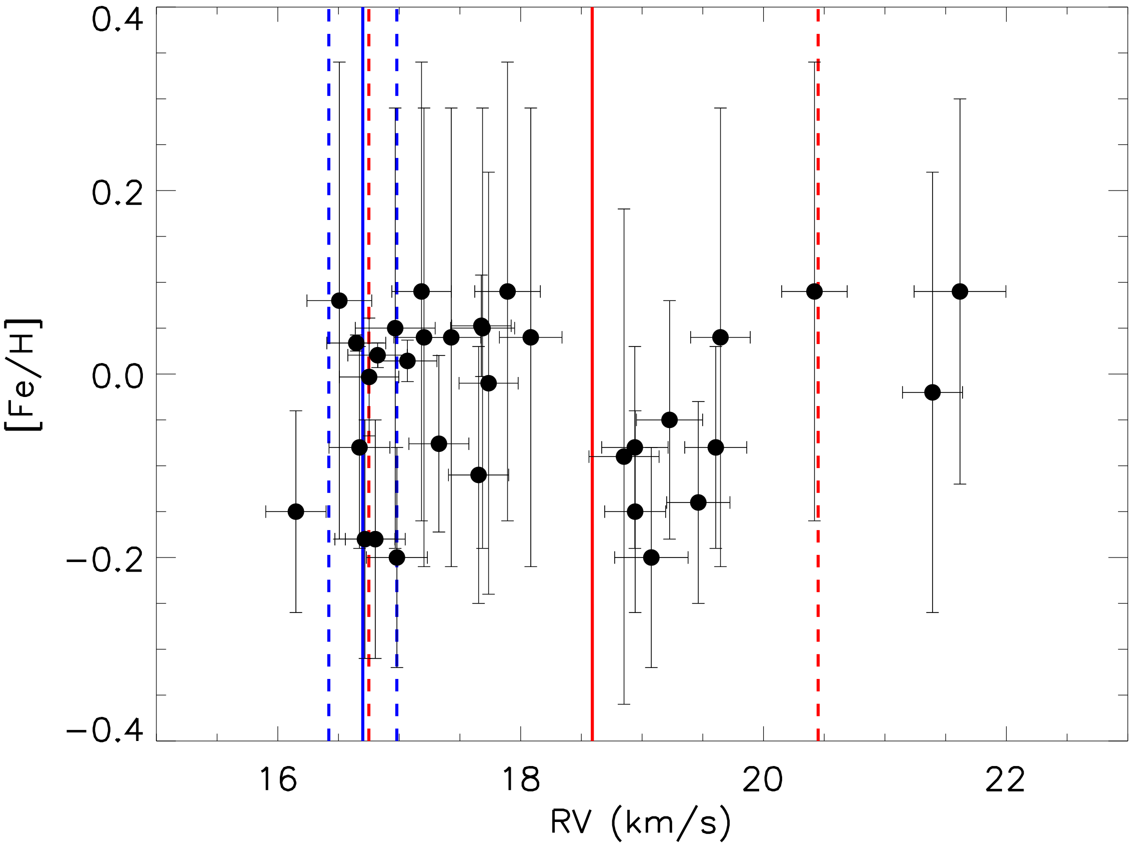

Figure 6.10: Iron abundance of the GIRAFFE members with $T_{\rm eff}$>4000 K as a function of their RVs. The red and blue solid lines mark the centre of the two kinematic components of the cluster. The dashed lines corresponds to $\pm\sigma$.

having one outlier out of eight members is rather small, but not negligible. Under the assumption that the star is a genuine metal-rich cluster member, we propose the following scenario to explain it.

First, we believe that the chemical enrichment due to the explosion of a nearby SN is unlikely since it should have enriched the whole cloud and other members. A more likely process is the accretion of circumstellar rocky material onto the star that is mixed in the stellar convective envelope causing an overall metallicity enhancement (Laughlin & Adams 1997). If the star is cool and young, its extended outer convection zone will effectively mix the accreted material with only a minimal metallicity enhancement. On the other hand, if the star is mostly radiative with a thin convective layer, the pollution could be much more important, leading to observable consequences.

Applying the scenario proposed by Laughlin & Adams (1997), a solar-type star, like J08095427-4721419, starts its PMS contraction with a fully convective structure, but after ∼2 Myr a radiative core appears that grows in mass as the star ages, shrinking the outer convective layers. Such a star maintains a thick convective envelope until about 10 Myr. For later-type stars the grown of the radiative core takes more time and the final thickness of the convective layer is larger; in earlier-type stars the radiative core develops quickly until a fully radiative configuration is reached. Circumstellar discs are found in most of young stellar objects and generally they accrete onto the central star during the first 10 Myr, when their internal structure is still mainly convective. However the condensation of heavy elements could lead to the formation of rocky blocks or planets preventing from a quick accretion of this material during the time when the star is mainly convective. In the last decade several surveys have shown that a great number of extrasolar planets have surprisingly small orbits, suggesting that after their formation significant orbital migration takes place in the proto-planetary system. A possible outcome of this inward migration is that part of the planetary material reaches the central star even after the completion of the main accretion phases.

6.6.4 A quantitative estimate of the effects of rocky material accretion on the mainly radiative PMS star J08095427−4721419

Using $T_{\rm eff}$ =5756 K and $L_{\rm bol}$ =2.5 $L_\odot$ for J08095427−4721419 and the Siess models for a sub-solar metallicity(Siess et al. 2000), we derive a stellar mass of $\sim$1.3 $M_\odot$ and an age of ∼15-16 Myr. Thus, this star appears older than the average age of the cluster, but consistent with the age dispersion found by Jeffries et al. 2009). As we said above, the *Spitzer* data show evidence for the presence of a debris disc (Hernández et al. 2008). Thus, we can imagine that part of the circumstellar matter has condensed into hydrogen-depleted rocks, or even planets, and that this rocky material has recently accreted onto the star. The Siess models also predict that such a star is almost fully radiative, but that about 5 Myr in the past it had a thin convective layer of $\sim$0.05 $M_\odot$. We now estimate the mass of heavy elements (expressed in Earth masses, $M_\oplus \sim 3\times10^{-6}$ $M_\odot$) that must have been accreted onto the star during the last 5 Myr in order to produce an iron enhancement similar to that observed in J08095427−4721419.

For this purpose, we assume that the accreted material is mixed in a convective region containing 0.05 $M_{\odot}$. We also assume that the star has an initial iron abundance equal to that found for Gamma Velorum ($[\mathrm{Fe/H}]_{\mathrm{init}}=-0.058$ dex). Now, the rocky material being hydrogen-depleted, it has a mass ratio of metals to total of $Z_p=1$ and we assume that it has the heavy element distribution as the solar mix given by Grevesse et al. (2007). Hence, a mixing of 50, 60 and 70 $M_{\oplus}$ in the 0.05 $M_{\odot}$ convective layer would be enough to produce a metallicity variation (ΔZ) of 3.0×10^{-3}, 3.6×10^{-3} and 4.1×10^{-3}, corresponding to a final iron abundance of $[\mathrm{Fe/H}]_{fin}=+0.05$, +0.07 and +0.08 dex. This is just the right amount needed to explain the observed iron abundance. The same effect could be achieved by the accretion of two Jupiters (M_J=0.001 $M_{\odot}$) with a metallicity Z =0.1.

We recall that the mass of heavy elements currently contained in the planets of the solar system is estimated to be in the range 60-120$M_{\oplus}$ (Wuchterl et al. 2000). This number is also in the range of heavy-element mass for exoplanets found by Miller & Fortney (2011). Thus, our estimate of the accreted mass is consistent with these numbers. On the other hand, we have found only one star with a significant metallicity enhancement, whereas the presence of circumstellar discs is a frequent phenomenon around young stars and more than just one example should have been found in Gamma Velorum. However, our proposed scenario requires the tuning of several factors. First, the star must be of the right mass in order to possess a convective region that shrinks significantly while contracting. Then, this star should have the right amount of mass in the convective layer since otherwise the accreted metals could be too diluted or, conversely, enhanced with respect to the observed abundance. Third, the accretion episode must have occurred only after the star has had time to contract significantly for the retreat of the convection layer and this requires several Myr. The fact that J08095427-4721419 is a bit older than the other members of the cluster, judging from its isochronal age, gives support to our interpretation. It is interesting to note that a similar scenario has been recently suggested by Théado & Vauclair (2012) in the context of the predicted modifications of the light element abundances of accreting exoplanet-host stars. Although the case of J08095427−4721419 is the only one found so far in Gamma Velorum, we should also mention other examples of metal-rich stars in otherwise solar or sub-solar young clusters and star forming regions (e.g., Biazzo et al. 2011a; Wilden et al. 2002).

6.7 Conclusions

In this paper we have made use of the dataset provided by the Gaia-ESO Survey in order to identify the Gamma Velorum members in the UVES sample and to study their elemental abundances, in particular to derive the mean cluster metallicity. The main findings can be summarized as follows:

i) Using radial velocities, surface gravity and the presence of Li in the stellar atmospheres, we identify eight high probability members among the stars observed with UVES. We have also detected a strong lithium line in one of the SB2 systems that could be considered a likely member. Furthermore, we have identified five hot-candidate-members of the cluster based on their position in the CM diagram.

ii) Based on the UVES members we find that the Gamma Velorum cluster has a slightly sub-solar mean iron abundance: <[Fe/H]>=−0.057 ± 0.018, if we exclude the metal-rich star J08095427−4721419. The analysis of other heavy element (α, iron peak, etc.) abundances for two members is not conclusive, given the large uncertainties. This is the first estimate of the metallicity of Gamma Velorum. When compared with the metallicity of other clusters belonging to the Vela complex and observed by the Gaia-ESO Survey (but whose analysis has not yet been completed), it will possibly allow shading light on the star formation process in the complex.

iii.) No major difference in the [Fe/H] distribution is found for the two kinematic population identified by Jeffries et al.

iii) We have found a metal-rich member, J08095427−4721419. Its mass (∼1.3 $M_\odot$) and age (∼15 Myr) are consistent with an internal structure characterized by a thin convective envelope. We have suggested a scenario to account for the observed increase of the atmospheric abundances based on the accretion of ∼60 $M_\oplus$ of rocky hydrogen-depleted material onto the star.

On the more technical aspects, the comparison of the parameters from the UVES and Giraffe analysis of the same stars observed in Gamma Velorum can be summarized as follows:

i) The GIRAFFE radial velocities of the first release are systematically higher with respect to the UVES values by 1.1±0.4 km/s (see Sacco 2014a for a detailed discussion).

ii) The stellar parameters log g and $T_{\rm eff}$ and the measured Li EWs are generally in good agreement, although small discrepancies are present for T_{eff}>5500 K and EW(Li)<30 m$\AA$.

iii) There is a reasonable agreement between the iron abundances derived using GIRAFFE and UVES, but the intrinsic dispersion of the latter is significantly smaller.

Table 6.4: Stellar parameters of the 80 UVES stars.

ID	Star	R.A. (J2000)	DEC. (J2000)	$T_{\rm eff}$ (K)	log g	[Fe/H]
1	08063616-4748206	08 06 36.16	-47 48 20.6	6726±347	4.16±0.21	-1.51±0.20
2	08064772-4659492	08 06 47.72	-46 59 49.2	5776±49	4.20±0.08	-0.02±0.03
3	08065592-4704528	08 06 55.92	-47 04 52.8	4471±119	2.60±0.27	-0.02±0.14
4	08065688-4717247	08 06 56.88	-47 17 24.7	7536±313	3.96±0.32	-0.18±0.20
5	08070521-4734401	08 07 05.21	-47 34 40.1	5607±75	4.30±0.08	0.23±0.04
6	08070717-4721463	08 07 07.17	-47 21 46.3	5257±132	2.90±0.20	0.09±0.08
7	08071363-4725156	08 07 13.63	-47 25 15.6	5838±66	4.41±0.15	-0.03±0.04
8	08071383-4736156	08 07 13.83	-47 36 15.6	4348±126	2.04±0.25	-0.18±0.11
9	08071501-4658153	08 07 15.01	-46 58 15.3	6272±110	3.99±0.16	0.01±0.12
10	08071937-4710143	08 07 19.37	-47 10 14.3	4564±75	2.40±0.24	-0.09±0.06
11	08072516-4712522	08 07 25.16	-47 12 52.2	—	—	—
12	08073209-4746433	08 07 32.09	-47 46 43.3	6053±68	4.26±0.08	0.03±0.03
13	08073237-4722119	08 07 32.37	-47 22 11.9	7105±145	4.16±0.14	-0.06±0.18
14	08073315-4744513	08 07 33.15	-47 44 51.3	5136±45	2.91±0.16	0.02±0.05
15	08073447-4716569	08 07 34.47	-47 16 56.9	5988±84	4.29±0.15	0.12±0.04
16	08073722-4705053	08 07 37.22	-47 05 05.3	—	—	—
17	08074016-4721020	08 07 40.16	-47 21 02.0	6926±160	4.14±0.12	-0.01±0.12
18	08074019-4730403	08 07 40.19	-47 30 40.3	5077±68	3.91±0.23	-0.11±0.04
19	08074278-4659566	08 07 42.78	-46 59 56.6	6962±246	4.15±0.17	-0.14±0.20
20	08074671-4658173	08 07 46.71	-46 58 17.3	4700±103	2.60±0.15	0.23±0.14
21	08075167-4706085	08 07 51.67	-47 06 08.5	4604±98	2.93±0.21	0.06±0.14
22	08080053-4702145	08 08 00.53	-47 02 14.5	5742±78	4.56±0.06	-0.04±0.03
23	08080431-4716272	08 08 04.31	-47 16 27.2	5245±68	4.61±0.06	-0.08±0.04
24	08080526-4722060	08 08 05.26	-47 22 06.0	—	—	—
25	08080690-4715075	08 08 06.90	-47 15 07.5	—	—	—
26	08080882-4736515	08 08 08.82	-47 36 51.5	4554±57	2.41±0.22	-0.07±0.10
27	08081245-4705593	08 08 12.45	-47 05 59.3	—	—	—
28	08081445-4701498	08 08 14.45	-47 01 49.8	5840±84	3.91±0.24	-0.22±0.03
29	08082630-4721083	08 08 26.30	-47 21 08.3	7396±294	3.96±0.33	-0.17±0.20
30	08083232-4722553	08 08 32.32	-47 22 55.3	4613±78	2.51±0.26	0.14±0.12
31	08083707-4727371	08 08 37.07	-47 27 37.1	7058±238	4.10±0.22	-0.21±0.22
32	08083759-4736060	08 08 37.59	-47 36 06.0	6013±50	3.95±0.05	-0.33±0.03
33	08083990-4741513	08 08 39.90	-47 41 51.3	5659±81	4.39±0.17	-0.41±0.04
34	08085306-4704067	08 08 53.06	-47 04 06.7	6037±60	4.35±0.07	0.02±0.04
35	08085455-4700053	08 08 54.55	-47 00 05.3	4914±78	2.68±0.17	-0.45±0.03
36	08085599-4659333	08 08 55.99	-46 59 33.3	5093±65	2.95±0.08	0.00±0.06
37	08090431-4741026	08 09 04.31	-47 41 02.6	7501±328	4.08±0.24	-0.16±0.17

Table 6.4: continued.

ID	Star	R.A. (J2000)	DEC. (J2000)	$T_{\rm eff}$ (K)	$\log g$	[Fe/H]
38	08090542-4740261	08 09 05.42	-47 40 26.1	5226±170	3.10±0.28	-0.09±0.09
39	08090738-4738136	08 09 07.38	-47 38 13.6	—	—	—
40	08090850-4701407	08 09 08.50	-47 01 40.7	6501±141	4.07±0.16	-0.04±0.15
41	08091397-4722030	08 09 13.97	-47 22 03.0	4586±62	2.44±0.16	-0.10±0.04
42	08091638-4713374	08 09 16.38	-47 13 37.4	—	—	—
43	08091875-4708534	08 09 18.75	-47 08 53.4	6052±128	4.03±0.16	-0.03±0.13
44	08092627-4731001	08 09 26.27	-47 31 00.1	5238±78	4.48±0.14	-0.06±0.10
45	08093304-4737066	08 09 33.04	-47 37 06.6	5471±177	4.06±0.25	-0.06±0.12
46	08093589-4718525	08 09 35.89	-47 18 52.5	5277±215	4.42±0.52	-0.49±0.12
47	08094221-4719527	08 09 42.21	-47 19 52.7	5087±108	4.41±0.17	-0.09±0.11
48	08094301-4718353	08 09 43.01	-47 18 35.3	6950±312	4.08±0.22	-0.26±0.23
49	08094390-4703094	08 09 43.90	-47 03 09.4	6869±267	4.15±0.15	-0.17±0.19
50	08094711-4740038	08 09 47.11	-47 40 03.8	4839±77	2.79±0.21	0.02±0.06
51	08095042-4657080	08 09 50.42	-46 57 08.0	—	—	—
52	08095427-4721419	08 09 54.27	-47 21 41.9	5756±93	4.25±0.16	0.07±0.07
53	08095429-4710344	08 09 54.29	-47 10 34.4	4970±122	2.60±0.22	-0.25±0.07
54	08095783-4701385	08 09 57.83	-47 01 38.5	4958±84	2.62±0.14	-0.26±0.05
55	08095967-4726048	08 09 59.67	-47 26 04.8	5228±109	4.51±0.14	-0.07±0.11
56	08101160-4737555	08 10 11.60	-47 37 55.5	4354±36	2.10±0.06	-0.41±0.05
57	08101201-4720464	08 10 12.01	-47 20 46.4	6296±26	4.01±0.13	-0.49±0.02
58	08101211-4718398	08 10 12.11	-47 18 39.8	4850±155	2.70±0.17	0.03±0.10
59	08101307-4722227	08 10 13.07	-47 22 22.7	4770±60	2.75±0.21	0.16±0.05
60	08103648-4659502	08 10 36.48	-46 59 50.2	4850±75	2.70±0.09	-0.04±0.05
61	08103782-4702584	08 10 37.82	-47 02 58.4	4750±94	2.72±0.10	-0.03±0.09
62	08103799-4723323	08 10 37.99	-47 23 32.3	6959±134	3.64±0.08	-0.64±0.15
63	08103996-4714428	08 10 39.96	-47 14 42.8	—	—	—
64	08104495-4723015	08 10 44.95	-47 23 01.5	4782±63	2.66±0.12	-0.07±0.06
65	08105180-4746394	08 10 51.80	-47 46 39.4	4927±53	2.79±0.14	-0.17±0.08
66	08105382-4719579	08 10 53.82	-47 19 57.9	—	—	—
67	08105813-4729136	08 10 58.13	-47 29 13.6	7553±307	4.08±0.25	-0.18±0.16
68	08105888-4700140	08 10 58.88	-47 00 14.0	6310±312	4.08±0.20	-1.52±0.22
69	08110285-4724405	08 11 02.85	-47 24 40.5	5137±86	4.41±0.15	-0.05±0.12
70	08111229-4704491	08 11 12.29	-47 04 49.1	4694±48	2.56±0.17	-0.34±0.06
71	08111619-4713188	08 11 16.19	-47 13 18.8	—	—	—
72	08111853-4704187	08 11 18.53	-47 04 18.7	4969±81	3.40±0.15	-0.15±0.09
73	08112119-4654274	08 11 21.19	-46 54 27.4	6019±74	4.22±0.06	0.11±0.04
74	08112188-4711281	08 11 21.88	-47 11 28.1	7106±172	4.17±0.14	-0.16±0.16
75	08112306-4733019	08 11 23.06	-47 33 01.9	4707±34	2.72±0.19	0.03±0.11
76	08112313-4737105	08 11 23.13	-47 37 10.5	5023±67	4.54±0.18	0.08±0.14
77	08114116-4720345	08 11 41.16	-47 20 34.5	4970±37	2.81±0.11	0.08±0.07
78	08114979-4700130	08 11 49.79	-47 00 13.0	4733±78	3.00±0.09	0.04±0.10
79	08115305-4654115	08 11 53.05	-46 54 11.5	—	—	—
80	08115451-4655430	08 11 54.51	-46 55 43.0	6540± 8	4.24±0.05	-0.09±0.05

Table 6.5: Quantities used for the membership analysis of the UVES sample. The table shows that we have identified eight high probability members and 8 HCMs (see text).

ID	RV (km/s)	EW(Li) (mÅ)	$(B-V)_0$	V_0	RV mem.	$\log g$ mem.	Li mem.	CMD mem.	Final
1	13.5	<20	0.13	1.97	N	Y	HCM	N	N
2	10.4	<10	0.64	4.99	N	Y	N	—	N
3	99.7	<27	1.30	4.96	N	N	—	—	N
4	21.5	<10	0.06	1.88	N	Y	HCM	N	N
5	64.7	<5	0.73	4.48	N	Y	N	—	N
6	35.5	51±2	1.05	4.01	N	N	—	—	N
7	12.9	35±1	0.63	4.84	N	Y	N	—	N
8	47.9	15±6	1.46	4.70	N	N	—	—	N
9	25.2	<30	0.41	3.23	N	Y	N	—	N
10	49.0	<14	1.26	4.90	N	N	—	—	N
11	—	<5	0.38	3.54	SB2	—	—	—	?
12	11.7	37±1	0.57	4.09	N	Y	N	—	N
13	-16.7	<20	0.28	2.83	N	Y	HCM	N	N
14	28.7	19	0.94	3.18	N	N	—	—	N
15	14.5	62±1	0.60	4.06	Y	Y	N	—	N
16	—	<5	0.50	3.94	SB2	—	—	—	?
17	21.6	<20	0.39	2.60	N	Y	N	—	N

Table 6.5: continued.

ID	RV (km/s)	EW(Li) (m$\AA$)	(B-V)$_0$	V_0	RV mem.	log g mem.	Li mem.	CMD mem.	Final
18	0.6	13±3	0.88	4.39	N	N	—	—	N
19	—	<8	0.30	3.98	—	Y	N	—	N
20	61.0	<41	1.14	3.62	N	N	—	—	N
21	43.4	<13	1.22	5.08	N	N	—	—	N
22	5.3	50±1	0.68	4.92	N	Y	N	—	N
23	22.2	<10	0.78	4.76	N	Y	N	—	N
24	—	<5	0.04	2.70	—	—	HCM	N	N
25	50.8	<30	-0.01	1.36	N	—	HCM	N	N
26	28.6	26±16	1.29	4.80	N	N	—	—	N
27	—	<8	0.08	2.53	—	—	HCM	N	N
28	24.5	74±2	0.59	4.77	N	Y	N	—	N
29	—	<11	0.22	3.07	—	Y	HCM	N	N
30	3.8	<14	1.25	4.38	N	N	—	—	N
31	—	<11	0.23	2.92	—	Y	HCM	N	N
32	9.4	42±1	0.54	4.32	N	Y	N	—	N
33	16.0	16±3	0.61	4.45	Y	Y	N	—	N
34	21.8	72±1	0.58	4.23	N	Y	N	—	N
35	51.7	<5	0.95	3.62	N	N	—	—	N
36	28.3	<7	0.94	3.49	N	N	—	—	N
37	10.7	<50	0.17	2.13	N	Y	HCM	N	N
38	1.9	<10	0.82	4.24	N	N	—	—	N
39	—	<50	0.03	1.28	—	—	HCM	Y	HCM
40	20.2	<78	0.37	2.93	Y	Y	Y	Y	M
41	10.1	89±10	1.34	4.70	N	N	—	—	N
42	-12.4	<130	0.02	1.46	N	—	HCM	N	N
43	12.7	129±6	0.49	4.61	N	Y	Y	Y	M?
44	17.7	353±6	0.86	4.66	Y	Y	Y	Y	M
45	-28.3	247±2	0.78	4.07	N	Y	Y	Y	M
46	—	214±5	1.00	4.90	SB2	—	Y	—	M?
47	—	431±5	0.88	4.50	—	Y	Y	Y	M
48	—	<51	0.10	1.87	—	Y	HCM	Y	HCM
49	25.6	<22	0.32	3.75	N	Y	N	—	N
50	27.5	<7	1.01	4.00	N	N	—	—	N
51	40.7	<50	0.08	2.90	N	—	HCM	N	N
52	20.8	246±3	0.65	3.95	Y	Y	Y	Y	M
53	37.4	<5	1.14	4.55	N	N	—	—	N
54	25.0	380±5	1.03	4.73	N	N	—	—	N
55	—	355±5	0.75	4.11	—	Y	Y	Y	M
56	10.5	<16	1.42	4.70	N	N	—	—	N
57	56.7	<15	0.44	4.65	N	Y	N	—	N
58	64.1	<20	1.10	4.00	N	N	—	—	N
59	28.7	<14	1.14	3.62	N	N	—	—	N
60	-3.2	<9	1.07	4.40	N	N	—	—	N
61	7.2	31±2	1.12	4.14	N	N	—	—	N
62	-2.9	30±2	0.30	4.03	N	N	—	—	N
63	—	<5	0.56	4.17	SB2	—	—	—	?
64	-3.2	<7	1.15	4.35	N	N	—	—	N
65	6.8	<12	1.18	4.98	N	N	—	—	N
66	—	<20	0.32	2.80	SB2	—	—	—	?
67	17.1	<40	0.18	2.06	Y	Y	HCM	Y	HCM
68	—	<50	0.08	3.06	—	Y	HCM	N	N
69	16.2	387±10	0.90	5.10	Y	Y	Y	Y	M
70	-3.5	<10	1.07	3.81	N	N	—	—	N
71	—	<6	0.01	1.28	—	—	HCM	Y	HCM
72	40.1	<10	0.93	4.55	N	N	—	—	N
73	59.3	48±1	0.57	4.96	N	Y	N	—	N
74	—	<7	0.26	2.45	—	Y	HCM	Y	HCM
75	62.7	<13	1.22	4.30	N	N	—	—	N
76	9.9	32±6	0.90	4.75	N	Y	N	—	N
77	33.2	<11	1.11	3.75	N	N	—	—	N
78	56.6	<10	1.09	4.36	N	N	—	—	N
79	—	<5	0.58	5.03	SB2	—	—	—	?
80	-8.2	<7	0.39	2.55	N	Y	N	—	N

* RV values liste in the table are not corrected for the 1.1 km/s systematic shift.

Chapter 7

Gaia-ESO Survey: the first metallicity determination of the Chamaeleon I star forming region

L. Spina
S. Randich - INAF–Osservatorio Astrofisico di Arcetri
F. Palla - INAF–Osservatorio Astrofisico di Arcetri
K. Biazzo - INAF–Osservatorio Astrofisica di Catania
L. Magrini - INAF–Osservatorio Astrofisico di Arcetri
E. Franciosini - INAF–Osservatorio Astrofisico di Arcetri
G.G. Sacco - INAF–Osservatorio Astrofisico di Arcetri
L. Morbidelli - INAF–Osservatorio Astrofisico di Arcetri
E. Alfaro - Instituto de Astrofísica de Andalucía
J.I. González Hernández - Instituto de Astrofísica de Canarias
and Gaia-ESO Survey builders

The Chamaeleon I cluster is one of the most nearby star forming region and, as for Gamma Velorum, the Gaia mission will provide accurate proper motions and distances for its members. A variety of youth features and diagnostics have been used to search for members of the cluster that, currently, counts 237 objects. Although most of these latter are late type stars (<M0), the cluster is sufficiently rich for a statistically significant analysis

of its metallicity. Contrary to Gamma Velorum, this star forming region is relatively isolated from other clusters and confusion with other populations or effects of chemical pollution are minimal. Because of its age and its proximity to the Sun, Chamaeleon I has been a valuable laboratory for studies on circumstellar disks. *Spitzer* observations have been used to identify objects that exhibit excess emission indicative of disks. In Appendix A I report a study concluded during my first year of PhD showing that the Chamaeleon I is also characterized by a number of subsolar-mass stars with unusually short disk lifetimes.

Chamaeleon I has been the first star forming region observed by the Gaia-ESO Survey. As mentioned in Section 5, I performed the target selection, the fiber allocations and observing blocks configurations for the Gaia-ESO observations. In this Chapter I present the results on the metallicity determination of this star forming region using the Survey recommended products derived from these observations.

This work has been submitted to the Gaia-ESO Survey college of readers[1].

7.1 Abstract

Context. The abundance distribution of nearby star forming regions is still poorly known, in spite of the implication on general issues such as the study of the chemical pattern of the Solar neighborhood, the correlation between stellar metallicity and the circumstellar disks lifetime or the ability of forming planets.
Aims. We present the analysis of the metallicity of the Chamaeleon I star forming region, based on the products distributed in the first internal release of the Gaia-ESO Survey.
Methods. The Chamaeleon I candidate members have been observed with the spectrographs UVES and GIRAFFE, depending on their brightness and spectral-type. In order to derive a solid metallicity determination for the cluster, membership of the observed stars must be first assessed. To this aim, we use the recommended stellar parameters; specifically, the membership criteria include surface gravity estimates, the detection of photospheric lithium line and the position in the Hertzsprung-Russell diagram.

---

[1] All journal publications using Gaia-ESO data have to be submitted to the internal Gaia-ESO refereeing at least 3 weeks prior to journal submission.

Results. Out of the 48 targets observed with UVES, we identify 15 very likely members. Considering metallicity determinations of 11 of these latter, we found that the iron abundance of Chamaeleon I is slightly sub-solar, with a mean metallicity [Fe/H]=-0.068 ± 0.013. This result is consistent with the metallicity determinations of the other nearby star forming regions. This result suggests that the chemical pattern of the youngest stars in Solar neighborhood is indeed more metal-poor than the Sun. Here we speculate that this evidence may reflects the chemical nature of the Gould Belt, that contains most of the nearby star forming regions.

7.2 Introduction

The metallicity determination of young clusters (age$\lesssim$50 Mry) and Star Forming Regions (SFRs; age$\lesssim$5 Mry) has implications on fundamental topics, such as the history of their birth and early evolution, the evolution of circumstellar disks and the ability of forming planets (see, Spina et al. 2013 and references therein). Furthermore, these young environments are of particular interest since they are close to their birthplace and contain a homogeneous stellar population that has not had time to disperse through the Galactic disk. Thus, young clusters and SFRs are key object in order to trace the chemical pattern of the Galactic thin disk in space and time. Interestingly, in the last decade many abundance analysis have been performed focusing on open clusters with ages $\gtrsim$100 Myr (Friel 1995; Magrini et al. 2009), but the metallicity of young clusters and SFRs have been scarcely investigated (see, e.g., James et al. 2006; Santos et al. 2008; Biazzo et al. 2011a,b). So far, the evidence for young clusters is of a metallicity close to the solar value, but for SFRs it is surprisingly lower (D'Orazi et al. 2009; Biazzo et al. 2011a).

The Gaia-ESO Survey (GES) (Gilmore et al. 2012; Randich & Gilmore 2012), a Large, Public, Spectroscopic Survey observing about 10^5 stars of the Galaxy components (bulge, thin disk, thick disk and halo), includes also about 30 young open clusters and SFRs with the motivation of studying their internal kinematics and dynamics. Among the most important by-products, the GES will provide an homogeneous metallicity determination for all these clusters. In this framework, in a recent study we have determined the metal content of Gamma Velorum, the first young cluster observed by the Survey (Spina 2014). This paper is devoted to the analysis of the metallicity of the first SFR targeted by the GES: Chamaeleon I (hereafter, Cha I).

With a mean ∼2 Myr (Luhman 2007) and proximity to the Sun (d=160-165 pc; Whittet et al. 1997), Cha I is one of best-studied SFRs. It is part of a wider association distributed in a region of few square degree that contains two younger and smaller molecular clouds, Cha II and Cha III (Schwartz 1977). Cha I has been the target of many spectroscopic and photometric surveys that have uncovered a large population of embedded and optically visible sources (see the review by Luhman 2008a; hereafter L08). The current sample of known members contains 237 sources (hereafter "L08-members"), extending down to the brown dwarfs regime. The census is nearly complete in the central regions of Cha I (11 05 $\leq$ R.A. $\leq$ 11 11; $-77.8 \leq$ DEC ≤ -76.3) for M/$M_{\odot} \geq 0.03$ and $A_J \leq 1.2$, but outside this area is still not completely determined (Luhman 2007). Recently, Lǿpez Martí et al. (2013) have identified 51 new kinematical candidate members that await for confirmation through accurate spectroscopic data. The Initial Mass Function (IMF) of Cha I has been explored to substellar masses by Luhman (2007) and, as with other SFRs, it reaches a maximum between 0.1 and 0.2 $M_{\odot}$. Luhman (2008a), using *Spitzer* colors to study the disk population, argued that the lifetimes of disks around solar-mass stars are longer in Cha I than in other young clusters, probably because of the lower stellar density. On the other hand, Cha I is also characterized by a number of subsolar-mass stars with unusually short disk lifetimes (Luhman 2008a; Robberto et al. 2012).

The association is clearly separated in two sub-clusters, Cha I North (DEC>-77) and Cha I South (DEC<-77), with different star formation histories. The distribution of isochronal ages suggests that star formation began ∼5-6 Myr ago in the northern portion and developed later in the southern extension (Luhman 2007).

Cha I is relatively isolated from other SFRs and suffers of little confusion with other young populations. The region appears to be slightly metal poor with <[Fe/H]> = -0.11 ± 0.14 (Santos et al. 2008), but this estimate is based on the analysis of four sources located in a wide area of the Chamaeleon complex, away from the main molecular clouds. Thus, the metallicity could be not representative of Cha I and a new dedicated study is both necessary and timely.

In Section 7.3 we describe the target selection and spectral analysis. The identification of the cluster members on the basis of the surface gravity, the detection of lithium in the stellar atmosphere and their position on the

Hertzsprung-Russell diagram is presented in Section 7.4. The results of the elemental abundance determination is discussed in Section 7.5. In Section 7.6 we overview and discuss in a broader context the metal content of SFRs. Section 7.7 summarizes our findings.

7.3 Gaia-ESO pipeline

The analysis presented in this paper is based on the spectroscopic observations obtained by the GES consortium and following analysis released in the GESviDR1Final catalog. In this section we describe the properties of Cha I, the target selection, the observations and the available data products of the GES analysis.

7.3.1 Target selection and Observations

The selection criteria are based on homogeneous photometric data, covering a large area of the cluster field. The object list has been compiled including only sources with 2MASS photometry (Cutri et al. 2003) with R_{USNO}≤17.0 (Monet et al. 2008), lying in an area corresponding to the highest extinctions and wide enough to extend into the cluster boundaries: 10 45 ≤RA ≤11 30; −79 00 ≤ DEC≤ −75 00. The selection was done following the GES guidelines for cluster observations (see Bragaglia 2014).

The GES observations are performed with the multi-object optical spectrograph FLAMES at the VLT (Pasquini et al. 2002). The instrument consists of two spectrographs: namely, GIRAFFE fed by 132 fibers and UVES with 8 fibers.

A total of 25 Observing Blocks (OBs) were observed in the runs C, E and D (March - May, 2012), using for UVES the CD#3 cross disperser (λ =4770-6820 $\AA$; R=47000) and for GIRAFFE the HR15N grating setting (λ =6440-6820 $\AA$; R∼17000). Eighteen fields have been chosen in order to cover the central region of the cluster (hereafter on-fields), characterized by a higher extinction and rich of confirmed members. In order to obtain a complete sampling of the members and possibly discover other candidates missed in previous studies, 7 additional fields (off-fields) have been observed in the northwestern and southern periphery of the association (see Fig. 7.1). Of all the OBs, 16 were observed for 20 min in total and 9 for 50 min. Some of the stars have a longer exposure time because of the partial overlap of the OBs.

The UVES targets have R<13.2 mag. A total of 674 GIRAFFE medium-resolution spectra and 48 UVES high-resolution spectra were acquired in the Cha I fields. These include 97 “L08-mem” observed with GIRAFFE and 18 with UVES. Of the kinematic candidate members identified by Lǿpez Martí et al. (2013), only one has been observed with UVES: 2MASS J10593816−7822421. Three stars of the whole sample were observed with both spectrographs. The SNR of the UVES spectra is in the range 5-300.

7.3.2 Available data form GES

The GES is structured in 20 Working Groups (WGs) dedicated to different tasks. The spectra observed in the Cha I fields have been analyzed by both WG8 and WG12. The former derives the radial velocity (RV) and the projected rotational velocity ($v \sin i$) and it also produces the spectroscopic cross correlation function (CCF). The latter WG (consisting of four nodes) is devoted to the spectroscopic analysis of F-G-K young stars. Three nodes of WG12 perform a LTE analysis of the iron lines (FeI and FeII), the so called “iron-EWs method”, while one node does the analysis through the comparison with a grid of observational templates. The consortium uniformly makes use of MARCS models of stellar atmospheres (Gustafsson et al. 2008) that assume the solar abundances from Grevesse et al. (2007). Also, common atomic data from Heiter (2014) have been used for the GES analysis.

In the first internal data distribution, GES released the radial and rotational velocities, CCFs and the products of the spectrum analysis. The latter include the main atmospheric parameters ($T_{\rm eff}$, log g and [Fe/H]) and other parameters (including veiling, measurements of the Li line at 6708 $\AA$ and Hα, etc.) along with their uncertainties (Gilmore 2014; Randich 2014; Smiljanic 2014; Lanzafame 2014). Individual elemental abundances are also determined from the UVES spectra whenever possible.

In the case of the Cha I observations, WG12 has produced values of the main parameters for 42 of the initial 48 UVES spectra and for 556 GIRAFFE stars. The remaining stars could not be analyzed due to the poor SNR or because of the presence of an active circumstellar disk. The recommended values are the mean of the results of four nodes and the errors have been derived considering a weighted standard deviation (Lanzafame 2014). Since

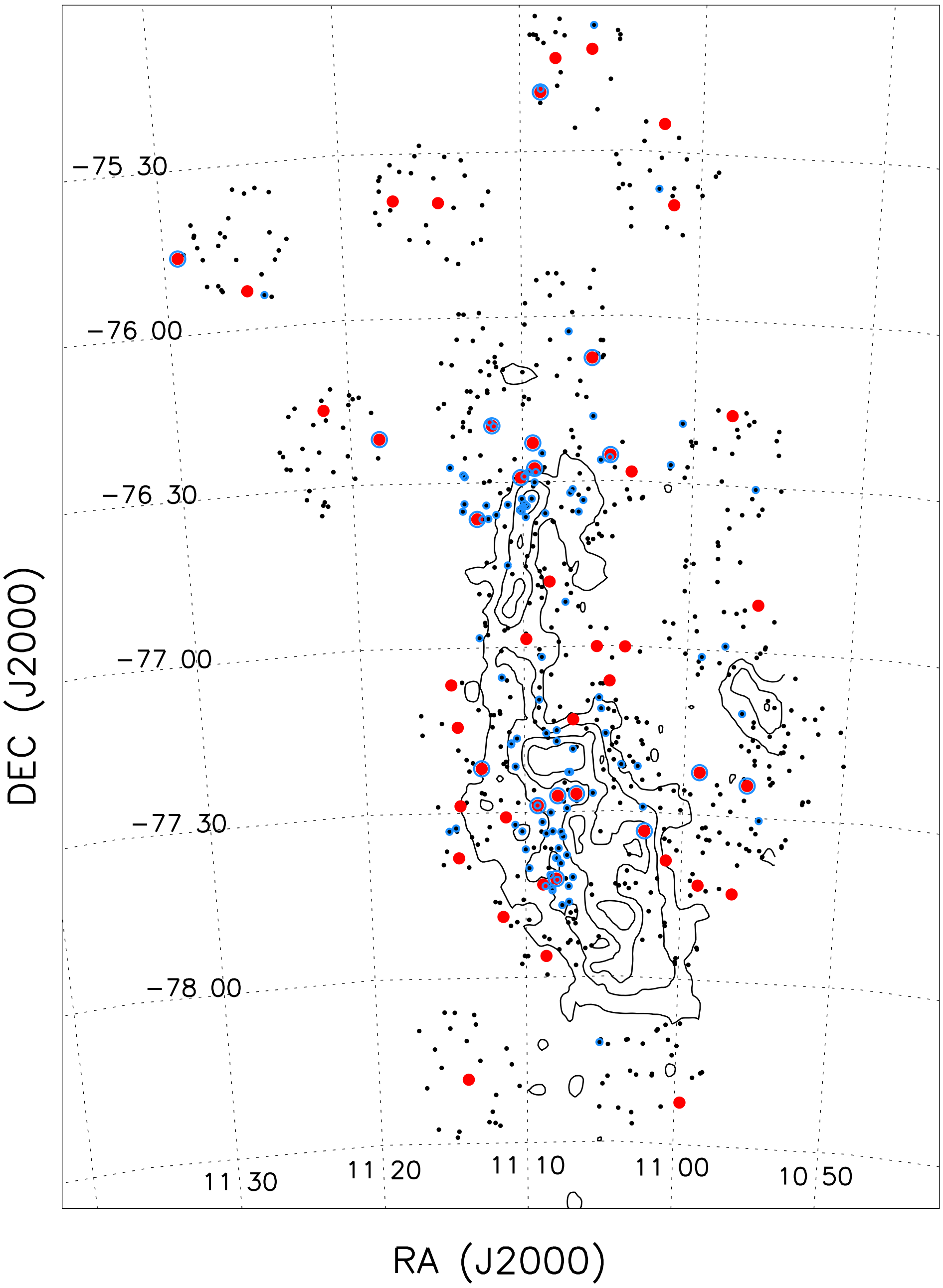

Figure 7.1: Map of the observed sources in the Chamaeleon I fields. Black dots are the GIRAFFE targets and red dots are the UVES ones. Blue circles mark the “L08-mem”. The contours correspond to the extinction levels A_V=2, 4, 6 and 8 from Cambresy (1998).

the main aim of this paper is to determine the metal content of Cha I, in the following we consider only those stars with main parameters avaliable. The GES consortium has produced [Fe/H] values for all the spectra for which the main parameters have been derived, but since the analysis of high-resolution spectra yields more reliable iron abundance values (Spina 2014), hereafter we will concentrate on the results of the UVES observations. However, in the spirit of performing some science verification, we will also discuss the GIRAFFE results from the more extended sample.

Table 7.3 lists the following quantities for the 42 UVES sources present in the catalog: sequential number, 2MASS name, coordinates, values of the mean stellar parameters and equivalent widths of the Li line, along with the information on binarity and membership (see Section 7.4). The mean uncertainties of the main parameters for the 42 UVES stars are: $<\sigma_{Teff}>$=126 K, $<\sigma_{log\ g}>$=0.25 dex, $<\sigma_{[Fe/H]}>$=0.13 dex.

7.4 Membership analysis

We have identified two double-lined binaries (SB2) through the spectral CCFs: #22 and #27. We will not consider these systems for membership analysis, even though GES provides the stellar parameters for one of them.

Following the same procedure adopted by Spina (2014) for the Gamma Velorum cluster, in this Section we use the spectroscopic information, along with the position of the targets in the Hertzsprung-Russell diagram (HRD) to carry out the membership analysis. This is then performed on 41 UVES and 553 GIRAFFE stars whose main parameters have been determined by the GES consortium and that have not flagged as SB2. This sample contains 15 "L08 mem" observed with UVES and 59 with GIRAFFE.

7.4.1 Identification of the giant contaminants

With the aim of identifying the giant contaminants observed in the Cha I fields, in Fig. 7.2 we plot the spectroscopic log g values as function of $T_{\rm eff}$ for the GIRAFFE and UVES samples. Stars are clearly divided in two groups with different surface gravities: main-sequence (MS), PMS and dwarf stars with log g$\sim$4-5 dex and the giant branch at lower values. We also plot the 1 Myr isochrone (solid line) and the 3-10 Myr isochrones (dashed lines) from Siess et al. (2000) models for a stellar metallicity of Z=0.01, close to the value of the solar metallicity $Z_{\odot}$=0.012 used in the MARCS models. Thus, we consider as giant contaminants all the stars that lie above the 1 Myr isochrone. Using our criterion, among the 41 UVES stars with log g determination, there are 21 UVES stars that lie below the isochrone while the remaining 20 UVES stars have been rejected from further analysis as contaminants. As expected, all the UVES stars flagged as "L08 mem" are below the isochrone. On the other hand, we count six "L08 mem" of the GIRAFFE sample that lay above the isochrone and that will be included in the lithium analysis.

We note that the log g values are higher that those expected for a 2 Myr cluster. The influence of this overestimation on other parameters is under investigation, but it is likely a minor effect.

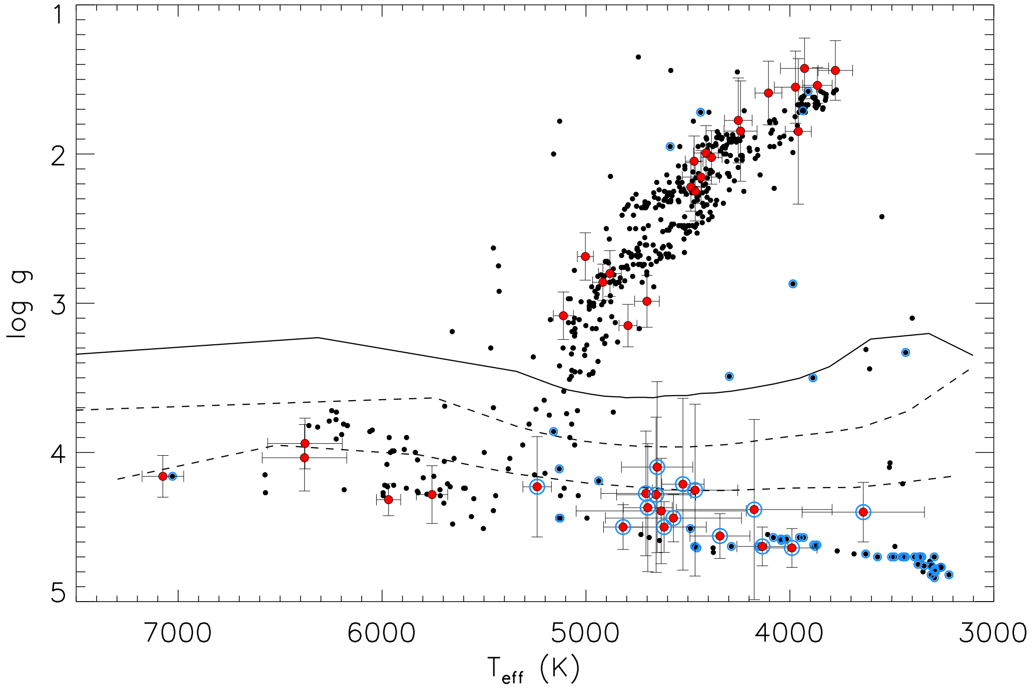

Figure 7.2: log g versus T_{eff}: this diagram allows us to identify in the UVES sample (bigger red dots) and in the GIRAFFE sample (smaller black dots) all the giant contaminants defined as objects that lay above the 1 Myr irochrone (solid lines) from Siess et al. (2000) models. The isochrones corresponding to 3 and 10 Myr are shown with dashed lines. The blue circles mark the "L08 mem" present in both samples.

7.4.2 Lithium members

Lithium is a youth indicator and a very useful diagnostic for the membership of young stars. In Fig. 7.3 we show the EWs(Li) as a function of $T_{\rm eff}$ for the 21 UVES sources that have not been rejected as SB2 or giant contaminants. There are 15 stars with EW(Li)>300 m$\AA$, 3 stars with Li detections in the range 20-100 m$\AA$, and 3 stars with only upper limits. Along with the UVES stars, we plot the GIRAFFE sources that have not been flagged as giants, plus the six "L08 mem" lying above the 1Myr isochrone. As expected, the largest majority of the "L08 mem" are in a sequence of stars with EW(Li)>300 m$\AA$ and $T_{\rm eff}$<5500 K. All the stars in this range of temperatures, but with a lower EW(Li) are likely contaminants. Unfortunately, EW(Li) is not a reliable indicator of membership for the hotter stars. However, we can use the information available on the Pleiades cluster members (age$\sim$120 Myr; Soderblom et al. 1993; Jones et al. 1996) to define a sequence of candidate members amongst the hottest stars. In fact, stars with $T_{\rm eff}$>6100 K still maintain the initial Li abundances and have a position in the diagram consistent with some of the UVES and GIRAFFE targets. We can thus identify the locus of the sequence of candidate members as a function of the temperature, as shown by the solid black line in Fig. 7.3. Then, the field contaminants are stars that fall below the black line. However, considering the age difference between the Pleiades and Cha I members, we will consider as "hot-candidate-members" (HCMs) the UVES and GIRAFFE targets with $T_{\rm eff}$>5500 K that are located above the black line and we will further assess their association with Cha I from their position in the HRD.

We note that five of the six "L08 mem" from the GIRAFFE sample that lay above the 1 Myr isochrone in Fig. 7.2 have been flagged as "Li members". These stars are 2MASS J11075792−7738449, J11080297−7738425, J11095340−7634255, J11095873−7737088 and J11101141−7635292. The elevated accretion activity that characterizes these sources (FHWM 10%Hα>380 km/s) and the presence of a circumstellar disk may have affected the measurement of the stellar parameters. The last star 2MASS J11070350−7631443 is a likely contaminant given that EW(Li)=23±2 m$\AA$.

In summary, from the analysis of the Li membership we conclude that the UVES sample includes 15 "Li-members", all of the "L08 mem", and 2 "HCM".

7.4.3 Hertzsprung-Russell diagram

The HRD can be used to test the reliability of our membership analysis and to provide some additional information about the HCMs for which we

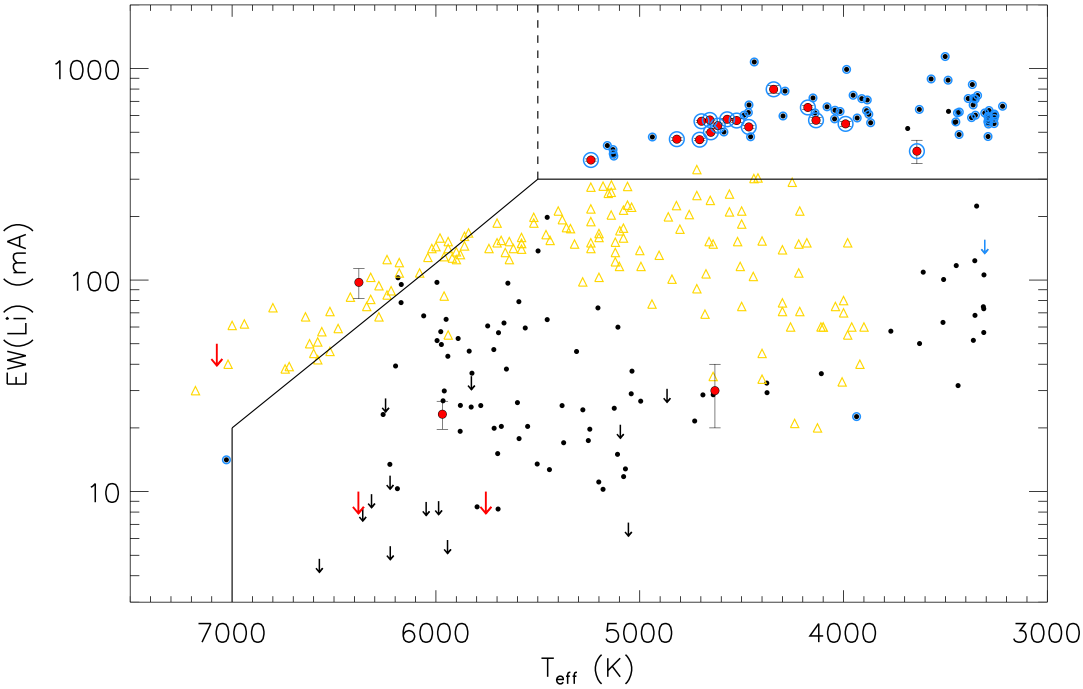

Figure 7.3: Lithium EW as a function of the T$_{\rm eff}$ for the candidate memebrs of Cha I. The bigger red dots identify the UVES stars, while the GIRAFFE stars are shown by the smaller black dots. The solid line demarcates the portion of the diagram occupied by the Li-members (above) and non-Li members (below). The dashed line separates Li-members (right) from hot candidate members (left). As a reference, we have also plotted the data of the ~120 Myr old Pleiades members (in yellow; Soderblom et al. 1993; Jones et al. 1996.

were not able to establish a secure membership based on lithium. In Fig. 7.4 we plot the UVES members and HCMs, together with the GIRAFFE stars. The bolometric luminosity $L_{\rm bol}$ has been derived from the extinction-corrected 2MASS J mag and bolometric correction Kenyon & Hartmann (1995). Overlaid on the data are the 1, 5, 10 and 20 Myr isochrones, the zero-age-main-sequence (ZAMS) and the evolutionary tracks for stars with 0.5, 1 and 2 $M_{\odot}$ from the Siess et al. (2000) models adopted in Fig. 7.2. The largest majority of the Li-members (T_{eff}<5500 K) occupy a region of the diagram between the 1 and 5 Myr isochrones, in agreement with the age estimate of Cha I quoted by Luhman (2007). On the other hand, four (2 UVES and 2 GIRAFFE)of the five HCMs (with T_{eff}>5500 K) are close or below the ZAMS, suggesting that they are likely contaminants. Therefore, we rejected them from further analysis.

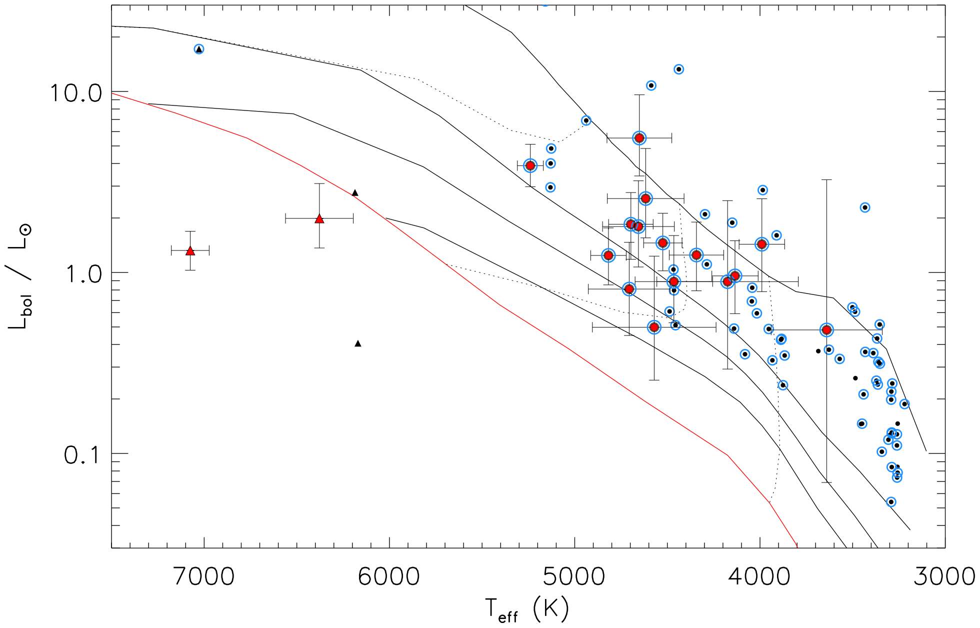

Figure 7.4: HR diagram of the UVES Li-members (red dots) and HCMs (red triangles). The GIRAFFE Li-members (smaller black dots) and HCMs (smaller black triangles) are shown as small dots. All the "L08 mem" are marked with a blue circle. The solid and dashed lines are the evolutionary tracks for 0.5, 1 and 2 $M_\odot$ and isochrones for 1, 5, 10, 20 Myr and ZAMS from Siess et al. (2000) for a chemical composition with Z =0.01.

7.4.4 Discussion on the membership analysis

In Table 7.3 we collect the parameters of the 48 UVES stars used for the membership analysis described above, together with the information on binarity (column 9) and membership status from the surface gravity, EW(Li) and HRD (columns 11 and 12): "Y" stands for member, "N" for field contaminant, and "HCM" for hot candidate member. The last two columns give the membership according to L08 and our own assessment. Finally, Table 7.1 summarizes the results of the individual membership indicators.

In total, there are 15 secure members that satisfy our criteria for membership. Since all these stars have been previously defined as Cha I members by

Table 7.1: Summary of the selection procedure for UVES

Observed	48	3 in common with GIRAFFE 18 L08 members
Binaries	2 SB2	both are L08 members 1 has main parameters available
Main parameters	42 − 1 (SB2) = 41	15 L08 members
log g selection	21 MS/PMS stars	15 L08 members
	20 giants	no L08 members
EW(Li)	15 Li members	all L08 members
	2 HCM	no L08 members
	4 Li non-members	no L08 members
HRD	15 above ZAMS	all L08 & Li memebrs
	2 below the ZAMS	both HCMs

Luhman (2008a), we have not identified any new member among the UVES targets. We also found that the kinematical candidate member identified by Lǿpez Martí et al. (2013), #7, is not a cluster member due to the lack of photospheric lithium and to a surface gravity resembling that of a giant star. In Table 7.2 we list for all the secure members the identification number (column 1), the SNR column 2), RV (column 3), and L_{bol} (column 4). The last five columns provide a comparison between the recommended values of T_{eff} and [Fe/H] and those derived from the comparison with the grid of templates. This point will be discussed below in Section 7.5.

The RV distribution of the GIRAFFE and UVES members is displayed in Figure 7.5, where the blue histogram is for the "L08 mem" subsample. In agreement with Sacco (2014b), we find that the distribution of Cha I members deviates from a gaussian likely because of the youth of the cluster that has not yet virialized. However, most members have RVs in the interval 11 to 19 km/s. Remarkably, also the new members of the GIRAFFE sample have a RV compatible with the cluster. On the other hand, the only two outliers are GIRAFFE "L08 mem", suggesting that they are SB1 or runaway stars.

In Fig. 7.6 we show the spatial location of the 15 UVES and GIRAFFE members with respect to the main cloud, including the GIRAFFE HCMs.

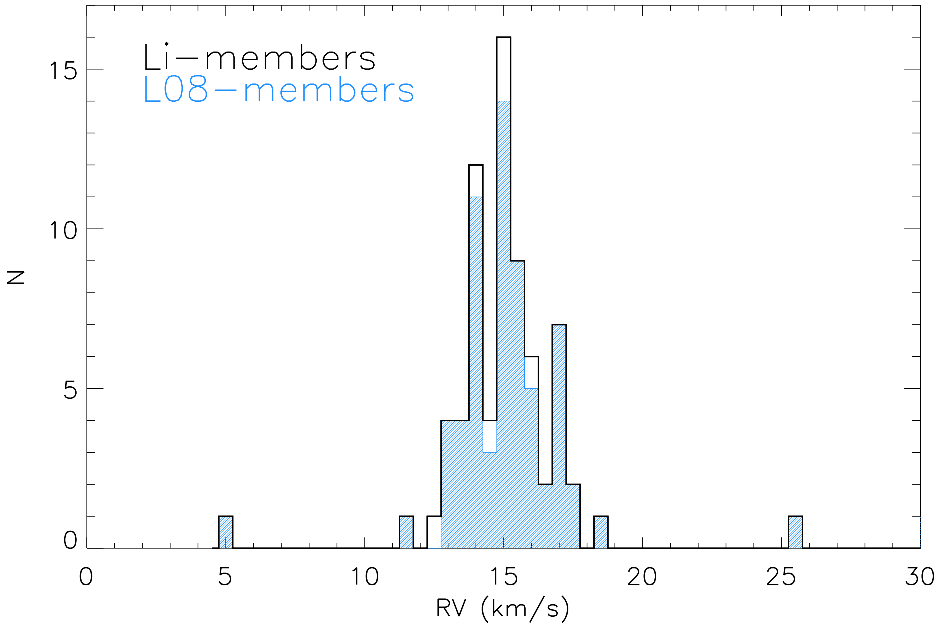

Figure 7.5: Radial velocity distribution of the Cha I GIRAFFE + UVES members. The blue histogram is for the "L08 mem" subsample.

The stars belong to the two concentrations corresponding to the subclusters Cha I North and South. However, we have also confirmed the membership of 7 (1 UVES and 6 GIRAFFE) stars in the off-fields, away from the main molecular complex. This confirms that the census of members with spectral types earlier than mid-M is almost complete in the central regions, but not in the cluster periphery. These new members have values of the RV consistent with the main RV distribution of the cluster, indicating that they did not migrate to the current positin but were likely born there. This is an important finding as it will allow us to check if a difference in metallicity is present between the two subclusters of the main SFR and the distributed members.

7.5 The metallicity of Cha I

As mentioned in Section 7.3.2, the main stellar parameters are the average of the values obtained by four nodes, using different methods. Among the 15 members of the cluster identified in Section 7.4, we will consider for the analy-

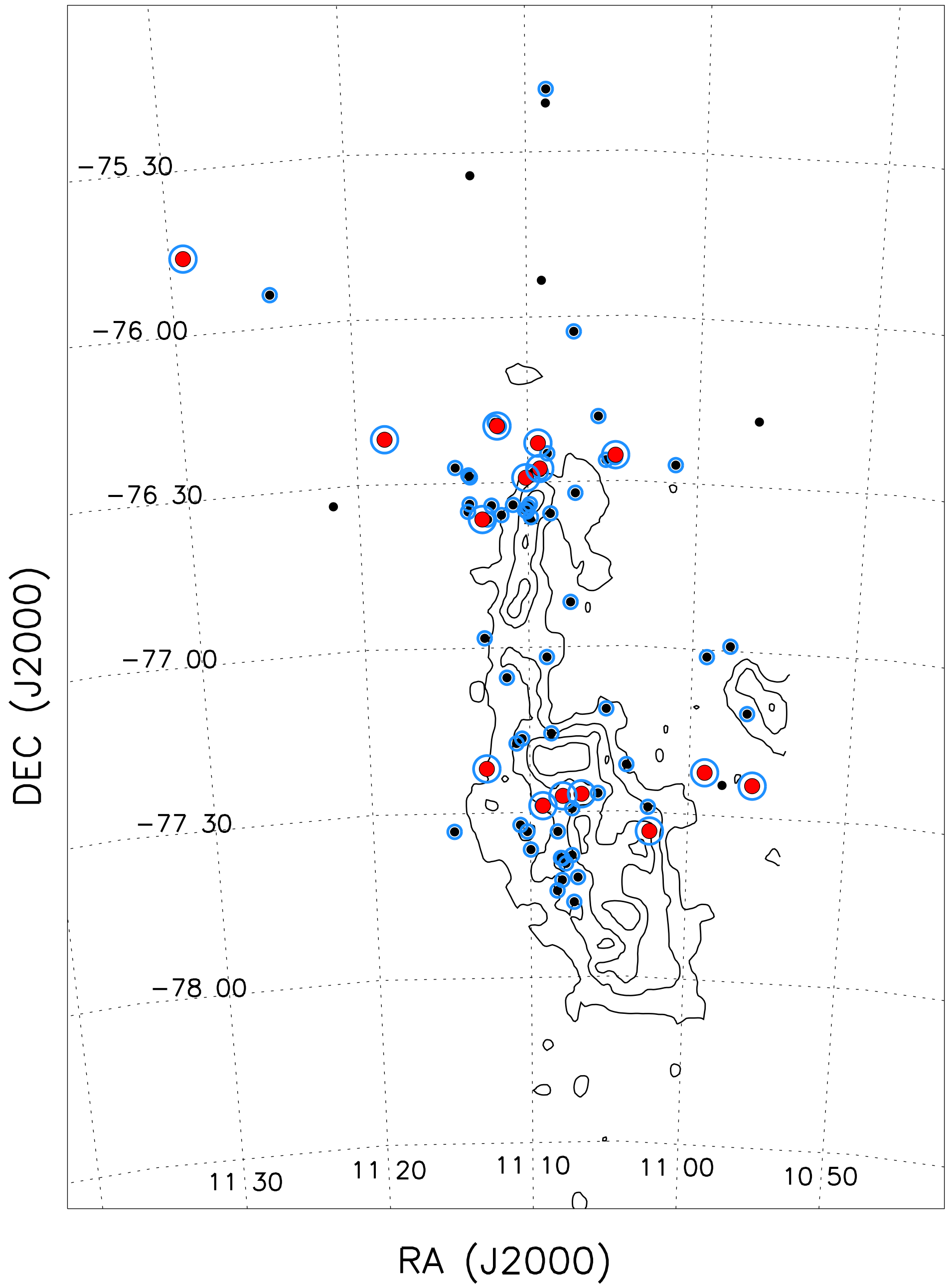

Figure 7.6: Map of the spatial location of the Cha I members. The symbols are the same as in Fig. 7.4. The contours correspond to the extinction levels A_V=2, 4, 6 and 8 from Cambresy (1998).

sis of the metal content the 11 UVES targets with T_{eff}>4200 K. Their [Fe/H] distribution is plotted in Fig. 7.7. The average value is <[Fe/H]>=−0.13±0.09, showed by the solid line. The metallicity ranges from -0.32 to $+0.00$ dex, with five stars in the narrow interval -0.09 to -0.05 dex. We point out that the large excursion of [Fe/H] is the result of the average of highly discordant metallicity estimates provided by the different nodes. In fact, spectra of cool stars (spectral type < K5) generally have few or weak Fe II lines for which the EWs are barely measurable. The results obtained via the "iron-EWs method" are more prone to this source of uncertainties than those obtained through the grid of templates. This effect is even more significant if the star is a rapid rotator or in the case of low SNR spectra. We note that giant stars are less affected by these effects, making their identification more robust.

As a consequence, since the node making use of the grid of templates provided the main parameters for all the 11 members, we compare the errors (σ_{Teff}, $\sigma_{log\ g}$ and $\sigma_{[Fe/H]}$) of each star to the mean errors of the sample ($<\sigma_{Teff}>$, $<\sigma_{log\ g}>$ and $<\sigma_{[Fe/H]}>$) reported in Section 7.3.2. This allowed us to identify stars affected by the problem mentioned above. We identified six members having a set of GES parameters satisfying at least one of the following conditions:
$\sigma_{Teff} > 2 \cdot <\sigma_{Teff}>$
$\sigma_{log\ g} > 2 \cdot <\sigma_{log\ g}>$
$\sigma_{[Fe/H]} > 2 \cdot <\sigma_{[Fe/H]}>$.
These six stars, for which different nodes obtained very discordant atmospheric parameters, have been highlight with the red color in the distribution showed in Fig. 7.7: as expected these stars are all outliers. A large improvement is found if we replace the recommended GES parameters of these outliers with those obtained through the grid of templates. This is shown in Figure 7.8. Columns 5 to 8 in Table 7.2 compare the T_{eff} and [Fe/H] provided by the GES with those obtained from the templates. The mean value of the new distribution is $<$[Fe/H]$>=-0.068\pm0.013$ dex, that is adopted as the final value of mean iron abundance in Cha I with a very small dispersion. Thus, we conclude that the stars of Cha I North and South and the sparse population (represented by sources #48 and 45) are characterized by a homogeneous metallicity.

We now consider the iron abundance obtained for the GIRAFFE members with T_{eff}>4000 K and vsin i<50 km/s. Rapid rotation produces the blending of the absorption features and makes the abundance estimate highly uncertain. The iron distribution of these stars is shown in Figure 7.9. The resulting mean value is $<$[Fe/H]$>_{GIRAFFE}=-0.05\pm0.12$ dex, very close to

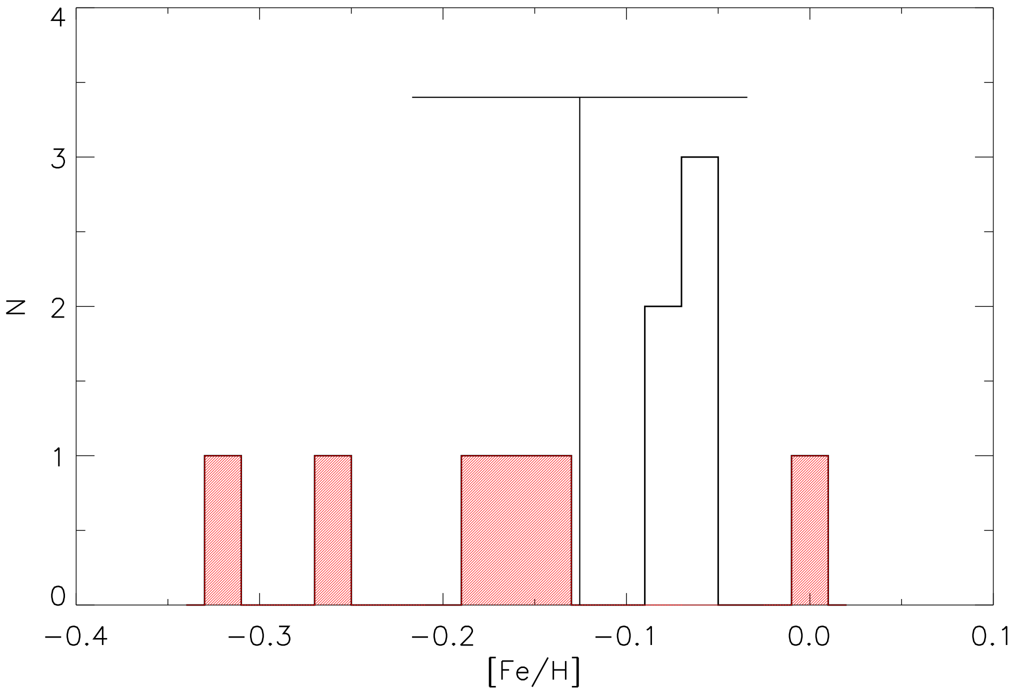

Figure 7.7: Iron abundance obtained with the GES recommended values for the 11 UVES members of Cha I with T_{eff}>4200 K. The red histogram shows the stars whose GES parameters suffer of high uncertainties due to the use of the “iron-EWs method”.

the mean value obtained from the UVES spectra, although the distribution is much broader. This result is similar to that found by Spina (2014) for Gamma Velorum who concluded that the higher dispersion of the GIRAFFE values is due to the lower resolution and shorter spectral range of the GIRAFFE spectra.

Finally, Figure 7.9 displays the iron abundance distribution of the GIRAFFE stars separately for the populations of Cha I North and South. The sample does not include members from the distributed population. Not unexepctedly, we see no difference in the two populations.

Table 7.2: Members and HCMs. Parameters considered for the iron abundance analysis are in boldface.

ID	S/N	RV (km/s)	L_{bol} ($L_{\odot}$)	T_{eff}^{GES} (K)	[Fe/H]^{GES} dex	$T_{eff}^{templ.}$ (K)	[Fe/H]$^{templ.}$ dex
2	6.37422	—	$0.48^{+2.77}_{-0.41}$	3640± 300	-0.10±0.20	3640± 300	-0.10±0.20
6	26.9617	15.3±0.6	$0.96^{+0.54}_{-0.36}$	4135± 125	-0.09±0.13	4135± 125	-0.09±0.13
11	77.3617	14.2±0.6	$1.79^{+1.42}_{-0.72}$	4656± 193	-0.16±0.11	**4519± 174**	**-0.10±0.14**
15	27.9064	13.5±0.6	$0.50^{+0.73}_{-0.24}$	4571± 333	0.00±0.16	**4335± 123**	**-0.05±0.13**
19	9.68413	15.4±0.6	$1.25^{+0.65}_{-0.46}$	**4343± 147**	**-0.07±0.13**	4343± 147	-0.07±0.13
21	38.2723	17.5±0.6	$5.53^{+4.05}_{-2.12}$	4651± 174	-0.25±0.23	**4648± 211**	**-0.07±0.13**
28	39.7842	14.8±0.6	$0.89^{+1.60}_{-0.60}$	4175± 381	-0.45±0.44	3905± 117	-0.21±0.12
29	58.2841	15.1±0.6	$1.46^{+0.67}_{-0.43}$	4524± 103	-0.14±0.12	**4541± 171**	**-0.06±0.13**
30	93.6460	—	$1.43^{+1.12}_{-0.65}$	3990± 123	-0.09±0.13	3990± 123	-0.09±0.13
32	59.2019	14.0±0.6	$1.85^{+0.92}_{-0.66}$	4697± 120	-0.32±0.27	**4168± 169**	**-0.08±0.14**
35	147.154	16.2±0.6	$2.56^{+2.28}_{-1.01}$	**4617± 207**	**-0.06±0.14**	4617± 207	-0.06±0.14
36	169.072	14.2±0.6	$3.89^{+1.22}_{-0.92}$	**5239± 70**	**-0.08±0.08**	5190± 89	-0.06±0.11
37	92.8436	14.3±0.6	$0.81^{+0.66}_{-0.36}$	**4706± 220**	**-0.06±0.11**	4550± 179	-0.07±0.13
45	40.5884	13.8±0.6	$0.89^{+0.71}_{-0.36}$	4465± 209	-0.19±0.21	**4317± 127**	**-0.06±0.13**
48	38.8763	15.2±0.6	$1.24^{+0.52}_{-0.39}$	**4818± 96**	**-0.06±0.14**	4818± 96	-0.06±0.14

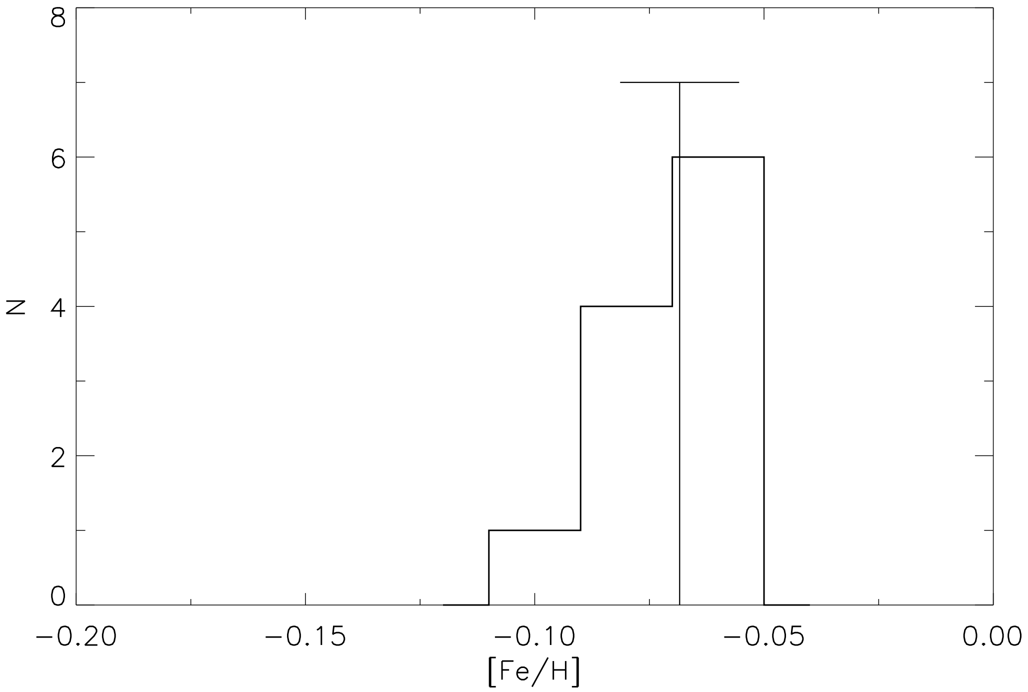

Figure 7.8: Final iron abundance distribution corrected for the uncertainties that affect the 'iron-EWs" analysis. The resulting mean metallicity of Cha I is <[Fe/H]>=−0.068±0.013 dex.

7.6 Discussion

7.6.1 Comparison with previous works

As described in Section 4, our iron abundance analysis is based on a sample of 11 stars observed with UVES. Of these, only one (namely, CS Cha; #11 in Table 2), has been previously observed and analyzed in terms of the iron abundance by Padgett (1996). For this star, we find [Fe/H]=-0.10 ± 0.14, while Padgett (1996) obtained [Fe/H]=$+0.11 \pm 0.14$. Even if the two measurements agree within the errors, the absolute [Fe/H] values differ by Δ[Fe/H]=0.21 dex, a value that could result from a variety of factors.

- The analysis by Padgett was based on few iron lines (16).
- Very strong lines, mostly affected by the treatment of damping, were not excluded in Padgett's list; in particular, for CS Cha, 5 among the 16 lines used for the iron abundane have $EW > 150$ mÅ.

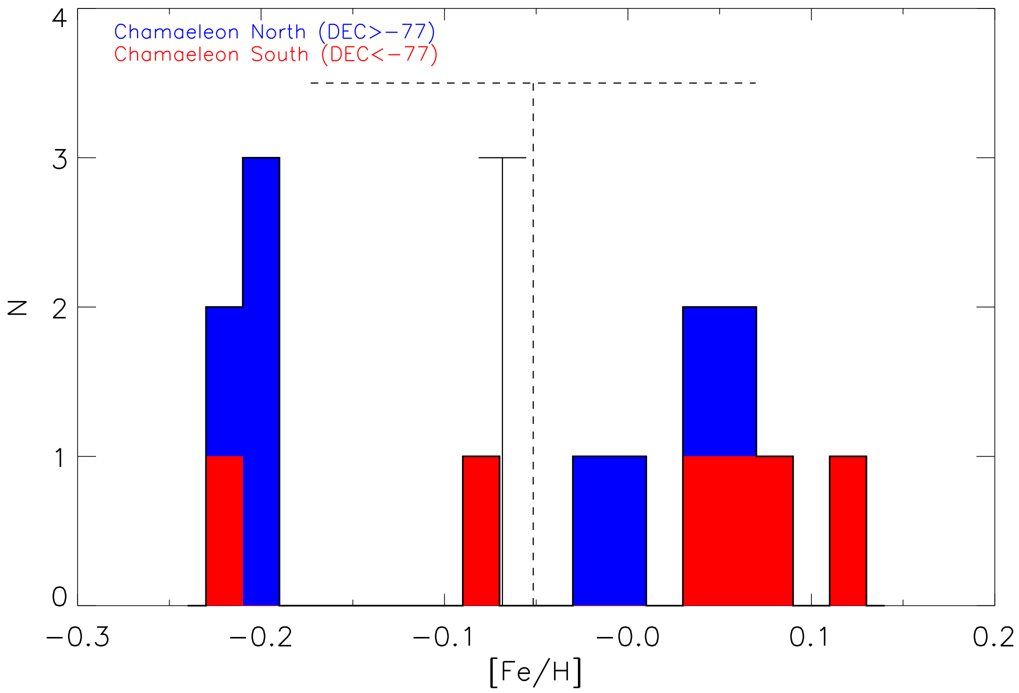

Figure 7.9: Iron abundance of the GIRAFFE members with T_{eff}>4000 K and vsin i<50 km/s. The mean value is <[Fe/H]>$_{GIRAFFE}$=−0.05±0.12 dex (dashed line), similar to that obtained from the UVES analysis (solid line). The blue color highlights the distribution of The Cha I North and South groups are displayed in blue and red, respectively.

- The microturbulence velocity found by Padgett (1996) $\xi = 0.3 \pm 0.6$ km/s is lower than the mean value of $\sim$ 1.7 km/s reported for the other four stars analyzed by the author and the typical value found for very young stars (see, e.g., Biazzo et al. 2011a). Low values of ξ could lead to overestimate the iron abundance. In fact, in the Padgett sample, CS Cha is the star with the highest iron of Chamaeleon, [Fe/H]=+0.11 ± 0.14 against the other values ranging from −0.26 and 0.00 dex).

7.6.2 Iron abundance in the Chamaeleon complex

We discuss now the overall metallicity of the Chamaeleon complex. In Figure 7.10 our average [Fe/H] determination for Cha I is compared with previous estimates by Padgett (1996), Santos et al. (2008), and Biazzo et al.

(2012). As mentioned, the first authors analyzed five stars associated with the Cha I dark cloud, Santos et al. (2008) measured iron, nickel, and silicon abundances of four stars located in a wide area of the Chamaeleon region[2], while Biazzo et al. (2012) analyzed only one target in Chamaeleon II (namely, Hn 23). The mean iron abundance of [Fe/H]=-0.068 ± 0.013 found by us for the Cha I stars is in good agreement within the errors with the results by Padgett (1996) and Santos et al. (2008), who derived mean values of [Fe/H]=-0.06 ± 0.14 and [Fe/H]=-0.15 ± 0.12[3], and Biazzo et al. (2012), who obtained [Fe/H]=-0.12 ± 0.14 for Hn 23.

However, from Fig. 7.10 it is also clear how our [Fe/H] distribution is narrower than that obtained in previous studies. In fact, in the work by Padgett (1996) the metallicity ranges from -0.26 to $+0.11$ dex, while in Santos et al. (2008) the internal dispersion is smaller, from -0.28 to -0.03 dex, still larger than our values from -0.10 to -0.05 dex. This means than the star-to-star scatter is smaller than the observational errors and that the standard deviation of [Fe/H] within this young association is not larger than in older clusters, as concluded in general by Padgett (1996) or by Santos et al. (2008) for Chamaeleon. The [Fe/H] variations previously claimed in Chamaeleon probably reflect uncertainties affecting the abundance analysis of young stars (e.g., low quality spectra, uncertainty in the stellar parameters, high activity level, etc.) with respect to older stars or some unidentified systematic effect in the data, as suggested by Santos et al. (2008), and not a real dispersion in metallicity of a given region. Similar homogeneous abundance measurements in young clusters have also been found in several star-forming regions (see, e.g., the case of several sub-groups of the Orion complex reported by D'Orazi et al. 2009, Biazzo et al. 2011a,b and the Taurus-Auriga association analyzed by D'Orazi et al. 2011).

---

[2] From the recent work on proper motions by López Martí et al. (2013), two stars analyzed by Santos et al. (2008), namely, RX J1158.5−7754a and RX J1159.7−7601, seem to be kinematical members of the ϵ Cha cluster, another one (RX J140.3−8321) seems to belong to the η Cha cluster, while RX J1233.5−7523 seems to be a field star.

[3] For consistency, we are reporting the arithmetic mean of [Fe/H] as averaged value of the iron abundance estimated by us and previous works, and as error the standard deviation around the mean.

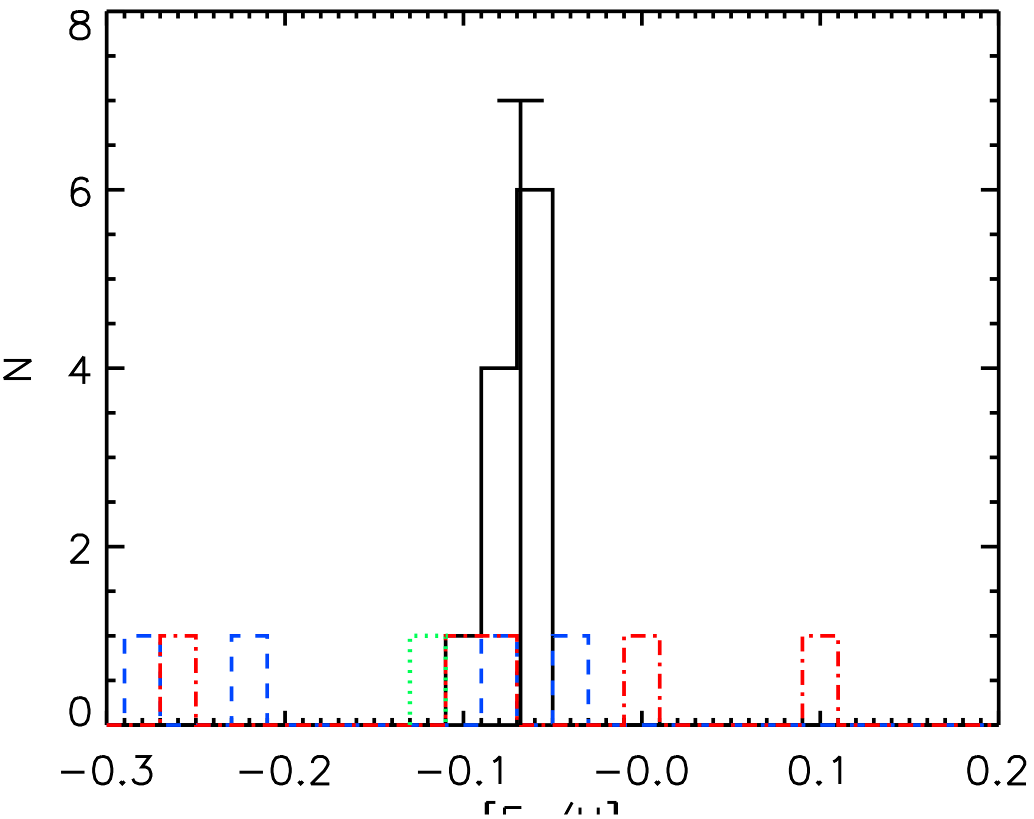

Figure 7.10: Comparison between our [Fe/H] distribution (solid line) with previous estimates by Padgett (1996) (dash-dotted line), Santos et al. (2008) (dashed line), and by Biazzo et al. (2012) (dotted line). The mean [Fe/H] for the Cha I members and its standard deviation are also indicated by the dotted line.

7.6.3 Metallicity in nearby SFRs

Recently, Biazzo et al. (2011a) have presented a comprehensive view of the metallicity determinations in young clusters and SFRs, showing that the majority of the SFRs are slightly more metal-poor than the Sun, while none is more metal-rich. On the other hand, the metal content of the young clusters in the Solar neighborhood is identical to the Solar one, as also found by D'Orazi et al. (2009). This evidence has led Biazzo et al. (2011a) to conclude that the metal-poor nature of SFRs is indeed a relic of the process of star formation in the Solar neighborhood, rather than the effect of chemical evolution. This suggestion supports the conclusion of Santos et al. (2008) who also suggested that the nearby interstellar medium has suffered from a recent infall of metal-poor gas. These initial results have reinforced by our analysis of Cha I and also by the metallicity estimates of Gamma Velorum with [Fe/H]=−0.057±0.019 dex (Spina 2014) and Cha II with [Fe/H]=−0.12±0.14 dex (Biazzo et al. 2012).

In a more general context, it is interesting to consider the Gould Belt, a structure clearly visible in the sky as a large ring of mainly O- and B- type stars (for a detailed discussion see Poppel 1997). The ring has a diameter of ∼1000 pc and it is tilted toward the Galactic plane by ∼20°. The Gould Belt is a relatively recent structure that formed between 20 and 90 Myr ago (Torra et al. 2000). Currently, the Sun is located within the ring at ∼100 pc from its center (Guillout et al. 1998). The most interesting part is that, according to the study by Guillout et al. (1998) of the late-type stellar populations associated to the Gould Belt, it contains most of the nearby SFRs, such as Orion, Rho Ophiuchi, Scorpius, Lupus and Chamaeleon, with the remarkable exception of Taurus. The latter is the most metal-rich SFR in the Solar vicinity with [Fe/H]=−0.01±0.05 dex (D'Orazi et al. 2011). These star forming environments probably represent the latest star formation event in the local interstellar medium caused by the condensation of a ring of gas with a metallicity distinctively lower than that of the Sun. If this scenario is confirmed by additional kinematical studies and abundance measurements, it could offer a reasonable explanation for the metal-poor nature found for most of the youngest stars in the Solar neighborhood.

7.7 Conclusions

In this paper we have made use of the dataset provided by the Gaia-ESO Survey in order to identify the Chamaeleon I members and to study their elemental abundances. The main findings can be summarized as follows:

i) We confirmed the membership of 15 UVES targets on the basis of surface gravity, the presence of photospheric lithium and their position in the HRD. These stars, previously identified as Cha I members by Luhman (2008a), belong to the two subclusters Cha I North and South and to the sparse population around the main molecular cloud. The sample of UVES targets does not contain any new members of Cha I.

ii) Cha I has a slightly sub-solar iron abundance: $<$[Fe/H]$>= -0.068\pm0.013$ dex. This value has been derived from the metallicity determination of 11 UVES members. The small dispersion suggests that the two subclusters and the sparse population have a homogeneous metal content, as expected for a T Tauri association such as Chamaeleon I, isolated from other SFRs, young clusters and OB associations.

iii) The iron abundance distribution found for the GIRAFFE members has a mean value close to that found for the 11 UVES targets, but with a larger dispersion: $<$[Fe/H]$>_{GIRAFFE}= -0.05\pm0.12$ dex. We attribute the dispersion of the GIRAFFE distribution to the larger errors that affect the metallicity determinations, rather than to a real variation. This is supported by the lack of significant differences between the metal content of the two subclusters studied also by means of the GIRAFFE members.

iv) The newly derived metallicity of Cha I is in agreement with previous determinations obtained by Padgett (1996), by Santos et al. (2008) in a wide area away from the molecular cloud of the Chamaeleon complex and by Biazzo et al. (2012) in Cha II. These results indicate that the whole Chamaeleon region is more metal-poor than the Sun.

v) The metallicity of Cha I is similar to those of other SFRs in the Solar neighborhood. The metal-poor nature of these young environments could be the result of a common and widespread star formation episode that involved the Gould Belt and that gave birth to most of the SFRs in the Solar vicinity.

Table 7.3: Stellar parameters of the 48 UVES stars. Cluster members and likely members are in boldface.

ID	2MASS name	R.A. (J2000)	DEC. (J2000)	T_{eff} (K)	log g	[Fe/H]	EW(Li) mÅ	bin.	log g mem.	Li mem.	HRD mem.	L08 mem.	final mem.
1	J10554858-7651504	10 55 48.58	-76 51 50.4	—	—	—	<15	N	—	—	—	N	—
2	**J10555973-7724399**	**10 55 59.73**	**-77 24 39.9**	**3640±300**	**4.40±0.20**	**-0.10±0.20**	**406±51**	**N**	**Y**	**Y**	**Y**	**Y**	**Y**
3	J10564115-7744292	10 56 41.15	-77 44 29.2	4384±51	2.02±0.18	-0.33±0.08	104±1	N	N	—	—	N	N
4	J10574797-7617429	10 57 47.97	-76 17 42.9	5110±49	3.08±0.16	0.19±0.12	15±10	N	N	—	—	N	N
5	J10585418-7743115	10 58 54.18	-77 43 11.5	4701±60	2.99±0.17	0.13±0.10	<15	N	N	—	—	N	N
6	**J10590108-7722407**	**10 59 01.08**	**-77 22 40.7**	**4135±125**	**4.63±0.13**	**-0.09±0.13**	**569±18**	**N**	**Y**	**Y**	**Y**	**Y**	**Y**
7	J10593816-7822421	10 59 38.16	-78 22 42.1	4464±55	2.25±0.20	-0.09±0.12	<10	N	N	—	—	N	N
8	J11010007-7738516	11 01 00.07	-77 38 51.6	3958±63	1.85±0.49	-0.31±0.15	317±5	N	N	—	—	N	N
9	J11012887-7539520	11 01 28.87	-75 39 52.0	—	—	—	<2	N	—	—	—	N	—
10	J11020524-7525093	11 02 05.24	-75 25 09.3	4253±67	1.77±0.28	-0.23±0.08	<5	N	N	—	—	N	N
11	**J11022491-7733357**	**11 02 24.91**	**-77 33 35.7**	**4656±193**	**4.28±0.52**	**-0.16±0.11**	**571±5**	**N**	**Y**	**Y**	**Y**	**Y**	**Y**
12	J11033599-7628242	11 03 35.99	-76 28 24.2	4242±80	1.85±0.34	-0.22±0.06	35±2	N	N	—	—	N	N
13	J11034945-7700101	11 03 49.45	-77 00 10.1	3865±72	1.54±0.12	0.03±0.11	<30	N	N	—	—	N	N
14	J11044460-7706240	11 04 44.60	-77 06 24.0	4411±60	1.99±0.18	-0.30±0.07	<10	N	N	—	—	N	N
15	**J11045100-7625240**	**11 04 51.00**	**-76 25 24.0**	**4571±333**	**4.44±0.16**	**0.00±0.16**	**575±6**	**N**	**Y**	**Y**	**Y**	**Y**	**Y**
16	J11053303-7700120	11 05 33.03	-77 00 12.0	4631±417	4.39±0.35	-0.12±0.12	30±10	N	Y	N	—	N	N
17	J11055780-7607488	11 05 57.80	-76 07 48.9	—	—	—	<5	N	—	—	—	Y	—
18	J11060511-7511454	11 06 05.11	-75 11 45.4	5003±39	2.69±0.16	-0.33±0.17	<5	N	N	—	—	N	N
19	**J11064510-7727023**	**11 06 45.10**	**-77 27 02.3**	**4343±147**	**4.56±0.15**	**-0.07±0.13**	**797±32**	**N**	**Y**	**Y**	**Y**	**Y**	**Y**
20	J11065856-7713326	11 06 58.56	-77 13 32.6	3777±85	1.44±0.20	0.02±0.11	212±45	N	N	—	—	N	N
21	**J11075588-7727257**	**11 07 55.88**	**-77 27 25.7**	**4651±174**	**4.10±0.57**	**-0.25±0.23**	**499±3**	**N**	**Y**	**Y**	**Y**	**Y**	**Y**
22	J11080148-7742288	11 08 01.48	-77 42 28.8	4327±131	4.44±0.12	-0.10±0.14	555±13	Y	—	—	—	Y	—
23	J11080411-7513273	11 08 04.12	-75 13 27.3	4436±91	2.15±0.18	-0.11±0.10	36±9	N	N	—	—	N	N
24	J11082577-7648315	11 08 25.77	-76 48 31.5	4485±53	2.22±0.16	-0.01±0.16	<5	N	N	—	—	N	N
25	J11084041-7756310	11 08 40.41	-77 56 31.0	6378±183	3.94±0.17	-0.01±0.12	97±15	N	Y	HCM	N	N	N
26	J11085230-7743329	11 08 52.31	-77 43 32.9	—	—	—	<5	N	—	—	—	N	—
27	J11085326-7519374	11 08 53.26	-75 19 37.4	—	—	—	428±8	Y	—	—	—	Y	—
28	**J11091172-7729124**	**11 09 11.72**	**-77 29 12.4**	**4175±381**	**4.38±0.60**	**-0.45±0.44**	**654±15**	**N**	**Y**	**Y**	**Y**	**Y**	**Y**
29	**J11091769-7627578**	**11 09 17.69**	**-76 27 57.8**	**4524±103**	**4.21±0.58**	**-0.14±0.12**	**567±10**	**N**	**Y**	**Y**	**Y**	**Y**	**Y**
30	**J11092379-7623207**	**11 09 23.78**	**-76 23 20.7**	**3990±123**	**4.64±0.13**	**-0.09±0.13**	**547±15**	**N**	**Y**	**Y**	**Y**	**Y**	**Y**
31	J11095119-7658568	11 09 51.19	-76 58 56.8	5755±76	4.28±0.19	0.49±0.15	<10	N	Y	N	—	N	N
32	**J11100704-7629376**	**11 10 07.04**	**-76 29 37.7**	**4697±120**	**4.37±0.43**	**-0.32±0.27**	**563±6**	**N**	**Y**	**Y**	**Y**	**Y**	**Y**
33	J11111333-7731178	11 11 13.33	-77 31 17.8	4794±43	3.15±0.14	0.21±0.16	<10	N	N	—	—	N	N
34	J11112801-7749213	11 11 28.01	-77 49 21.3	3928±118	1.43±0.20	-0.11±0.12	20±10	N	N	—	—	N	N
35	**J11114632-7620092**	**11 11 46.32**	**-76 20 09.2**	**4617±207**	**4.50±0.17**	**-0.06±0.14**	**537±15**	**N**	**Y**	**Y**	**Y**	**Y**	**Y**
36	**J11124268-7722230**	**11 12 42.68**	**-77 22 23.0**	**5239±70**	**4.23±0.34**	**-0.08±0.08**	**369±4**	**N**	**Y**	**Y**	**Y**	**Y**	**Y**
37	**J11124299-7637049**	**11 12 42.99**	**-76 37 04.9**	**4706±220**	**4.27±0.42**	**-0.06±0.11**	**461±5**	**N**	**Y**	**Y**	**Y**	**Y**	**Y**
38	J11135757-7818460	11 13 57.57	-78 18 46.0	—	—	—	<5	N	—	—	—	N	—
39	J11140585-7729058	11 14 05.85	-77 29 05.8	3972±103	1.55±0.24	0.00±0.10	<28	N	N	—	—	N	N
40	J11140942-7714492	11 14 09.41	-77 14 49.2	4105±65	1.59±0.21	-0.29±0.07	<10	N	N	—	—	N	N
41	J11141568-7738326	11 14 15.68	-77 38 32.6	7075±102	4.16±0.14	-0.09±0.13	<50	N	Y	HCM	N	N	N
42	J11142964-7707062	11 14 29.64	-77 07 06.3	5968±59	4.32±0.11	0.03±0.04	23±3	N	Y	N	—	N	N
43	J11143515-7539288	11 14 35.15	-75 39 28.8	4469±43	2.05±0.17	-0.26±0.08	<10	N	N	—	—	N	N
44	J11170509-7538518	11 17 05.09	-75 38 51.8	4882±56	2.80±0.15	0.08±0.14	15±5	N	N	—	—	N	N
45	**J11182024-7621576**	**11 18 20.24**	**-76 21 57.6**	**4465±209**	**4.25±0.58**	**-0.19±0.21**	**529±7**	**N**	**Y**	**Y**	**Y**	**Y**	**Y**
46	J11213017-7616098	11 21 30.17	-76 16 09.8	4917±50	2.86±0.12	0.05±0.08	<10	N	N	—	—	N	N
47	J11252677-7553273	11 25 26.77	-75 53 27.3	6380±207	4.04±0.22	-0.01±0.15	<10	N	Y	N	—	N	N
48	**J11291261-7546263**	**11 29 12.61**	**-75 46 26.3**	**4818±96**	**4.50±0.15**	**-0.06±0.14**	**463±7**	**N**	**Y**	**Y**	**Y**	**Y**	**Y**

In the GESviDR1Final catalog, the errors of the main parameters of the UVES star #20 are suspiciously high: σ_{Teff}=371 K, $\sigma_{log\ g}$=8.6 dex and $\sigma_{[Fe/H]}$=3.5 dex. The star has been independently analyzed by two nodes. One of them has derived extremely large errors for the parameters: σ_{Teff}=475 K, $\sigma_{log\ g}$=10 dex, and $\sigma_{[Fe/H]}$=10 dex). Thus, we adopt the main parameters obtained by the second node that are reported in the Table.

Chapter 8

Conclusions and Future Perspectives

> I am busy just now again on electromagnetism, and think I have got hold of a good thing, but can't say. It may be a weed instead of a fish that, after all my labor, I may at last pull up.
>
> Michael Faraday, 1831

In this final Chapter, I present the main conclusions on the research activity carried out during the PhD. I will describe my effort to improve the techniques and methodologies of spectral analysis that have been necessary for a project like the Gaia-ESO Survey. Then, I will present a general summary of the scientific findings and their implications on the general issues detailed in Section 1.2.6. Finally, I will illustrate the future developments of my research and how the achievements of the Gaia-ESO Survey and the Gaia mission, launched in December, will provide key contributions towards a final answer to the open questions related to the elemental abundances in YOC/SFRs.

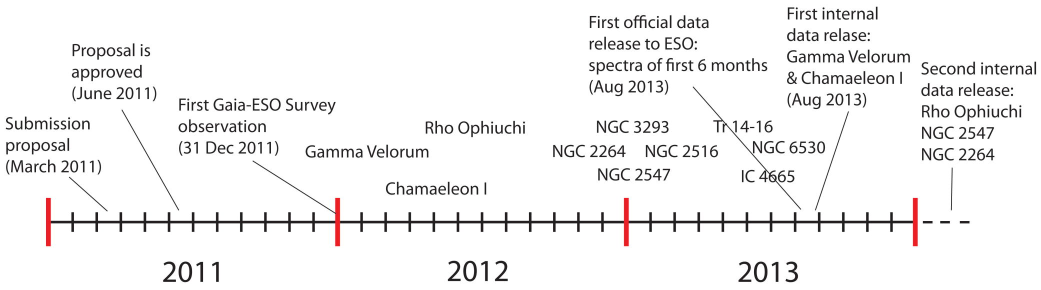

Figure 8.1: Timeline of the Gaia-ESO Survey.

8.1 Methodology

The advent of the first large public spectroscopic survey of all the components of the Milky Way, the Gaia-ESO Survey, represents a critical and unique opportunity to improve methods of spectral analysis and elemental abundance determinations. The main driver behind such a large collaboration has been the need to produce homogeneous results that could be avaliable to the community. Prior to this Survey, the groups working in stellar spectroscopy have developed methods, techniques and procedures for the analysis independently of each other, very often focusing on specific types of stars. In general, each team made use of their own tools, such as linelists and atmospheric models; also, until a few years ago, most tools were based on a star-by-star analysis without any attempt of automatization. Very often these circumstances have led to inconsistencies between the analysis and results of the various teams. On the other hand, the large number of stellar spectra, collected by the Gaia-ESO Survey, required the development of fast and automatic procedures producing values that have to be comparable with those derived by the other teams.

While preparatory activities and letter of intent for a large public spectroscopic survey had started in 2010, the period 2011-2013 of the PhD has covered the initial stages of the Gaia-ESO Survey: proposal preparation with the submission in March 2011, the approval by ESO in June 2011, the first observations on December 31^{st} 2011 and the beginning of scientific exploitation, with the first internal data release in August 2013 (see Fig. 8.1). As of today, 22 observing runs have been accomplished, for a total of more than 1000 hours. As a result, being at the institute of one of the Co-PIs, I actively participated in most of the Gaia-ESO activities. In particular, I contributed in the development and validation of the procedures used by the Arcetri team and also in the homogenization of the final parameters and abundances derived by each node of WG12, namely:

- **Optimization of the tools for the analysis.** The analysis procedure of the Arcetri team earlier than the Gaia-ESO Survey consisted in the EW measurement "by hand" of about ∼100 iron lines and the minimization "by eye" of the trends between A(FeI) and χ and EWs and of the difference between A(FeI) and A(FeII). The procedure adopted in my PhD not only allowed a faster analysis, but also removed the subjectiveness by adopting codes for automatic measurements of EWs and minimization of trends. This has been the result of several tests on ARES (Sousa et al. 2007), DAOSPEC and FAMA. The first two codes were already public and avaliable, while FAMA has been developed at Arcetri during the Survey. As a result, I have contributed to the performance tests of FAMA. As an original application of the procedure, I have carried out the automatic analysis of 1700 ELODIE spectra available in the archive of this instrument. The results, discussed in Section 4.4, indicate that the procedure satisfies all the requirements for a homogeneous, fast, reproducible and standardized analysis.

- **Comparison with other teams and homogenization.** A great effort has been dedicated to quality control of the results obtained by different nodes, i.e. my own one and those based in Madrid, Porto and Catania. The lesson from working with different analysis teams has been: i) the need to have a full understanding of the other methods, considering also their advantages and limitations; ii) the appreciation of the effect that even small differences in input quantities, such as the linelist or the atomic parameters, have on the final results; iii) the need for a preliminary calibration of each method through the analysis of a sample of benchmark stars whose parameters are known from independent and possibily not-spectroscopic methods. This is indeed an activity where the Gaia-ESO teams are dedicating a great effort; iv) the necessity of reproducibility of the analysis. The determination of atmospheric parameters and abundances and their homogenization has produced large sets of self-consistent data. Altough inconsistencies are still present between the groups, this step represent a significant improvement of the situation prior to the beginning of the Survey. It is also significant that this strategy has been applied to a wide variety of stars in differend evolutionary phases and in a wide metallicity interval (from very low, to supersolar values), not just the stars of my specific concern for the PhD project.

- **Science validation.** An important part of my work has been in producing a validation of the quantities derived during the initial phase of the Survey. This has been done in particular for the first young cluster observed, Gamma Velorum. The Gaia-ESO Survey collects spectra from two different spectrographs: GIRAFFE and UVES. The outcome of the observations and analysis are the atmospheric parameters, lithium EWs and radial velocities. The detailed comparison, discussed in Section 6.4, revealed an overall good agreement of the parameters obtained from the two spectrographs. Not surprisingly, the GIRAFFE data are more scattered and have larger errors, due to the lower resolution and more limited spectral range. Also the lithium EWs are in agreement and small discrepancies only affect the weakest lines. I also found that a systematic shift of 1.1 km/s is present between the RVs obtained from the two spectrographs. The cause of this behavior shall to be investigated.

8.2 Abundances in YOC/SFRs

Due to the paucity of information on the metallicity in YOC/SFRs, I have undertaken a large project aimed to study the main topics listed in Section 1.2.6. This project is of course closely, but not exclusively, connected with the Gaia-ESO Survey that in the near future will give a comprehensive view of the properties of the stellar populations associated with the environments (see Section 8.3). So far, the Survey has released products related to one YOC (Gamma Velorum) and one SFR (Chamaeleon I). My overall scientific contribution resulted in the metallicity determination of Gamma Velorum and Chamaeleon I as part of the Gaia-ESO Survey. It is important to note that the spectral analysis for all these regions has been conducted with the same procedure, guaranteeing a homogeneous determination. The main results can be summarized as follows:

- The iron abundance has been derived both these clusters. The values found for Gamma Velorum and Chamaeleon are well constrained and based on a significant number of members: 7 and 11 stars, respectively. I have shown that these regions have a slightly sub-solar metallicity.

- The assumption of solar metallicity made for these associations in order to determine their ages and distances appears to be correct. The most metal-poor cluster of the analyzed sample is Chamaeleon I. Its iron abundance of -0.068 dex implies that the region is 15% more metal-poor than the Sun. Assuming the relation given by Sherry et al. (2008) for a 2 Myr isochrone, $\Delta V \sim -0.75 \times [Fe/H]$ (see Section 1.2.1), we obtain $\Delta V = 0.05$ mag. Such a variation in the distance modulus corresponds to a displacement of Chamaeleon I system of only ~4 pc.

- The composition of the studied clusters does not show evidence of star-to-star variation among their members, with the only exception of one star in Gamma Velorum. This confirms the assumption that, apart from few cases, all the stars born within a cloud share the same chemical content. An important implication is that, with a homogeneous and detailed spectral analysis, one will be able to perform chemical tagging also in young clusters.

- Elemental abundances have been determined for two Gamma Velorum members. The results show that one star has anomaly abundances, but highly uncertain. The other star does not indicate anomalies in its chemical abundances with respect to the solar values. However, Gamma Velorum lies in the Vela complex, a composite region characterized, *inter alia*, by the presence of other PMS clusters that, like in the case of NGC2547 that have been already targeted by the Gaia-ESO Survey. Thus, the metallicity determination of Gamma Velorum is very important because it will allow me to perform a critical comparison with the results of the other clusters of the complex.

- A member of Gamma Velorum is significantly more metal-rich (at the 4-σ level) than its cluster ($<[Fe/H]> = -0.057 \pm 0.018$ dex). There is no reason to believe that this star is not a member of Gamma Velorum: its radial velocity, surface gravity, lithium EW and position in the CMD are all consistent with those of the other cluster members, a fact reinforced by its X-ray emission and the presence of a debris disk. I have speculated that its higher metallicity may imply an episode of planet accretion and I have calculated that an amount of $\sim 60\ M_{\oplus}$ rocky material can produce the observed iron overabundance. If this scenario is confirmed, we can imagine two implications: i) the presence of planets in some cases affects the metallicity of the hosting star; ii) the youngest generation of stars of the Milky Way is still forming planets.

8.3 Future perspectives

The metallicity distribution of YOC/SFRs in the Solar neighborhood is shown in Fig. 8.2, where I included all the young clusters with age<100 Myr, closer than 500 pc to the Sun and with a metallicity determination. This sample also includes the results of my analysis. The histogram shows that the YOCs have solar metallicity, while SFRs are slightly sub-solar, in analogy with the vision presented by Biazzo et al. (2011a) (see Fig. 1.4). The properties of all the objects in Fig. 8.2 are listed in Tab. 8.1.

As emphasized before, the Survey is only in the initial phase. Table 8.3 lists the clusters that have been targeted as of December 2013: the Survey has released data of two PMS clusters and the spectra of three other regions have been already analyzed, but not yet released. Furthermore, observations of four additional clusters have been already completed and about 10 clusters will be targeted in the coming years.

The detailed chemical analysis of a large sample of YOC/SFRs with large samples of stars will allow me to study:

- Chemical composition of the Solar neighborhood. As mentioned in Chapter 1, since YOC/SFRs are still close to their birthplaces and contain homogeneous stellar populations that have not had time to disperse through the Galactic disk, these clusters are key objects in order to trace the current metallicity of the Solar neighborhood. The Gaia-ESO Survey will give more insights on the metal-poor nature of the SFRs. In this context, it is interesting to consider the Gould Belt, a structure clearly visible in the sky as a large ring of stars, mainly O- and B- type stars (for a detailed discussion see Poppel 1997). Its diameter is of ∼1000 pc and it is tilted toward the Galactic plane by ∼20°. The Gould Belt is a relatively recent structure that probably formed 30-50 Myr ago. Currently, the Sun is located within the ring at ∼100 pc from its center. The most interesting part is that it contains about 60% of the young stars in the Solar neighborhood and a large number of SFRs. Fig. 8.3 shows a sketch of the Gould Belt, along with the SFRs located within and outside of the structure. The regions

Table 8.1: YOCs and SFRs closer than 500 pc to the Sun with an availiable [Fe/H] determination.

Cluster	Age (Myr)	Distance (pc)	[Fe/H]
Young Open Clusters			
Blanco1	207	90	0.04±0.02
Alpha Persei*	172.4	60	−0.06±0.05
NGC2451a	188	57	−0.01±0.06
IC4665**	360	36	−0.03±0.04
IC2602	145	30	0.00±0.01
IC2391	149	55	−0.01±0.02
Gamma Velorum**	350	5-10	−0.03±0.02
25 Ori*	400	10	−0.05±0.05
lambda Ori	400	10	0.01±0.01
Upper Sco*	140	10	−0.11±0.10
Star Forming Regions			
ONC*	1-3	414	−0.11±0.08
OB1b*	3	440	−0.05±0.05
Chamaeleon I *	2	160	−0.070±0.014
Rho Oph*	1	120	−0.08±0.12
Corona Aus*	3	150	−0.06±0.05
Lupus*	5	200	−0.05±0.01
σ-Ori*	3	360	−0.02±0.09
Taurus	1	140	−0.01±0.05

* marks clusters belonging to the Gould Belt.

** their association to the Gould Belt is uncertain.

References: Ford et al. (2005); van Leeuwen (2009); Panagi & O'dell (1997); Zuckerman et al. (2012); Hünsch et al. (2004); Robichon et al. (1999); Kharchenko et al. (2005); Shen et al. (2005); Hoogerwerf et al. (2001); D'Orazi & Randich (2009); Stauffer et al. (1997); Spina (2014); Jeffries et al. (2009); Biazzo et al. (2011b); Briceno et al. (2005); Dolan & Mathieu (2001); Pecaut & Mamajek (2012); Preibisch & Mamajek (2008); Biazzo et al. (2011a); Santos et al. (2008); González Hernández et al. (2008); Brown et al. (1994); Oliveira et al. (2002); D'Orazi et al. (2011); Kenyon et al. (1994); Briceno et al. (1999); Bally (2008); Menten et al. (2007); Luhman (2007); Neuhäuser & Forbrich (2008); Comerón (2008); Comerón et al. (2003); Viana Almeida et al. (2009)

Table 8.2: Gaia-ESO Survey master list of observed YOC/SFRs

Cluster	Age (Myr)	Distance (pc)	Period of observations
Data products released on Aug 2013			
Gamma Velorum	5-10	350	Feb 2012
Chamaeleon I	2	160	Mar-May 2012
Spectra analyzed - data products release scheduled for Feb 2014			
Rho Ophiuchi	1	120	Apr-Aug 2012
NGC2547	35	360	Dec 2012 - Feb 2013
NGC2264	3	760	Oct-Dec 2012
NGC2516	100	400	Feb-Mar 2013
NGC3293*	10	2300	Jan 2013
Observations completed - spectra not analyzed yet			
IC4665	36	360	May-Aug 2013
NGC6530*	2-3	1250	Mar-Sep 2013
Trumpler 14-16*	6	2733	May-Jun 2012

* The Gaia-ESO Survey will observe also massive stars members of these clusters.

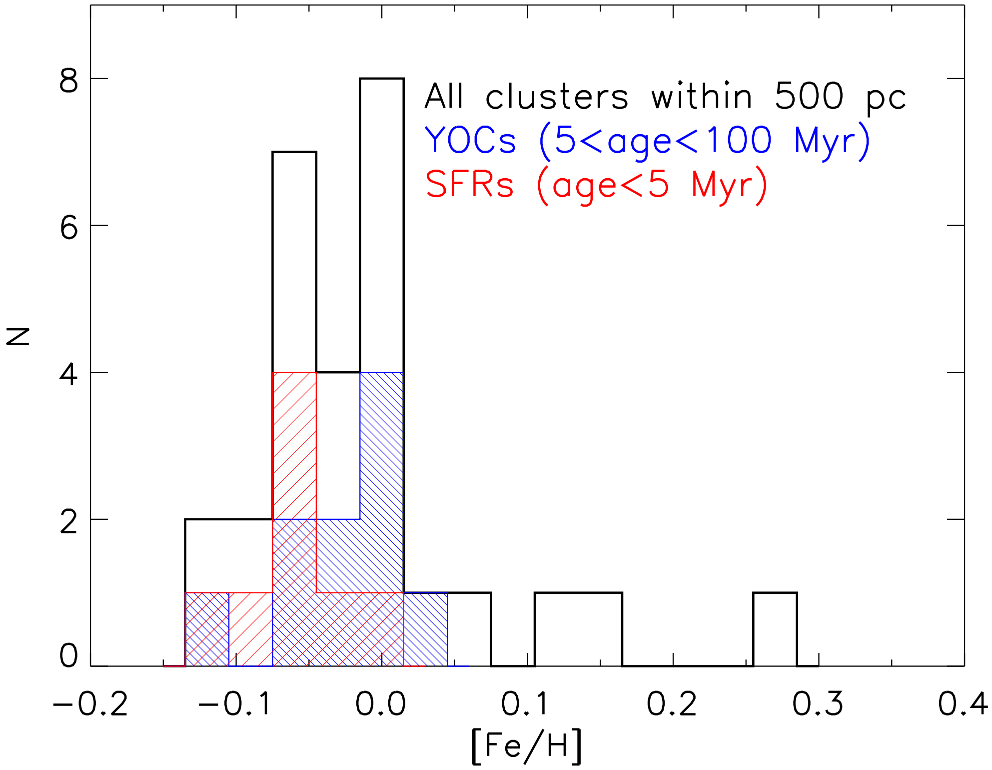

Figure 8.2: [Fe/H] distribution for the clusters within 500 pc from the Sun. Blue and red histograms show the fraction of YOCs and SFRs, respectively. The mean abundance of YOCs is $<[\mathrm{Fe/H}]>_{YOCs}=-0.03$ dex, while that for SFRs is $<[\mathrm{Fe/H}]>_{SFRs}=-0.06$ dex. The names of the YOC/SFRs along with their iron abundances and references are listed in Tab. 8.1.

belonging to the Gould Belt (listed in Tab. 8.1 and marked with an asterisk) include: i) the three most metal-poor YOCs (α-Persei, Upper Sco and 25-Ori), ii) all the SFRs with the only exception of Taurus, that is also the most metal-rich SFR in the Solar neighborhood. These considerations suggest that the Gould Belt has a metallicity distinctively lower than that of the Sun. If this scenario is confirmed by additional abundance measurements, it could offer a reasonable explanation for the metal-poor nature found for most of the youngest stars in the Solar neighborhood.

- The possible correlation between the stellar abundance of refractory elements (such as Mg, Al, Sc, Ti, Si, etc...) and the probability that the star hosts planets. The discovery of clusters rich of such elements would represent a great opportunity to study their disk population during the phase of planet formation.

- The star-(proto)planets interactions, similar to what I have done in the case of the metal-rich member of Gamma Velorum. The cases of stars with a metallicity significantly higher than that of their own cluster are few, but exist. For example, Wilden et al. (2002) and Biazzo et al. (2011a) found metal-rich members in the Pleiades and in the Orion Nebula Cluster, respectively. Both these stars have T_{eff}~5900 K, similar to that of the metal-rich member of Gamma Velorum. The Gaia-ESO Survey will provide metallicity determinations for a large number of stars in each cluster, thus I expect to find other anomalies in the abundances of young stars of intermediate-mass due to planetary accretion events.

- Environmental effects and chemical tagging. Some of the young clusters scheduled for the observations by the Gaia-ESO Survey belong to composite associations. These environments could show chemical segregations due to the enrichment effects caused by SNe explosions or reveal an homogeneity in the chemical content. An interesting example is NGC2547 that lies in the Vela complex, close to Gamma Velorum. The whole region experienced a number of SNe explosion in the past, thus a chemical segregation is plausible to be present in this association.

- So far, only SFRs in the Solar neighborhood have been studied and these regions showed small variations in their metal contents. This precluded definitive conclusions about the effect of metallicity on the lifetime of circumstellar disks. However, the Gaia-ESO Survey will observe farther regions, such as NGC6530, NGC3293 and Tr14-16, that could reveal metallicities significantly different than that of the Sun. This will shed light on the mechanisms that drive disk dispersion around newly formed stars.

- In a few years other wide-field, multi-object, high-resolution spectrographs will be operative (i.e. MOONS, 4MOST, WEAVE). These projects will receive important benefits by the innovative effort of the Gaia-ESO Survey.

I would like to finish this Chapter by also mentioning the fundamental complementary contribution expected from the Gaia satellite that will be launched on December 19, 2013. Gaia will obtain accurate astrometry, positions and distances that, coupled with the radial velocities determined by the Gaia-ESO Suvery, will complete the information on the 6D phase-space of clusters and field stars. Then, it will be possible to derive the complete kinematics and energy and angular momentum distributions for different groups of stars from the PMS to the late stages of stellar evolution. The results of the Gaia mission will also have tremendously impact on YOC/S-FRs by resolving the vexing problem of uncertain membership and distance determinations. Obtaining accurate and complete HRDs will allow to fully understand structures like the Gould Belt or smaller associations, such as the Vela complex, for which the Gaia-ESO Survey has provided accurate and homogeneous abundances determinations.

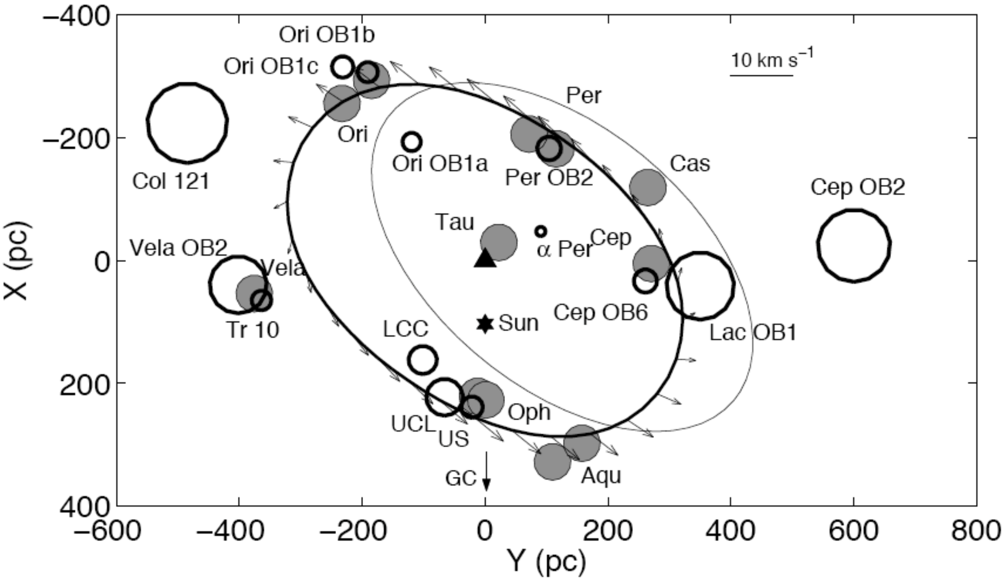

Figure 8.3: Present position of the Gould Belt projected on the Galactic plane. The x and y axes point to the Galactic Centre and in the direction of the Galactic rotation, respectively. Both are centred on the Belt centre. The velocity field outlines the Belt expansion with respect to the Local Standard of Rest. Nearby OB associations are plotted as thick circles using Hipparcos estimates of their distance and dimensions from de Zeeuw et al. (1999). The shaded circles mark the location of the main nearby H2 cloud complexes. The thick and thin ellipses note the Belt rim as obtained in this work and earlier from the HI data by Olano (1982). The triangle and star note the Belt centre and the Sun, respectively. Figure from Perrot & Grenier (2003).

Appendix A

An HST Imaging Survey of Low-Mass Stars in the Chamaeleon I Star Forming region

M. Robberto - Space Telescope Science Institute, Baltimore (USA)
L. Spina
N. Da Rio - European Space Agency–ESTEC (N)
D. Apai - Department of Astronomy, University of Arizona (USA)
I. Pascucci - Space Telescope Science Institute, Baltimore (USA)
L. Ricci - California Institute for Technology, Pasadena (USA)
C. Goddi - European Southern Observatory, Garching (D)
L. Testi - European Southern Observatory, Garching (D)
F. Palla - INAF–Osservatorio Astrofisico di Arcetri
F. Bacciotti - INAF–Osservatorio Astrofisico di Arcetri

This work has been published to the Astronomical Journal.

A.1 Abstract

We present new HST/WFPC2 observations of 20 fields centered around T Tauri stars in the Chamaeleon I star forming region. Images have been obtained in the F631N ([OI]λ6300), F656N (Hα) and F673N ([SII]$\lambda\lambda$6716, 6731) narrow-band filters, plus the Johnson V-band equivalent F547M filter. We detect 31 T Tauri stars falling within our fields. We discuss the optical morphology of 10 sources showing evidence of either binarity, circumstellar material, or mass loss. We supplement our photometry with a compilation of optical, infrared and sub-millimeter data from the literature, together with new sub-mm data for three objects, to build the Spectral Energy Distributions (SED) of 19 single sources. Using an SED model fitting tool, we self-consistently estimate a number of stellar and disk parameters, while mass accretion rates are directly derived from our Hα photometry. We find that bolometric luminosities derived from dereddened optical data tend to be underestimated in systems with high α_{2-24} IR spectral index, suggesting that disks seen nearly edge-on may occasionally be interpreted as low luminosity (and therefore more evolved) sources. On the other hand, the same α_{2-24} IR spectral index, a tracer of the amount of dust in the warmer layers of the circumstellar disks, and the mass accretion rate appear to decay with the isocronal stellar age, suggesting that the observed age spread ($\simeq 0.5-5$ Myr) within the cluster is real. Our sample contains a few outliers that may have dissipated their circumstellar disks on shorter time-scale.

A.2 Introduction

The formation of stars, brown dwarfs, and planets is associated with a rich phenomenology spanning almost the entire electromagnetic spectrum. During the star formation process, the circumstellar disk material can be accreted into one (or more) central objects, ejected along the stellar polar axis, dispersed through photo-evaporation or condensed into planetesimals. Each of these processes is traced by a characteristic set of morphological and spectroscopic signatures, such as UV excess for stellar mass accretion (Hartmann et al. 1998; Muzerolle et al. 2001; Bouvier et al. 2007), shock-excited line-emission from jets and Herbig-Haro objects (Bally et al. 2000, 2007; Reipurth et al. 2000; Whelan et al. 2005; Podio et al. 2006), CO outflows from the disks (Richer et al. 2000; Arce et al. 2007), or mid-IR and sub-mm signatures in the spectral energy distribution due to grain growth and possible disk clearing by a forming planetary system (e.g. Ricci et al. 2010; Andrews et al. 2011; Calvet et al. 2002; Dominik et al. 2007; Espaillat et al. 2008; Blum & Wurm 2008; Pascucci & Sterzik 2009). Each tracer provides critical information on different aspects of the protostellar system, but only a comprehensive view allows reconstructing the full evolutionary scenario. In particular, by combining optical and IR observations it is possible to address key open questions like the formation of stellar companions, the fraction of disk mass accreted into the central star vs. time, the timescale of planetesimal formation (Krumholz 2006; Meyer et al. 2006; Apai & Lauretta 2010).

The Hubble and the Spitzer Space Telescopes offer the best available combination of field-of-view, sensitivity, spatial resolution, and wavelength coverage for studying most of these phenomena (Padgett et al. 1999; O'dell & Wen 1994; Bally et al. 2000; Robberto et al. 2004; Ricci et al. 2008; Allen et al. 2004; Gutermuth et al. 2004; Megeath et al. 2004; Muzerolle et al. 2004; Apai et al. 2005; Pascucci et al. 2008; Luhman 2008b; Luhman et al. 2008). The HST has repeatedly targeted the Orion Nebula and its associated young cluster, the archetype of star forming regions (O'dell & Wen 1994; Bally et al. 2000; Robberto et al. 2004; Colgan et al. 2007; Ricci et al. 2008; O'Dell & Henney 2008). HST observations resolved about 200 circumstellar disks, tens of jets and provided accurate broad-band photometry needed to determine the fundamental stellar parameters. Unfortunately, the Orion cluster is relatively distant (∼420pc), crowded and projected over the bright M42 HII region. Those factors make the Orion Nebula cluster a problematic target for Spitzer, while ground-based mid-IR observations having adequate spatial resolution attain low sensitivity limits longward than $\simeq 3.5\mu$m (Robberto et al. 2005; Smith et al. 2005). On the other hand, there are other closer regions that have been extensively investigated by Spitzer, but none of them has been studied with the HST with comparable detail. Among them, the Chamaeleon I region is possibly the best site for combining the unique Spitzer and HST capabilities. It is one of the nearest star-forming regions (d=160-170 pc; for a review see Luhman 2008b) and nearly coeval to Orion (Da Rio et al. 2010, age ∼2 Myr,), making its low-mass members approximately 10 times brighter than Orion. The cluster is young enough that it retains a significant population of primordial disks, but it is old enough that most of its members are no longer highly obscured by dust (typically $A_V < 2$). Like Orion, because of the relatively low extinction, optical wavelengths are accessible for the spectral classification of the stellar population (Comerón et al. 2004; Luhman 2004, and references therein) and for measuring accretion diagnostics (Mohanty et al. 2005; Muzerolle et al. 2005). Optical and near-IR imaging and spectroscopic surveys of Chamaeleon I have produced an extensive and virtually complete census of the stellar and substellar cluster members in the field (Luhman 2007): there are 237 known members, 33 of which have spectral types indicative of brown dwarfs ($> M6$). The IMF of Chamaeleon I reaches a maximum at a mass of 0.1-0.15 $M_{\odot}$, somewhat lower than the IMF peak in Orion.

In this paper we report on a study aimed at probing a sample of Chamaeleon I sources with the Wide Field Planetary Camera 2 (WFPC2) onboard HST. Given the extent of region, about 5.5° × 1.5°, we targeted selected fields centered on brown dwarfs, class I and II Pre-Main-Sequence (PMS) objects measured by Spitzer to uncover substellar companions down to 15 AU separation and to directly image circumstellar disks and jets. We concentrate here on the sample of stellar PMS objects, leaving the discussion of the brown dwarf survey to a second paper (Luhman et al., in preparation). In Section 2 we illustrate our observing and data reduction strategy, detailing the extraction of photometry for both point sources and extended objects. In Section 3 we present the HST photometry, complemented by a compilation of IR and millimeter data available in the literature, including new data in the sub-mm range for 3 sources. We also list the main physical parameters of the stellar sources taken from the literature and derive mass accretion rates from our Hα photometry. In Section 4 we illustrate the morphology of individual objects, while in Section 5 we model the SEDs for 19 sources using a SED fitting tool; we derive disk parameters that can be compared wih stellar mass, age, luminosity and mass accretion rate. Finally, in Section 6 we summarize our findings.

A.3 Observations

A.3.1 HST Data Acquisition and Reduction

The data presented in this paper have been obtained with the Wide Field Planetary Camera 2 (WFPC2) onboard the Hubble Space Telescope (HST) in early 2009 (HST GO program 11983, P.I. Robberto). These are among the latst data taken with the aging instrument, just preceeding the Servicing Mission 4 which replaced WFPC2 with WFC3.

We targeted 20 fields centered on T Tauri stars, detecting 18 of them[1].

---

[1] The HST archive contains four other fields, centered on 2MASSJ11095493-7635101,

For two sources, ISO-ChaI 150 and Cha J11081938-7731522, known for being highly obscured by circumstellar dust (Cambresy 1998; Luhman 2007), we can only provide detection upper limits. Other 13 members of the Chamaeleon I complex lying in our imaged fields have also been identified and are presented in this paper. One HST orbit was dedicated to each field, placing the target on the standard aperture spot of the WFPC2 Planetary Camera (PC) chip, with 45.5 mas/pixel scale. We did not constrain the telescope roll angle.

Observations were carried out in the narrow-band filters F631N ([OI] λ6300) , F656N (Hα), and F673N (centered on the [SII] $\lambda\lambda$6716, 6731 doublet), plus the F547M medium-band filter roughly corresponding to the Johnson V-band. The single exposure times were set at 100 s (F631N), 40 s (F656N), 100 s (F673N) and typically 40 s for the F547M filter (only for the brightest stars the F547M were shorter to prevent saturation) with four exposures per filter taken in two groups of two. Each group was centered at a slightly different position ("two-point dither") for optimal bad pixels and cosmic ray rejection (Burrows & U.S.).

Each set of four images was processed by the OPUS pipeline and combined using the MultiDrizzle software (Fruchter & et al. 2009). We used the MultiDrizzle parameters recommended for two-point dithered observations, treating separately the PC chip from the other 3 Wide Field (WF) chips, due to the different pixel scale.

A.3.2 Source Identification and Photometry

The images processed by MultiDrizzle are corrected for geometric distortion introduced by the WFPC2 optics, cleaned from bad pixels and cosmic rays, and recombined into a single integrated image properly oriented in Right Ascension and Declination. We used STARFIND (in the STSDAS library of PYRAF) to determine the location on the CCDs of all sources in the field.

After visually inspecting each individual source to reject false identifications we performed aperture photometry with DAOPHOT using a circular aperture of 3 pixels in radius (corresponding to $0\farcs137$ on the PC and $0\farcs299$ on the WF chips). The small extraction radius was chosen to optimally estimate the magnitude of weak sources, the large majority. We did not

---

HN10E, ISO235 and ISO79. They have been observed but the images appear compromised and have not been used in this work.

perform PSF photometry due to the non-negligible Charge Transfer Inefficiency trails of the aging instrument. Since the values of the zero points derived from the PHOTOFLAM keyword refer to counts measured within an "infinite" aperture[2], we performed an aperture correction to convert the counts measured in our 3 pixel extraction radius to the value expected in the $0\farcs5$ radius associated with the zero points. To this purpose we selected, for each filter and camera, a set of bright unsaturated and isolated sources and compared the results obtained with the two apertures. The average ratio, estimated with a sigma clipping algorithm, provided the aperture correction, together with the corresponding standard deviation. This allowed us to derive absolute magnitudes and errors in the HST STMAG system. For the narrowband filters we derived the flux in the more appropriate PHOTFLAM (erg $\mathrm{cm}^{-2}\mathrm{s}^{-1}\text{Å}^{-1}$) system (for the conversion from counts to flux see Baggett 2002). Finally, we applied a correction for Charge Transfer Efficiency (CTE) loss following Dolphin (2009).

A direct measure of the FWHM reveals that a number of sources are extended. To discriminate between extended and non-extended sources, we used the set of bona-fide point sources to build average Point Spead Functions valid for the PC and WF cameras. The FWHM of these PSFs turned out slightly larger than the theoretical FWHM provided by the HST PSF simulator Tiny Tim (of the order of 2 pixels for both channels), as expected since MultiDrizzle cannot fully recover the optimal PSF with only two pointings. The photometry of extended sources was determined using extraction radii large enough to contain all the signal above $\simeq 3\sigma$ sky noise floor. We did not apply any corrections for CTE losses, as this is mostly relevant for small apertures.

A.3.3 Sub-mm and mm observations

As part of a larger project carried our with the Atacama Pathfinder EXperiment (APEX) and with the Australia Telescope Compact Array (ATCA) facilities, we obtained new millimeter wavelength data for three sources: ESO Hα-559 (source #10) , ISO-ChaI 10 (#5) and HH48 A (#7). The first two were observed with APEX, a 12-m submm telescope in Chile's Atacama desert, with the Large APEX BOlometer CAmera (Siringo et al. 2009,

---

[2] in the case of WFPC2 the flux in an infinite aperture is estimated to provide 1.096 times, i.e. a tenth of a magnitude, the counts measured in a $0\farcs5$ radius aperture.

LABOCA;) operating at the central frequency of 345 GHz (or 870 μm). The angular resolution of LABOCA is about 19 arcseconds and its total field of view is about 11 arcminutes. The observations, conducted under the project 086.C-0653, were carried out on 2010 October 20-21 for a total of 4.4 h (on source) for ESO Hα-559 and on 2010 October 29-30 for a total 4.8 h (on source) for ISO-ChaI 10. Atmospheric conditions were excellent, with a precipitable water vapor around 0.34 mm, corresponding to a zenith opacity of 0.18. The sky opacity was measured every hour with skydips. The pointing of the telescope was checked every hour on the nearby quasar PKS1057-79. The absolute flux calibration was performed by observing the secondary calibrator B13134 every one or two hours. The telescope focus was checked by observing the star η Carinae, at least once per day. The observations were performed on the fly mode with a rectangular scanning pattern. The data were reduced with the BOlometer Array Analysis Software, following the procedures described in Siringo et al. (2009). The total (flux) calibration error is about 20% and the rms noise level in the final maps was $\sim$5 mJy. We report a clear detection of the submm emission from ESO Hα-559, but only an upper limit could be derived from our data for ISO-ChaI 10.

HH 48 A was observed at 3.3 mm with ATCA and the new CABB digital filter bank, which provides a total continuum bandwidth of 4 GHz. Observations were carried out at a central frequency of 91.000 GHz (3.294 mm) on 2009 Oct 14. The ATCA array was in the hybrid H168 configuration, providing an angular resolution of about 3 arcsec at 3.3 mm. The gain was calibrated with frequent observations of 1057-797. The passband was calibrated using 1921-293, and the absolute flux scale was determined through observations of Uranus. The uncertainty on the ATCA calibrated flux is about 30% at 3.3 mm. The MIRIAD package was used for visibilities calibration, Fourier inversion, deconvolution and imaging. The rms noise on the ATCA map was about 0.45 mJy.

We also searched the literature finding seven more sources previously detected at wavelengths longer than 100 μm.All fluxes are reported in Table A.4, illustrated in the next section.

Table A.1: Main target list

Visit	HST Target	Source name
17	T14A	HH 48 IRS
18	ISO225	ISO-ChaI 225
19	OTS32	ISO-ChaI 232
20	T14	CT Cha
21	IRN	ISO-ChaI 150*
22	T47	HBC 584
23	CHSM15991	CHSM15991
24	CRHF574	ESO-Hα 574
25	CRHF569	ESO-Hα 569
26	CHAJ11081938-7731522	Cha J11081938-7731522*
27	2MASSJ10533978-7712338	2MASS J10533978-7712338
28	HN21E2	Hn 21E
29	T12	ISO-ChaI 10
30	T42	CED 112 IRS 4
31	T3A	SX Cha
32	T5	Ass Cha T 2-5
33	ISO252	ISO-ChaI 252
34	CHXR20	UX Cha
35	T16	Ass Cha T 2-16
36	CRHF559	ESO-Hα 559

* Main target not detected.

A.4 Results

A.4.1 Final source list and HST photometry

The location of our 20 WFPC2 fields, each composed of 3 WF images of $\sim 72\farcs8 \times 72\farcs8$ and 1 PC image of $\sim 36\farcs4 \times 36\farcs4$, is shown in Figure A.1. A few fields in the northern region appear partially superimposed, but they have been processed and analyzed separately. To facilitate data retrieval, in Table A.1 we provide, for each field, the original HST visit number (by order of execution) and target name reported by the HST data archive, together with the more common SIMBAD target name used in this paper.

Besides our 18 detected targets, other 13 objects previously known to

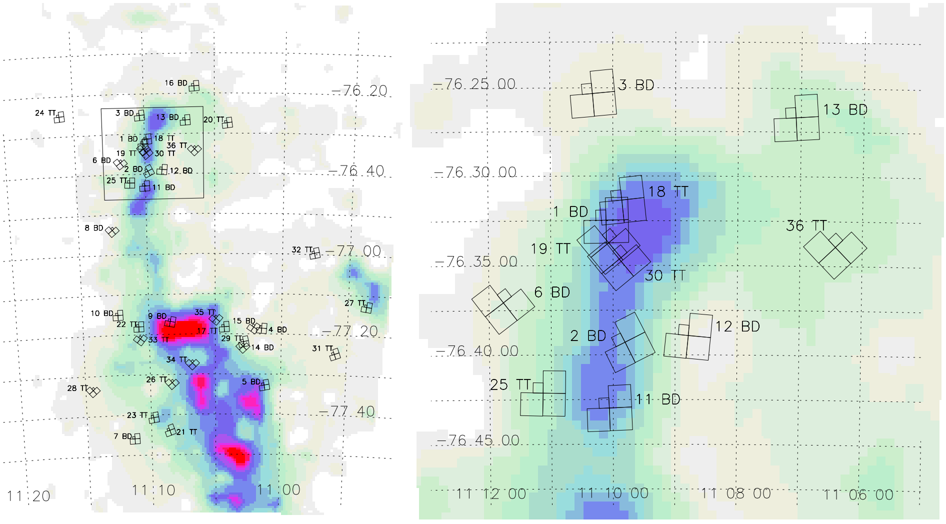

Figure A.1: All WFPC2 fields observed in our program superimposed to a map of the A$_J$ extinction in Chamaeleon I (Cambresy et al. 1997). The highest contour corresponds to $A_J = 10.7$ while the lowest contour to $A_J = 0$. The label of each field provides the visit number and a suffix, either TT (T Tauri star) or BD (Brown Dwarf), to indicate the nature of the primary target. In this paper we concentrate on the TT fields. The random orientation of the characteristic WFPC2 chevron pattern is due to unconstrained HST roll angle. For the association between HST visit and the corresponding target see Table 1.

be members of the Chamaeleon I association (Luhman et al. 2008) ended up in our imaged fields. For each of these 31 sources, Table A.2 provides: an entry number (column 1), the coordinate-based 2MASS source identifier, when available (column 2); an alternate ID taken from the literature(column 3); equatorial coordinates from the original fits header (column 4 and 5); the HST visit, and the (x,y) coordinates on the drizzled fits files (column 6 and 7). The accuracy of the celestial coordinates, driven by the absolute positions of the HST guide stars, is typically about 0.″25.

In Table A.3 we provide the WFPC2 photometry together with the photometric extraction area for extended sources. If a source is not detected we report the 3σ upper limit estimated over a 3 pixel aperture radius.

Table A.4 provides a compilation of near-IR photometric data for the 31 detected sources, either from the ground or from Spitzer (Luhman et al.

Table A.2: Observed members of the Chamaeleon I association

Nr	2MASS	SIMBAD	R.A. (J2000.0)	Decl. (J2000.0)	Visit	FITS COORD. (X-Y)
1	2MASS J10533978-7712338		10 53 39.78	-77 12 33.9	27	1674-2119
2		Ass Cha T 2-3 B	10 55 59.73	-77 24 39.9	31	1883-2291
3		SX Cha	10 55 59.76	-77 24 40.1	31	1837-2245
4	2MASS J10574219-7659356	Ass Cha T 2-5	10 57 42.20	-76 59 35.7	32	1705-2153
5	2MASS J11025504-7721508	ISO-ChaI 10	11 02 55.05	-77 21 50.8	29	1681-2143
6	2MASS J11040909-7627193	CT Cha	11 04 09.09	-76 27 19.4	20	1631-2084
7	2MASS J11042275-7718080	HH 48 A	11 04 22.69	-77 18 09.1	17	1545-1991
8		HH 48 B	11 04 23.31	-77 18 07.5	17	1502-2024
9	2MASS J11045701-7715569	Ass Cha T 2-16	11 04 57.01	-77 15 56.9	35	2346-2647
10	2MASS J11062554-7633418	ESO-Hα 559	11 06 25.55	-76 33 41.9	36	2382-2652
11	2MASS J11064510-7727023	UX Cha	11 06 45.10	-77 27 02.3	34	2381-2665
12	2MASS J11081648-7744371	Ass Cha T 2-34	11 08 16.49	-77 44 37.2	21	1551-577
13	2MASS J11081703-7744118	ISO-ChaI 137	11 08 17.03	-77 44 11.8	21	1534-832
14		Cha J11081938-7731522	11 08 19.38	-77 31 52.2	26	not detected
15		ISO-ChaI 150	11 08 37.1	-77 43 51	21	not detected
16	2MASS J11094525-7740332	ISO-ChaI 201	11 09 45.26	-77 40 33.3	23	983-972
17	2MASS J11094621-7634463	Hn 10E	11 09 46.21	-76 34 46.4	30	1349-996
18	2MASS J11095262-7740348	CHSM 15991	11 09 52.62	-77 40 34.9	23	1634-2091
19	2MASS J11095340-7634255	CED 112 IRS 4	11 09 53.41	-76 34 25.5	30	2401-2638
20	2MASS J11095437-7631113	ISO-ChaI 225	11 09 54.38	-76 31 11.4	18	1585-2054
21	2MASS J11100010-7634578	WW Cha	11 10 00.11	-76 34 57.9	19	1212-329
22	2MASS J11100369-7633291	ISO-ChaI 232	11 10 03.69	-76 33 29.2	19	2386-2684
23	2MASS J11100469-7635452	Cha T 2-45a	11 10 04.69	-76 35 45.3	30	704-405
24	2MASS J11102852-7716596	Hn 12W	11 10 28.52	-77 16 59.6	22	1366-1401
25	2MASS J11103481-7722053	[LES2004]* ChaI 405	11 10 34.81	-77 22 05.3	33	1274-426
26	2MASS J11104141-7720480	ISO-ChaI 252	11 10 41.42	-77 20 48.1	33	2313-2633
27	2MASS J11104959-7717517	HBC 584	11 10 50.00	-77 17 51.8	22	1463-1921
28	2MASS J11105076-7718031	ESO-Hα 568	11 10 50.77	-77 18 03.2	22	630-763
29	2MASS J11111083-7641574	ESO-Hα 569	11 11 10.83	-76 41 57.4	25	1494-1950
30	2MASS J11142454-7733062	Hn 21W	11 14 24.54	-77 33 06.2	28	2441-2862
31	2MASS J11142611-7733042	Hn 21E	11 14 26.11	-77 33 04.3	28	2328-2905
32	2MASS J11145031-7733390	BYB 53	11 14 50.32	-77 33 39.0	28	278-980
33	2MASS J11160287-7624533	ESO-Hα 574	11 16 02.88	-76 24 53.3	24	1558-2022

* López Martí et al. (2004).

Table A.3: Photometry with F547M, F631N, F656N and F673N filters

N	F547M [mag]	F631N [10^{-16} erg s^{-1} cm^{-2} Å^{-1}]	F656N [10^{-16} erg s^{-1} cm^{-2} Å^{-1}]	F673N 10^{-16} erg s^{-1} cm^{-2} Å^{-1}]	Notes
1	19.38 ± 0.18	~0.37	1.6 ± 0.9	1.1 ± 0.5	
2	16.14 ± 0.08	11 ± 3	37 ± 9	16 ± 4	
3	16.71 ± 0.03	15 ± 0.8	66 ± 4	15.6 ± 0.8	extended; $0''.5$ aperture
4	14.80 ± 0.03	31.2 ± 1.7	195 ± 10	40 ± 2	binary; $0''.5$ aperture
5	16.25 ± 0.08	10 ± 3	62 ± 14	12 ± 3	
6	13.00 ± 0.07	>230	>770	>250	companion; $0''.5$ aperture
7	17.89 ± 0.03	4.1 ± 0.3	17.4 ± 1.1	3.8 ± 0.2	disk; $0''.5$ aperture
8	21.3 ± 0.3	0.32 ± 0.16	2.8 ± 0.8	0.44 ± 0.11	disk; $1''$ aperture
9	18.91 ± 0.04	1.75 ± 0.15	3.4 ± 0.4	2.27 ± 0.16	extended; $0''.5$ aperture
10	20.7 ± 0.3	~0.35	~1.3	~0.43	
11	14.78 ± 0.07	88 ± 18	130 ± 30	100 ± 20	
12	16.53 ± 0.05	11 ± 3	27 ± 5	15 ± 3	
13	18.51 ± 0.11	1.7 ± 0.7	5.3 ± 1.7	2.4 ± 0.8	
14	>24	<0.035	<0.14	<0.023	
15	>24	<0.037	<0.15	<0.025	
16	19.94 ± 0.02	0.62 ± 0.06	2.4 ± 0.2	0.86 ± 0.06	
17	18.41 ± 0.10	2.6 ± 0.9	20 ± 4	3.4 ± 1.0	
18	21.47 ± 0.09	0.20 ± 0.04	0.32 ± 0.13	0.24 ± 0.03	
19	19.50 ± 0.11	2.9 ± 0.2	9.85 ± 0.7	2.15 ± 0.15	extended; $0''.5$ aperture
20	21.6 ± 0.5	~0.13	~0.33	~0.17	
21	14.10 ± 0.02	148 ± 8	650 ± 30	1.49 ± 8	extended; $1''$ aperture
22	18.78 ± 0.14	2.6 ± 1.0	4.6 ± 1.8	4.2 ± 1.3	
23	14.68 ± 0.03	70 ± 12	94 ± 17	81 ± 13	
24	17.93 ± 0.09	2.8 ± 1.0	8 ± 2	3.5 ± 1.0	
25	20.9 ± 0.3	~0.34	~1.2	~0.52	
26	~22.4	~0.094	2.4 ± 1.2	~0.13	
27	16.64 ± 0.08	10 ± 3	49 ± 11	13 ± 3	
28	18.27 ± 0.03	2.72 ± 0.18	6.3 ± 0.5	3.4 ± 0.2	
29	20.28 ± 0.14	0.21 ± 0.15	2.4 ± 0.7	0.35 ± 0.12	disk; $1''$ aperture
30	18.20 ± 0.12	2.5 ± 1.0	25 ± 6	3.8 ± 1.2	
31	20.7 ± 0.3	~0.28	~0.88	~0.34	
32	<15	67 ± 4	99 ± 5	78 ± 4	
33	19.60 ± 0.07	1.28 ± 0.18	2.7 ± 0.6	1.96 ± 0.18	disk; $1''$ aperture

2008; Luhman & Muench 2008). We also list fluxes at 0.87 mm, 1.3 mm and 3.3 mm from previously published data (Belloche et al. (2011), using APEX/LABOCA at 870 micron and $\approx 19''$ angular resolution; Henning et al. (1993), using SEST at 1.3 mm and $\approx 23''$ angular resolution), together with our new data for 3 sources (see Section 3.2). The appropriate reference for each individual source is given in the Appendix.

In Table A.5 we present a compilation of the main physical parameters of the stellar sources (spectral type, effective temperature, extinction and bolometric luminosity) reported in the literature, together with the equivalent width of the $H\alpha$ line, accretion luminosity and mass accretion rate, estimated as follows. We have computed for each star the photospheric continuum in the F656N filter and subtracted it from the measured flux. The continuum has been evaluated performing synthetic photometry. The set of *BT-Settle* synthetic spectra of Allard et al. (2011) was first interpolated at the $T_{\rm eff}$ of each source and then reddened using the A_J from Luhman (2007). For each spectrum we computed the photospheric $(F547M - F656N)$ color; then using the measured F547M magnitude as a reference, we rescaled the photometry to observed fluxes to derive the photospheric continuum F656N$_0$. The Equivalent Width (E.W.) of the H_α excess was then derived from the ratio between the flux excess and the continuum, multiplied by the equivalent width of the F656N filter profile. We converted the H_α excess in units of stellar luminosity by estimating the fraction of stellar (photospheric) flux entering in the F656N filter window, using once again the BT-Settle spectra. Then, knowing the bolometric luminosity of the sources from (from Luhman 2007, see Table 4), we derived the H_α excess in units of solar luminosity $L_\odot$. The H_α luminosity can be then related to the overall accretion luminosity $L_{\rm accr}$ assuming the formula from De Marchi et al. (2010):

$$\log L_{\rm accr} = 1.72 + \log L_{H\alpha} \tag{A.1}$$

and therefore the mass accretion rates using the relationship Gullbring et al. (1998):

$$L_{\rm accr} \simeq 0.8 \cdot \frac{GM_* \dot{M}_{\rm acc}}{R_*} \tag{A.2}$$

under the assumption that the mass infall onto the stellar surface starts from a distance of about 5 stellar radii.

Table A.4: IR and sub-mm photometry

N.	R^a [mag]	I^b [mag]	J^c [mag]	H^c [mag]	Ks^c 3.6 μm [mag]	4.5 μm [mag]	5.8 μm [mag]	8.0 μm [mag]	24 μm [mag]	$F_{0.87mm}$ [mag]	$F_{1.3mm}$ [mJy]	$F_{3.3mm}$ [mJy]
1		15.56 ± 0.06	13.28 ± 0.03	12.14 ± 0.02	11.58 ± 0.02	11.49 ± 0.02	11.09 ± 0.02	10.60 ± 0.03	9.76 ± 0.04	5.28 ± 0.04		
2		12.35 ± 0.02										
3		12.35 ± 0.02	10.65 ± 0.02	9.84 ± 0.02								
4		12.17 ± 0.03	10.43 ± 0.02	9.56 ± 0.02	9.25 ± 0.02	8.74 ± 0.02		8.07 ± 0.03		4.35 ± 0.04		
5	15.17 ± 0.05	13.40 ± 0.05	11.56 ± 0.03	10.86 ± 0.03	10.45 ± 0.02	9.78 ± 0.02		9.20 ± 0.03	8.65 ± 0.03	5.90 ± 0.04	<14.8	
6			9.71 ± 0.02	8.94 ± 0.05	8.66 ± 0.02					2.44 ± 0.04		
7			16.42^d	14.32^d	12.54^d	10.06 ± 0.02	9.23 ± 0.02	8.25 ± 0.03	6.97 ± 0.04	3.47 ± 0.04		
8			18.43^d	15.66^d	13.85^d							
9	16.65 ± 0.05	14.68 ± 0.04	12.17 ± 0.02	10.97 ± 0.02	10.41 ± 0.02	9.80 ± 0.02	9.57 ± 0.02	9.18 ± 0.04	8.63 ± 0.04	6.11 ± 0.04		
10		15.88 ± 0.06	13.01 ± 0.03	12.01 ± 0.02	11.49 ± 0.02	10.83 ± 0.02	10.42 ± 0.02	10.07 ± 0.03	9.38 ± 0.04	5.34 ± 0.04	44.1	
11		12.07 ± 0.02	10.18 ± 0.02	9.20 ± 0.02	8.880 ± 0.019	8.51 ± 0.02	8.36 ± 0.02	7.93 ± 0.03	6.94 ± 0.04	4.45 ± 0.04		
12		13.12 ± 0.03	11.20 ± 0.03	10.34 ± 0.03	10.02 ± 0.02	9.78 ± 0.02	9.75 ± 0.02	9.73 ± 0.03	9.71 ± 0.03			
13		14.34 ± 0.04	11.79 ± 0.03	11.06 ± 0.03	10.67 ± 0.02	10.25 ± 0.02	10.18 ± 0.02	10.13 ± 0.03	10.15 ± 0.04			
16	18.02 ± 0.05	15.37 ± 0.06	12.36 ± 0.03	11.45 ± 0.02	11.03 ± 0.02	10.55 ± 0.02	10.40 ± 0.02	10.39 ± 0.03	10.39 ± 0.04	9.82 ± 0.18		
17		14.72 ± 0.05	11.95 ± 0.02	10.74 ± 0.02	10.05 ± 0.02	9.49 ± 0.02	8.92 ± 0.02	8.46 ± 0.03	7.59 ± 0.04	3.70 ± 0.06	1552	
18			16.05 ± 0.11	14.87 ± 0.07	14.13 ± 0.07	11.98 ± 0.02	11.37 ± 0.02	10.71 ± 0.03	9.87 ± 0.03	7.21 ± 0.05		
19	15.10 ± 0.05	13.52 ± 0.05	9.47 ± 0.02	7.79 ± 0.05	6.46 ± 0.03			3.72 ± 0.03	3.04 ± 0.03		71	
20		17.27 ± 0.12	15.05 ± 0.11	13.80 ± 0.10	13.14 ± 0.07	11.22 ± 0.02	10.35 ± 0.02	9.61 ± 0.07	8.70 ± 0.04	4.85 ± 0.04	<290	
21		10.95 ± 0.04	8.71 ± 0.03	7.21 ± 0.08	6.08 ± 0.05			3.70 ± 0.03	3.15 ± 0.04		1501	407.9
22		14.72 ± 0.05	11.77 ± 0.03	10.26 ± 0.02	9.44 ± 0.02	8.18 ± 0.02	7.52 ± 0.02	6.84 ± 0.03	6.04 ± 0.04	3.23 ± 0.04	<290	
23		12.39 ± 0.04	10.56 ± 0.02	9.64 ± 0.02	9.24 ± 0.02	8.70 ± 0.02	8.41 ± 0.02	8.10 ± 0.03	7.55 ± 0.03	4.58 ± 0.04		
24		13.97 ± 0.05	11.73 ± 0.02	11.11 ± 0.02	10.78 ± 0.03	10.37 ± 0.02	10.23 ± 0.02	10.26 ± 0.03	10.26 ± 0.04	10.00 ± 0.09		
25		15.61 ± 0.06	12.04 ± 0.02	10.72 ± 0.02	10.03 ± 0.02	9.60 ± 0.02	9.43 ± 0.02	9.42 ± 0.03	9.42 ± 0.04	9.19 ± 0.10		
26	20.06 ± 0.05	17.27 ± 0.05	13.86 ± 0.03	12.89 ± 0.03	12.27 ± 0.02	11.45 ± 0.02	11.02 ± 0.02	10.57 ± 0.03	9.75 ± 0.03	7.05 ± 0.04		
27		13.84 ± 0.05	11.15 ± 0.02	9.95 ± 0.02	9.17 ± 0.02		8.13 ± 0.02		6.37 ± 0.04	2.96 ± 0.04	44.95	
28	16.65 ± 0.05	14.50 ± 0.05	12.04 ± 0.02	11.10 ± 0.02	10.75 ± 0.02		10.26 ± 0.02		10.22 ± 0.05			
29		17.34 ± 0.12	15.95 ± 0.09	15.06 ± 0.09	14.58 ± 0.10	14.21 ± 0.03	13.76 ± 0.03	13.23 ± 0.06	12.50 ± 0.05	7.12 ± 0.04	72	
30		14.24 ± 0.04	11.98 ± 0.05	11.09 ± 0.05	10.65 ± 0.04	10.06 ± 0.04	9.84 ± 0.04	9.54 ± 0.04	8.96 ± 0.04	6.42 ± 0.04		
31		15.47 ± 0.05	12.76 ± 0.03	11.97 ± 0.03	11.49 ± 0.02	11.01 ± 0.04	10.89 ± 0.04	10.79 ± 0.06	10.57 ± 0.08			
32		11.83 ± 0.05	10.48 ± 0.03	9.75 ± 0.02	9.55 ± 0.02	9.35 ± 0.02	9.28 ± 0.02	9.26 ± 0.03	9.24 ± 0.03	9.06 ± 0.05		
33		17.25 ± 0.12	15.80 ± 0.07	14.97 ± 0.08	14.61 ± 0.11							

Data at $\lambda > 3.6\mu m$ are fromLuhman et al. (2008); Luhman & Muench (2008); Belloche et al. (2011); Henning et al. (1993) ; this paper.

a López Martí et al. (2004).

b López Martí et al. (2004); Second DENIS Release.

c 2MASS Point Source Catalog.

d Haisch et al. (2004), labeled as Cha I T14a

Table A.5: Source Physical Parameters

N	Sp. Type^a	T$_{eff}$ [K]	A$_J$ [mag]	L$_{bol}$ [L$_\odot$]	Hα excess E.W. [Å]	log L_{acc} [L$_\odot$]	log $\dot{M}_{acc}$ [M$_\odot$/yr]
1	M2.75	3451	0.63	0.032	11.9±23.5	-3.14±0.47	-10.3±0.5
2	M3.5	3342	0.79	0.42	8.5±9.4	-2.23±0.32	-8.8±0.3
3	M0	3850	0.79	0.42	122.8±10.8	-0.85±0.04	-7.8±0.1
4	M3.25	3379	0.34	0.33	47.5±5.8	-1.58±0.05	-8.2±0.1
5	M4.5	3198	0	0.081	75.0±24.6	-2.04±0.12	-8.8±0.1
6	K5	4350	0.45	0.95			
7	K7	4060	0.45	0.013	124.4±10.8	-2.23±0.04	-10.0±0.1
9	M3	3415	1.6	0.21	0.9±4.3	-3.49±0.77	-10.3±0.8
10	M5.25	3091	1.01	0.052	39.6±26.1	-2.56±0.22	-9.3±0.2
11	K6	4205	1.08	1.1	19.2±11.2	-1.05±0.20	-8.1±0.2
12	M3.75	3306	0.29	0.15	22.3±9.7	-2.28±0.16	-9.0±0.2
13	M5.5	3058	0.32	0.083	24.3±17.4	-2.63±0.23	-9.2±0.2
16	M5.75	3024	0.5	0.058	52.0±7.4	-2.44±0.06	-9.0±0.1
17	M3.25	3379	1.01	0.15	140.6±38.9	-1.39±0.11	-8.3±0.1
18	M3	3415	0.79	0.0029	21.7±20.8	-3.92±0.29	-11.6±0.3
19	K5	4350	1.47	3	202.1±27.6	0.44±0.05	-6.5±0.1
20	M1.75	3596	1.24	0.013	19.7±26.0	-3.29±0.36	-10.8±0.4
21	K5	4350	1.35	5.5	91.4±6.0	0.42±0.03	-6.6±0.1
22	K8	3955	2.14	0.66	13.7±17.0	-1.30±0.35	-8.7±0.3
23	M1	3705	0.54	0.43	10.2±7.0	-1.91±0.23	-8.9±0.2
24	M5.5	3058	0	0.066	28.5±14.8	-2.65±0.18	-9.2±0.2
25	M4	3270	1.91	0.32	19.5±19.4	-2.02±0.30	-8.6±0.3
26	M6	2990	0.97	0.022	599.2±369.4	-1.73±0.21	-8.6±0.2
27	M2	3560	1.17	0.42	49.0±18.3	-1.38±0.14	-8.2±0.1
28	M4.25	3234	0.81	0.11	12.9±3.8	-2.68±0.11	-9.4±0.1
29	M2.5	3488	0.68	0.003	98.8±40.9	-3.28±0.15	-10.9±0.2
30	M4	3270	0.72	0.11	136.5±43.6	-1.64±0.12	-8.4±0.1
31	M5.75	3024	0.56	0.042	34.8±26.0	-2.66±0.24	-9.5±0.2
32	M2.75	3451	0	0.24			
33	K8	3955	0.45	0.0034	82.9±25.5	-3.04±0.12	-10.99±0.11

a Luhman (2007); Luhman & Muench (2008).

A.5 Source Morphology as Revealed by HST Data

In this section we illustrate our findings on the only 10 sources that appear either extended, binaries, or associated with jets and Herbig-Haro objects in the immediate vicinity. The other 23 sources appear point-like in our images. Our dataset is not homogeneous because of two main factors: a) the different sampling scales of the WFPC2 pixels (about 50 mas/pixel for the PC chip, where the main targets were located, vs. 100 mas/pixel for the WF chips where most of the other sources are found); b) the presence of CTE tail, which depends on the position and brightness of the source on the chip. To mitigate the risk of misinterpreting extended features, we have indicated the direction of the CTE deferred-charge trails with an arrow in each image. For the brightest sources, i.e. Ass Cha T2-16 (#9), CED 112 IRS4 (#19), and WW Cha (#21), we have also plotted on each image the isophotal contours of the corresponding PSF, for an immediate comparison. All images shown have the standard orientation with North up and East to the left.

SX Cha (#3)

The T Tauri star SX Cha, spectral type M0.5 (Lawson et al. 1996), has a companion of comparable brightness ∼$2''.1$ at P.A.∼310° (Natta et al. 2000). Spitzer data show the characteristic amorphous silicate emission of circumstellar disks at 10 and 20 μm, whereas the spectral features observed in the 33-35 μm range are characteristic of crystalline enstatite and forsterite grains (Kessler-Silacci et al. 2006). Our HST images (Fig. A.2) show SX Cha (source on the left) with its companion at ∼$2''.2$ (350 AU) distance. The protuberance on the western side of SX Cha visible in the F673N ([SII]) image with a length of ∼$0''.55$ (87 AU), cannot be attributed to the CTE losses. The line intensity, together with the narrow and twisted morphology, suggests that it is a collimated jet. In this case, the circumstellar disk surrounding SX Cha would be oriented somewhat perpendicularly to the plane of the binary orbit.

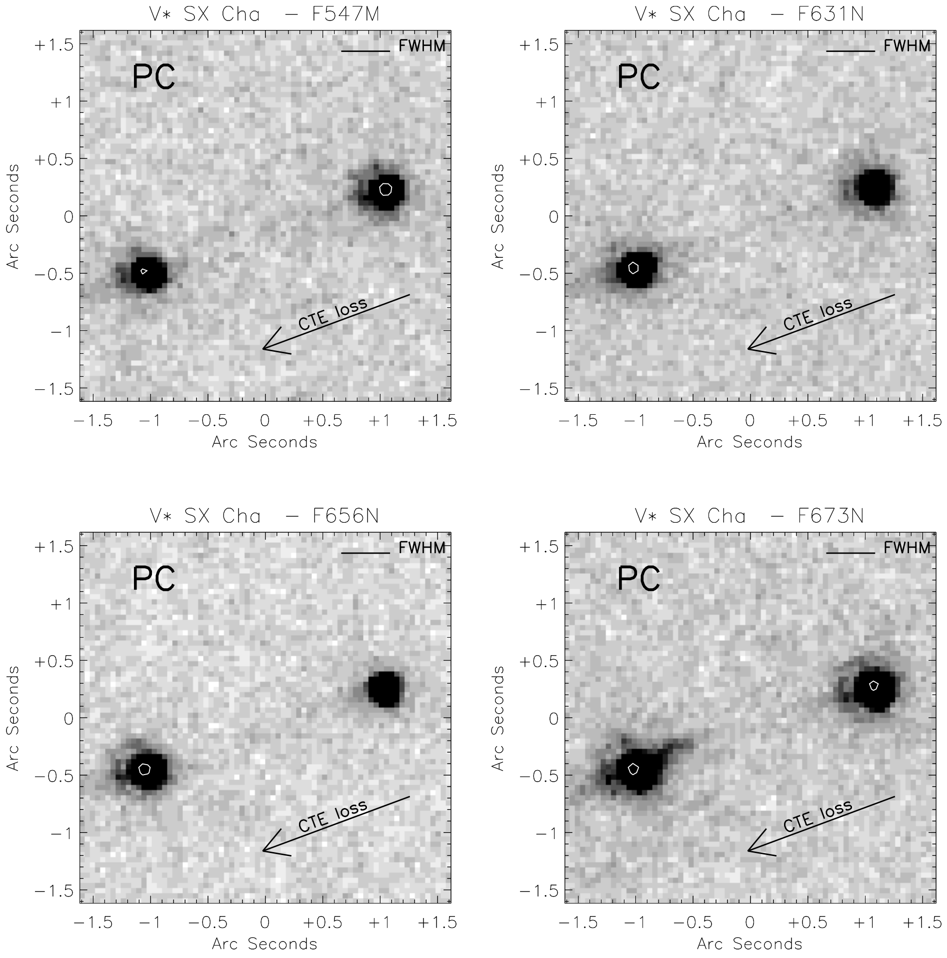

Figure A.2: SX Cha observed in the PC chip (45.5 mas/pixel scale). Image centered at R.A.=10:55:59.53, Decl.=-77:24:40.3 (J2000.0).

Ass Cha T 2-5 (#4)

Detected for the first time by Schwartz (1977), Ass Cha T 2-5 has spectral type M3.25 according to Luhman (2007). Our images (Fig. A.3) resolve this source in a close binary with separation $\simeq 0\farcs15$, corresponding to $\sim$25 AU projected distance at 160pc. The southern star appears brighter in all filters with the exception of Hα, where the northern source strongly dominates. This may indicate that the northern component has been observed in a phase of strong accretion activity. The ratios between the peak counts of the northern vs. the southern star are approximately 0.57 (V-band), 0.89

([OI]), 2.8 (Hα) and 1.1 ([SII]).

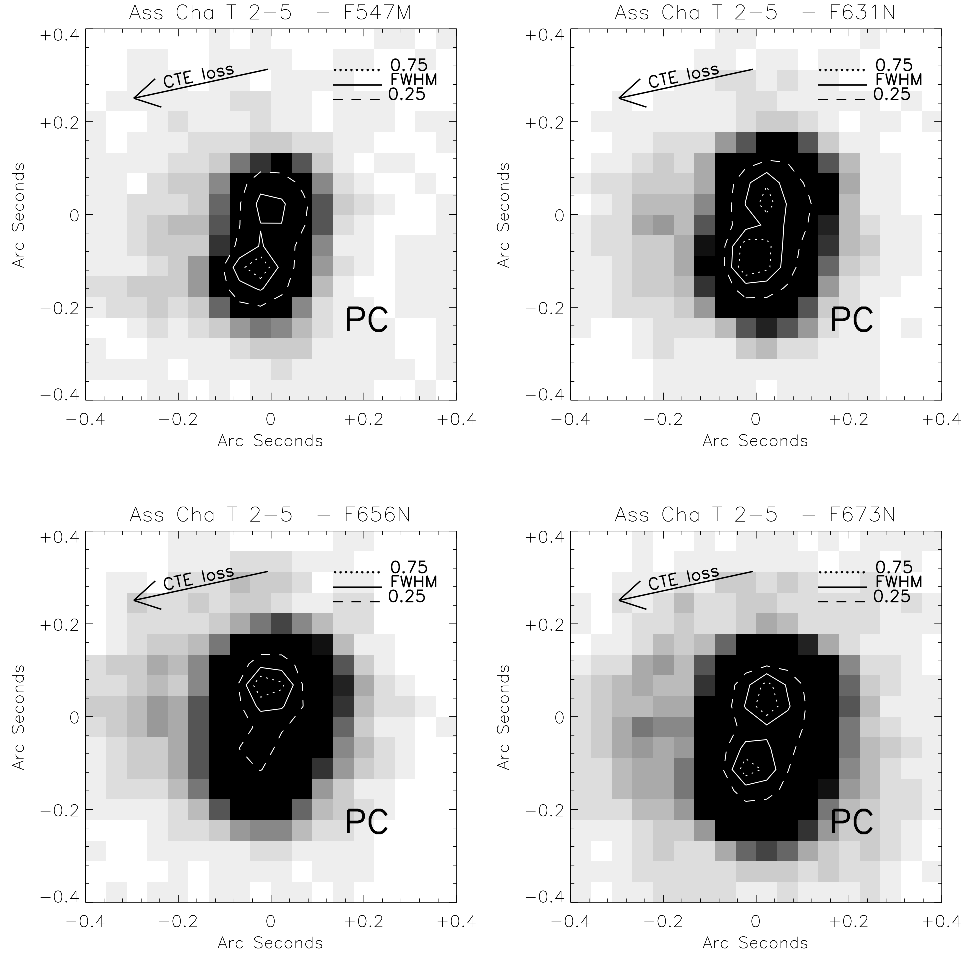

Figure A.3: Ass Cha T 2-5 observed in the PC chip. The countours levels are given 0.75, 0.5 and 0.25 of the peak counts. Image centered at R.A.=10:57:42.22, Decl.=-76:59:36.4 (J2000.0).

CT Cha (#6)

CT Cha has been initially classified as an emission-line star because of its Hα line variations (Henize & Mendoza v 1973) and later as a classical T Tauri star on the basis of its strong IRAS excess (Gauvin & Strom 1992). ISO data have shown evidence of silicate emission in a circumstellar disk (Natta et al. 2000). The variations of Hα line emission have been interpreted as accretion signatures by Hartmann et al. (1998), compatible with early observations of spectral veiling (Rydgren 1980). More recent observations of CT Cha have revealed the presence of two faint companions close to the star (Schmidt et al. 2008). The first (source C1), about 6.3 mag fainter than the primary in the Ks-band, is located $2''\!.670 \pm 0''\!.038$ at P.A.$\sim$315° of the star, corresponding to $\sim$430 AU projected distance at 160 pc. The second (C2) is about $2''$ at P.A.$\sim$45° of the primary. Schmidt et al. (2008) classified C1 as physically associated with the primary due to its common proper motion, whereas for C2 they concluded that it must be a background object. In our PC images (Fig. A.4) source C1 is not detected while C2 is clearly visible at $1''\!.96\pm0''\!.05$ projected distance (Fig. A.5, right). We have found on the ESO data archive an H-band image taken with NACO in February 2006 in which only C1 is visible (Fig. A.5, left). A second image taken two years later, also with NACO but in the Ks filter, shows both C1 and C2, with C2 at a distance of $1''\!.91\pm0''\!.03$ from the primary (Fig. A.5, center). Source C2 in our images is visible only in the [OI] and [SII] filters (Fig. A.5, right). This, together with the fact that C2 (like source C1) has not changed position seems to indicate that it is indeed physically associated with V* CT Cha. Its nature, however, remains enigmatic. Finally, the point-like source in the [OI] image about $1''\!.5$ to the south of the main source may be real, as it cannot be easily attributed to a filter ghost.

HH 48 A and B (#7, #8)

The classic Herbig-Haro object HH 48 (Schwartz 1977) is composed by two close condensations, designated as HH 48 A and HH 48 B. Wang & Henning (2006) found that HH 48 A and B are elongated in directions that are roughly perpendicular, while a set of newly detected features (labeled C to F) are aligned along a direction pointing to HH 48 A. This suggests the presence of two outflows driven from an embedded source, probably a binary star (Bally et al. 2006). Our images (Fig. A.6) show only HH 48 A and B, i.e. HH 48 C-F are not detected. In all filters, HH 48 A appears as a bright point source associated with faint extended emission. While the elongation on the East side may be contaminated by CTE losses, the elongation on the West side is unambiguous. HH 48 B, located at $\sim 2''\!.5$ (400 AU) to the northeast of HH 48 A, is fainter and elongated nearly east-west, with a length of $\simeq 0.7''$, in the V-band filter. In the [OI] and Hα filters, however, it appears nearly

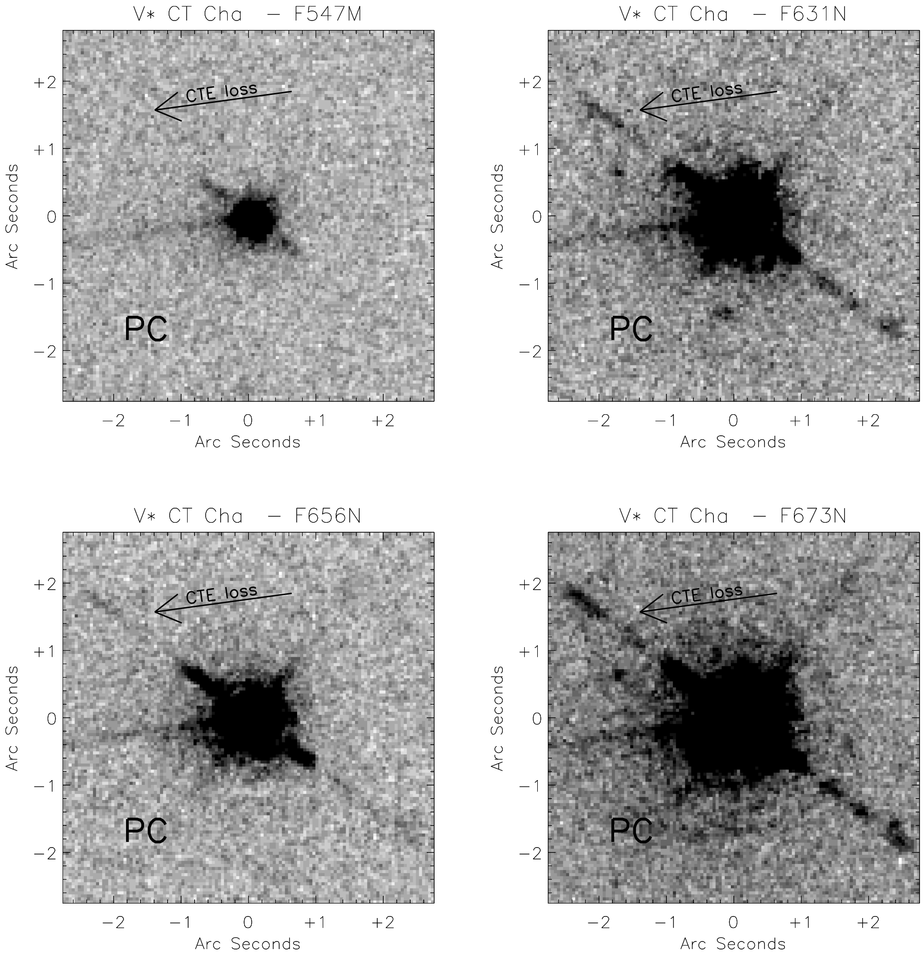

Figure A.4: CT Cha observed in the PC chip. Image centered at R.A.=11:04:09.00, Decl.=-76:27:19.5 (J2000.0).

unresolved. We speculate that the morphology of HH 48 B is compatible with the presence of a disk seen nearly edge-on, as the V-band elongation could be attributed to scattered light from a disk face, whereas the fainter line emission could arise from the inner disk region. Overall, our HST images confirm that HH 48 A and B point to different directions, forming an angle close to ∼30°.

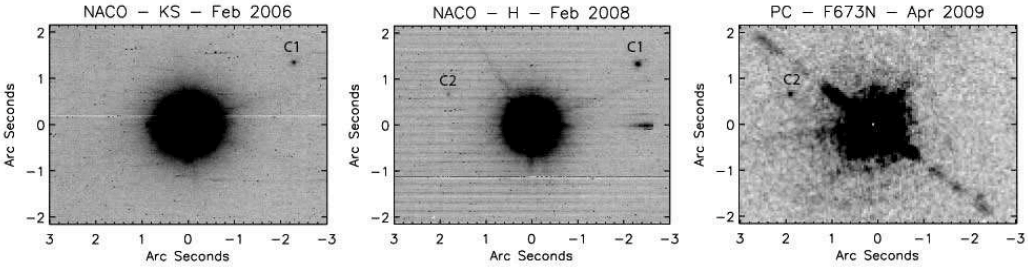

Figure A.5: CT Cha and the probable companions "C1" and "C2" (NACO's images from the ESO's archive and PC image). Our detection upper limits for source "C1" are: F547M: $m > 22.7$; F631N: $F_\lambda < 7.0 \times 10^{-19}$ erg cm^{-2} s^{-1} Å^{-1}; F656N: $F_\lambda < 2.8 \times 10^{-18}$ erg cm^{-2} s^{-1} Å^{-1}; F673N: $F_\lambda < 4.6 \times 10^{-19}$ erg cm^{-2} s^{-1} Å^{-1}.

Ass Cha T 2-16 (#9)

This source has been classified as a M3 emission-line star with a mass of $\sim$0.26 $M_\odot$ (Lafrenière et al. 2008). Our images (Fig. A.7) indicate that Ass Cha T 2-16 has been resolved by the HST, in particular in the [OI] where the FWHM$\simeq$4 pixels is twice the size of the FWHM of unresolved sources. The SED of this source is shown in Section A.6.

CED 112 IRS 4 (#19)

CED 112 IRS 4 is a T Tauri star located in a region rich of HH objects and circumstellar emission. Wang & Henning (2006) suggested that one of these objects, HH 914, $\sim 24''$ to the east of CED 112 IRS 4, is driven by it (see Fig.3 of Wang & Henning 2006, , where CED 112 IRS 4 is indicated as Sz 32). Recent ATCA data at 16mm show a large contribution to the 16mm flux of CED 112 IRS 4 from free-free emission (Lommen et al. 2009). Our HST images (Fig. A.8) clearly show that the source is much brighter in the three narrow-band line filters than in the broad V-band. In particular, the narrow band images consistently show a feature protruding eastward, which we interpret as the HH 914 object of Wang & Henning (2006). The Hα image is especially remarkable, as in this filter HH 914 is most clearly detached, showing as a second peak $\sim 0''.30$ (47 AU) to the East about 7.6 times fainter than the primary one. The elongation in the V-band to the northeast is most probably due to CTE losses. The SED of this source is shown in Section A.6.

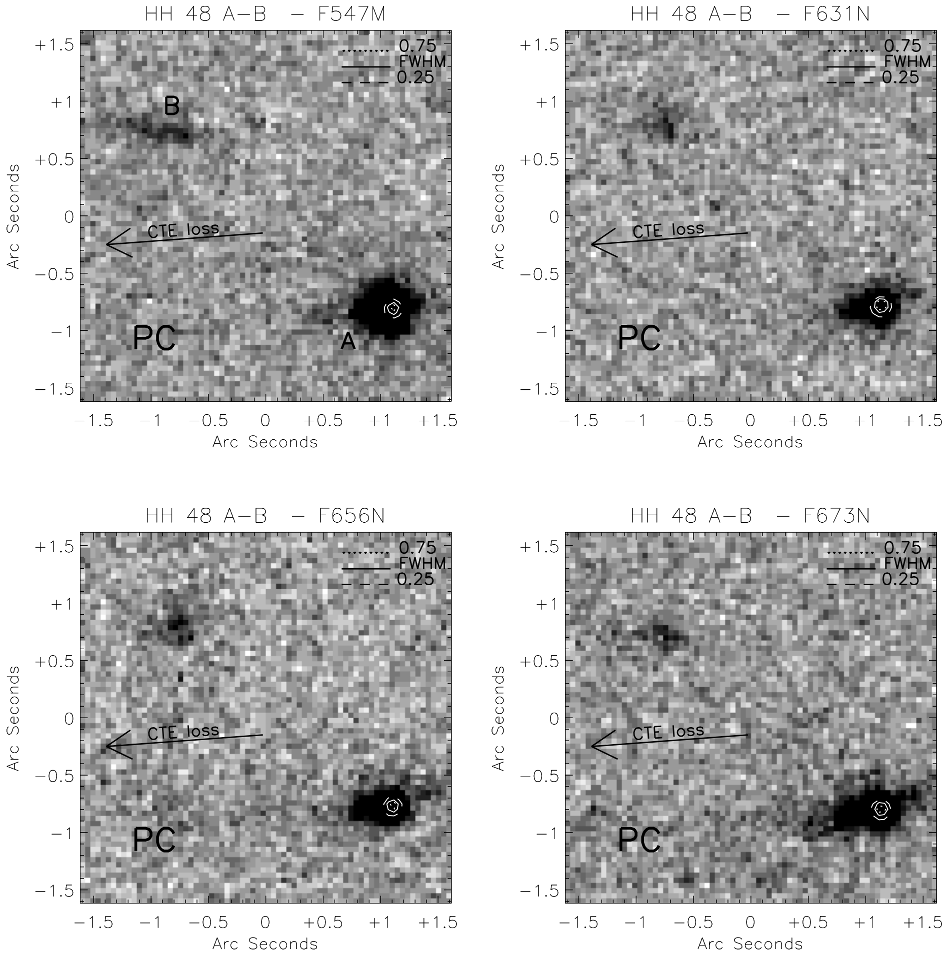

Figure A.6: HH 48 A and B observed in the PC chip. Image centered at R.A.=11:04:23.04, Decl.=-77:18:08.3 (J2000.0).

WW Cha (#21)

WW Cha, a K5 T Tauri star in the vicinity of the previous source CED 112 IRS4 (Schegerer et al. 2006), is thought to drive the highly collimated jets HH 915. Bally et al. (2006) report the presence of a giant bow shock, HH 931, about 13′ further away from WW Cha at P.A.∼135°, in the same direction of HH 915. Wang & Henning (2006) suggest that two near-infrared H_2 emission knots, A and D, detected by Gómez et al. (2004) on the opposite side of WW Cha may represent the counter-jet of HH 915. There is finally a faint chain of Hα knots which links the brightest part of the bow shock to

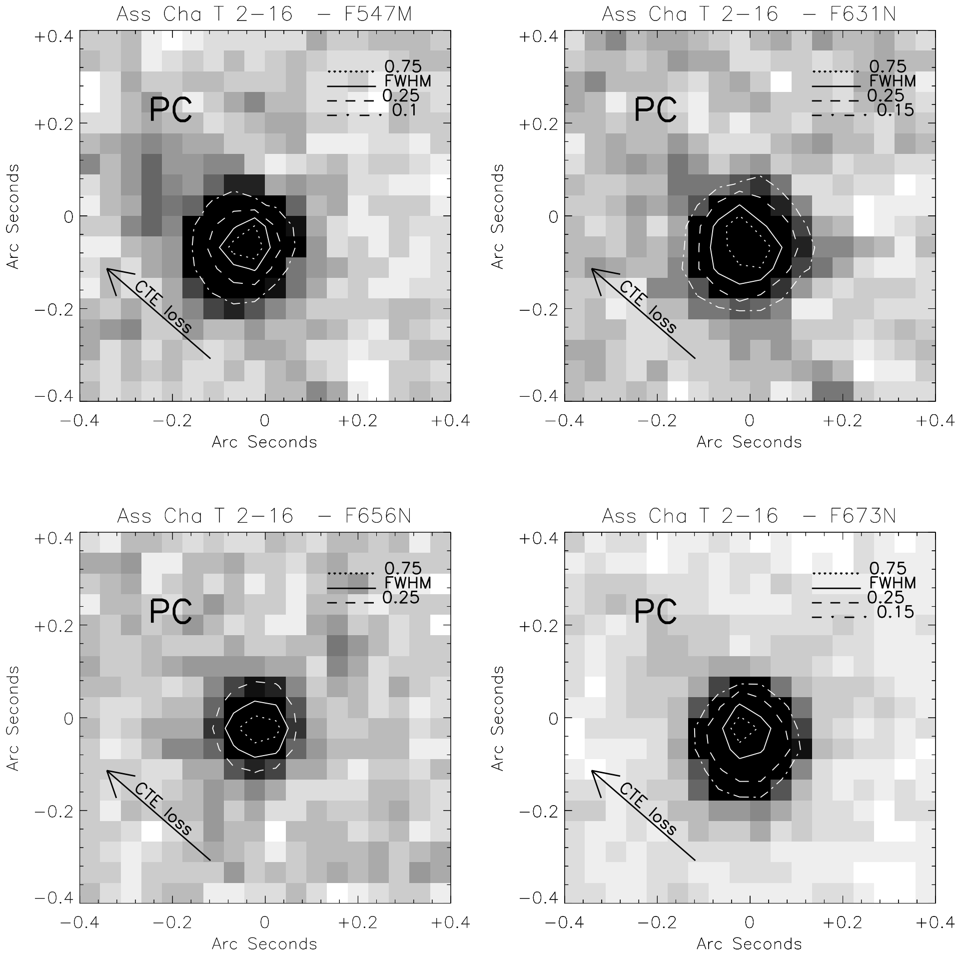

Figure A.7: Ass Cha T 2-16 observed in the PC chip. Image centered at R.A.=11:04:57.01, Decl.=-77:15:57.3 (J2000.0). The insets at the bottom-left corner show the contours for the typical PSF.

the southern side of the reflection nebula illuminated by WW Cha. Studies of the source variability at millimeter wavelengths indicate that the 16 mm flux is dominated by cm-size pebbles' emission, which makes WW Cha the second star known to have a protoplanetary disk containing grains of suche a large size (Lommen et al. 2009). Our images (Fig. A.9) do not show evidence of the rich HH phenomenology associated to this source. Hovewer, they show the bright core extended in the [SII] filter, with a FWHM contour elongated in the SE-NW direction. If the [SII] elongation traces shock emission, then the HH 915 objects would be co-aligned and part of the same jet system.

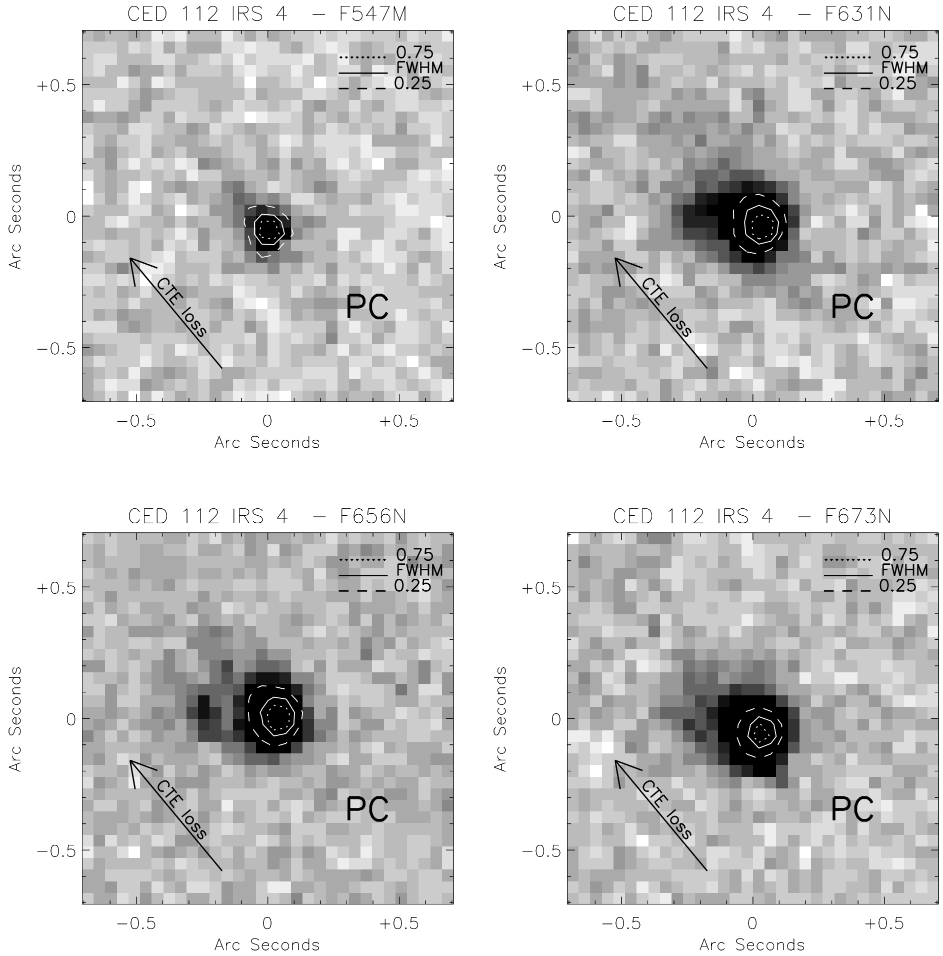

Figure A.8: CED 112 IRS 4 observed in the PC chip. Image centered at R.A.=11:09:53.35, Decl.=-76:34:25.5 (J2000.0). The insets at the bottom-left corner show the contours for the typical PSF.

The SED of this source is shown in Section A.6.

ESO-Hα 569 (#29)

ESO-Hα 569, spectral type M2.5, is a highly variable faint object with signatures of both accretion and outflow (Comerón et al. 2004). Also according to Comerón et al. (2004), the non-detection of this source in the mid-IR by ISOCAM (Persi et al. 2000) indicates that the amount of warm dust associated with this object is very small, meaning that its faintness cannot be

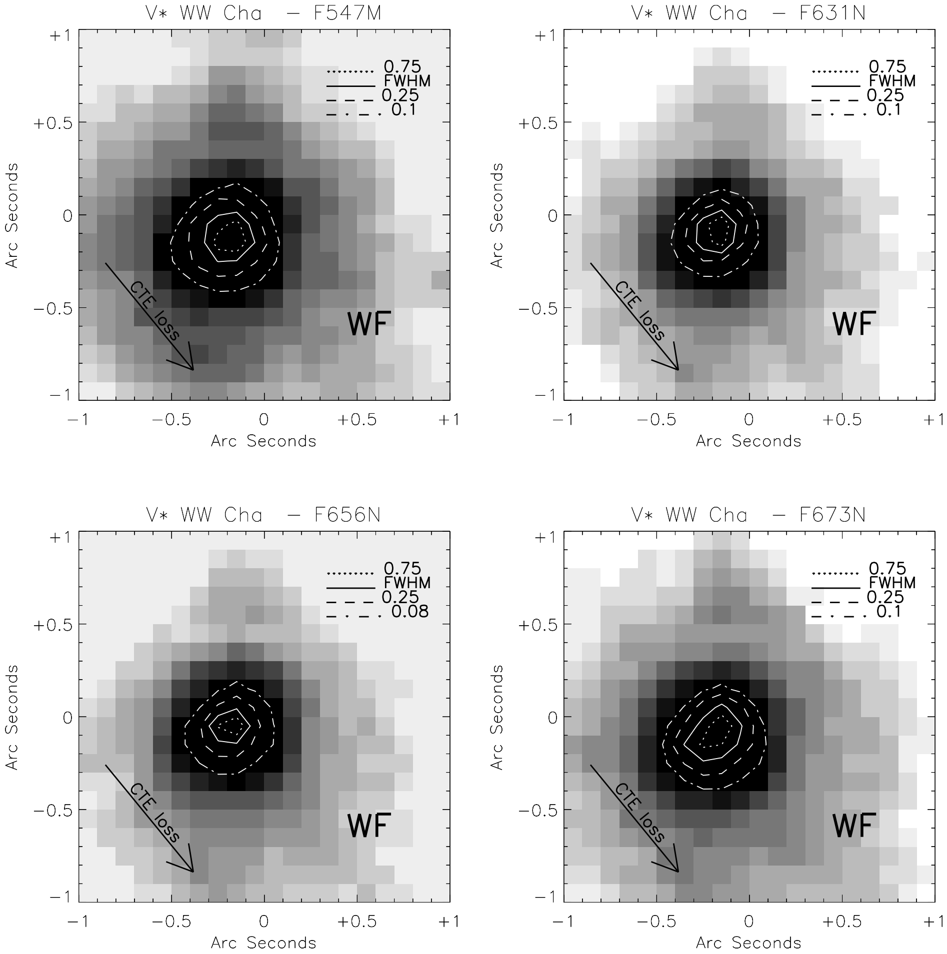

Figure A.9: WW Cha observed in the WF chip. Image centered at R.A.=11:10:00.03, Decl.=-76:34:57.3 (J2000.0). The insets at the bottom-left corner show the contours for the typical PSF.

attributed to occultation by circumstellar material. On the other hand, the more recent detection of this source with Spitzer (Luhman et al. 2005) and the X-ray images of Feigelson & Lawson (2004) support the presence of an edge-on disk (Luhman 2007). This source is located ∼22″ to the northeast of HH 919, an Herbig-Haro object that could be driven by a jet originated by ESO-Hα 569 (Bally et al. 2006). In our V-band and Hα images, ESO-Hα 569 (Fig. A.10) is just above our detection limit, but it appears extended in the V-band in the NW-SE direction. We do not detect HH 919, nor its associated bipolar jet.

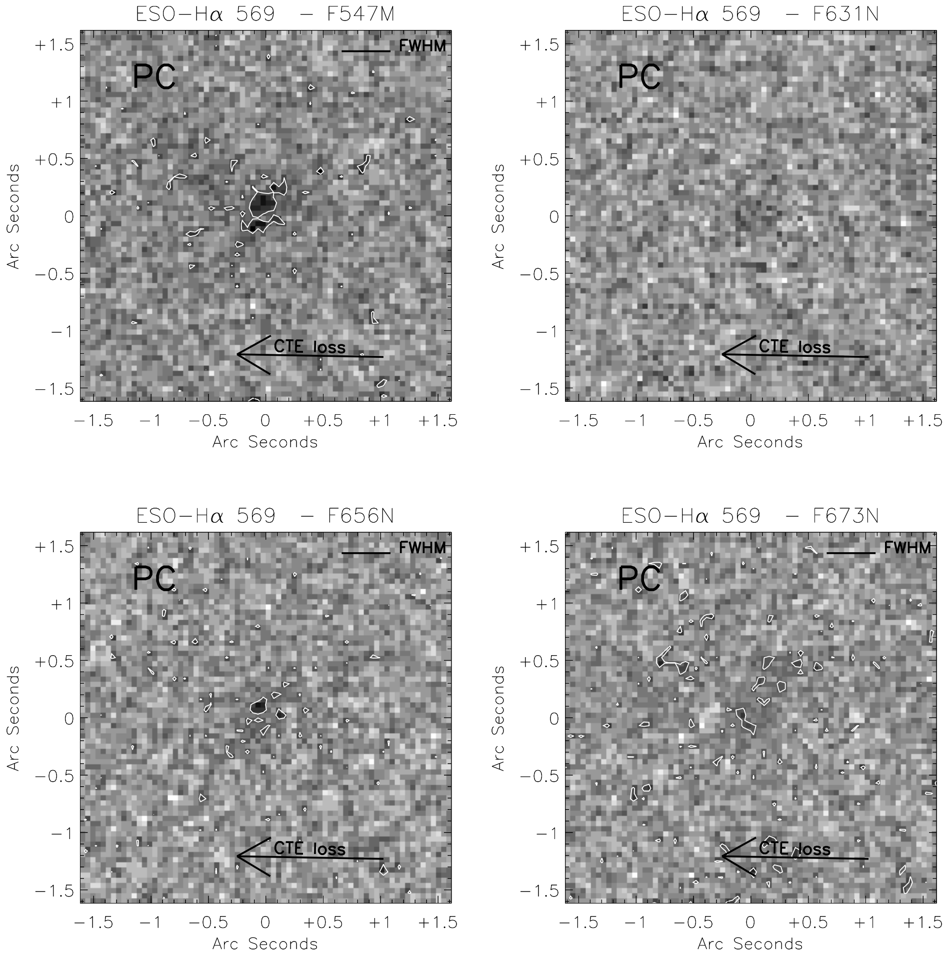

Figure A.10: ESO-Hα 569 observed in the PC chip. Image centered at R.A.=11:11:10.70, Decl.=-76:41:57.6 (J2000.0).

ESO-Hα 574 (#33)

ESO-Hα 574 was discovered by Comerón et al. (2004) as a very faint source with the characteristic colors of a lightly reddened late-type star. It has a rich emission-line spectrum dominated by the forbidden lines typically associated with stellar outflows. Comerón & Reipurth (2006) observed ESO-Hα 574 in the [SII] lines and with the low-resolution spectrograph at the ESO-VLT. They detected a well-developed jet (HH 872) protruding from the source and discussed the physical proprieties of the emitting source on the basis of the spectrum sampled at the base of the jet. Recently, Bacciotti et al. (2011)

have attributed the unusual low luminosity of the source in the continuum to the presence of an edge-on disk. Accounting for the disk obscuration on the luminosity of the accretion tracers, they estimate a mass accretion rate of $\sim 1.7 \times 10^{-8}$ $M_{\odot}$ yr^{-1}. They also independently derive a mass outflow rate in the jet knots of about 1.5×10^{-9}, leading to a mass ejection/accretion ratio over the two lobes of ~ 0.3. This is in the range expected for magneto-centrifugal jet launch (Cabrit 2009).

Our WFPC2 images of ESO-Hα 574 (Fig. A.11) resolve this source into a nearly edge-on disk. In the V-band the disk is bright and extends at P.A.$\sim$135°, reaching a length of $\sim 0\farcs6$ and a thickness, measured at the center of the disk, of $\sim 0\farcs4$. These values correspond to 96 AU and 64 AU, respectively, assuming a distance of 160 parsec. The disk and a faint trace of a jet are also detectable in the [OI] filter, whereas in the [SII] filter the jet is clearly visible, perpendicular to the disk and extended toward the northeast direction. We resolved knot A, previously detected by Comerón & Reipurth (2006), in three knots: the brightest one, knot A3, stretches $\sim 0\farcs9$ (144 AU) from the center of the disk. The second knot, knot A2, is $\sim 1\farcs1$ (176 AU) away from the disk. The third one, knot A1 (previously identified by Bacciotti et al. 2011), is visible at a distance of $\sim 2\farcs3$ (368 AU) from the disk and rather than being well collimated as knot A3 it appears bow-shaped. Our [SII] image does not show evidence of the southewestern counter-jet resolved by Bacciotti et al. (2011) in their position-velocity diagram, probably because of the relatively low sensitivity of the WFPC2/PC to diffuse structures. The SED of this source is shown in Section A.6.

A.6 Model fitting of the Spectral Energy Distributions

In order to estimate the main parameters of the star+disk systems combining the IR observations (mostly from Spitzer) with the constraints posed by our HST imaging survey we have used the online tool from Robitaille et al. (2006) to fit the Spectral Energy Distributions (SEDs) of a number of sources. The tool, based on a grid of 20,000 synthetic models, aims at reproducing the SEDs of disks around stars with masses between 0.1 and $50 M_{\odot}$ and ages between 10^3 and 10^7 years.

Consistently with these limitations, we have fitted only the SEDs of

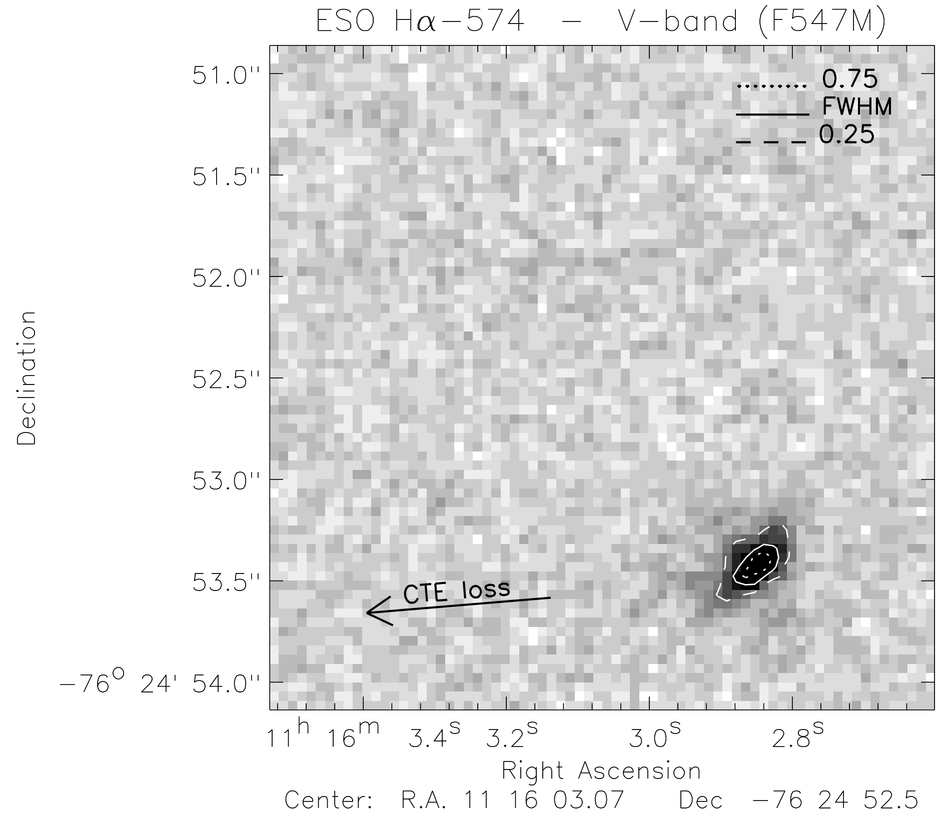

Figure A.11: ESO-Hα 574 observed in the PC chip. Image centered at R.A.=11:16:03.08, Decl.=-76:24:52.6.

sources having spectral class earlier than M6. We also limited ourselves to sources detected by Spitzer in at least one IRAC band, with some flux information at 24μm or longer wavelengths, typically in the sub-mm, as these data points provide a critical constrain to the IR excess from the disk. We used the photometric data reported in Tables 4 and 5, plus our own F547M photometry presented in Table 3. We excluded from the fit the sources #4, #7 and #25 since these are confirmed tight binaries (see Section 4.1 and Lafrenière et al. (2008)). Sources #17, #27 and #29 have a cluster member within the beam size of the sub-mm observations (Kraus & Hillenbrand 2007) and therefore those data points were neglected.

The SED model fitting tool from Robitaille et al. (2006) aims at reproducing the photometric fluxes by varying a set of 16 parameters, of which the extinction (A_V) and the distance (d) vary in ranges defined by the user. The remaining 14 "free" parameters characterize each model, whose SED is computed at 10 different viewing angles. For each angle of each SED, the fitting tool calculates a χ^2 to estimate the goodness of the fit. In practice, the free parameters are typically constrained by the fluxes at certain wavelengths. For example, the mass or the temperature of the star are characterized by the optical region of the SED, the inner radius or the flaring angle of the disk by the mid-far IR excess, while to constrain the disk mass one needs fluxes at $\lambda \gtrsim 100\mu$m.

Given the lack of far-IR data, and the uncertainties due to the non-simultaneity of the observations, our problem is under-constrained and the SED model fitting tool returns several possible solutions. To clean-up the ensemble, for each source we considered only the solutions corresponding to values of T_{eff} and A_V falling within ±100K and ±1mag from the values given in Table 4. This is appropriate, considering that the spectral types and absolute temperature scale of low-mass stars have typical uncertainty of one sub-class. We also constrain the distance to be in the range between 130pc and 190pc, an artifice to allow for some variability of the source luminosity (see e.g. Morales-Calderón et al. 2011). As the average of the calculated distances remains close to 160 pc, this does not introduce systematic trends in the derived luminosities. We finally require that the difference between the χ^2 and the best χ^2 of each source must be smaller than 3. This latter criterion, also adopted by Robitaille et al. (2007) to fit low-mass young stellar object (YSO) SEDs, has been necessary because the model grid is too sparse to reliably search for the true minima of the χ^2 hypersurface.

Since the minima of the χ^2 hypersurface are difficult to resolve, we could not reliably identify the best fit model that formally represents the physics of the source, with its associated confidence interval. However, as shown by Grave & Kumar (2009), the distributions of fundamental parameters such as the stellar mass, age and total luminosity tend to show peaks independently on the finesse of the model grid. Following these authors, we have used these distribution (constrained by our knowledge of the stellar parameters) to derive the "best fit" parameters with their uncertainties, computing a weighted mean and a weighted standard deviation for each parameter and each source. For the weights we used the inverse of the χ^2 returned by the SED model fitting tool. The mean and the standard deviation were computed on a logarithmic scale because the parameters in the grid are usually uniformly sampled in logarithmic scale. The resulting distributions of the stellar age and mass show that when a large number of models can be found, they tend to produce a rather narrow peak in the distribution of stellar parameters. Only for three sources, #18, #20 and #29, the number of models passing our selection criteria is small and the corresponding histograms do not show a peak. Following this approach we were able to fit 19 SEDs, shown in Fig. A.12. The physical parameters derived from the SED fitting, together with their uncertainties, are listed in Tables A.6 and A.7.

A.6.1 Parameters derived from SED fitting

Table A.6 provides the parameters related to the central source: the entry number we assigned to each star in Table 2 (column 1); the χ^2 per datapoint of the best fit (column 2); the number of fits that satisfy our selection criteria on T_{eff}, A_V and χ^2 (column 3); and finally, in the last four columns, the bolometric luminosity, age, mass and radius of the central source. Most of the sources have sub-solar mass down to 0.12 $M_{\odot}$, a value close to the low-mass limit of the fitting tool. The median age, 2.5 Myr, is in agreement with previous estimates, while the spread between is 0.5 Myr and 5 Myr, with a few outliers. In general, this spread is in line with what typically found using isochronal timing of PMS clusters (Hillenbrand et al. 2008). It is known that several factors may affect the estimate of the absolute stellar luminosity ofPMS stars (see e.g. Hartmann 2001; Reggiani et al. 2011), and in particular edge-on disks can explain the most extreme cases of sub-luminous sources. If the age spread is real, star formation in Chamaeleon I proceeded rather slowly and may still be ongoing, as suggested by Luhman (2007) and Belloche et al. (2011).

Table A.7 refers to the main disk parameters. For each source we list the entry number (column 1); the infrared spectral index α_{2-24}, defined as $\alpha = d\log(\lambda F_{\lambda})/d\log\lambda$ (Lada & Wilking 1984), calculated between 2.2μm and 24μm and dereddened using the extinction from Table 4 and the reddening law from Flaherty et al. (2007) (column 2); the mass of the disks, either derived by the fitting tool (column 3) or directly estimated from the data at 870μm (column 4); the dust sublimation radius $R_{sub} = R_{*}(T_{*}/T_{sub})^{2.1}$ (Robitaille et al. 2006) for a dust sublimation temperature, $T_{sub} = 1600$ K (column 65; the inclination of the disk to the line of sight (column 6). The SED fitting tool also estimates disk scale height factors $z_{factor} \sim 0.8$ and disk flaring parameters $\beta \sim 1.0$. These values turn out to be similar for all sources within about 10%.

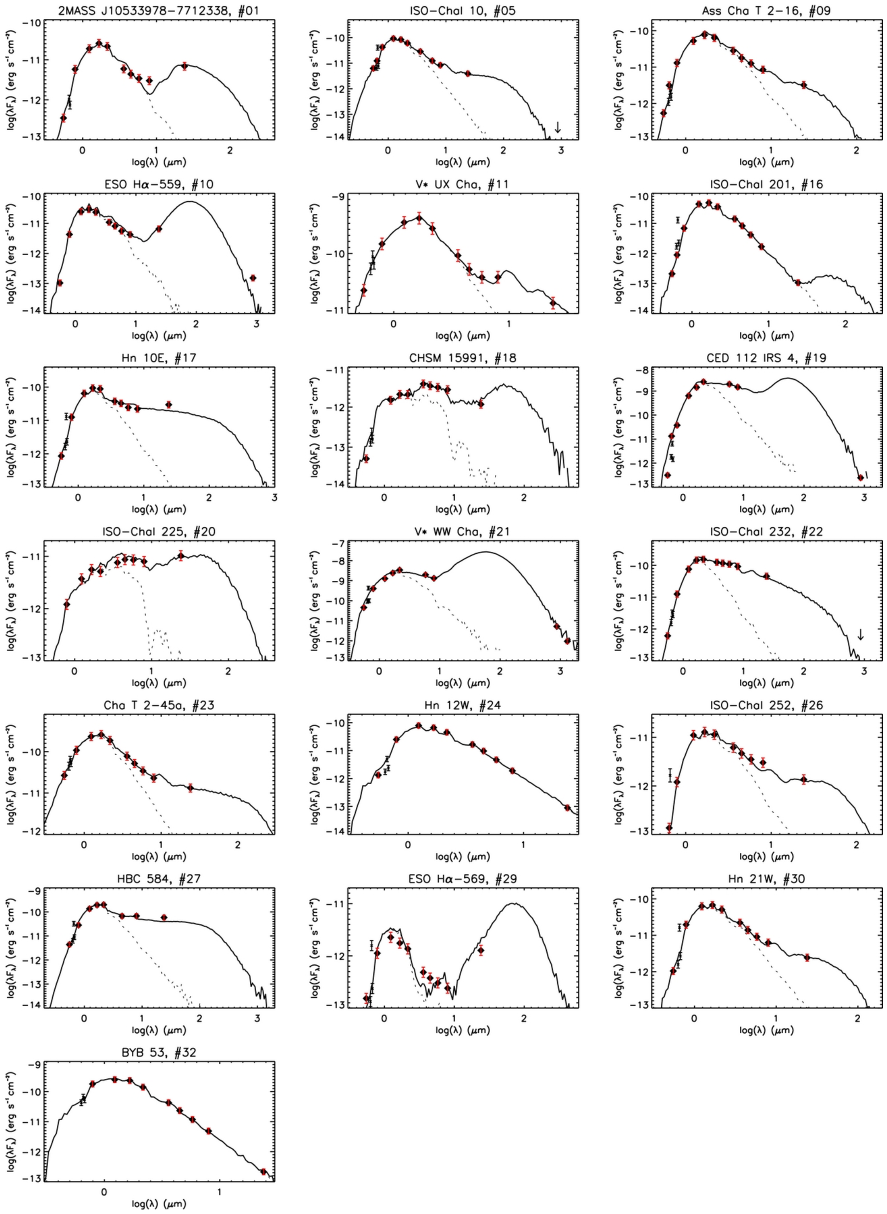

Figure A.12: SEDs of our sample of sources. Data obtained in our HST line-filters have not been used for the fit as they may be contaminated by accretion or mass loss. They are presented in the plot with black error bars. The data actually used for the fit have red error bars.

In Table A.7 we provide the model disk mass M_d^{SED} only for sources with some flux measure at $\lambda \gtrsim 100\mu$m, which allows constraining the amount of dust in the outer disk regions where most of the mass resides. These estimates can be compared with the the disk mass estimated from the flux density of sub-mm continuum dust emission (column 4), calculated assuming optically thin emission at long-wavelengths. The flux density in the sub-mm, $F_{\mathrm{sub-mm}}$, can be converted into an estimate of the disk mass through the relation $M_{\mathrm{disk}} \simeq d^2 F_{\mathrm{sub-mm}}/(\kappa_\nu B_\nu(T_c))$, where d is the distance (160 pc), κ_ν is the total (gas + dust) mass opacity, $B_\nu(T_c)$ is the Planck function at the characteristic temperature T_c of the emitting dust. For the mass opacity we adopted the opacity law of Beckwith et al. (1990), i.e. $\kappa_\nu = 0.1 \times (\nu/10^{12}\mathrm{Hz})\ \mathrm{cm}^2/\mathrm{g}$, whereas we considered a value of 20 K for the characteristic outer disk temperature (see e.g. Andrews & Williams 2005). Unfortunately, the sub-mm data can be reliably used to derive the disk mass only for 3 sources, as in the other cases we have either a non-detection or a cluster member, according to the lists of Kraus & Hillenbrand (2007) and Lafrenière et al. (2008), close enough to potentially affect the measured sub-mm flux. The values obtained in those cases can be regarded as upper limits to the real disk mass, and are therefore reported in square brackets.

A.6.2 Analysis of the Best-fit Model Parameters

In this final section we discuss a number of diagrams useful to address the presence of evolutionary trends between the main parameters of our star+disk systems.

First, as a sanity check, we compare the values of stellar age and mass returned by the fitting tool with those obtained from the direct interpolation of T_{eff} and L_{bol} in the HR diagram using the Siess tracks (Siess et al. 2000), which are the same tracks adopted by the fitting tool. Fig. A.13 and A.14 show that there is strong agreement. In particular, the strong correlation between the mass values is expected, since the model fitting assumed temperatures within ±100 K from the stellar temperatures and in this temperature range the mass is strongly correlated to the temperature. There are, however, four sources (#1, #10, #19, #21) for which the fitting tool provides ages and masses which are discrepant from those found in the literature. The younger ages we derive are a result of the higher bolometric luminosities returned by the fitter. For disk seen at high inclinations, taking into account the IR part of the SED allows to recover a non-negligible frac-

Table A.6: Stellar parameters obtained from the fit

N	χ^2 best fit	Accepted Fits	L_{bol}	Age	M_*	R_*
			$[L_\odot]$	[log yr]	$[M_\odot]$	$[R_\odot]$
1	1.1	242	0.09 ± 0.03	6.81 ± 0.13	0.28 ± 0.03	0.81 ± 0.12
5	0.087	818	0.10 ± 0.05	6.57 ± 0.13	0.19 ± 0.03	1.0 ± 0.2
9	0.62	768	0.18 ± 0.06	6.49 ± 0.14	0.31± 0.03	1.2 ± 0.2
10	4.3	12	0.2 ± 0.3	5.9 ± 0.6	0.17 ± 0.02	1.5 ± 0.8
11	0.055	1524	0.8 ± 0.3	6.5 ± 0.2	0.93 ± 0.07	1.7 ± 0.3
16	0.46	1584	0.08 ± 0.03	6.4 ± 0.3	0.12 ± 0.02	1.0 ± 0.2
17	0.80	226	0.28 ± 0.13	6.4 ± 0.2	0.30 ± 0.03	1.4 ± 0.4
18	0.33	6	0.6 ± 0.4	6.0 ± 0.3	0.31 ± 0.02	2.1 ± 0.7
19	3.4	33	25 ± 14	5.2 ± 0.2	1.7 ± 0.4	9 ± 2
20	0.74	6	1.2 ± 0.3	5.8 ± 0.2	0.40 ± 0.03	2.8 ± 0.5
21	0.44	90	20 ± 12	5.3 ± 0.3	1.6 ± 0.4	7 ± 3
22	0.27	54	1.2 ± 0.4	6.4 ± 0.3	0.69 ± 0.08	1.6 ± 0.4
23	0.042	1070	0.39 ± 0.16	6.4 ± 0.2	0.47 ± 0.03	1.4 ± 0.3
24	0.41	1640	0.08 ± 0.04	6.5 ± 0.2	0.13 ± 0.02	1.0 ± 0.2
26	0.33	679	0.06 ± 0.06	6.5 ± 0.4	0.12 ± 0.02	0.8 ± 0.4
27	0.73	126	0.5 ± 0.3	6.2 ± 0.2	0.39 ± 0.03	1.8 ± 0.6
29	2.0	5	0.8 ± 0.4	5.8 ± 0.2	0.33 ± 0.03	2.5 ± 0.6
30	0.076	1602	0.10 ± 0.05	6.59 ± 0.15	0.23 ± 0.03	1.0 ± 0.2
32	0.030	614	0.22 ± 0.09	6.38 ± 0.13	0.32 ± 0.02	1.3 ± 0.2

Table A.7: Disk parameters obtained from the fit

N.	α_{2-24}	M_d^{SED} $[M_\odot]$	$M_d^{sub-mm*}$ $[M_\odot]$	R_{sub} [AU]	Inclination [deg]
1	-0.52 ± 0.12	—	—	0.02	81.4
5	-1.14 ± 0.12	—	<0.13	0.02	75.5
9	-1.35 ± 0.12	—	—	0.03	75.5
10	-0.60 ± 0.12		0.003	0.03	87.1
11	-1.27 ± 0.27	—	—	0.06	63.3
16	-2.45 ± 0.25	—	—	0.016	87.1
17	-0.53 ± 0.14	—	[0.12]	0.03	18.2
18	-0.29 ± 0.17	—	—	0.05	87.1
19	—	0.001 ± 0.004	0.005	0.3	75.5
20	0.20 ± 0.17	—	< 0.03	0.8	87.1
21	—	0.02 ± 0.08	0.12	0.3	31.8
22	-0.66 ± 0.12	—	[< 0.03]	0.05	41.4
23	-1.14 ± 0.12	—	—	0.04	69.5
24	-2.58 ± 0.17	—	—	0.016	81.4
26	-0.95 ± 0.12	—	—	0.016	75.5
27	-0.59 ± 0.12	—	[0.003]	0.05	18.2
29	-0.08 ± 0.19	—	[0.005]	0.05	87.1
30	-1.32 ± 0.14	—	—	0.02	75.5
32	-2.69 ± 0.13	—	—	0.03	56.6

* In this column we report the disk mass derived from the data at 870μm (see Section 2.3). The values relative to sources with a visual companion within the beam are given in brackets and can be considered as upper limits to the real disk masses.

tion of the stellar flux which would otherwise remain unaccounted for by a applying a simple reddening correction to the optical photometry. Luhman (2004) and Luhman (2007), who derived L_{bol} from I and J band magnitudes for almost the entire known population of Chamaeleon I, already noticed that sources with unusually low L_{bol} values, which apparently lie below the Main Sequence in the HR diagram, may be highly affected by an underestimate of the dust column density. Unfortunately these systems are also the most challenging to model, due to the lack of direct information e.g. on the disk flaring angle and on the dust properties at the disk surface. With the exception of source #10, whose age (i.e. luminosity) derived from the fit is highly uncertain, the other three sources are distributed at the two extremes of the age range: source #1 is the most luminous while source #19 and #21 are the faintest ones. Our HST images show that these last two objects are associated with diffuse emission, consistent with sources seen mainly in scattered light.

Table A.7 shows that 14 out of 19 disks have tilt angle within 30 degrees from edge-on, about twice the number one would expect if disks are oriented randomly. While this may be partially due to the sparse sampling of this parameter provided by the theoretical model, we must remark that the model may actually be biased toward larger angles, as it may not sample disks that are enough settled. The model adopts a fully flared disk (in vertical hydrostatic equilibrium) and mimics the dust settling by multiplying the scale height at the dust sublimation radius by a “zfactor”. Figure 6 in Robitaille et al. (2006) shows that the zfactor is a function of the disk outer radius, becoming equal or less than 0.5 only for relatively large disks. However, Szűcs et al. (2010) notice that the average SED of T-Tauri stars in the Chamaeleon-I region already requires a reduction of a factor of 2 in the disk scale height; similar results are also reported by the Spitzer Infrared Spectrograph GTO team for Taurus sources (Furlan et al. 2011). This suggests that the grid of Robitaille et al. may not properly sample the typical settling of TTau disks. In conclusion, the returned values for the tilt angle are only indicative, and therefore we use them to flag outliers without drawing any further conclusion.

To further investigate the possible correlations between the disk structure and the derived stellar properties, we compare the infrared spectral index α_{2-24}, a tracer of the amount of dust in the warmest layers of the circumstellar disk, to the main parameters of the central sources, like luminosity

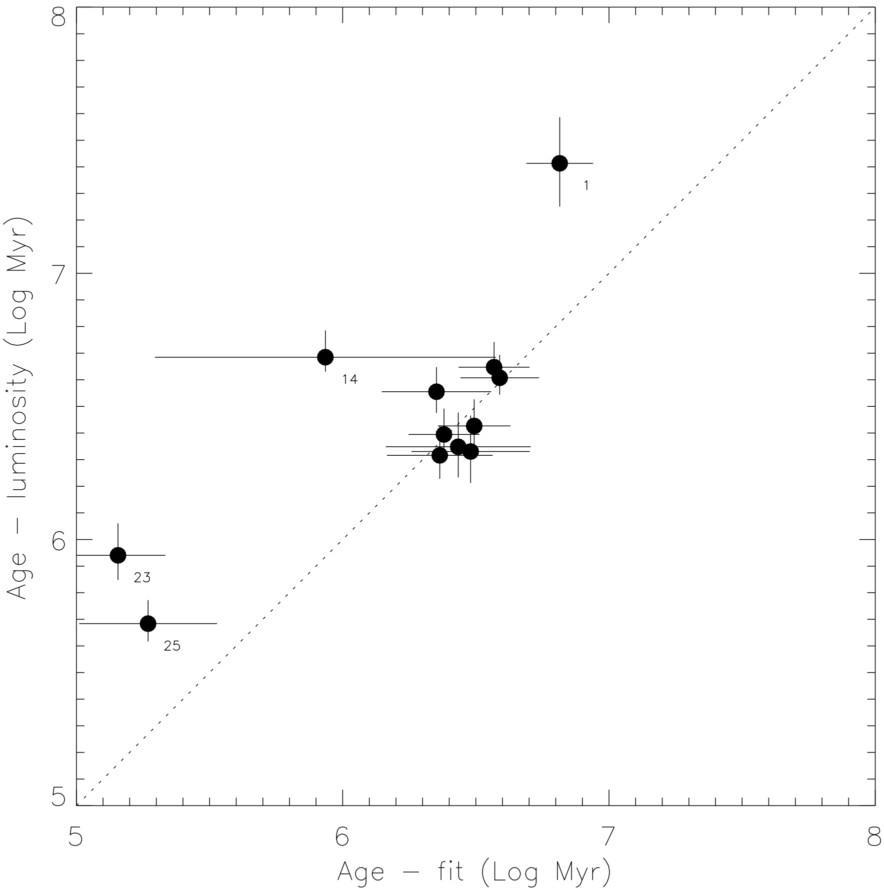

Figure A.13: Comparison between the ages estimated with Luhman luminosities + Siess tracks and the SED model fitting tool from Robitaille et al. (2006).

and mass. Fig. A.15 shows the difference between the values of L_{bol} derived by the fitting tool and by Luhman (2007) against the spectral index α_{2-24}. Three sources with discrepant luminosity stand out in the plot: #18, #20 and #29. These three sources, with nearly flat IR SEDs, were positioned according to Luhman (2007) below the Zero-Age-Main-Sequence and therefore, having no estimate for their mass and age, did not appear in Figures A.13 and A.14. The fitting tool returns for them a small number of successes, confirming that these systems have extreme properties. In particular, these are the sources with the highest tilt angle, seen nearly edge-on. Our derived ages and mass are now in-line with the main population (see Figures A.16 and A.17 below). Sources #19 and #21 do not appear in this plot as they have no detection at 24 μm.

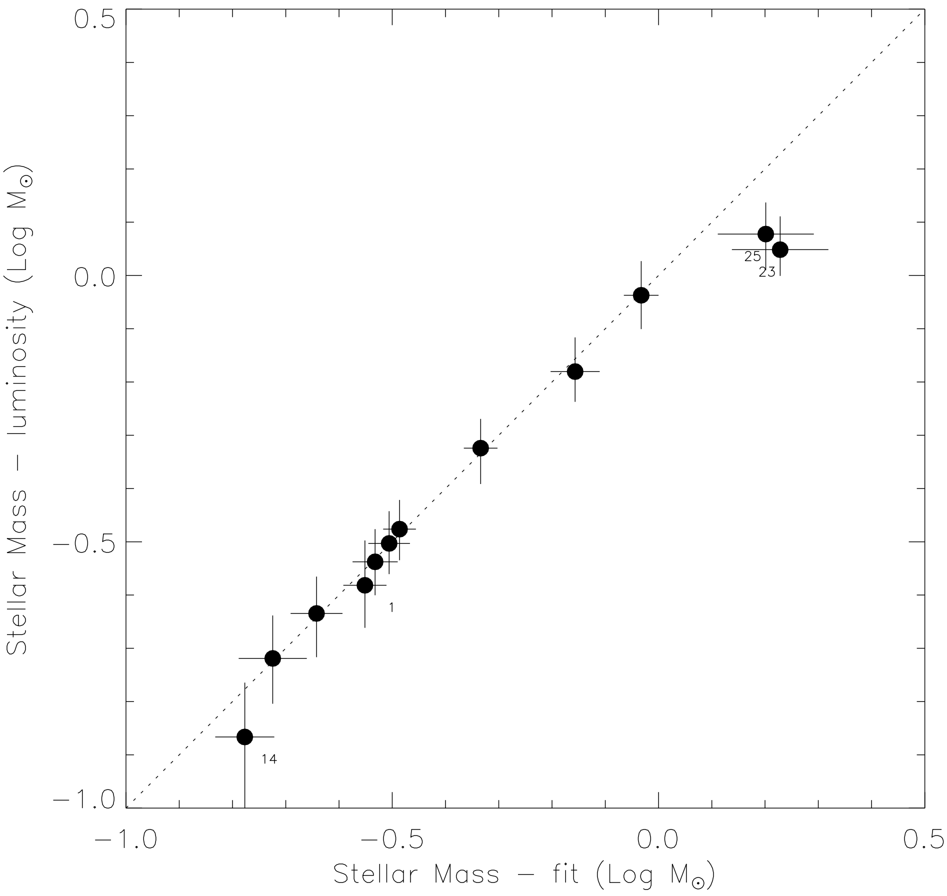

Figure A.14: Comparison between the stellar masses estimated with Luhman luminosities + Siess tracks and the SED model fitting tool from Robitaille et al. (2006).

Fig. A.15 also shows that for the other sources the difference between the estimated luminosities appears to increase with the spectral index: there is a correlation between the amount of warm dust seen in the outer disk layers and the apparently low bolometric luminosity derived from dereddening the I and J-band magnitudes. In general, this plot seems to confirm an underestimate of the dust column density toward the edge-on sources.

Fig. A.16 shows that the index α_{2-24} decreases with time for nearly all sources (#19, and #21, younger than 0.2 Myr and without a 24 μm measure, are not plotted), indicating that the disks become flatter with age. This is most probably related to the gradual settling of the dust grains on the disk plane. Our linear fit to the main distribution is provided by the formula shown in the figure. Luhman et al. (2008) set $\alpha_{2-24} = -2.2$ as the

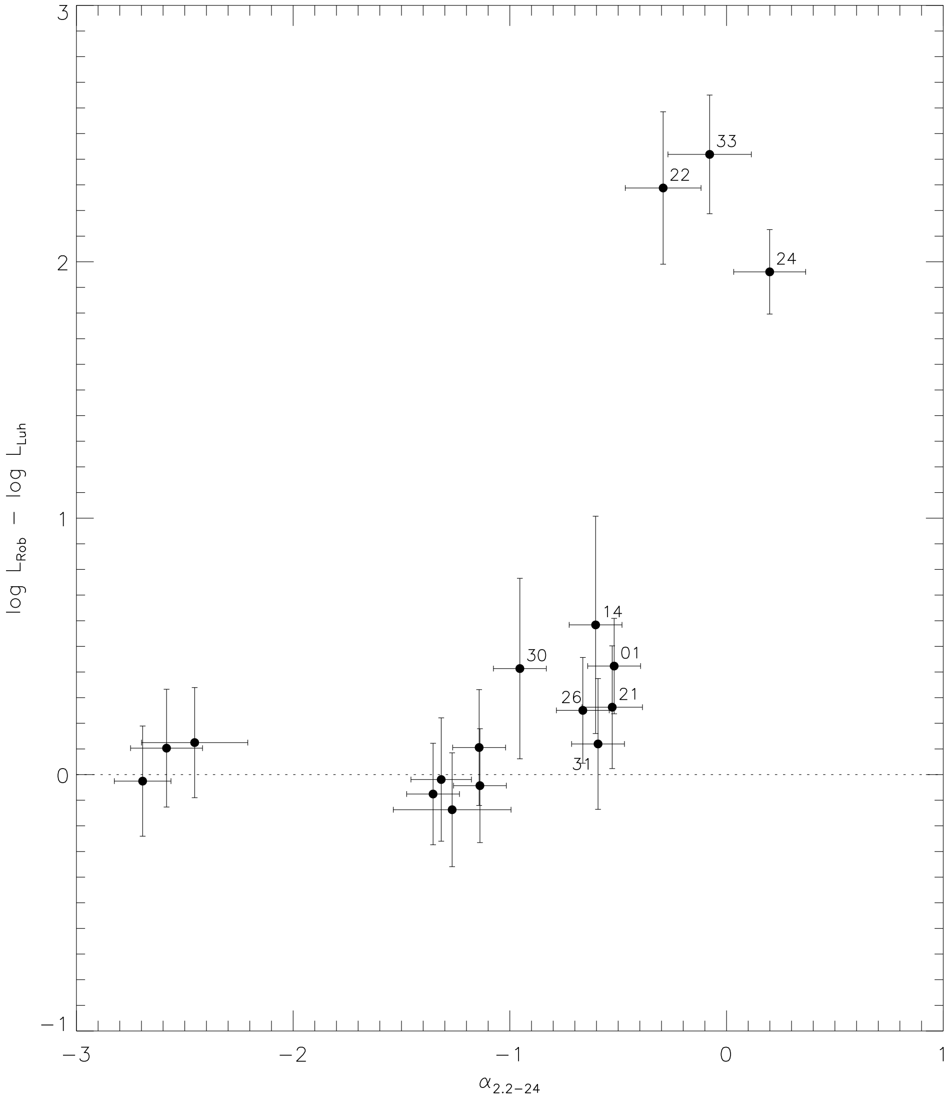

Figure A.15: Difference between the values of L_{bol} derived in this work and those from Luhman (2007) versus the infrared spectral index α_{2-24} that is a tracer of the structure of the inner disk, being mostly dependent on the flaring angle and on the presence of an inner rim.

lower limit for disk dissipation. According to our expression, this value is reached at a time $\simeq 10^7$ yr, compatible with the scenario that disks around *most* young solar analog stars clean out their small dust grains within 1 AU in $\approx$ 10 Myr or less (Pascucci & Tachibana 2010). The three sources that strongly deviate from the main trend, #16, #24 and #32, are those exhibiting negligible IR excess. These outliers seem to have dissipated their inner disk relatively quickly, less than $\sim$ 3 Myr. Various effects may lead to rapid disk dissipation, all intimately linked to the physical or chemical properties of the environment, like e.g. higher UV or X ray flux from the central star, tidal forces due to the presence of a close companion or of a giant planet (Cieza et al. 2009), or low disk metallicity which can increment the dust photoevaporation rate (Ercolano & Clarke 2010). A larger statistical sample is needed to quantify the frequency of premature versus delayed disk dissipation.

A plot of the α_{2-24} index against stellar mass (Fig. A.17), does not show any clear correlation. However, two of the three sources at the bottom of the plot, without an inner disk, have stellar mass close to our lower limit. For this sources inner disk dissipation may be more likely driven by tidal forces or rapid formation of a giant planet rather than photoevaporation, which is expected to be dominant in more massive sources. Luhman et al. (2008) noticed that Chamaeleon I, unlike other star forming regions, contains a significant fraction of low-mass stars with inner-disk lifetimes shorter than those of more massive stars.

In what concerns the mass accretion rates derived from our HST Hα photometry, several observations have shown a correlation between the mass accretion rate and the age, mass or the IR spectral index of YSOs (Muzerolle et al. 2003, 2005; Mohanty et al. 2005; Natta et al. 2006; Alexander & Armitage 2006; Gatti et al. 2008; Sicilia-Aguilar et al. 2010; Manara et al. 2012). Based on the values reported in Table A.6 and the magnitudes listed in Table A.4 we investigate the correlation between these parameters and the mass accretion rates estimated from our HST images. For sources #18, #20 and #29 we use our new luminosity estimates (Table A.6) to rederive the mass accretion rates, obtaining $\log \dot{M}_{acc} = -8.2$, -7.9 and -7.38 $M_\odot/yr^{-1}$, respectively, and use these values instead of those presented in Table A.5. We also discard sources # 7 and #25, as they are confirmed tight binaries (see Section 4.1 and Lafrenière et al. 2008).

In Fig. A.18 we plot the mass accretion rate as a function of stellar age. The largest accretion rates are found for the two youngest stars, while the majority of older sources show a spread of about 2 orders of mangnitude. These characteristics, a general decrease of the mass accretion rate vs. time associated with a large scatter at any given age, cannot be explained by a any reasonable systematic overestimate of the stellar luminosity (which would make the stars younger while enhancing the estimated accretion luminosity)

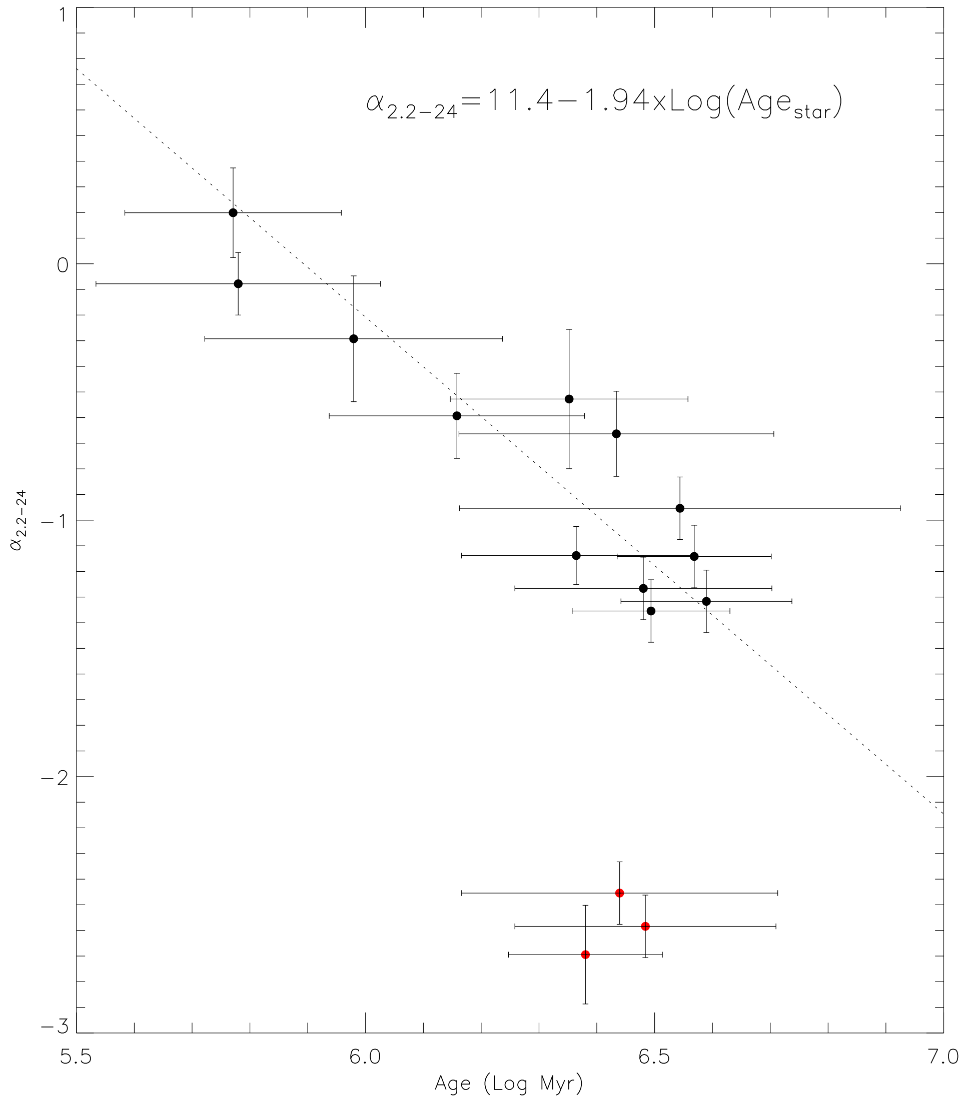

Figure A.16: Infrared spectral index α_{2-24} as a function of the age. Black dots represent the sources used to fit the main trend (dashed line) and red dots represent the diskless sources.

and are consistent with what typically found in other star forming regions (see e.g. Hartmann et al. 1998).

In Fig. A.19 we show the mass accretion rate as a function of the stellar mass. The plot shows a gradual rise of the mass accretion rate with the mass of the central source. The dashed line shows the $\dot{M}_{acc} \propto {M_*}^2$ scaling relation reported by various authors (Muzerolle et al. 2003, 2005; Mohanty et al. 2005; Natta et al. 2006) and discussed e.g. in the context of accelerated

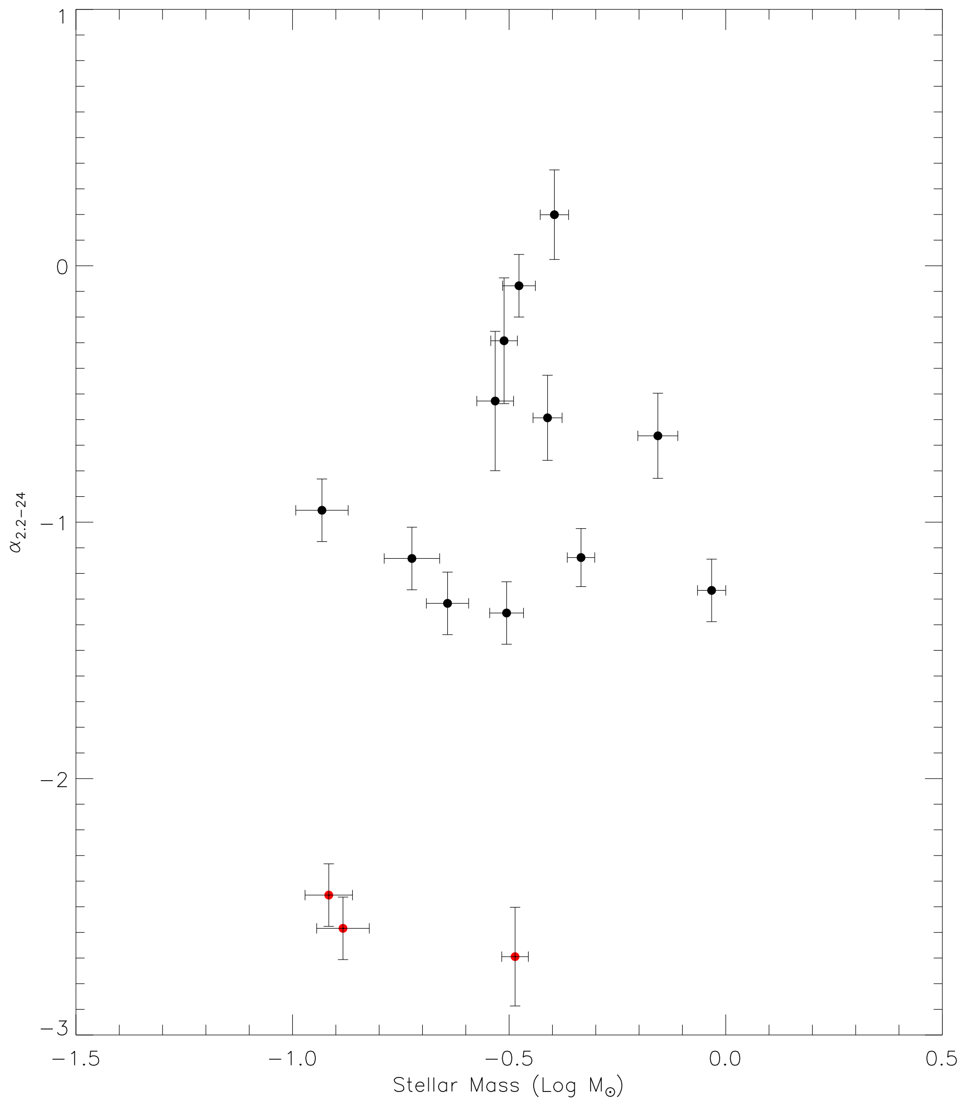

Figure A.17: Infrared spectral index α_{2-24} in function of the mass. Red dots represent the diskless sources.

disk clearing by Clarke & Pringle (2006) or of systematic differences in disk initial conditions by Alexander & Armitage (2006).

Finally, in Fig. A.20 we show the relation between the mass accretion rate and the IR spectral index α_{2-8}, more sensitive to the warmer dust in the inner disk than the α_{2-24} index. The α_{2-8} index is a tracer of both disk evolutionary status and tilt angle. While the scatter of points in Fig. A.20 may be attributed to the tilt angle, the systematic trend suggests that more evolved inner disks tend to have smaller accretion rates. A similar correlation

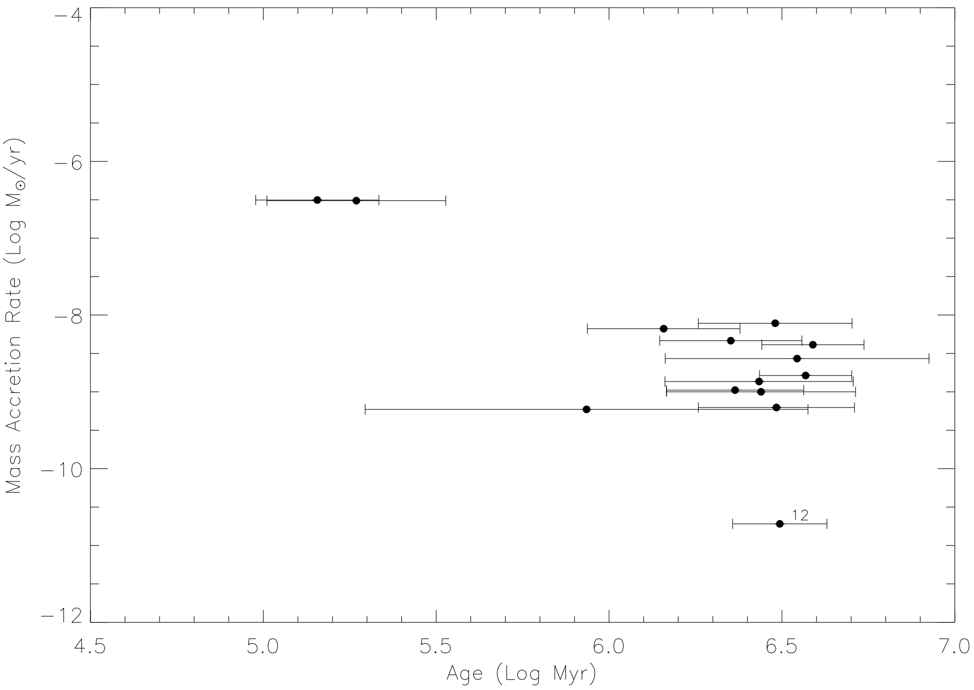

Figure A.18: Mass accretion rate plotted as a function of the stellar age. The age values are those extrapolated from the SED fitting tool and listed in Table A.6.

has been found by Sicilia-Aguilar et al. (2010).

A.7 Conclusions

We have used the WPC2 instrument onboard the HST to observe 20 fields centered on T Tau stars in the star forming region Chamaeleon I. Our images, obtained in narrow-filters centered on the [OI], Hα and [SII] lines, plus a Johnson-V band equivalent filter, allowed us to detect 31 previously known T Tauri stars. In this paper we have presented the images relative to 10 sources that appear either extended, binaries, or surrounded by a circumstellar disk and/or mass outflow. We have complemented our photometry with a compilation of optical, IR and sub-mm observations, adding new sub-mm data for three sources, together with published values of T_{eff}, A_J and L_{bol}. Using our Hα photometry we have estimated the mass accretion rates for 28 sources. Using all available data, we have reconstructed the optical-IR SEDs of 19 sources and derived a number of disk parameters using the SED-model fitting tool of Robitaille et al. (2007). Our main results are:

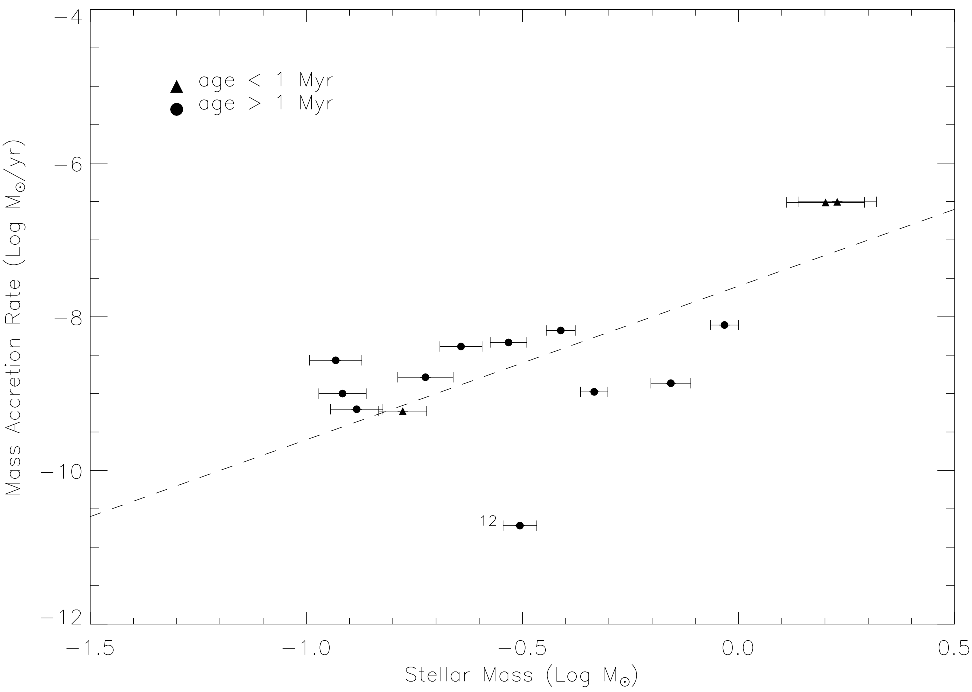

Figure A.19: Mass accretion rate plotted as a function of the stellar mass. The mass of the central sources are those extrapolated from the SED fitting tool and listed in Table A.6. The dots represent the sources with age>1 Myr, whereas the younger sources are indicated by a triangle. The dashed line represent the relation $\dot{M}_{acc} \propto M_*^2$.

1. We resolved 10 Chamaeleon I sources into binaries or diffuse objects with evidence of circumstellar material, either disks or jets.

2. The SED fitting shows that most of the sources have mass between 1.7 $M_\odot$ and 0.12 $M_\odot$ and isochronal ages typically ranging between 0.5 Myr and 5 Myr.

3. The L_{bol} derived from the fitting tool is generally higher than the values reported by Luhman (2007), leading to apparently younger ages. The discrepancy increases with the IR spectral index α_{2-24} (see Fig. A.15). A few sources identified by Luhman (2004, 2007) and Luhman & Muench (2008) as anomalously faint in the near-IR appear to be affected by high dust column density and most probably are associated with disks seen nearly edge-on.

4. For 13 sources the IR spectral index α_{2-24} appears to decrease with time. The rate of decay would imply that disk dissipation in Chamaeleon I

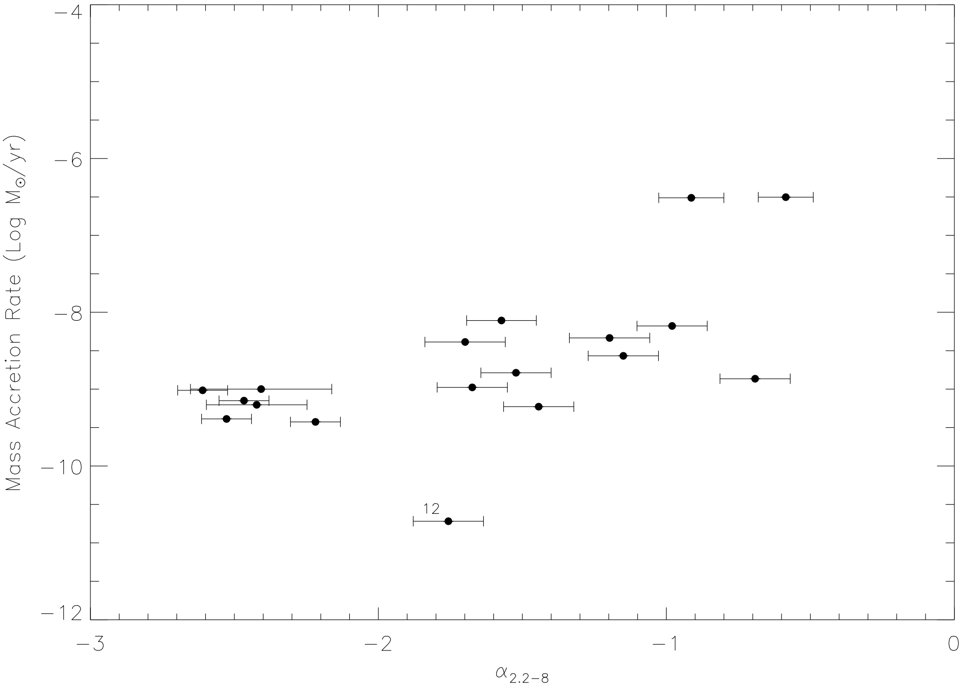

Figure A.20: Mass accretion rate plotted as a function of the IR spectral index α_{2-8}.

requires $\simeq 10^7$ yr, a relatively long disk lifetime. There are 3 sources that deviate from the main trend, exhibiting an unusual absence of IR excess for their apparently young age.

5. The mass accretion rate decreases with the stellar age, showing a spread of about two orders of magnitude at ~ 3 Myr, consistently with what typically found in other star forming regions. The mass accretion increases with the stellar mass roughly following the same scaling relation, $\dot{M}_{acc} \propto M_*^2$ found in other PMS clusters.

6. The fact that both the IR spectral index α_{2-24} and the mass accretion rates decrease with our estimated isochronal time suggests that the age spread observed in our sample is real. This is in contrast with the recent suggestion by Jeffries et al. (2011) that individual stellar ages from the Hertzprung-Russel diagram are unreliable since, at least in the Orion Nebula Cluster, they do not correlate with the presence of disks inferred from near-IR excess. There are clearly several factors that may contribute to the observed luminosity dispersion, and we have shown that the case of highly tilted disks is one of those. A comprehen-

sive analysis of the rich phenomenology associated with the presence of accreting circumstellar disks may allow to reveal the intrinsic age spread within a cluster.

A.8 Acknowlegments

The authors would like to thank Kevin Luhman for discussions and contribution to the source selection process and Basmah Riaz for early analysis of SED fitting. Support for program 11983 was provided by NASA through a grant from the Space Telescope Science Institute, which is operated by the Association of Universities for Research in Astronomy, Inc., under NASA contract NAS 5-26555.

A.9 Appendix: SEDs of individual sources

2MASS J10533978-7712338 (#1): for this source the SED fitting tool is unable to reproduce the relatively flat slope of the Spitzer/IRAC data (3.5-8.0μm). The absence of near-IR excess drives the solution toward a highly tilted system, i.e. a disk with 81.4° inclination with respect to the plane of the sky. The high tilt angle agrees with previous suggestions (Luhman & Muench 2008) that this source (unresolved in our HST images) is probably mainly seen in scattered light. The low bolometric luminosity makes this source the oldest one of our sample.

ISO-ChaI 10 (#5): for this source we obtain a good fit, with stellar mass is in agreement with the value of ~0.18 $M_\odot$ reported by Lafrenière et al. (2008). This source has been indicated as a possible binary (López Martí et al. 2004) but remains unresolved in our HST observations.

Ass Cha T 2-16 (#9): also for this source we obtain a a good fit, The stellar mass 0.19 $M_\odot$ is smaller than the previous estimate of 0.26 $M_\odot$ by Lafrenière et al. (2008). In Section A.5 we showed some evidence for a spatially resolved PSF, especially in the [OI] line filter.

ESO Hα-559 (#10): for this source we have a sub-mm detection. The best fit indicates a disk seen nearly edge-on (at 87.1° tilt) with a disk mass ~$2{\cdot}10^{-3}$ $M_\odot$ and an age ~7.9 Myr, consistent with Comerón et al. (2004).

V* UX Cha (#11): the SED of this source is typical of a transition disk that has almost entirely dissipated the inner region. The fit returns a stellar mass of ~0.9 $M_\odot$, the same value assigned by Kirk & Myers (2011).

ISO-ChaI 201 (#16): the SED of this source is compatible with a pure photosphere up to 24 μm. The inner disk has been cleared rather rapidly, as the source seems only ~2.5 My old. This source has been classified as a candidate brown dwarf with spectral type M5.75; our fit assigns a mass of ~0.12 $M_\odot$, close to the lower limit of the grid values.

Hn 10E (#17): the best fit for this source provides a marginally acceptable match to the flat IR SED. The derived stellar parameters are consistent with those reported by Feigelson & Lawson (2004).

CHSM 15991 (#18): even if the fitting tool provides a small number of acceptable solutions, the best fit for this source shows good agreement with the data. We derive an extreme disk inclination, 87.1°, in areement with Luhman et al. (2008). Cases like this of extreme disk inclination make the estimates of the absolute stellar lumiosity problematic. Luhman (2007) estimated for this source $L_{bol} \sim 0.0029$ $L_\odot$, which puts below the Main Sequence it in the H-R diagram. Our best fit returns a much higher luminosity, L_{bol}~0.6 $L_\odot$ and an age ~1.0 Myr, for a ~0.31 $M_\odot$ stellar mass.

CED 112 IRS 4 (#19): we obtain a good fit for this source, resolved in our HST images and detected at 870μm. The young age, 0.14 Myr, is well compatible with the HST images showing a young active source associated with HH 914. The disk inclination, 75.5°, seems also compatible with the HST morphology.

ISO-ChaI 225 (#20): for this source we find a small number of acceptable models. In fact, our best fit poorly reproduces the near-IR photometry. The extreme tilt angle, 87.1°, would imply that the source, unresolved in our HST images, is mainly seen in scattered light. This may well be the case, as Luhman (2007) estimates L_{bol}~0.013 $L_\odot$ putting the star below the mean sequence. We derive a much higher value, L_{bol}~1.2 $L_{\odot}$, thus an age of ~0.59 Myr for a mass ~0.40 $M_{\odot}$.

V* WW Cha (#21): this source, marginally resolved in our HST images, has two detections in the mm region. SED fitting provides a disk mass of ~0.02 $M_{\odot}$ and an age of ~$2{\cdot}10^{5}$ yr. As for CED 112 IRS 4, high dust extinction may explain the difference between a stellar mass ~1.6 $M_{\odot}$ returned from the fit and the estimate of ~0.7 $M_{\odot}$ by Lafrenière et al. (2008).

ISO-ChaI 232 (#22): we obtain a good fit for this source, which shows strong IR excess and mass loss, being associated with objects HH 917 (Bally et al. 2006), HH 912 and HH 916 (Wang & Henning 2006). The stellar mass returnd by the fitter, 0.69 ± 0.09 M$_{\odot}$, is slightly higher than the 0.55 $M_{\odot}$ estimated by Lafrenière et al. (2008).

Cha T 2-45a (#23) : we obtain a good SED fit. The derived stellar mass, 0.47 ± 0.03 M$_{\odot}$, is in agreement with the estimate (~0.51 $M_{\odot}$) of Lafrenière et al. (2008).

Hn 12W (#24): The SED shows no evidence of IR excess up to 24μm. The stellar mass $0.13{\pm}0.02$ M$_{\odot}$ is again in agreement with the estimate (~0.15 $M_{\odot}$) of Lafrenière et al. (2008).

ISO-ChaI 252 (#26): we obtain a genarally good fit except for the IRAC 8micron data point. The stellar mass, 0.12 ± 0.02 $M_{\odot}$ is in agreement with the estimates of Lafrenière et al. (2008) and Muzerolle et al. (2005), lying out the borderline between stars and brown dwarfs.

HBC 584 (#27): for this source with incompled Spitzer/IRAC coverage and strong α_{2-24} index, the best fit indicates a stellar mass 0.39 ± 0.03 $M_{\odot}$, in agreement with the estimated by Lafrenière et al. (2008) of 0.35$M_{\odot}$.

ESO Hα-569 (#29): a problematic fit for this faint source at optical wavelenghts. The SED does not show a strong excess at $\lambda < 10$ μm, but the 24μm data point is remarkably high.For this source, non detected in the X-rays by Feigelson & Lawson (2004), an extinction $A_k \gtrsim 60$, possibly due to an edge-on circumstellar disk has been suggested by Luhman (2007). The steep rise of the flux at $\lambda < 10$ μm confirms that the low optical luminosity can be attributed to high dust column density. Our best fit supports this scenario, with a ∼87.1° disk inclination. The L_{bol}∼0.003 $L_{\odot}$ derived by Luhman (2007) places this source below the Main Sequence in the H-R diagram, but integrating the emission reprocessed at longer wavelengths our fit provides $L_{bol} \sim 0.1\ L_{\odot}$, with an age $\sim$ 0.63 Myr and a mass $\sim 0.33\ M_{\odot}$.

Hn 21W (#30): we obtain a good fit to the SED, with a stellar mass 0.23 ± 0.03 $M_{\odot}$ in agreement with the 0.20 $M_{\odot}$ value reported by Lafrenière et al. (2008).

BYB 53 (#32): a class III SED. The age returned by the fit is consistent with the 2 Myr estimated by Gómez & Mardones (2003), indicating that the source has depleted its disk very quickly.

Appendix B

Ringraziamenti

Alla fine di questi anni di dottorato vorrei ringraziare Francesco Palla e Sofia Randich per tutto il tempo che mi hanno dedicato, la loro pazienza e disponibilità. Un grazie enorme per avermi introdotto al mestiere dell'astrofisico ed all'arte della spettroscopia, per aver costantemente corretto ed al tempo stesso incoraggiato e per aver continuamente ravvivato e accresciuto la mia passione per l'astrofisica. Di questo gli sono particolarmente grato. Un ringraziamento speciale va a Laura Magrini che, con un'eccezionale disponibilità e senso pratico, mi ha insegnato i trucchi del mestiere ed ha sempre voluto accogliere le mie richieste di aiuto dandomi l'idea giusta per risolvere le varie problematiche in cui mi sono imbattuto nel mio lavoro. Non posso dimenticarmi di Massimo Robberto: lo ringrazio moltissimo per la sua costante disponibilità ed i suoi consigli preziosi, ma anche per la sua amicizia. Vorrei ringraziare anche Elena Franciosini, Enrico Maiorca e Germano Sacco per essersi sempre interessati al mio lavoro contribuendo sia con suggerimenti, sia condividendo i tools del mestiere. Un ringraziamento anche a Lorenzo Morbidelli, altro infaticabile lavoratore di questo team, e Filippo Mannucci per i suoi commenti alla tesi.

Desidero ringraziare anche i miei amici che hanno sempre saputo sostenermi e sopportarmi, soprattutto in questi ultimi mesi di fatiche. In particolare ringrazio i miei fantastici coinquilini Ahmad, Garbu, Matteo e Simo che mi hanno sempre voluto bene e, nonostante la mia presenza-assenza da casa, mi hanno sempre fatto trovare un piatto caldo e non hanno subaffittato il mio letto. Ringrazio le mie amiche, colleghe e coinquiline del dungeon-dottorandi, Sara e Susi, per i loro instancabili "ciao, come stai?", "vieni a pranzo oggi?"

e "sali che ti prepariamo il caffe". Un ringraziamento particolare anche a Bausi, Benny, Emanuele, Francesco, Frosky, Lapo, Lizzy, Marta, Mati, MH (detta Macca), Tommi e tutti gli altri, perché la nostra grande amicizia ha resto questi anni di studio una bellissima avventura.

Last but not least, desidero ringraziare i miei genitori e la mia famiglia per la loro completa gratuità nell'offrirmi aiuti e sostegni di ogni tipo.

Bibliography

Adibekyan, V. Z., Figueira, P., Santos, N. C., et al. 2013, A&A, 554, A44

Adibekyan, V. Z., Santos, N. C., Sousa, S. G., et al. 2012, A&A, 543, A89

Alexander, R. D. & Armitage, P. J. 2006, ApJ, 639, L83

Allard, F., Homeier, D., & Freytag, B. 2011, in Astronomical Society of the Pacific Conference Series, Vol. 448, 16th Cambridge Workshop on Cool Stars, Stellar Systems, and the Sun, ed. C. Johns-Krull, M. K. Browning, & A. A. West, 91

Allen, L. E., Calvet, N., D'Alessio, P., et al. 2004, ApJS, 154, 363

Alonso, A., Arribas, S., & Martinez-Roger, C. 1996, A&A, 313, 873

Alonso, A., Arribas, S., & Martínez-Roger, C. 1999, A&AS, 139, 335

Alonso, A., Salaris, M., Arribas, S., Martínez-Roger, C., & Asensio Ramos, A. 2000, A&A, 355, 1060

Andrews, S. M. & Williams, J. P. 2005, ApJ, 631, 1134

Andrews, S. M., Wilner, D. J., Espaillat, C., et al. 2011, ApJ, 732, 42

Apai, D., Pascucci, I., Bouwman, J., et al. 2005, Science, 310, 834

Apai, D. A. & Lauretta, D. S. 2010, Protoplanetary Dust: Astrophysical and Cosmochemical Perspectives

Arce, H. G., Shepherd, D., Gueth, F., et al. 2007, Protostars and Planets V, 245

Bacciotti, F., Whelan, E. T., Alcalá, J. M., et al. 2011, ApJ, 737, L26

Baggett, S., e. a. 2002, ed. B. Mobasher, Baltimore, STScI

Bally, J. 2008, Overview of the Orion Complex, ed. B. Reipurth, 459

Bally, J., O'Dell, C. R., & McCaughrean, M. J. 2000, AJ, 119, 2919

Bally, J., Reipurth, B., & Davis, C. J. 2007, Protostars and Planets V, 215

Bally, J., Walawender, J., Luhman, K. L., & Fazio, G. 2006, AJ, 132, 1923

Baranne, A., Queloz, D., Mayor, M., et al. 1996, A&AS, 119, 373

Beckwith, S. V. W., Sargent, A. I., Chini, R. S., & Guesten, R. 1990, AJ, 99, 924

Belloche, A., Schuller, F., Parise, B., et al. 2011, A&A, 527, A145

Bensby, T., Zenn, A. R., Oey, M. S., & Feltzing, S. 2007, in Astronomical Society of the Pacific Conference Series, Vol. 374, From Stars to Galaxies: Building the Pieces to Build Up the Universe, ed. A. Vallenari, R. Tantalo, L. Portinari, & A. Moretti, 181

Bessell, M. S., Brett, J. M., Scholz, M., & Wood, P. R. 1991, A&AS, 89, 335

Biazzo, K., Alcalá, J. M., Covino, E., et al. 2012, A&A, 547, A104

Biazzo, K., Randich, S., & Palla, F. 2011a, A&A, 525, A35

Biazzo, K., Randich, S., Palla, F., & Briceño, C. 2011b, A&A, 530, A19

Blum, J. & Wurm, G. 2008, ARA&A, 46, 21

Boss, A. P. 1997, in Lunar and Planetary Inst. Technical Report, Vol. 28, Lunar and Planetary Institute Science Conference Abstracts, 137

Boss, A. P. 2002, ApJ, 568, 743

Bouvier, J., Alencar, S. H. P., Harries, T. J., Johns-Krull, C. M., & Romanova, M. M. 2007, Protostars and Planets V, 479

Bragaglia, A. 2014, in preparation

Brandt, J. C. & Maran, S. P. 1971, in Bulletin of the American Astronomical Society, Vol. 3, Bulletin of the American Astronomical Society, 396

Briceno, C., Calvet, N., Hernandez, J., et al. 2005, in Star Formation in the Era of Three Great Observatories

Briceno, C., Hartmann, L., & Martin, E. 1999, NOAO Proposal, 308

Brown, A. G. A., de Geus, E. J., & de Zeeuw, P. T. 1994, A&A, 289, 101

Buchhave, L. A., Latham, D. W., Johansen, A., et al. 2012, Nature, 486, 375

Burrows, C. & (U.S.), S. T. S. I. 1993, Hubble Space Telescope: wide field-planetary camera 2 instrument handbook, Hubble Space Telescope (Space Telescope Science Institute)

Cabrit, S. 2009, Observational Constraints to Steady Jet Models in Young Stars, ed. K. Tsinganos, T. Ray, & M. Stute, 247–257

Calvet, N., D'Alessio, P., Hartmann, L., et al. 2002, ApJ, 568, 1008

Cambresy, L. 1998, in Astrophysics and Space Science Library, Vol. 230, The Impact of Near-Infrared Sky Surveys on Galactic and Extragalactic Astronomy, ed. N. Epchtein, 157

Cambresy, L., Epchtein, N., Copet, E., et al. 1997, A&A, 324, L5

Carretta, E., Bragaglia, A., Gratton, R. G., & Tosi, M. 2004, A&A, 422, 951

Carroll, B. W. & Ostlie, D. A. 1996, An Introduction to Modern Astrophysics

Cayrel, R. 1988, in IAU Symposium, Vol. 132, The Impact of Very High S/N Spectroscopy on Stellar Physics, ed. G. Cayrel de Strobel & M. Spite, 345

Cieza, L. A., Padgett, D. L., Allen, L. E., et al. 2009, ApJ, 696, L84

Clarke, C. J. & Pringle, J. E. 2006, MNRAS, 370, L10

Colgan, S. W. J., Schultz, A. S. B., Kaufman, M. J., Erickson, E. F., & Hollenbach, D. J. 2007, ApJ, 671, 536

Comerón, F. 2008, The Lupus Clouds, ed. B. Reipurth, 295

Comerón, F., Fernández, M., Baraffe, I., Neuhäuser, R., & Kaas, A. A. 2003, A&A, 406, 1001

Comerón, F. & Reipurth, B. 2006, A&A, 458, L21

Comerón, F., Reipurth, B., Henry, A., & Fernández, M. 2004, A&A, 417, 583

Cunha, K. & Lambert, D. L. 1992, ApJ, 399, 586

Cunha, K. & Lambert, D. L. 1994, ApJ, 426, 170

Cunha, K., Smith, V. V., & Lambert, D. L. 1998, ApJ, 493, 195

Cutri, R. M., Skrutskie, M. F., van Dyk, S., et al. 2003, 2MASS All Sky Catalog of point sources.

Da Rio, N., Robberto, M., Soderblom, D. R., et al. 2010, ApJ, 722, 1092

De Marchi, G., Panagia, N., & Romaniello, M. 2010, ApJ, 715, 1

de Zeeuw, P. T., Hoogerwerf, R., de Bruijne, J. H. J., Brown, A. G. A., & Blaauw, A. 1999, AJ, 117, 354

Dias, W. S., Alessi, B. S., Moitinho, A., & Lépine, J. R. D. 2002, A&A, 389, 871

Dolan, C. J. & Mathieu, R. D. 2001, AJ, 121, 2124

Dolphin, A. E. 2009, PASP, 121, 655

Dominik, C., Blum, J., Cuzzi, J. N., & Wurm, G. 2007, Protostars and Planets V, 783

Donati, P. 2014, in preparation

D'Orazi, V., Biazzo, K., & Randich, S. 2011, A&A, 526, A103

D'Orazi, V. & Randich, S. 2009, A&A, 501, 553

D'Orazi, V., Randich, S., Flaccomio, E., et al. 2009, A&A, 501, 973

Eldridge, J. J. 2009, MNRAS, 400, L20

Ercolano, B. & Clarke, C. J. 2010, MNRAS, 402, 2735

Espaillat, C., Calvet, N., Luhman, K. L., Muzerolle, J., & D'Alessio, P. 2008, ApJ, 682, L125

Feigelson, E. D. & Lawson, W. A. 2004, ApJ, 614, 267

Flaherty, K. M., Pipher, J. L., Megeath, S. T., et al. 2007, ApJ, 663, 1069

Ford, A., Jeffries, R. D., & Smalley, B. 2005, MNRAS, 364, 272

Forestini, M. 1994, A&A, 285, 473

Freeman, K. & Bland-Hawthorn, J. 2002, ARA&A, 40, 487

Friel, E. D. 1995, ARA&A, 33, 381

Fruchter, A. & et al. 2009, HST MultiDrizzle Handbook

Fuhrmann, K. 2004, Astronomische Nachrichten, 325, 3

Furesz, G., Szentgyorgyi, A. H., & Meibom, S. 2008, in Precision Spectroscopy in Astrophysics, ed. N. C. Santos, L. Pasquini, A. C. M. Correia, & M. Romaniello, 287–290

Furlan, E., Luhman, K. L., Espaillat, C., et al. 2011, ApJS, 195, 3

Gatti, T., Natta, A., Randich, S., Testi, L., & Sacco, G. 2008, A&A, 481, 423

Gauvin, L. S. & Strom, K. M. 1992, ApJ, 385, 217

Gilli, G., Israelian, G., Ecuvillon, A., Santos, N. C., & Mayor, M. 2006, A&A, 449, 723

Gilmore, G. 2014, in preparation

Gilmore, G., Randich, S., Asplund, M., et al. 2012, The Messenger, 147, 25

Gómez, M. & Mardones, D. 2003, AJ, 125, 2134

Gómez, M., Persi, P., Marenzi, A. R., Roth, M., & Tapia, M. 2004, A&A, 423, 629

Gonzalez, G. 1998, in Astronomical Society of the Pacific Conference Series, Vol. 134, Brown Dwarfs and Extrasolar Planets, ed. R. Rebolo, E. L. Martin, & M. R. Zapatero Osorio, 431

Gonzalez, G. 2009, MNRAS, 399, L103

González Hernández, J. I., Caballero, J. A., Rebolo, R., et al. 2008, A&A, 490, 1135

Grave, J. M. C. & Kumar, M. S. N. 2009, A&A, 498, 147

Gray, D. F. 1992, Science, 257, 1978

Grevesse, N., Asplund, M., & Sauval, A. J. 2007, Space Sci. Rev., 130, 105

Guillout, P., Sterzik, M. F., Schmitt, J. H. M. M., Motch, C., & Neuhaeuser, R. 1998, A&A, 337, 113

Gullbring, E., Hartmann, L., Briceno, C., & Calvet, N. 1998, ApJ, 492, 323

Gustafsson, B., Edvardsson, B., Eriksson, K., et al. 2008, A&A, 486, 951

Gutermuth, R. A., Megeath, S. T., Muzerolle, J., et al. 2004, ApJS, 154, 374

Haisch, Jr., K. E., Jayawardhana, R., & Alves, J. 2004, in Bulletin of the American Astronomical Society, Vol. 36, American Astronomical Society Meeting Abstracts, 1365

Hartmann, L. 2001, AJ, 121, 1030

Hartmann, L., Calvet, N., Gullbring, E., & D'Alessio, P. 1998, ApJ, 495, 385

Haywood, M. 2008, A&A, 482, 673

Haywood, M. 2009, ApJ, 698, L1

Heiter. 2014, in preparation

Henize, K. G. & Mendoza v, E. E. 1973, ApJ, 180, 115

Henning, T., Pfau, W., Zinnecker, H., & Prusti, T. 1993, A&A, 276, 129

Hernández, J., Hartmann, L., Calvet, N., et al. 2008, ApJ, 686, 1195

Hillenbrand, L. A., Bauermeister, A., & White, R. J. 2008, in Astronomical Society of the Pacific Conference Series, Vol. 384, 14th Cambridge Workshop on Cool Stars, Stellar Systems, and the Sun, ed. G. van Belle, 200

Høg, E., Fabricius, C., Makarov, V. V., et al. 2000, A&A, 355, L27

Hoogerwerf, R., de Bruijne, J. H. J., & de Zeeuw, P. T. 2001, A&A, 365, 49

Humphreys, R. M. 1978, ApJS, 38, 309

Hünsch, M., Randich, S., Hempel, M., Weidner, C., & Schmitt, J. H. M. M. 2004, A&A, 418, 539

Ida, S. & Lin, D. N. C. 2004, in Bulletin of the American Astronomical Society, Vol. 36, AAS/Division of Dynamical Astronomy Meeting #35, 850

James, D. J., Melo, C., Santos, N. C., & Bouvier, J. 2006, A&A, 446, 971

Jeffries, R. D. 2014, in preparation

Jeffries, R. D., Littlefair, S. P., Naylor, T., & Mayne, N. J. 2011, MNRAS, 418, 1948

Jeffries, R. D., Naylor, T., Walter, F. M., Pozzo, M. P., & Devey, C. R. 2009, MNRAS, 393, 538

Johnson, J. A., Aller, K. M., Howard, A. W., & Crepp, J. R. 2010, PASP, 122, 905

Jones, B. F., Shetrone, M., Fischer, D., & Soderblom, D. R. 1996, AJ, 112, 186

Kang, W., Lee, S.-G., & Kim, K.-M. 2011, ApJ, 736, 87

Kenyon, S. J., Gomez, M., Marzke, R. O., & Hartmann, L. 1994, AJ, 108, 251

Kenyon, S. J. & Hartmann, L. 1995, ApJS, 101, 117

Kessler-Silacci, J., Augereau, J.-C., Dullemond, C. P., et al. 2006, ApJ, 639, 275

Kharchenko, N. V., Piskunov, A. E., Roeser, S., Schilbach, E., & Scholz, R.-D. 2005, VizieR Online Data Catalog, 344, 403

Kirk, H. & Myers, P. C. 2011, ApJ, 727, 64

Kraus, A. L. & Hillenbrand, L. A. 2007, ApJ, 662, 413

Krumholz, M. R. 2006, ApJ, 641, L45

Lada, C. J. & Wilking, B. A. 1984, ApJ, 287, 610

Lafrenière, D., Jayawardhana, R., Brandeker, A., Ahmic, M., & van Kerkwijk, M. H. 2008, ApJ, 683, 844

Lanzafame, A. 2014, in preparation

Laughlin, G. & Adams, F. C. 1997, ApJ, 491, L51

Lawson, W. A., Feigelson, E. D., & Huenemoerder, D. P. 1996, MNRAS, 280, 1071

Lejeune, T. & Schaerer, D. 2001, VizieR Online Data Catalog, 6102, 0

Lodders, K. 2003, Meteoritics and Planetary Science Supplement, 38, 5272

Lommen, D., Maddison, S. T., Wright, C. M., et al. 2009, A&A, 495, 869

López Martí, B., Eislöffel, J., Scholz, A., & Mundt, R. 2004, A&A, 416, 555

Lǿpez Martí, B., Jiménez-Esteban, F., Bayo, A., et al. 2013, A&A, 556, A144

Luhman, K. L. 2004, ApJ, 602, 816

Luhman, K. L. 2007, ApJS, 173, 104

Luhman, K. L. 2008a, Chamaeleon, ed. Reipurth, B., 169

Luhman, K. L. 2008b, in Handbook of Star Forming Regions. vol. 2, 169-212 (2008), 169–212

Luhman, K. L., Allen, L. E., Allen, P. R., et al. 2008, ApJ, 675, 1375

Luhman, K. L., Lada, C. J., Hartmann, L., et al. 2005, ApJ, 631, L69

Luhman, K. L. & Muench, A. A. 2008, ApJ, 684, 654

Magrini, L., Randich, S., Friel, E., et al. 2013, A&A, 558, A38

Magrini, L., Sestito, P., Randich, S., & Galli, D. 2009, A&A, 494, 95

Manara, C. F., Robberto, M., Da Rio, N., et al. 2012, ApJ, 755, 154

Mayor, M., Marmier, M., Lovis, C., et al. 2011, ArXiv e-prints

Mayor, M. & Queloz, D. 1995, Nature, 378, 355

Megeath, S. T., Allen, L. E., Gutermuth, R. A., et al. 2004, ApJS, 154, 367

Meibom, S., Andersen, J., & Nordstroem, B. 2002, VizieR Online Data Catalog, 338, 60187

Menten, K. M., Reid, M. J., Forbrich, J., & Brunthaler, A. 2007, A&A, 474, 515

Meyer, M. R., Hillenbrand, L. A., Backman, D., et al. 2006, PASP, 118, 1690

Miller, N. & Fortney, J. J. 2011, ApJ, 736, L29

Millour, F., Petrov, R. G., Chesneau, O., et al. 2007, A&A, 464, 107

Mohanty, S., Jayawardhana, R., & Basri, G. 2005, ApJ, 626, 498

Monet, A. K. B., Harris, H. C., & Hilton, J. 2008, in AAS/Division of Dynamical Astronomy Meeting, Vol. 39, AAS/Division of Dynamical Astronomy Meeting #39, #15.11

Morales-Calderón, M., Stauffer, J. R., Hillenbrand, L. A., et al. 2011, ApJ, 733, 50

Mordasini, C., Alibert, Y., Benz, W., Klahr, H., & Henning, T. 2012, A&A, 541, A97

Mordasini, C., Alibert, Y., Benz, W., & Naef, D. 2009, A&A, 501, 1161

Moultaka, J., Ilovaisky, S. A., Prugniel, P., & Soubiran, C. 2004, PASP, 116, 693

Muzerolle, J., Calvet, N., & Hartmann, L. 2001, ApJ, 550, 944

Muzerolle, J., D'Alessio, P., Calvet, N., & Hartmann, L. 2004, ApJ, 617, 406

Muzerolle, J., Hillenbrand, L., Calvet, N., Briceño, C., & Hartmann, L. 2003, ApJ, 592, 266

Muzerolle, J., Luhman, K. L., Briceño, C., Hartmann, L., & Calvet, N. 2005, ApJ, 625, 906

Natta, A., Meyer, M. R., & Beckwith, S. V. W. 2000, ApJ, 534, 838

Natta, A., Testi, L., & Randich, S. 2006, A&A, 452, 245

Neuhäuser, R. & Forbrich, J. 2008, The Corona Australis Star Forming Region, ed. B. Reipurth, 735

Neves, V., Santos, N. C., Sousa, S. G., Correia, A. C. M., & Israelian, G. 2009, A&A, 497, 563

Nissen, P. E. 1981, A&A, 97, 145

North, J. R., Tuthill, P. G., Tango, W. J., & Davis, J. 2007, MNRAS, 377, 415

O'Dell, C. R. & Henney, W. J. 2008, AJ, 136, 1566

O'dell, C. R. & Wen, Z. 1994, ApJ, 436, 194

Olano, C. A. 1982, A&A, 112, 195

Oliveira, J. M., Jeffries, R. D., Kenyon, M. J., Thompson, S. A., & Naylor, T. 2002, A&A, 382, L22

Padgett, D. L. 1996, ApJ, 471, 847

Padgett, D. L., Brandner, W., Stapelfeldt, K. R., et al. 1999, AJ, 117, 1490

Panagi, P. M. & O'dell, M. A. 1997, A&AS, 121, 213

Pascucci, I., Apai, D., Hardegree-Ullman, E. E., et al. 2008, ApJ, 673, 477

Pascucci, I. & Sterzik, M. 2009, ApJ, 702, 724

Pascucci, I. & Tachibana, S. 2010, The Clearing of Protoplanetary Disks and of the Protosolar Nebula, ed. D. A. Apai & D. S. Lauretta, 263–298

Pasquini, L., Avila, G., Blecha, A., et al. 2002, The Messenger, 110, 1

Pecaut, M. & Mamajek, E. E. 2012, in American Astronomical Society Meeting Abstracts, Vol. 219, American Astronomical Society Meeting Abstracts #219, 327.05

Perrot, C. A. & Grenier, I. A. 2003, A&A, 404, 519

Persi, P., Marenzi, A. R., Olofsson, G., et al. 2000, A&A, 357, 219

Pettersson, B. 2008, Young Stars and Dust Clouds in Puppis and Vela, ed. B. Reipurth, 43

Podio, L., Bacciotti, F., Nisini, B., et al. 2006, A&A, 456, 189

Pollack, J. B., Hubickyj, O., Bodenheimer, P., et al. 1996, Icarus, 124, 62

Poppel, W. 1997, Fund. Cosmic Phys., 18, 1

Pozzo, M., Jeffries, R. D., Naylor, T., et al. 2000, MNRAS, 313, L23

Preibisch, T. & Mamajek, E. 2008, The Nearest OB Association: Scorpius-Centaurus (Sco OB2), ed. B. Reipurth, 235

Preibisch, T. & Zinnecker, H. 2007, in IAU Symposium, Vol. 237, IAU Symposium, ed. B. G. Elmegreen & J. Palous, 270–277

Prisinzano. 2014, in preparation

Prugniel, P., Soubiran, C., Koleva, M., & Le Borgne, D. 2007, VizieR Online Data Catalog, 3251, 0

Randich, S. 2014, in preparation

Randich, S. & Gilmore, G. 2012, in Science from the Next Generation Imaging and Spectroscopic Surveys

Recio-Blanco, A. 2014, submitted

Reddy, B. E., Lambert, D. L., & Allende Prieto, C. 2006, VizieR Online Data Catalog, 736, 71329

Reggiani, M., Robberto, M., Da Rio, N., et al. 2011, A&A, 534, A83

Reipurth, B., Yu, K. C., Heathcote, S., Bally, J., & Rodríguez, L. F. 2000, AJ, 120, 1449

Ricci, L., Robberto, M., & Soderblom, D. R. 2008, AJ, 136, 2136

Ricci, L., Testi, L., Natta, A., et al. 2010, A&A, 512, A15

Richer, J. S., Shepherd, D. S., Cabrit, S., Bachiller, R., & Churchwell, E. 2000, Protostars and Planets IV, 867

Robberto, M., Beckwith, S. V. W., Panagia, N., et al. 2005, AJ, 129, 1534

Robberto, M., Song, J., Mora Carrillo, G., et al. 2004, ApJ, 606, 952

Robberto, M., Spina, L., Da Rio, N., et al. 2012, AJ, 144, 83

Robichon, N., Arenou, F., Mermilliod, J.-C., & Turon, C. 1999, VizieR Online Data Catalog, 334, 50471

Robitaille, T. P., Whitney, B. A., Indebetouw, R., & Wood, K. 2007, ApJS, 169, 328

Robitaille, T. P., Whitney, B. A., Indebetouw, R., Wood, K., & Denzmore, P. 2006, ApJS, 167, 256

Rydgren, A. E. 1980, AJ, 85, 444

Sacco, G. G. 2014a, in preparation

Sacco, G. G. 2014b, in preparation

Santos, N. C., Israelian, G., & Mayor, M. 2001, A&A, 373, 1019

Santos, N. C., Israelian, G., & Mayor, M. 2004, A&A, 415, 1153

Santos, N. C., Melo, C., James, D. J., et al. 2008, A&A, 480, 889

Schaerer, D., Schmutz, W., & Grenon, M. 1997, ApJ, 484, L153

Schegerer, A., Wolf, S., Voshchinnikov, N. V., Przygodda, F., & Kessler-Silacci, J. E. 2006, A&A, 456, 535

Schmidt, T. O. B., Neuhäuser, R., Seifahrt, A., et al. 2008, A&A, 491, 311

Schwartz, R. D. 1977, ApJS, 35, 161

Shen, Z.-X., Jones, B., Lin, D. N. C., Liu, X.-W., & Li, S.-L. 2005, ApJ, 635, 608

Sherry, W. H., Walter, F. M., Wolk, S. J., & Adams, N. R. 2008, AJ, 135, 1616

Sicilia-Aguilar, A., Hartmann, L., Calvet, N., et al. 2006, ApJ, 638, 897

Sicilia-Aguilar, A., Henning, T., & Hartmann, L. W. 2010, ApJ, 710, 597

Siess, L., Dufour, E., & Forestini, M. 2000, A&A, 358, 593

Siringo, G., Kreysa, E., Kovács, A., et al. 2009, A&A, 497, 945

Slawson, R. W. & Reed, B. C. 1988, JRASC, 82, 276

Smiljanic, R. 2014, in preparation

Smith, L. F. 1968, MNRAS, 141, 317

Smith, N., Bally, J., Shuping, R. Y., Morris, M., & Kassis, M. 2005, AJ, 130, 1763

Sneden, C. 1973, ApJ, 184, 839

Sneden, C., Bean, J., Ivans, I., Lucatello, S., & Sobeck, J. 2012, MOOG: LTE line analysis and spectrum synthesis, astrophysics Source Code Library

Soderblom, D. R., Jones, B. F., Balachandran, S., et al. 1993, AJ, 106, 1059

Soubiran, C., Le Campion, J.-F., Cayrel de Strobel, G., & Caillo, A. 2010, A&A, 515, A111

Sousa, S. G., Santos, N. C., Israelian, G., Mayor, M., & Monteiro, M. J. P. F. G. 2007, A&A, 469, 783

Sousa, S. G., Santos, N. C., Israelian, G., Mayor, M., & Udry, S. 2011, A&A, 533, A141

Sousa, S. G., Santos, N. C., Mayor, M., et al. 2008, A&A, 487, 373

Spezzi, L., de Marchi, G., Panagia, N., Sicilia-Aguilar, A., & Ercolano, B. 2012, MNRAS, 421, 78

Spina, L. 2014, submitted

Stauffer, J. R., Hartmann, L. W., Prosser, C. F., et al. 1997, ApJ, 479, 776

Stetson, P. B. & Pancino, E. 2008, PASP, 120, 1332

Sushch, I., Hnatyk, B., & Neronov, A. 2011, A&A, 525, A154

Szűcs, L., Apai, D., Pascucci, I., & Dullemond, C. P. 2010, ApJ, 720, 1668

Théado, S. & Vauclair, S. 2012, ApJ, 744, 123

Torra, J., Fernández, D., & Figueras, F. 2000, A&A, 359, 82

Udry, S., Benz, W., & von Steiger, R., eds. 2006, Planetary Systems and Planets in Systems

Valenti, J. A. & Fischer, D. A. 2005, in Protostars and Planets V, 8592

van Leeuwen, F. 2007, A&A, 474, 653

van Leeuwen, F. 2009, A&A, 500, 505

Viana Almeida, P., Santos, N. C., Melo, C., et al. 2009, A&A, 501, 965

Wang, H. & Henning, T. 2006, ApJ, 643, 985

Whelan, E. T., Ray, T. P., Bacciotti, F., et al. 2005, Nature, 435, 652

Whittet, D. C. B., Prusti, T., Franco, G. A. P., et al. 1997, A&A, 327, 1194

Wilden, B. S., Jones, B. F., Lin, D. N. C., & Soderblom, D. R. 2002, AJ, 124, 2799

Wuchterl, G., Guillot, T., & Lissauer, J. J. 2000, Protostars and Planets IV, 1081

Yasui, C., Kobayashi, N., Tokunaga, A. T., Saito, M., & Tokoku, C. 2010, ApJ, 723, L113

Zuckerman, B., Melis, C., Rhee, J. H., Schneider, A., & Song, I. 2012, ApJ, 752, 58